Title
Design, Analysis, Hybrid Testing and Orientation Control of a Floating Platform with Counter-Rotating Vertical-Axis Wind Turbines

Author
Kanner, Samuel Adam Chinman

Publication Date
2015

Peer reviewed|Thesis/dissertation

Design, Analysis, Hybrid Testing and Orientation Control of a Floating Platform with Counter-Rotating Vertical-Axis Wind Turbines

By

Samuel Adam Chinman Kanner

A dissertation submitted in partial satisfaction of the

requirements for the degree of

Doctorate of Philosophy

in

Engineering - Mechanical Engineering

in the

Graduate Division

of the

University of California, Berkeley

Committee in Charge:

Professor Ronald W. Yeung, Chair
Professor Ömer Savaş
Professor Dennis K. Lieu
Professor Per-Olof Persson

Fall 2015

Abstract

Design, Analysis, Hybrid Testing and Orientation Control of a Floating Platform with Counter-Rotating Vertical-Axis Wind Turbines

by

Samuel Adam Chinman Kanner

Doctor of Philosophy in Engineering - Mechanical Engineering

University of California, Berkeley

Professor Ronald W. Yeung, Chair

The design and operation of two counter-rotating vertical-axis wind turbines on a floating, semi-submersible platform is studied. The technology, called the Multiple Integrated and Synchronized Turbines (MIST) platform has the potential to reduce the cost of offshore wind energy per unit of installed capacity. Attached to the platform are closely-spaced, counter-rotating turbines, which can achieve a higher power density per planform area because of synergistic interaction effects. The purpose of the research is to control the orientation of the platform and rotational speeds of the turbines by modifying the energy absorbed by each of the generators of the turbines.

To analyze the various aspects of the platform and wind turbines, the analysis is drawn from the fields of hydrodynamics, electromagnetics, aerodynamics and control theory. To study the hydrodynamics of the floating platform in incident monochromatic waves, potential theory is utilized, taking into account the slow-drift yaw motion of the platform. Steady, second-order moments that are spatially dependent (i.e., dependent on the platform's yaw orientation relative to the incident waves) are given special attention since there are no natural restoring yaw moment. The aerodynamics of the counter-rotating turbines are studied in collaboration with researchers at the UC Berkeley Mathematics Department using a high-order, implicit, large-eddy simulation. An element flipping technique is utilized to extend the method to a domain with counter-rotating turbines and the effects from the closely-spaced turbines is compared with existing experimental data.

Hybrid testing techniques on a model platform are utilized to prove the controllability of the platform in lieu of a wind-wave tank. A 1:82 model-scale floating platform is fabricated and tested at the UC Berkeley Physical-Model Testing Facility. The vertical-axis wind turbines are simulated by spinning, controllable actuators that can be updated in real-time of the model scale. Under certain wind and wave headings, it is possible to control the orientation of the platform in regular waves to maximize the power output from the turbines. A time-domain numerical simulation tool is able to confirm some of the experimental findings, taking into account the decoupled properties of the slow-drift hydrodynamics and wind turbine aerodynamics. Future platform designs are discussed, including the French-based,

pre-commercial design from Nenuphar Wind, called the *TwinFloat*, which is closely related to concepts examined in the thesis.

Dedication

This work is dedicated to all of my family, friends, former coaches and teachers who instilled in me a belief that the only things in life worth pursuing require dedication, patience and perseverance.

"I really don't know why it is that all of us are so committed to the sea, except I think it's because in addition to the fact that the sea changes, and the light changes, and ships change, it's because we all came from the sea. And it is an interesting biological fact that all of us have in our veins the exact same percentage of salt in our blood that exists in the ocean, and, therefore, we have salt in our blood, in our sweat, in our tears. We are tied to the ocean. And when we go back to the sea - whether it is to sail or to watch it - we are going back from whence we came."

John F. Kennedy, September 14, 1962

Acknowledgments

First and foremost, I would like to acknowledge my adviser, Professor Ronald W. Yeung, who has guided me through this research project. Through his patient assistance he has helped me navigate the turbulent waters of aimlessness, indecision, and mistakes. He has supported me and my fellow colleagues in our dream of becoming world-class ocean engineers. I also must express my sincere gratitude to Professor Per-Olof Persson, who has introduced me to the field of computational fluid dynamics and allowed me the use of his numerical codes. Working beside him, I realized what is meant by the phrase a '10x' coder. He has been a role model for me in terms of work ethic, family-work balance, and professional career. Professor Dennis K Lieu made an extremely important suggestion regarding the generator rotors during the design phase of this project, for which I am grateful. Professor Ömer Savaş also provided helpful discussion when working on the aerodynamics of low-Reynolds airfoils. Of course, I would like to thank all four committee members for their efforts on my dissertation committee.

I must acknowledge all of the help I have received from current and former post-docs, graduate students and undergraduates who have worked in the Ocean Engineering Group: Dr. Yichen Jiang, Louis Couston, Dr. Nathan Tom, Daewoong Son, Farshad Madhi, Elena Koukina, Qian Zhong, Steffan Paiva, Aakash Agarwal and many others who provided ideas and their efforts to furthering this project. The staff members in the UC Berkeley Mechanical Engineering Machine Shop provided invaluable support and assistance when designing and building the model for this research. These staff members, Mick Franssen, Scott McCormick, Jesse Lopez and especially Gordon Long, are truly unheralded wizards of the Mechanical Engineering Department with their help in manufacturing custom-designed parts. Another UC Berkeley staff member, Tom Clark, was a great source of information for electro-mechanical devices, such as rotary encoders, motors, microprocessors, etc. I used the open-source software of countless individuals, most of whom I do not know their real names. Their contributions on the Arduino, Matlab, Simulink, Solidworks, LaTeX and other forums saved me untold hours of work.

Without the support of former advisers such as Professor Bill Titus of Carleton College and Professor Jim Lerczak of Oregon State University, I would never have ended up at such a high-caliber research university with funding for five years. I express my appreciation to the Department of Defense's National Defense Science and Engineering Graduate Fellowship as well as the NSF's Graduate Research Fellowship Program for providing generous funding that has allowed me to pursue my dreams. Finally I express my sincere gratitude to my parents, Susan and Alan, my sisters, Lisa and Lauren, and my partner, Emma Dobbins for their unwavering support and patience while I worked long hours in the lab and at the wave tank turning my ideas into reality.

Contents

List of Figures

List of Tables

Nomenclature

General

ν	Kinematic viscosity of fluid
Fr	Froude number $U/\sqrt{gL}$
g	Acceleration due to gravity
Kc	Keulegan-Carpenter number Uf/L
Re	Reynolds number UL/ν
t	Time

Chapter 2

(x_0^j, y_0^j)	Horizontal center of column j
$\bar{x}\bar{y}\bar{z}$	Slow-drift frame Cartesian coordinates
β_o	Incident wave direction
$\lambda_{jk}^{(\ell)}$	Damping in j^{th} direction due to motion in k^{th} direction of order ℓ
$\mathcal{X}_j^{(\ell)}$	Wave-exciting force in j^{th} direction of order ℓ
$\mu_{jk}^{(\ell)}$	Added mass in j^{th} direction due to motion in k^{th} direction of order ℓ
ν_o	Wave parameter, σ_o^2/g
ρ_o	Density of fluid (water)
σ_e	Encounter wave frequency
σ_o	Incident-wave frequency
θ_0	Total yaw displacement, $X_6 + \xi_6$
Θ_o	Yaw slow-drift displacement, X_6
ξ_j	Complex amplitude of body motion in j^{th} direction
a_i	Radius of i^{th} cylinder
A_o	Incident-wave amplitude
b_{jk}	Damping coefficient of mooring system in j^{th} direction due to motion in k^{th}

d_i Bottom clearance of i^{th} cylinder

h Water depth

I_b Yaw mass moment of inertia of floating body

I_r Yaw mass moment of inertia of turbine

k_o Incident-wave wavenumber

k_{jk} Stiffness coefficient of mooring system in j^{th} direction due to motion in k^{th}

M_{ij}^b Mass matrix of floating body

m_b Mass of floating body

m_o Nondimensional wavenumber, $k_o h$

N_{col} Number of columns on platform

N_t Truncation number

p Hydrodynamic pressure

p_a Atmospheric pressure

Q_e Total hydrodynamic yaw moment of platform

R_{ij} Distance between column i and column j

U_j Slow-drift velocity in j^{th} direction

$x'y'z'$ Body-fixed coordinates

X_j Slow-drift displacement in j^{th} direction

$x_j y_j z_j$ Slow-drift frame Cartesian coordinates, centered on cylinder j

XYZ Inertial Cartesian coordinates

Chapter 3

α Angle of attack

α_0 Pitch angle offset

$\bar{\theta}_1$ Turbine 1 azimuthal angle offset

$\bar{C}_p$ Power coefficient of isolated turbine

β_1 Incident wind direction

λ Tip-speed ratio, $\omega_1 R/U_\infty$

u_j Fluid velocity in j^{th} direction

ω_1 Turbine rotational speed

ρ_a Density of air

θ Azimuthal direction

c Chord length of airfoil

c_0 Chordwise blade mounting position

C_p^j Power coefficient of j^{th} turbine

C_T Tangential force coefficient $F_T/0.5\rho_a c^2 U_\infty^2$

N_b Number of blades on VAWT

R VAWT radius

t^* Normalized time, tU_∞/c

U_∞ Incident wind speed

Chapter 4

γ Gear ratio of planetary gearbox

ω_1^* Desired turbine rotational speed

ω_j Rotational velocity of Turbine j

θ_0 Azimuthal position of MIST Platform, $\Theta_o + \xi_6$

θ_0^* Desired platform yaw position

θ_j Azimuthal position of Turbine $j = 1, 2$

B_j Controllable damping of generator j

F_N^* Aerodynamic normal force

F_T Thrust/tangential force from actuator

F_T^* Aerodynamic thrust/tangential force

k_e Back-EMF constant of motor

L_g Terminal inductance of generator

R_g Terminal resistance of generator

R_j Controllable resistance in circuit of generator j

V_j Voltage induced by generator j

Chapter 5

y Output of MIMO system

θ_{gj} Azimuthal position of gearbox j

e_j Error of variable j

I_g Mass moment of inertia of gearboxes and generators

q_j State variable j

r_j Relative degree of j^{th} state

T_j Applied Torque from actuator j

T_j^* Aerodynamic torque on Turbine j, RF_T^*

T_{gj} Torque from generator j

u_j Control variable j

Chapter 1

Introduction

As fossil fuels supplies continue to dwindle and global warming becomes more of a pressing issue, countries around the world are looking to renewable energy to supply their citizens with clean, reliable, electrical power. Many political leaders, including those from the EU, US, China and Japan have mandated that their countries or states must produce a certain amount of electricity from these sources in the next few decades [5]. Although solar and nuclear energy have their merits, they also exhibit certain drawbacks. Nuclear energy has recently been spurned by governments in Germany and Japan over fears of its safety following the 2011 Fukushima Daiichi disaster [5]. However, nuclear plants can be built on a scale unrivaled by other renewable sources, on the order of gigawatts of power production. As Chinese manufacturers have entered the market, the efficiency of solar panels have been increasing while their unit costs have dropped. However, industrial-scale solar plants, using either photo-voltaic or solar concentrating technology, have not found public acceptance as much as residential rooftop installations. Meanwhile, the installed global capacity of wind energy has been increasing exponentially since the mid-1990s (see, for instance Figure 17, in [5]). Many industry experts believe that most of the ideal *onshore* installation sites in industrialized countries, such as the EU and US, have been exploited. Offshore wind has emerged as a relatively untapped sustainable resource, especially in deep water. We discuss the plentiful offshore wind resource specifically off of California in Section 1.1.1. Thus far, the cost of deepwater offshore wind has prohibited any commercial-scale installations to take place. The technology introduced in this thesis is an attempt to lower the cost of this technology per unit of installed capacity.

1.1 Motivation

The oil embargo and ensuing crisis in the 1970s led many governments to increase funding for renewable sources, such as wind energy. At this time, the wind community was testing many different types of wind turbines, including vertical and horizontal axis, with 2-4 blades in upwind and downwind configurations. Considering the main design constraints at the time, which were to maximize sub-MW, land-based turbine efficiency, vertical-axis wind turbines were proven to be inferior. Figure 1.1 compares the power coefficient of a BONUS 37-m horizontal-axis wind turbine with the Sandia 34-m two-speed vertical-axis wind turbine. A turbine's power coefficient will be defined explicitly in Chapter 3. For now, it can be considered a measure of a turbine's efficiency. The two-speed, vertical-axis wind turbine exhibits lower performance over the lower wind speeds, although the authors of [6] claim that a true variable speed turbine may reach the performance of a (mid-1990s) horizontal-axis turbine.

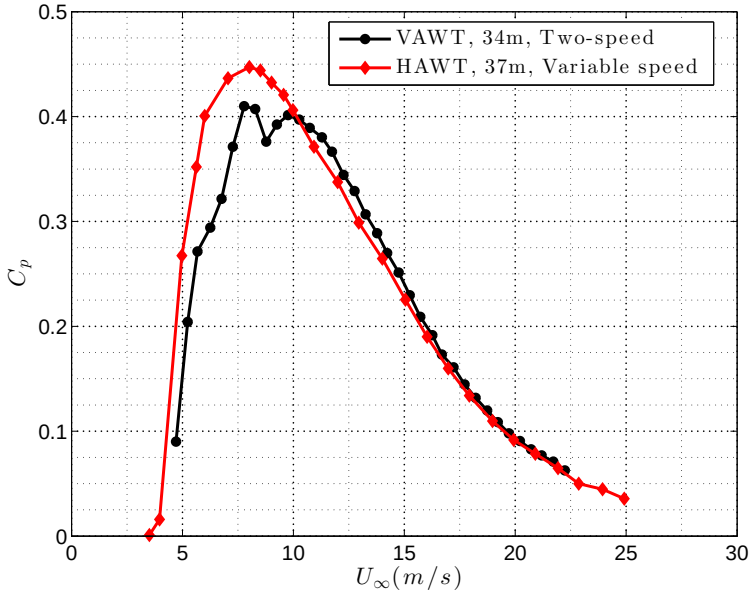

Figure 1.1: Power coefficients of Horizontal-Axis and Vertical-Axis wind turbines as a function of wind speed (VAWT data from [6]) .

Horizontal-axis wind turbine manufacturers have converged on a single design with a fairly high capacity factor: an upwind, three-bladed horizontal-axis turbine. However, this turbine is not necessarily the optimal design in a floating environment. A few inherent properties of HAWTs make them unattractive to the ocean engineer, as depicted in Fig 1.2:

- High center-of-gravity (mass of nacelle)
- Difficult to perform routine maintenance on drivetrain (large displacements of nacelle)
- Increased rotor size results in enhanced fatigue (operating cyclical gravity loads)

Thus, there is momentum in the offshore wind community to 'marinize' these wind turbines to make them more attractive to designers of floating platforms. By design, vertical-axis wind turbines do not have the characteristics described in the above bullet points. Researchers at Sandia National Laboratories [7], [8] as well as Cranfield University [9] have begun to create coupled aero-hydro-elastic codes (much like FAST [10] for vertical-axis wind turbines) to simulate floating turbines. We build upon this research, but instead focus on innovative ways to increase the power production of floating offshore wind turbines without a proportionate increase in the size and cost of the platform.

1.1.1 California's Offshore Wind Resource

California has an extensive offshore wind resource, which was estimated by researchers at Stanford University using the Penn State/National Center for Atmospheric Research *Mesoscale Model version 5* (MM5) and validated with offshore buoy data [11] from NOAA's

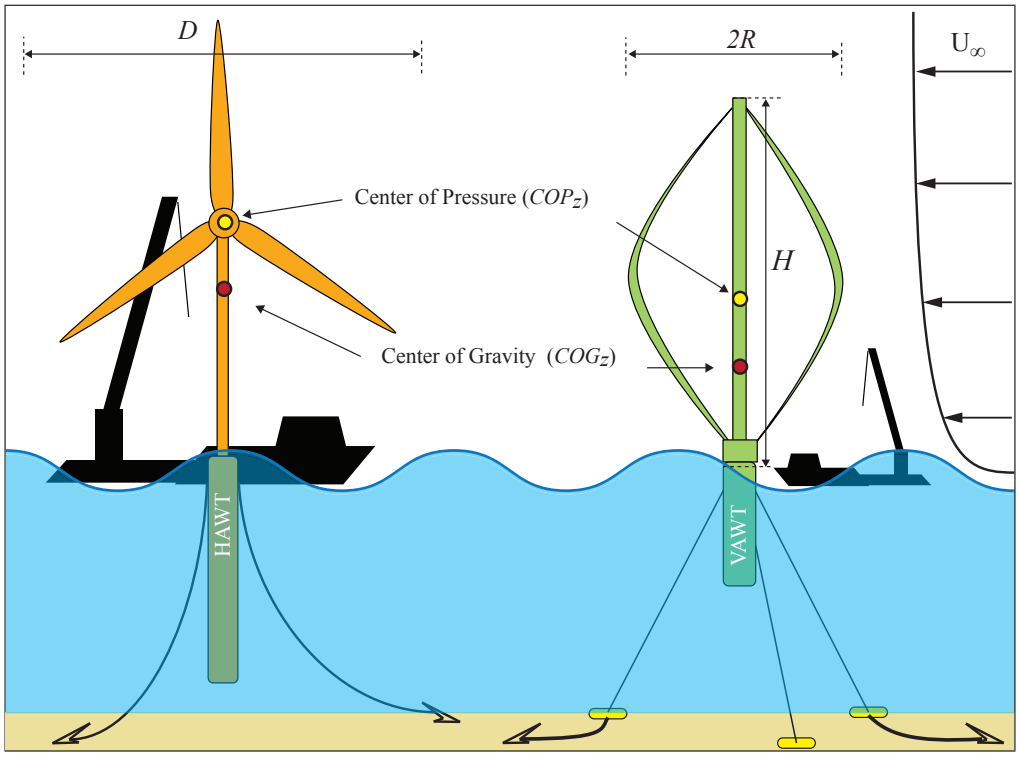

Figure 1.2: Depiction of floating horizontal-axis wind turbine (HAWT) and vertical-axis wind turbine (VAWT), with approximate centers of pressure and gravity.

National Buoy Data Center. The wind resource in California's state waters in water depths 0-200m is shown in Fig. 1.3, from [11]. As shown by the colors, the wind resource is much higher in northern California. An estimate of the total energy delivered from this resource is shown in Table 1.1, including all areas where the average wind speed is $\geq$ 7.0 m/s (NREL *Class 4*). The estimate includes a 33% exclusionary factor for shipping lanes, marine sanctuaries, etc. Further, the estimated resource has assumptions regarding the spacing of horizontal-axis wind turbines, $4D$ cross-stream and $7D$ downstream, which may be conservative for vertical-axis turbines (see Sec. 3.5). As shown in Table 1.1, the offshore resource in deep water ($\geq$ 50m) is more than 6 times that of shallow water. The deep water resource can only be feasibly accessed using floating technology. Further, as Table 1.1 shows, the total resource, including a 33% exclusionary factor, can meet California's electricity needs more than *twice* over.

1.2 Hybrid Testing

In order to validate numerical codes introduced in the literature, (e.g. the code introduced in [9]), model tests should be performed, with the floating structures subject to properly scaled wind and wave forces. As many authors note [12, 13, 14, 15, 16] , the model testing

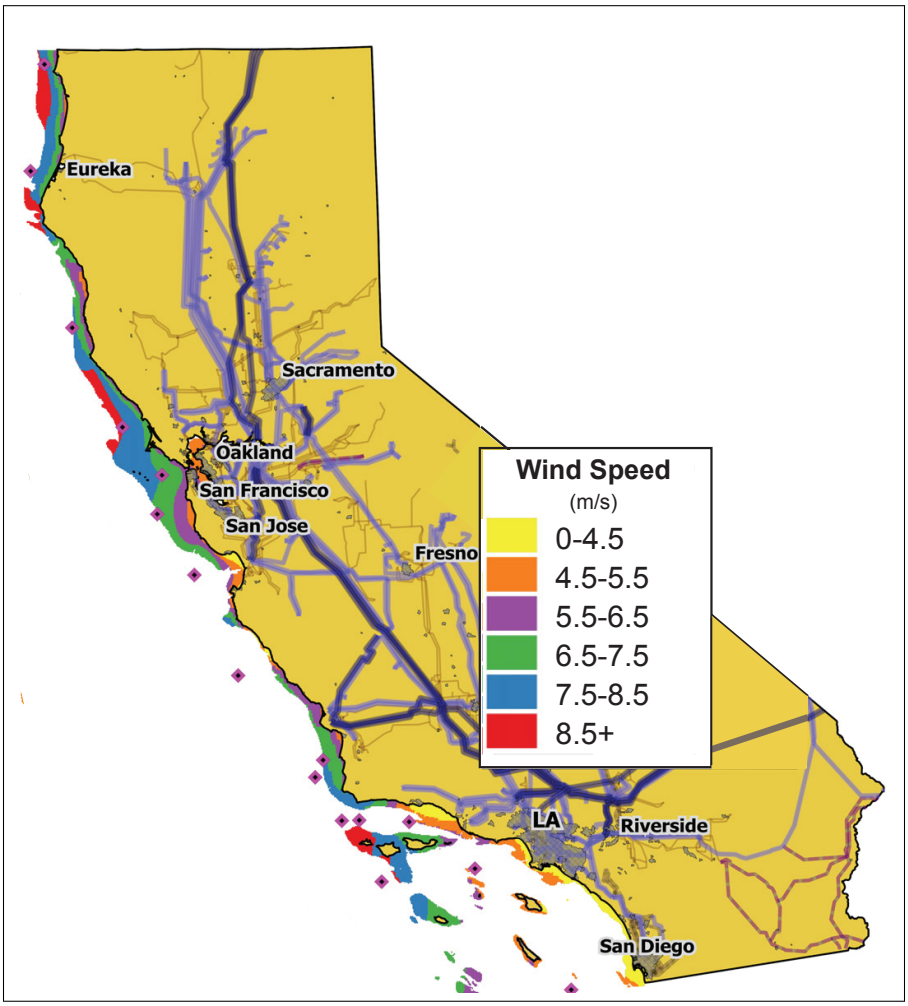

Figure 1.3: Map of average offshore wind speed in California in water depths 0-200 m (Adapted from [11]). Purple circles represent buoys from which wind data was garnered, while the onshore lines represent transmission lines, with thickness proportional to the voltage capacity.

Water Depth (m)	Northern CA (TWh)	Central CA (TWh)	Southern CA (TWh)	Total (TWh)	% CA consumption
0-50	40.2	19.3	23.2	92.7	31.4
50-200	195.9	204.6	167.8	568.3	192.6
Total	236.1	223.9	201.0	661.0	224.1

Table 1.1: Offshore wind resource in CA state waters based on water depth and region (Data from [11]).

of offshore wind turbines is especially difficult due to the scaling laws governing the various forces on such a structure. For instance, when testing a model platform, subject solely to waves, the testing parameters should be scaled according to Froude number Fr, since inertial forces dominate the system. The Fr number is

$$Fr = \frac{U}{\sqrt{gL}}, \tag{1.1}$$

where U and L are characteristic velocities and length-scales of the model, respectively, while g is acceleration due to gravity. A length-scale is normally used to define the scale of the model, such as,

$$\lambda_m = \frac{L_m}{L_p} \tag{1.2}$$

where L_p denotes the length of the full-scale prototype and L_m denotes the length of the model. When testing the resistance of a ship, for instance, the Fr must remain constant but the velocity of the model ship must be scaled by $\sqrt{\lambda_m}$ due to the following equations:

$$U_m = Fr\ \sqrt{gL_m} = \frac{\sqrt{gL_m}}{\sqrt{gL_p}} U_p = \sqrt{\lambda_m} U_p. \tag{1.3}$$

However, when testing a model turbine, or any such structure where viscous forces dominate the motions of the structure, the testing parameters should be scaled using the Re number, as defined in Sec. 2.8. Thus, the differences between these two scaling parameters set up an inherent contradiction when attempting to test a model-scale offshore wind turbine. Generally,

$$(Re)_m \neq (Re)_p \text{ when } (Fr)_m = (Fr)_p \tag{1.4}$$

In the recent literature, many researchers have decided to scale the entire model by Fr so that a model platform in a wave tank can be subject to actual waves. In order to take into account the change in the Re number, these researchers build a different model airfoil that attempts to provide the same lift and drag coefficients. Or, in the case of a wind turbine, they modify the turbine blades so that the turbine's thrust and torque coefficients remain the

same [17]. The lift and drag forces on these turbine blades are usually determined in wind tunnels where the airflow is generally laminar. Such a technique can pose problems when the actual thrust or torque of the turbine is difficult to measure in an experimental setting, such as an open-air wave tank. Moreover, it is difficult for a testing facility to produce laminar airflow above the free surface of a wave tank. Only a few locations exist in the world that can claim such testing facilities. To overcome these challenges, many researchers have suggested using hybrid simulation techniques, which combine numerical simulation and experimental testing [16]. This type of simulation technique was recently employed using a ducted fan in place of a horizontal-axis wind turbine in [13]. We will employ this testing technique when studying the technology introduced in this thesis.

1.3 Overview

This thesis will investigate a novel concept for floating vertical-axis turbines. Specifically, a triangular, semi-submersible floating platform supporting counter-rotating vertical-axis turbines will be investigated.

In Chapter 2, we introduce the hydrodynamics of a single, truncated floating cylinder in finite-depth waters undergoing slow-drift motion. The author's code for this application is benchmarked against the results from a well-developed in-house software [18] for a fixed cylinder. The velocity potential, describing the motion of the inviscid fluid particles is expanded in a double perturbation series with respect to the wave amplitude as well as the slow-drift velocities. The slow-drift motion introduces terms, such as the double-body added-mass as well as terms proportional to the amplitude of the response of the fast-scale motions. Furthermore, second-order, steady wave-exciting forces and moments, which can be represented by first-order terms are examined. We introduce how the hydrodynamic force can be transformed from the frequency domain into the time domain so that it can be useful for time-domain simulations. The method is then extended to multiple, interacting, truncated cylinders for the wave-exciting force, which results from the scattering potential. Results are shown in the frequency domain for a three-column, semi-submersible platform that was used for model testing.

In Chapter 3 the aerodynamics of vertical-axis wind turbines are discussed. First, a well-established blade-element momentum theory called the Double-Multiple Streamtube Method is introduced. The drawbacks of the model, including the need for experimental airfoil lift and drag data and dynamic stall modules motivate the discussion of higher-fidelity simulations of airfoils and turbines. Another in-house fluid dynamics software, utilizing a method known as Implicit Large Eddy Simulations (ILES), is briefly presented next. The method is used for three different applications, all of which are in the low-Reynolds regime: first, a single static airfoil over a wide range of angles of attack; second, a simple, two-bladed turbine that has detailed experimental data for validation; third, a pair of counter-rotating turbines with a variable distance between the rotors. These results are used to inform the types of forces to be applied to the model platform.

In Chapter 4 we introduce the Multiple Integrated Synchronized Turbine (MIST) platform. This semi-submersible, three-column platform has two, counter-rotating vertical axis wind turbines on two of the columns. The turbines are connected in such a way that constrains the turbines to rotate in equal and opposite directions. We discuss the concept of hybrid simulation and its application to the MIST platform. The experimental model platform and the related components, including the drivetrain, generators, circuit and control implementation are detailed. We briefly discuss the Wind-Input Generator (WIG) that was used to simulate the effect of the wind turbines on the platform. The communication system, which can send data between the microprocessors on the platform as well as to the datalogger, has redundant wired and wireless technologies. Data from the model tests concerning the open-loop control of the actuation system are presented.

In Chapter 5, we numerically recreate the model experiments described in Chapter 4, implementing the theory developed in Chapter 2. We detail how the constraints imposed by the drivetrain reduce the number of degrees of freedom in the system. In the numerical model, a non-linear control system can be used to control both the yaw position of the platform and the rotational velocity of the turbines. A type of non-linear control, called feedback linearization, is described and used to optimize the power from the turbines. We present results from simulations in the time-domain using the control software SIMULINK when the platform is subject to regular waves. The aerodynamics and hydrodynamics are decoupled, which is shown to be a reasonable assumption due to the minimal pitch and roll motion of the platform in operational sea states.

Chapter 6 includes some concluding remarks, including parallels with modern aerospace industry. We describe many of the ways the research could be extended and improved upon in the theoretical, numerical and experimental fields. Finally, we show a commercial development that has been inspired by this research.

Chapter 2

Hydrodynamics of Floating Body with Slow-Drift Motion

In this chapter we study the hydrodynamics of an array of cylinders undergoing slow-drift and wave-excited motion. This problem was studied extensively in the 1990s by the oil and gas industry during the development of tension-leg platforms (TLPs). These engineers realized that the motion of the platform consisted not only of high frequency motions, near the period of the dominant wave frequency, but also much lower frequency motions, with much slower velocities. These motions often occurred in the surge and sway directions where the restoring forces were much smaller (than for example, heave). Hence, the term 'slow-drift' motion. In fact, the interaction between the slow-drift motion and the waves, known as 'wave-drift damping' was first reported for a moored vessel in [19]. These researchers found that the logarithmic decrement of the slow-drift surge motion of the vessel, which was restrained by springs, was proportional to the square of the incident-wave height. Many contributions have been made since to this field, including [20, 21, 22, 23, 24, 25, 26, 27, 28, 29, 30]. In the present study we closely follow the derivation of Emmerhoff [20], who developed the equations of motion for the slow-drift motion and the wave-induced linear motion of an array of cylinders. We make a similar extension, as shown in [21], where we consider the total motion of the platform as a linear superposition of these two motions. However, unlike other researchers, we are interested in finding the forces on axisymmetric bodies, such as truncated cylinders, using the direct pressure integration method over the wetted surface. Instead of using discretization panels, like popular commercial software where the solution can depend on the discretization of the domain, we aim to find the slow-drift forces exactly on a non-interacting, multi-column platform using a quickly convergent series. We highlight the original contributions of this derivation with boxed equations.

2.1 Mathematical Formulation

We consider an array of floating truncated, vertical cylinders undergoing arbitrary slow-drift motion in the horizontal-plane (i.e. surge, sway, yaw motions). In this analysis, we consider the cylinders to be fixed rigidly to each other to form a platform and will freely interchange the term 'platform' with 'array of cylinders'. We define an inertial Cartesian coordinate system as $\mathcal{O}XYZ$, as shown in Fig. 2.1 with unit vectors $(\hat{\imath}, \hat{\jmath}, \hat{k})$. The plane $Z = 0$ coincides with the sea floor (assumed to be flat) with the Z-axis pointing upward. We introduce a non-inertial frame $\bar{\mathcal{O}}\bar{x}\bar{y}\bar{z}$ at the point $\boldsymbol{X_o} = [X_o(t), Y_o(t), 0]^T$ that is fixed on the slow-drift position of the structure. Thus a coordinate point may be described as $\boldsymbol{X} = [X, Y, Z]^T$ in the inertial coordinate system or $\bar{\boldsymbol{x}} = [\bar{x}, \bar{y}, \bar{z}]^T$ in the slow-drift system. The slow-drift

system moves relative to the inertial system with velocities defined by

$$\boldsymbol{\mathcal{U}_o} = \begin{bmatrix} \mathcal{U}_1 \\ \mathcal{U}_2 \\ 0 \end{bmatrix} = \begin{bmatrix} \dot{X}_o(t) \\ \dot{Y}_o(t) \\ 0 \end{bmatrix}, \tag{2.1a}$$

$$\boldsymbol{\Omega_o} = \begin{bmatrix} 0 \\ 0 \\ \mathcal{U}_6 \end{bmatrix} = \begin{bmatrix} 0 \\ 0 \\ \dot{\Theta}_o(t) \end{bmatrix}, \tag{2.1b}$$

where $(\dot{})$ denotes differentiation with respect to time. The transformations from the inertial system to the slow-drift system and vice-versa are defined as,

$$\bar{\boldsymbol{x}} = S(\Theta_o)(\boldsymbol{X} - \boldsymbol{X_o}), \tag{2.2a}$$

$$\boldsymbol{X} = \boldsymbol{X_o} + S^T(\Theta_o)\bar{\boldsymbol{x}}, \tag{2.2b}$$

with the matrix operator $S(\theta)$ defined as,

$$S(\theta) = \begin{bmatrix} \cos\theta & \sin\theta & 0 \\ -\sin\theta & \cos\theta & 0 \\ 0 & 0 & 1 \end{bmatrix}. \tag{2.3}$$

The rotation matrix S has the property that $S^T = S^{-1}$. Note that the since Θ_o is a function of time, the rotation matrix $S(\Theta_o)$ is as well. We will formulate the problem in the slow-drift system, where the slow horizontal velocities in this frame $\boldsymbol{U_o} = [U_1, U_2, 0]^T$ are,

$$\boldsymbol{U_o} = S(\Theta_o)\boldsymbol{\mathcal{U}_o}. \tag{2.4}$$

In this frame, the slow-drift accelerations are

$$\dot{\boldsymbol{U}}_{\boldsymbol{o}} = \frac{d}{dt}\left[S(\Theta_o)\boldsymbol{\mathcal{U}_o}\right] = \dot{S}(\Theta_o)\boldsymbol{\mathcal{U}_o} + S(\Theta_o)\dot{\boldsymbol{\mathcal{U}}}_{\boldsymbol{o}}. \tag{2.5}$$

The rotational velocity vector $\boldsymbol{\Omega_o}$ remains unchanged in the slow-drift frame of reference ($\mathcal{U}_6 = U_6$). Thus, the slow-drift acceleration in the horizontal plane $\dot{\boldsymbol{U}}_{\boldsymbol{b}} = [\dot{U}_1, \dot{U}_2, \dot{U}_6]^T$ can be represented by,

$$\dot{\boldsymbol{U}}_{\boldsymbol{b}} = \dot{S}(\Theta_o)\boldsymbol{\mathcal{U}_o} + S(\Theta_o)\dot{\boldsymbol{\mathcal{U}}}_{\boldsymbol{o}} + \dot{\boldsymbol{\Omega}}_{\boldsymbol{o}}. \tag{2.6}$$

The effective velocity is $\boldsymbol{s}$, defined by

$$\boldsymbol{s} = \boldsymbol{U_o} + \boldsymbol{\Omega_o} \times \bar{\boldsymbol{x}}, \tag{2.7}$$

representing the absolute translational velocity of a point $\bar{\boldsymbol{x}}$ in the $\bar{\mathcal{O}}\bar{x}\bar{y}\bar{z}$ frame.

The body is subject to monochromatic surface waves with height A_o, angular frequency σ_o ($2\pi/T_o$), wave number k_o (or $2\pi/\lambda_o$) , and wave heading β_o, which is defined relative to the $X-$ axis, as shown in Fig. 2.1. The water depth is denoted by h, as shown in Fig. 2.4.

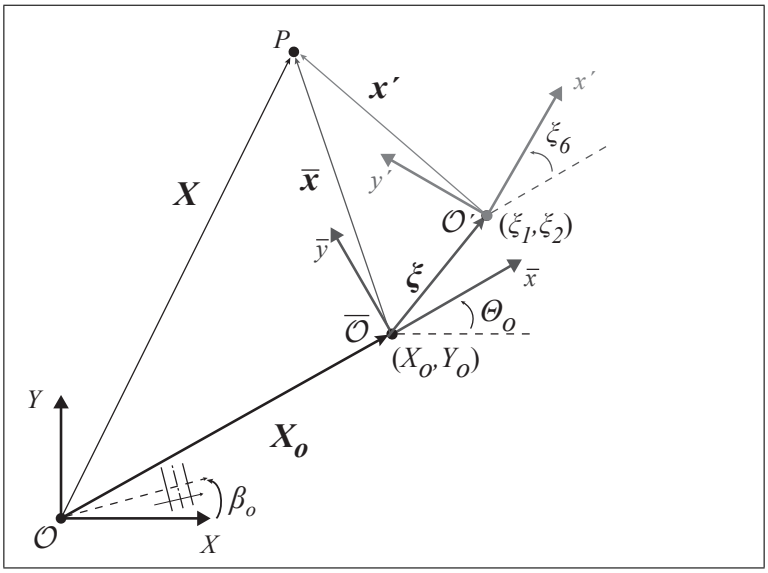

Figure 2.1: Schematic for inertial, ($\mathcal{O}XYZ$) slow-drift, ($\bar{\mathcal{O}}\bar{x}\bar{y}\bar{z}$) and body-fixed ($\mathcal{O}'x'y'z'$) coordinate systems, with incident wave angle β_o, relative to the inertial frame. All coordinate systems are coplanar on seafloor ($Z = 0$).

2.2 Motivation for Theoretical Development

As mentioned in the previous section, the desire to account for slow-drift motions in the development of the hydrodynamic forces arose from observations, such as those noticed by Wichers [19]. Likewise, in this study, a multi-column platform was built to support wind turbines and was tested in monochromatic waves. The single point mooring system, described in more detail in Sec. 2.5.4, allowed the platform to yaw, but restricted the drift motion in the surge and sway modes. In order to get a baseline understanding of the hydrodynamic yaw moment on the platform, the multi-column hull was subject to monochromatic waves of varying incident wave-heading angle β_o (with no other external forces on the platform). The experimental results from one such wave heading is shown in Fig. 2.2. The yaw motion is shown in blue and clearly consists of a linear response to the incident wave (ξ_6) and a slow-drift response (Θ_o). The pitch and roll motions, shown in green and red, respectively, exhibit simply a linear response (represented by the linear displacements ξ_j, to be formally defined in Sec. 2.3.3). The platform used in this case-study is described in greater detail in Sec. 2.7. The fast yaw oscillations of the platform match up exactly with the frequency of the incident-wave ($\sigma_o = 2\pi/1.1$ rad/sec), while the slow oscillations occur on a scale that is over an order of magnitude larger.

The results from the experimental tests are shown here to provide the reader with motivation to delve into the hydrodynamics of the slow-drift formulation. The question that drives this theoretical development is the nature of the moment that is causing the platform to undergo slow-drift yaw. The linear excitation of the platform in yaw is well-understood and not of major interest. However, the slow-drift moment, which causes a non-zero rotational velocity is clearly on a time-scale that is much slower than that of the incident wave.

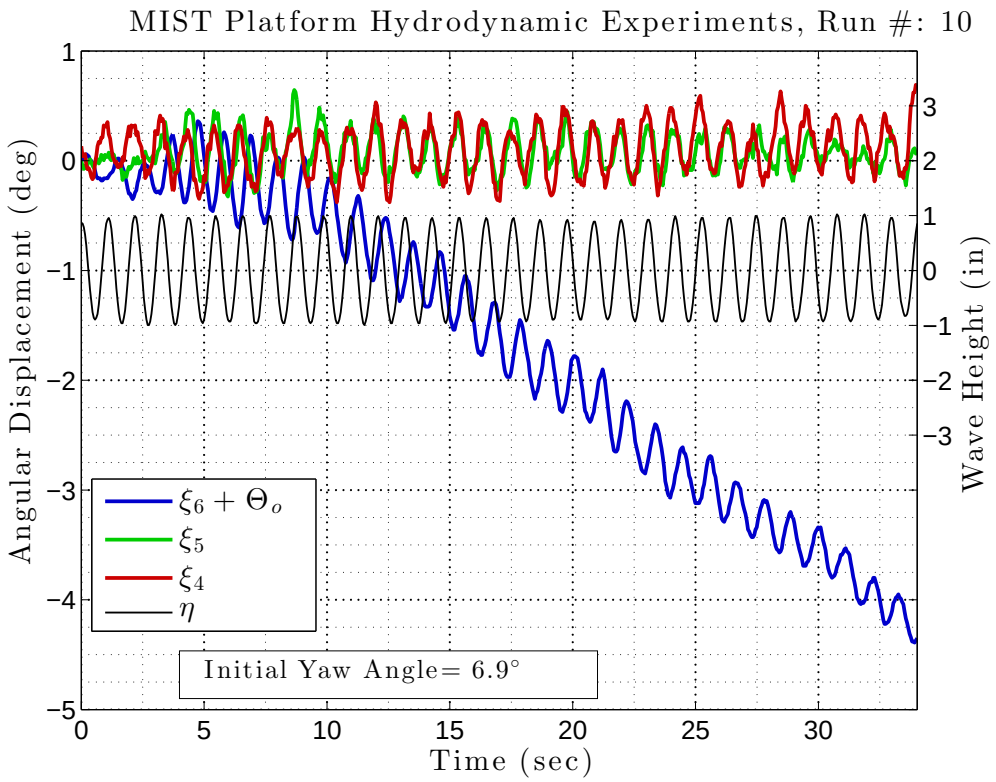

Figure 2.2: Typical response of model-scale (1:82.3) platform in yaw ($\xi_6 + \Theta_o$, blue curve), pitch (ξ_5, green curve) and roll (ξ_4, red curve) motions in monochromatic waves (wave height η, with T_o=1.1 sec, A_o= 1 in).

We shall prove in Appendix F.3, that without taking into account the slow-drift motion and with our assumptions that U_1 and U_2 are negligible, the steady (second-order) moment on the platform is null. Thus, we seek to describe this steady yaw moment on the platform using potential flow theory. Furthermore, the inclusion of the effect of viscosity will largely only effect the damping of the platform rather than the (steady) moment. Since there is no restoring moment in yaw and the yaw moment-of-inertia is quite large, once an external moment is applied to the platform it is quite difficult to reverse the rotational velocity of the platform. This effect can have significant consequences when trying to optimize power production from the wind turbines, as attempted in Chapter 5.

2.3 Boundary Value Problem for Velocity Potential

For now, we assume the fluid is ideal, such that it is inviscid and incompressible, and hence irrotational. In the inertial frame, we can define a velocity potential $\Phi(\boldsymbol{X}, t)$ that describes the velocity of the fluid particles. In the fluid domain it must satisfy a conservation of mass

statement, which is Laplace's equation,

$$\nabla^2\Phi = 0. \tag{2.8}$$

2.3.1 Boundary Conditions in Inertial Frame

In order to define a well-posed boundary value problem, the boundary conditions must be specified. The domain is bounded by a free-surface $Z = \eta(X, Y, t) + h$, a flat sea-bed ($Z = 0$) and floating body. Although they will not be specified explicitly here, far-field conditions need to be enforced so that the velocity of the fluid particles decay as $X, Y \to \infty$.

Free-Surface

Two conditions relating the continuity of fluid momentum and velocity must be specified at the boundary represented by the free-surface ($Z = \eta + h$). The unsteady, incompressible Euler momentum equation relates the pressure of the fluid on the free-surface with the fluid particle velocities as,

$$\left\{ \frac{p - p_a}{\rho_o} + \frac{\partial\Phi}{\partial t} + g\eta + \frac{1}{2}(\nabla\Phi \cdot \nabla\Phi) \right\} \Bigg|_{Z=\eta+h} = 0 \tag{2.9}$$

where p represents the hydrodynamic pressure, p_a represents the atmospheric air pressure and g represents the acceleration due to gravity. The dynamic free-surface boundary condition comes from the enforcement of pressure continuity across the free-surface, which means that the pressure at the free surface must equal the atmospheric pressure. Hence, the first term in Eq. (2.9) disappears. We take the material derivative of both sides of Eq. (2.9), which simplifies the analysis when we write the final, combined free-surface boundary condition. Mathematically,

$$\frac{\mathcal{D}}{\mathcal{D}t} \left\{ \frac{\partial\Phi}{\partial t} + g\eta + \frac{1}{2}(\nabla\Phi \cdot \nabla\Phi) \right\} \Bigg|_{Z=\eta+h} = 0. \tag{2.10}$$

Here, the material derivative is represented by $\mathcal{D}/\mathcal{D}t$, which is the time rate of change of a quantity, taking into account the transport by the moving fluid, itself. This operator can be represented as,

$$\frac{\mathcal{D}}{\mathcal{D}t} = \frac{\partial}{\partial t} + \nabla\Phi \cdot \nabla. \tag{2.11}$$

The expansion of Eq. (2.10) while utilizing Eq. (2.11), results in

$$\left(\frac{\partial^2\Phi}{\partial t^2} + g\frac{\partial\eta}{\partial t} + 2\nabla\Phi \cdot \frac{\partial\nabla\Phi}{\partial t} + \frac{1}{2}\nabla\Phi \cdot \nabla(\nabla\Phi \cdot \nabla\Phi) + g\nabla\Phi \cdot \nabla\eta \right) \Bigg|_{Z=\eta+h} = 0. \tag{2.12}$$

Solving for the free-surface in Eq. (2.10) (before the application of the material derivative), provides us the following expression for the free-surface:

$$\eta(X, Y, t) = -\frac{1}{g} \left(\frac{\partial\Phi}{\partial t} + \frac{1}{2}(\nabla\Phi \cdot \nabla\Phi) \right) \Bigg|_{Z=\eta+h}. \tag{2.13}$$

The kinematic free-surface boundary condition, requiring fluid particles on the free-surface to remain on the free-surface, can simply be written as,

$$\frac{\mathcal{D}(Z-(\eta+h))}{\mathcal{D}t}=0. \tag{2.14}$$

Again, we use the definition of the material derivative in Eq. (2.11), to rewrite the above equation as,

$$\left(-\frac{\partial\eta}{\partial t}+\frac{\partial\Phi}{\partial Z}-\nabla\Phi\cdot\nabla\eta\right)\Bigg|_{Z=\eta+h}=0. \tag{2.15}$$

The combination of Eqs. (2.12) and (2.15), results in the *combined, fully non-linear, free-surface boundary condition*, which is

$$\left(\frac{\partial^2\Phi}{\partial t^2}+2\nabla\Phi\cdot\frac{\partial\nabla\Phi}{\partial t}+\frac{1}{2}\nabla\Phi\cdot\nabla(\nabla\Phi\cdot\nabla\Phi)+g\frac{\partial\Phi}{\partial Z}\right)\Bigg|_{Z=\eta+h}=0 \tag{2.16}$$

where all derivatives are understood to be taken with respect to the inertial frame. This formulation of the free-surface boundary condition, which only involves the scalar quantity Φ, can be found in [31], among others.

Body

On the body, the fluid particles cannot penetrate the body and their normal velocity must equal that of the body. That is,

$$\boldsymbol{N_o}\cdot\nabla\Phi\Big|_{\boldsymbol{X}=\mathcal{B}(t)}=\boldsymbol{N_o}\cdot\boldsymbol{V_b}, \tag{2.17}$$

where $\boldsymbol{N_o}$ is the normal vector pointing into the body and $\mathcal{B}(t)$ denotes the time-varying submerged surface of the body, and $\boldsymbol{V_b}$ is the velocity of the body boundary.

Sea-Bed

On the flat bottom, a no-penetration conditions holds such that,

$$\frac{\partial\Phi}{\partial Z}\Big|_{Z=0}=0, \tag{2.18}$$

which holds in all frames of reference, replacing Z with z.

2.3.2 Double Perturbation Series

Let $\phi(\boldsymbol{x},t)=\Phi(\boldsymbol{X},t)$ be defined as the velocity potential in the slow-drift frame. To simplify the problem we take advantage of two independently small parameters in our study– the wave-slope parameter ϵ and the slow-drift parameter τ. Here, we assume that $U_o=\mathrm{O}\left(U_1\right)=$

$\mathrm{O}(U_2) = \mathrm{O}(RU_6)$, where R is a typical distance from a cylinder to its center of rotation. The orders of magnitude of the small parameters are,

$$\mathrm{O}(\epsilon) = \mathrm{O}(k_o A_o) \tag{2.19a}$$

$$\mathrm{O}(\tau) = \mathrm{O}\left(\frac{U_o \sigma_o}{g}\right) \tag{2.19b}$$

The results in Fig. 2.2 validate our assumption here that the slow-drift angular velocity of the semi-submersible platform is at least an order of magnitude smaller than the wave frequency. We assume we can write the velocity potential ϕ as a perturbation series expansion as,

$$\phi(\boldsymbol{x}, t) = \underbrace{\phi_{10}(\boldsymbol{x}, t)}_{\mathrm{O}(\epsilon)} + \underbrace{\phi_{01}(\boldsymbol{x}, t)}_{\mathrm{O}(\tau)} + \underbrace{\phi_{11}(\boldsymbol{x}, t)}_{\mathrm{O}(\tau\epsilon)} + \underbrace{\phi_{20}(\boldsymbol{x}, t)}_{\mathrm{O}(\epsilon^2)} + \mathrm{O}\left(\epsilon^2\tau, \epsilon\tau^2\right) \tag{2.20}$$

where we have neglected the interactions among the slow-drift velocities $\mathrm{O}(\tau^2)$. The double-body potential φ_{01} is also known as the steady disturbance potential, which represents the velocity potential for a drifting body without the presence of waves. The linear potential φ_{10} represents the first-order (in the wave-slope) velocity potential for a body is that not drifting but is subject to incident waves. The potential that includes leading order terms in both wave-slope and slow-drift, φ_{11}, represents the 'forward-speed' correction for a body moving in waves. This potential is well-known in the field of ship hydrodynamics, where ships advance with a constant speed and interact with incident-waves. In this analysis, we call this potential the interaction potential between the (linear) body and slow-drift motion. The other second-order velocity potential ϕ_{20} represents the effect of the sum and difference wave frequencies on the body. As mentioned previously, we are only interested in the steady, second-order forces and moments on the platform. Thus, we only consider the difference frequency second-order potential, which, for a monochromatic wave, is time-independent, denoted by $\bar{\phi}_{20}$.

We can also write the free-surface in a perturbation series, except that there is no contribution from $\mathrm{O}(\tau)$, as

$$\eta(\boldsymbol{x}, t) = \underbrace{\eta_{10}(\boldsymbol{x}, t)}_{\mathrm{O}(\epsilon)} + \underbrace{\eta_{11}(\boldsymbol{x}, t)}_{\mathrm{O}(\tau\epsilon)} + \underbrace{\eta_{20}(\boldsymbol{x}, t)}_{\mathrm{O}(\epsilon^2)} + \mathrm{O}\left(\epsilon^2\tau, \epsilon\tau^2\right) \tag{2.21}$$

The expressions for the linear and higher-order free-surface representations can be obtained once the solutions of the corresponding velocity potentials are known.

In the slowly-rotating frame of reference, the fluid undergoes a slow uniform rotation. The time derivative of Φ in this frame of reference is

$$\frac{\partial \Phi}{\partial t} = \left(\frac{\bar{\partial}}{\bar{\partial} t} - \boldsymbol{s} \cdot \nabla\right) \phi \tag{2.22}$$

where we have followed the notation in [23] rather than [25]. For clarity, we henceforth drop the 'bar' superscript from the partial derivatives and the spatial variables, $(\bar{x}\bar{y}\bar{z}) = (xyz)$.

We use a Taylor expansion of the right-hand side of Eq. (2.13) about the still-water plane $z = h$, and Eq. (2.22) to match orders in the perturbation series of the free surface, which allows us to write,

$$\eta_{10} = -\frac{1}{g}\frac{\partial \phi_{10}}{\partial t}\bigg|_{z=h}, \tag{2.23a}$$

$$\eta_{11} = -\frac{1}{g}\left(\frac{\partial \phi_{11}}{\partial t} + (\nabla\phi_{01} - \boldsymbol{s})\cdot\nabla\phi_{10}\right)\bigg|_{z=h}. \tag{2.23b}$$

We can explicitly separate the time-harmonic part of the potentials, such that

$$\phi_{kj}(\boldsymbol{x}, t) = \begin{cases} \mathrm{Re}\left[\varphi_{kj}(\boldsymbol{x})e^{-i\sigma_e t}\right], \text{ for } k = 1 \\ \mathrm{Re}\left[\varphi_{kj}(\boldsymbol{x})\right], \text{ otherwise} \end{cases} \tag{2.24}$$

where the encounter frequency σ_e is defined in Eq. (2.25) and we only include the time-independent terms of the $\mathrm{O}(\epsilon^2)$, thereby neglecting the double frequency terms, which have little effect on the global motions of the platform in regular sea-states. The encounter frequency is

$$\sigma_e = \sigma_o - k_o\left(U_1\cos\beta + U_2\sin\beta\right), \tag{2.25}$$

which is the wave frequency the body encounters after taking into account its slow-drift motions. For generality, we shall keep using the encounter frequency σ_e in the theoretical development, though it is important to note here that for our case where U_1 and U_2 are small, $\sigma_e = \sigma_o$. Here, β is the wave direction as felt by an observer in the slow-drift fame, such that

$$\beta(t) = \beta_o - \Theta_o(t). \tag{2.26}$$

Note that the time-derivatives of the velocity potentials of $\mathrm{O}(\tau)$ must include the time-dependent slow-drift velocities as,

$$\begin{aligned}
\frac{\partial \phi}{\partial t} &= \mathrm{Re}\left[\frac{\partial}{\partial t}(\varphi_{01} + [\varphi_{10} + \varphi_{11}]e^{-i\sigma_e t} + \mathrm{O}\left(\epsilon^2\tau\right))\right] \\
&= \mathrm{Re}\left[\left(-i\sigma_e(\varphi_{10} + \varphi_{11}) + \frac{d\Theta_o}{dt}\frac{\partial}{\partial\Theta_o}(\varphi_{10} + \varphi_{11})\right)e^{-i\sigma_e t}\right] \\
&= \mathrm{Re}\left[\left(\underbrace{-i\sigma_o\varphi_{10}}_{\mathrm{O}(\epsilon)} \underbrace{- i\sigma_o\varphi_{11} + ik_o(U_1\cos\beta + U_2\sin\beta)\varphi_{10} - U_6\frac{\partial\varphi_{10}}{\partial\beta}}_{\mathrm{O}(\epsilon\tau)}\right)e^{-i\sigma_e t}\right] + \mathrm{O}\left(\epsilon^2\tau\right)
\end{aligned} \tag{2.27}$$

To simplify notation, let the operator $\mathcal{L}_e[\varphi]$ be related to the last three terms of the final expression in Eq. (2.27) as,

$$\mathcal{L}_e[\varphi] = ik_o(U_1\cos\beta + U_2\sin\beta)\varphi - U_6\frac{\partial\varphi}{\partial\beta} \tag{2.28}$$

2.3.3 Body Motion

In order to simplify the non-linear body boundary condition found in Eq. (2.17), we can make some assumptions on the types of motion the body can undergo. As shown in Fig. 2.1, we define another Cartesian coordinate system relative to the slow-drift system that is body-fixed, denoted by $\mathcal{O}'x'y'z'$. We assume that the body experiences small-amplitude oscillatory motion of $\mathrm{O}(\epsilon)$ with respect to the slow-drift frame due to the linear excitation from the incident waves. Let $\boldsymbol{\xi}$ denote the translational modes and $\boldsymbol{\alpha}$ denote the rotational modes, such that

$$\boldsymbol{\xi} = \begin{bmatrix} \xi_1 \\ \xi_2 \\ \xi_3 \end{bmatrix}, \quad \boldsymbol{\alpha} = \begin{bmatrix} \xi_4 \\ \xi_5 \\ \xi_6 \end{bmatrix} \tag{2.29}$$

We restrict our focus to motion in the horizontal plane, such that $\xi_3 = \xi_4 = \xi_5 = 0$. The small-amplitude motion can be described using complex notation as

$$\xi_j = \mathrm{Re}\left[\mathcal{A}_j e^{-i\sigma_e t}\right], \tag{2.30}$$

where $i = \sqrt{-1}$, unless it is used in a summation, subscript or superscript. The amplitude of motion $\mathcal{A}_j$ can be complex valued since the phase of the body motion may lead or lag the phase of the incident wave. It follows from the perturbation series expansion described in Sec. 2.3.2 to expand the complex motion amplitude in terms of a perturbation series as

$$\xi_j = \underbrace{\xi_j^{(0)}}_{\mathrm{O}(\epsilon)} + \underbrace{\xi_j^{(1)}}_{\mathrm{O}(\tau\epsilon)} + \mathrm{O}\left(\tau^2\right). \tag{2.31}$$

Likewise, the complex motion amplitude can be decomposed as,

$$\mathcal{A}_j = \underbrace{\mathcal{A}_j^{(0)}}_{\mathrm{O}(\epsilon)} + \underbrace{\mathcal{A}_j^{(1)}}_{\mathrm{O}(\tau\epsilon)} + \mathrm{O}\left(\tau^2\right). \tag{2.32}$$

When we consider the various velocity potentials, the radiation potential will be multiplied by the time derivative of these small-amplitude oscillations ξ_j. It useful to remember that the time derivative of these complex motions can be expressed as,

$$\begin{aligned}
\frac{d\xi_j}{dt} &= \mathrm{Re}\left[\left(-i\sigma_e(\mathcal{A}_j^{(0)} + \mathcal{A}_j^{(1)}) + \frac{d}{dt}(\mathcal{A}_j^{(0)} + \mathcal{A}_j^{(1)})\right) e^{-i\sigma_e t} + \mathrm{O}\left(\epsilon^2\tau\right)\right] \\
&= \mathrm{Re}\left[\left(-i\sigma_e(\mathcal{A}_j^{(0)} + \mathcal{A}_j^{(1)}) + \frac{d\Theta_o}{dt}\frac{\partial}{\partial\Theta}(\mathcal{A}_j^{(0)} + \mathcal{A}_j^{(1)})\right) e^{-i\sigma_e t}\right] \\
&= \mathrm{Re}\left[\left(\underbrace{-i\sigma_o\mathcal{A}_j^{(0)}}_{\mathrm{O}(\epsilon)} \underbrace{- i\sigma_o\mathcal{A}_j^{(1)} + ik_o(U_1\cos\beta + U_2\sin\beta)\mathcal{A}_j^{(0)} - U_6\frac{\partial\mathcal{A}_j^{(0)}}{\partial\beta}}_{\mathrm{O}(\epsilon\tau)}\right) e^{-i\sigma_e t}\right] + \mathrm{O}\left(\epsilon^2\tau\right)
\end{aligned} \tag{2.33}$$

The last term in Eq. (2.33) represents another variable that should be solved for when determining the equations of motion of the floater. Thus, we define

$$\mathcal{A}^{(0)}_{j,\beta} = \frac{\partial \mathcal{A}^{(0)}_j}{\partial \beta}. \tag{2.34}$$

In order to solve for the total motion of the body, we have to solve for each of these motions individually. Let $\boldsymbol{X_b^o} = [X_o, Y_o, \Theta_o]^T$ be the vector that describes the slow-drift position of the platform in the horizontal plane. Similarly, let $\boldsymbol{\xi_b} = [\xi_1, \xi_2, \xi_6]^T$ describe the oscillatory motion in the horizontal plane. In the fixed frame of reference, the total motion of a cylinder $\boldsymbol{X_b} = [X_1^b, Y_1^b, \theta_0]^T$ is given as

$$\boldsymbol{X_b} = \boldsymbol{X}_b^o + S^T(\Theta_o)\boldsymbol{\xi_b}. \tag{2.35}$$

Thus, the total yaw displacement of the body, denoted by θ_0, is

$$\theta_0 = \Theta_o + \xi_6. \tag{2.36}$$

2.3.4 Boundary Conditions in Slow-Drift Frame

Free-Surface Condition

Utilizing a similar Taylor series expansion to Eqs. (2.16), (2.22), the wave elevations in Eq. (2.23), and matching orders in the perturbation series of the velocity potential, we find the first-order velocity potential boundary conditions on the linearized free surface ($z = h$ plane) as,

$$\mathrm{O}(\tau): \qquad \frac{\partial \varphi_{01}}{\partial z} = 0, \tag{2.37a}$$

$$\mathrm{O}(\epsilon): \qquad -\nu_0\varphi_{10} + \frac{\partial \varphi_{10}}{\partial z} = 0, \tag{2.37b}$$

since $\partial\phi_{01}/\partial t = 0$ (there is no incident-wave for $\mathrm{O}(\epsilon^0)$). We have defined the frequency parameter ν_o as,

$$\nu_o = \frac{\sigma_o^2}{g}. \tag{2.38}$$

We can write the second-order free-surface boundary conditions (on $z = h$ plane) by utilizing Eqs. (2.16), (2.27) and identities relating $\partial/\partial x = \partial/y\partial\theta$, as

$$\begin{aligned}\mathrm{O}(\tau\epsilon): -\nu_0\varphi_{11} + \frac{\partial \varphi_{11}}{\partial z} = &-\frac{2i\sigma_o}{g}\left(U_1\frac{\partial\varphi_{10}}{\partial x} + U_2\frac{\partial\varphi_{10}}{\partial y} + U_6\frac{\partial\varphi_{10}}{\partial\theta} - \nabla\varphi_{01}\cdot\nabla\varphi_{10}\right)\\ &+\frac{2k_o\sigma_o}{g}\left(U_1\cos\beta + U_2\sin\beta\right)\varphi_{10} - \frac{2i\sigma_o}{g}U_6\frac{\partial\varphi_{10}}{\partial\beta} - \frac{i\sigma_o}{g}\varphi_{10}\frac{\partial^2\varphi_{01}}{\partial z^2}.\end{aligned} \tag{2.39}$$

This boundary condition agrees with Eq. (17) in [28] (although these authors define the perturbation series explicitly in terms of the slow-drift velocities), Eq. (3.43) in [20] (although

this author considers bottom-mounted cylinders, such that $\partial^2\varphi_{01}/\partial z^2 = 0$) and Eq. (3.12) in [26] (although these authors set $U_1 = U_2 = 0$). The free-surface boundary condition for the second-order potential is,

$$\mathrm{O}\left(\epsilon^2\right): \quad g\frac{\partial\bar{\varphi}_{20}}{\partial z} = -\overline{\frac{\partial}{\partial t}\left(\nabla\phi_{10}\cdot\nabla\phi_{10}\right)} + \overline{\frac{1}{g}\frac{\partial\phi_{10}}{\partial t}\left[\frac{\partial^3\phi_{10}}{\partial z\partial t^2} + g\frac{\partial^2\phi_{10}}{\partial z^2}\right]}, \tag{2.40}$$

where $\overline{(\circ)}$ denotes the time average over a monochromatic wave period. Explicitly, the time-average operator is defined as,

$$\overline{f(t)} = \frac{1}{T_o}\int_{t-T_o}^{t} f(t)dt. \tag{2.41}$$

Grue and Palm [32] showed that the second-order free-surface boundary condition can be simplified to,

$$\mathrm{O}\left(\epsilon^2\right): \quad \frac{\partial\bar{\varphi}_{20}}{\partial z} = -\frac{\sigma_o}{2g}\,\mathrm{Im}\left[\varphi_{10}\frac{\partial^2\varphi_{10}^*}{\partial z^2}\right], \tag{2.42}$$

where the asterisk (*) denotes the complex conjugate. However, it will be shown that for the steady, second-order, zero-speed potential $\bar{\varphi}_{20}$, the important quantities related to the forces on the body (such as the slow-drift damping) can be derived from lower-order potentials as was done in [30] and [32].

Body Condition

Akin to the previous section, we reframe the non-linear body boundary condition found in Eq. (2.17) in the slow-drift frame. Since the terms in Eq. (2.17) are scalars, we can rewrite the body boundary condition in the slow-drift coordinates as,

$$\boldsymbol{n}\cdot\nabla\phi\Big|_{\boldsymbol{x}=\boldsymbol{x}_b(t)} = \boldsymbol{n}\cdot\boldsymbol{v_b} \tag{2.43}$$

where $\boldsymbol{v_b}(\boldsymbol{x},t) = \boldsymbol{V_b}(\boldsymbol{X},t)$ is the body velocity and $\boldsymbol{n}$ is the normal vector pointing into the instantaneous body position $\boldsymbol{x}_b(t)$ relative to the slow-drift coordinates. Let the point shown in Fig. 2.1 represent a point on the body. Relative to the slow-drift frame, the point's velocity can be represented by the vector equation,

$$\boldsymbol{v_b} = \boldsymbol{U_o} + \dot{\boldsymbol{x}} + \boldsymbol{\Omega_o}\times\boldsymbol{x} \tag{2.44}$$

In terms of the body-fixed coordinates the position and normal vectors in the slow-drift frame are

$$\boldsymbol{x} = \boldsymbol{x'} + \boldsymbol{\xi} + \boldsymbol{\alpha}\times\boldsymbol{x'}, \tag{2.45a}$$
$$\boldsymbol{n} = \boldsymbol{n'} + \boldsymbol{\alpha}\times\boldsymbol{n'}, \tag{2.45b}$$

where $\boldsymbol{n'}$ is the normal vector pointing in to the body relative to the body-fixed coordinates. To $\mathrm{O}(\tau)$, we can evaluate the gradient of the velocity potential at the slow-drift position of the body and then expand the velocity potential in terms of the first-order difference between this position and the exact position of the body. Thus, to the leading order, the body velocity in the slow-drift frame is the difference between the exact body surface and the slow-drift surface, such that

$$\boldsymbol{v}_b = \boldsymbol{U_o} + \dot{\boldsymbol{\xi}} + \dot{\boldsymbol{\alpha}} \times \boldsymbol{x'} + \boldsymbol{\Omega_o} \times \boldsymbol{x} + \mathrm{O}\left(\tau^2\right) \tag{2.46}$$

Therefore, we can rewrite Eq.(2.43) up to $\mathrm{O}(\tau^2)$ as,

$$(\boldsymbol{n'}+\boldsymbol{\alpha}\times\boldsymbol{n'})\cdot(\nabla\phi+[(\boldsymbol{x}-\boldsymbol{x'})\cdot\nabla]\nabla\phi) = (\boldsymbol{n'}+\boldsymbol{\alpha}\times\boldsymbol{n'})\cdot(\boldsymbol{U_o}+\dot{\boldsymbol{\xi}}+\dot{\boldsymbol{\alpha}}\times\boldsymbol{x'}+\boldsymbol{\Omega_o}\times\boldsymbol{x})+\mathrm{O}\left(\tau^2\right) \tag{2.47}$$

where all of the quantities are evaluated at the slow-drift position of the body $\boldsymbol{x} = \boldsymbol{x}_b$. By collecting terms of the proper orders, we can recover the boundary conditions as found by [20] and [25]:

$$\mathrm{O}(\tau): \qquad \boldsymbol{n'} \cdot \nabla\phi_{01} = \boldsymbol{n'} \cdot (\boldsymbol{U_o} + \boldsymbol{\Omega_o} \times \boldsymbol{x}), \tag{2.48a}$$

$$\mathrm{O}(\epsilon): \qquad \boldsymbol{n'} \cdot \nabla\phi_{10} = \boldsymbol{n'} \cdot \left(\dot{\boldsymbol{\xi}}^{(0)} + \dot{\boldsymbol{\alpha}}^{(0)} \times \boldsymbol{x'}\right), \tag{2.48b}$$

$$\mathrm{O}(\epsilon\tau): \qquad \boldsymbol{n'} \cdot \nabla\phi_{11} + \boldsymbol{n'} \cdot [\boldsymbol{\xi}^{(0)} + \boldsymbol{\alpha}^{(0)} \times \boldsymbol{x} \cdot \nabla]\nabla\phi_{01} + \boldsymbol{\alpha}^{(0)} \times \boldsymbol{n'} \cdot \nabla\phi_{01} = \boldsymbol{n'} \cdot \left(\dot{\boldsymbol{\xi}}^{(1)} + \dot{\boldsymbol{\alpha}}^{(1)} \times \boldsymbol{x'}\right) + \boldsymbol{\alpha}^{(0)} \times \boldsymbol{n'} \cdot (\boldsymbol{U_o} + \boldsymbol{\Omega_o} \times \boldsymbol{x}), \tag{2.48c}$$

$$\mathrm{O}\left(\tau^2\right): \qquad \boldsymbol{n'} \cdot \nabla\bar{\phi}_{20} + \overline{\boldsymbol{n'} \cdot [\boldsymbol{\xi}^{(0)} + \boldsymbol{\alpha}^{(0)} \times \boldsymbol{x} \cdot \nabla]\nabla\phi_{10}} + \overline{\boldsymbol{\alpha}^{(0)} \times \boldsymbol{n'} \cdot \nabla\phi_{10}} = + \overline{\boldsymbol{\alpha}^{(0)} \times \boldsymbol{n'} \cdot \left(\dot{\boldsymbol{\xi}}^{(0)} + \dot{\boldsymbol{\alpha}}^{(0)} \times \boldsymbol{x'}\right)}. \tag{2.48d}$$

We remove the time-harmonicity of both sides of the equations in Eqs. (2.48d), so that the boundary conditions become,

$$\mathrm{O}(\tau): \qquad \frac{\partial\varphi_{01}}{\partial n'} = U_j n'_j, \tag{2.49a}$$

$$\mathrm{O}(\epsilon): \qquad \frac{\partial\varphi_{10}}{\partial n'} = -i\sigma_o \mathcal{A}_j^{(0)} n'_j, \tag{2.49b}$$

$$\mathrm{O}(\epsilon\tau): \qquad \frac{\partial\varphi_{11}}{\partial n'} = -i\sigma_o \mathcal{A}_j^{(1)} n'_j + \mathcal{A}_j^{(0)} m'_j, \tag{2.49c}$$

$$\mathrm{O}\left(\epsilon^2\right): \qquad \frac{\partial\bar{\varphi}_{20}}{\partial n'} = -\mathcal{A}_j^{(0)} M'_j[\varphi_{10}^*] + \mathrm{O}\left(\mathcal{A}_j^{(0)}\mathcal{A}_k^{(0)}\right), \tag{2.49d}$$

where summation over the j modes of motion is assumed. The last cross-product in Eq. (2.48d) is not given explicitly in Eq. (2.49d) for brevity. For this study, we will only consider terms proportional to A_o^2 when considering $\bar{\varphi}_{20}$. In other words, only the diffraction problem of $\bar{\varphi}_{20}$ is considered. Here the body normals n'_j are defined as

$$n'_j = \begin{cases} n'_j \text{ for } j = 1, 2, 3 \\ (\boldsymbol{x'} \times \boldsymbol{n'}) \cdot \hat{e}_{j-3} \text{ for } j = 4, 5, 6 \end{cases} \tag{2.50a}$$

where $\hat{e}_j$ is the unit vector in the j^{th} mode of motion. We have introduced the m'_j terms from Appendix B of [20], originally formulated in [33] and in [34], such that

$$m'_j = \begin{cases} -M'_j[\varphi_{01}] \text{ for } j = 1,2,3 \\ -M'_j[\varphi_{01}] + (\boldsymbol{n'} \times (\boldsymbol{U_o} + \boldsymbol{\Omega_o} \times \boldsymbol{x'})) \cdot \hat{e}_{j-3} \text{ for } j = 4,5,6 \end{cases} \tag{2.51a}$$

with

$$M'_j[\varphi] = \begin{cases} (\boldsymbol{n'} \cdot \nabla)\nabla\varphi \cdot \hat{e}_j \text{ for } j = 1,2,3 \\ (\boldsymbol{n'} \cdot \nabla)(\boldsymbol{x'} \times \nabla\varphi) \cdot \hat{e}_{j-3} \text{ for } j = 4,5,6 \end{cases} \tag{2.52a}$$

This agrees with Eq. (2.37) in [35]. The m'_j terms are defined explicitly in this report's Appendix A.

2.3.5 Multiple Cylinders

In our analysis, we will consider multiple cylinders in our domain. It is convenient to define these potentials relative to a coordinate system fixed on the k^{th} cylinder as (x_k, y_k, z_k), such that $\varphi_{ij}(x,y,z) = \varphi^k_{ij}(x_k, y_k, z_k)$, as shown in Fig. 2.3. These coordinate systems are defined as,

$$x_k = x - x^k_0 \tag{2.53a}$$
$$y_k = y - y^k_0 \tag{2.53b}$$
$$z_k = z \tag{2.53c}$$

Let the distance from the origin with respect to the center of the cylinder be represented by,

$$R_k = |[x^k_0, y^k_0]|_2, \tag{2.54}$$

and the distance between cylinders by,

$$R_{jk} = |[x^j_0 - x^k_0, y^j_0 - y^k_0]|_2. \tag{2.55}$$

Clearly, the derivatives with respect to the Cartesian coordinates in the local and slow-drift frames are equivalent: that is, $\partial/\partial x = \partial/\partial x_k$, etc. In later sections, we will need the transformation of the circumferential derivative from the slow-drift frame to the local frame, which is

$$\frac{\partial\varphi}{\partial\Theta} = x^k_0 \frac{\partial\varphi^k}{\partial y_k} - y^k_0 \frac{\partial\varphi^k}{\partial x_k} + \frac{\partial\varphi^k}{\partial\theta_k} \tag{2.56}$$

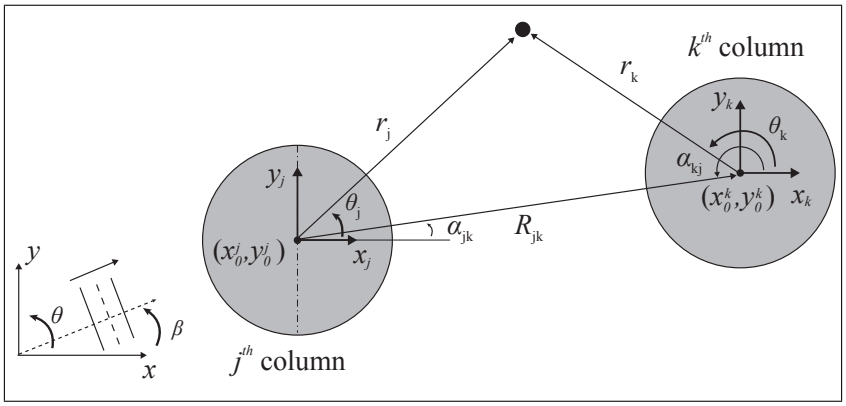

Figure 2.3: Plan view of multi-column platform, consisting of j^{th} and k^{th} columns, subject to incident waves with wave heading β.

2.4 Solutions for Velocity Potentials

In this section we explicitly solve the boundary value problem setup in Sec. 2.3 per Eq. (2.20) for the first and second-order velocity potentials, φ_{01}, φ_{10}, φ_{11}, φ_{20}. We begin with φ_{10} in Sec. 2.4.1, since it is the most common problem found in linear hydrodynamics of a truncated cylinder: that of a cylinder with small oscillations about a mean position. Although we show how to include the interaction effects among the cylinders in an array, we generally exclude them in the present analysis since $a << R$ where a is a typical cylinder radius and R is a typical cylinder spacing. We then consider the 'double-body' potential φ_{01}, which considers the cylinder moving with a slow-drift velocity without the effect of waves. The most involved potential is φ_{11}, which includes the interaction between the slow-drift of the cylinder and the incident, monochromatic waves. Finally, we briefly mention the second-order potential φ_{20} but do not attempt to solve it since we can write the second-order forces in terms of the lower-order potentials.

2.4.1 The zero forward-speed velocity potential φ_{10}

The zero forward-speed velocity potential is the classical isolated, truncated cylinder problem in monochromatic waves, oscillating about a mean position, rotating about the point (x_0^k, y_0^k, z_0^k). The formulation that follows borrows heavily from the solutions of Garrett [36] and Yeung [18], which was reformulated by Williams in [37] and [38] for multi-column structures. One of the original contributions in this field of interacting vertical cylinders is Okushu in 1976, which has been reprinted in [39], with follow-up work by Matsui and Tamaki in 1981 [40]. More recently, Yilmaz has contributed a concise method to this field [41]. Separately, and independent of the current work, a M.S. thesis on this topic was also completed by Zhong [42].

It is convenient to decompose the potential φ_{10} into its diffracted and radiated compo-

nents as,

$$\phi_{10} \underset{\text{Re}}{=} \left(A_o \psi_D - i\sigma_o \sum_{j=1,2,6} \psi_j \mathcal{A}_j^{(0)} \right) e^{-i\sigma_e t}, \tag{2.57}$$

where the diffraction potential ψ_D can be decomposed into an incident potential and scattering potential such that

$$\psi_D = \psi_0 + \psi_7. \tag{2.58}$$

Thus, the free-surface and body boundary conditions for the first-zeroth order diffraction

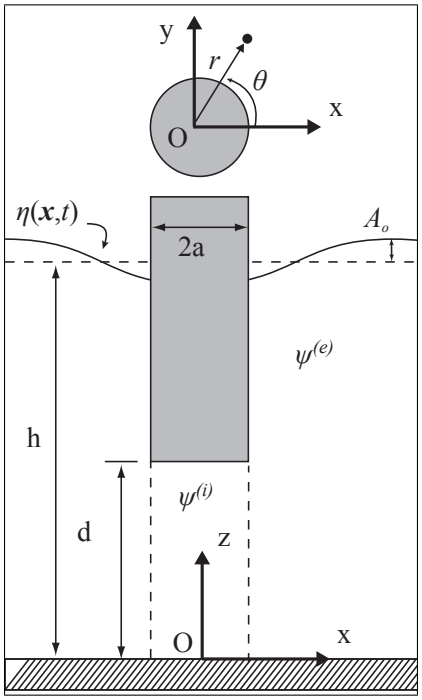

Figure 2.4: Plan view of an isolated, truncated cylinder with interior and exterior potentials.

and radiation potentials can be rewritten as,

$$-\nu_o \psi_7 + \frac{\partial \psi_7}{\partial z} = 0 \qquad \text{on } z = h, \tag{2.59a}$$

$$\frac{\partial \psi_7}{\partial n} = -\frac{\partial \psi_0}{\partial n} \qquad \text{on } \mathcal{S}_o, \tag{2.59b}$$

and

$$-\nu_o \psi_j + \frac{\partial \psi_j}{\partial z} = 0 \qquad \text{on } z = h, \tag{2.60a}$$

$$\frac{\partial \psi_j}{\partial n} = n_j' \qquad \text{on } \mathcal{S}_o \tag{2.60b}$$

where $\mathcal{S}_o$ is defined as the mean wetted surface of the cylinder in the slow-rotating frame.

Incident Velocity Potential

In the slow-drift frame (r, θ, z), the incident-wave, unit-amplitude velocity potential can be found to be,

$$\psi_0 = -\frac{ig}{\sigma_o}\frac{\cosh k_0 z}{\cosh k_0 h} e^{ik_0 r\cos(\theta-\beta)}. \tag{2.61}$$

In the local coordinates coordinates of the k^{th} cylinder, (r_k, θ_k, z), the potential is

$$\psi_0^k(r_k, \theta_k, z_k) = -P_k\frac{ig}{\sigma_o}\frac{\cosh k_0 z}{\cosh k_0 h} e^{ik_0 r_k\cos(\theta_k-\beta)}, \tag{2.62}$$

where P_k is the well-known 'phase-factor' associated with the k^{th} cylinder, defined as,

$$P_k = e^{-ik_0(x_0^k\cos\beta + y_0^k\sin\beta)}. \tag{2.63}$$

The incident potential can be represented by an infinite series as,

$$\psi_0^k = -\frac{g}{\sigma_o}\frac{\cosh k_o z}{\cosh k_o h} P_k \sum_{m=0}^{\infty} \epsilon_m i^{m+1} J_m(k_o r_k)\cos m(\theta_k - \beta). \tag{2.64}$$

Here, $\epsilon_0 = 1$ and $\epsilon_m = 2$ for $m \geq 1$ and J_m is the Bessel function of the first kind of order m. The incident-wave number k_o is related to the angular (inertial) frequency of the incident wave in arbitrary water depth h by the dispersion relation,

$$m_0 \tanh m_0 = \nu_o h, \tag{2.65}$$

where m_0 is the wavenumber, non-dimensionalized by the water-depth, $m_0 = k_o h$. The diffracted and radiated velocity potentials can be further decomposed according to the region around the cylinder $\psi^{(e)}$ and under the cylinder $\psi^{(i)}$ (as shown in Fig. 2.4), such that

$$\psi_j^k = \psi_j^{k(i)} + \psi_j^{k(e)} \text{ for } j = 1, 2, 6, 7, \tag{2.66}$$

where $j = 0$ is not included in the above equation since the incident potential only exists in the exterior domain. From this simple fluid decomposition, it is clear only the interior potential $\psi^{(i)}$ contributes to the heave force, while only the exterior potential $\psi^{(e)}$ contributes to the surge, sway and yaw forces. We then formulate a set of matching conditions on the boundaries of the interior and exterior regions so that the pressure and radial velocities are consistent,

$$\psi^{k(i)} = \psi^{k(e)}, \text{ on } r_k = a, 0 \leq \theta_k \leq 2\pi, 0 \leq z_k \leq d, \tag{2.67a}$$

$$\frac{\partial\psi^{k(i)}}{\partial r_k} = \frac{\partial\psi^{k(e)}}{\partial r_k}, \text{ on } r_k = a, 0 \leq \theta_k \leq 2\pi, 0 \leq z_k \leq d. \tag{2.67b}$$

As mentioned previously, there are many authors who have contributed to the development of the solution for the linear scattering and radiation potential, but the development in the following sections follows the works of [37] and [43] most closely.

Diffracted Velocity Potential

The diffraction potentials, $\psi_7^{(e)}$ and $\psi_7^{(i)}$ are required to satisfy Eqs. (2.8) and (2.18). However, only the exterior potential $\psi_7^{(e)}$ must satisfy Eq. (2.37b), since it is exposed to the free-surface. Further, the no-flux conditions on the body surface suggest,

$$\frac{\partial \psi_7^{k(i)}}{\partial z} = 0, \text{ on } r_k \leq a, 0 \leq \theta_k \leq 2\pi, z_k = d, \tag{2.68a}$$

$$\frac{\partial \psi_7^{k(e)}}{\partial r_k} = -\frac{\partial \psi_0^k}{\partial r_k}, \text{ on } r_k = a, 0 \leq \theta_k \leq 2\pi, d \leq z_k \leq h. \tag{2.68b}$$

Also, the exterior diffraction potential $\psi_7^{(i)}$ must satisfy a far-field radiation condition. Thus, by inspection of Eq. (2.68), we can form a class of admissible solutions for the diffraction potentials $\psi_7^{(i)}$ and $\psi_7^{(e)}$. These potentials ought to take the following form:

$$\psi_7^{k(i),(e)}(r_k, \theta_k, z_k) = -\frac{g}{\sigma_0} P_k \sum_{m=0}^{\infty} {}_7\Psi_m^{(i),(e)}(r_k, z_k) \cos m(\theta_k - \beta). \tag{2.69}$$

First, we consider the interior region. In this region, the dimensionless spatial solution ${}_7\Psi_m^{(i)}(r, z)$ that satisfies the boundary conditions can be expressed (from [37]) as,

$${}_7\Psi_m^{(i)}(r, z) = \frac{B_0^{(m)}}{2} \left(\frac{r}{a}\right)^m + \sum_{q=1}^{\infty} B_q^{(m)} \frac{I_m(\beta_q r)}{I_m(\beta_q a)} \cos(\beta_q z), \tag{2.70}$$

where $I_m()$ is the modified Bessel function of the first kind of order m and $B_q^{(m)}$ are the unknown coefficients to be discussed later. The wavenumbers β_q are defined as,

$$\beta_q = \frac{q\pi}{d}. \tag{2.71}$$

Now, let us consider the exterior region. A suitable form for the exterior spatial solution $\Psi_m^{(e)}(r, z)$ can be represented (also from [37]) by,

$$\begin{aligned} {}_7\Psi_m^{(e)}(r, z) = &-\epsilon_m i^{m+1} \frac{\cosh k_0 z}{\cosh k_0 h} \frac{J'_m(k_0 a)}{H'_m(k_0 a)} H_m(k_0 r) \\ &+ C_0^{(m)} \frac{H_m(k_0 r)}{H'_m(k_0 a)} Z_0(z) + \sum_{q=1}^{\infty} C_q^{(m)} \frac{K_m(k_q r)}{K'_m(k_q a)} Z_q(z), \end{aligned} \tag{2.72}$$

in which H_m is the Hankel function of the first kind and K_m is the modified Bessel function of the second kind, both of order m and primes ($'$) denote derivatives with respect to the argument. The vertical orthonormal functions $Z_q(z)$ are,

$$Z_q(z) = \begin{cases} Q_0^{-1/2} \cosh k_0 z, & \text{if } q = 0 \\ Q_q^{-1/2} \cos k_q z, & \text{if } q > 0 \end{cases} \tag{2.73}$$

in which

$$Q_q = \begin{cases} \frac{1}{2}\left(1 + \frac{\sinh 2k_0 h}{2k_0 h}\right), & \text{if } q = 0 \\ \frac{1}{2}\left(1 + \frac{\sin 2k_q h}{2k_q h}\right), & \text{if } q > 0 \end{cases} \tag{2.74}$$

The nondimensional wavenumber $m_q = k_q h$ are the positive real roots of

$$m_q \tan m_q = -\nu_o. \tag{2.75}$$

We recognize the series in Eqs. (2.70) and (2.72) as simply Fourier series, with unknown coefficients $B_q^{(m)}$ and $C_q^{(m)}$, respectively. We can solve for these coefficients using the matching conditions given in Eq. (2.67). The solutions for these unknown coefficients are given in Appendix B. Later in the analysis we will need a concise representation of the diffraction potential with explicit functions of the spatial variables. Thus, let,

$$\psi_D^{k(e)}(r,\theta,z) = -\frac{g}{\sigma_o} P_k(\beta) \sum_{m=0}^{\infty}\sum_{q=0}^{\infty} \check{Z}_q(z) G_q^{(m)}(r) \cos(m[\theta - \beta]), \tag{2.76}$$

where the *orthogonal* vertical functions are

$$\check{Z}_q(z) = Q_q^{1/2} Z_q(z), \tag{2.77}$$

and

$$G_0^{(n)}(r) = \frac{\epsilon_n i^{n+1}}{\cosh m_0}\left(J_n(k_0 r) - \frac{J_n'(k_0 a) H_n(k_0 r)}{H_n'(k_0 a)}\right) + C_0^{(n)} \frac{H_n(k_0 r) Q_0^{-1/2}}{H_n'(k_0 a)} \tag{2.78a}$$

$$G_q^{(n)}(r) = C_q^{(n)} \frac{K_n(k_q r) Q_q^{-1/2}}{K_n'(k_q a)}, \text{ for } q > 0. \tag{2.78b}$$

We will denote derivatives with respect to the argument of these functions with a prime ($'$), that is, $\partial G_p^{(n)}(r)/\partial r = G_p^{'(n)}(r)$. The horizontal forces will be related to the integrated quantities of these functions, evaluated on the cylinder wetted surface. Thus, let

$$Y_q^j = \frac{1}{a_j}\int_{d_j}^{h} Z_q(z) dz \text{ for } q \geq 0. \tag{2.79}$$

Radiation Velocity Potential

The radiation wave field arises from the prescribed oscillations of the cylinder. For this analysis we restrict the motion of the cylinder to 3 DOFs: surge, sway and yaw or in indicial notation j=1,2,6. For an inviscid fluid, the yaw motion of a cylinder about its own axis does not disturb the fluid. However, when considering the multi-column structure, the yaw motion of the platform consists simply of a combination of surge and sway motion of each column. The radiation potentials $\psi_j^{(i),(e)}$, j=1,2,6 are required to satisfy Eqs. (2.8), (2.18)

and (2.37b), as well as the body boundary conditions in Eq. (2.49b). In polar coordinates, the radiated potential in the j^{th} mode on the k^{th} cylinder can be written as,

$$\psi_j^{k(i),(e)} = a\Psi_j^{(i),(e)}(r_k, z_k)\cos(\theta_k - \chi_j) \quad j = 1, 2, \tag{2.80}$$

where

$$\chi_j = \begin{cases} 0 \text{ for } j = 1, \\ \pi/2 \text{ for } j = 2. \end{cases} \tag{2.81}$$

The radiated potential in the yaw mode is

$$\psi_6^{k(i),(e)} = a\left(y_0^k\Psi_1^{(i),(e)}(r_k, z_k)\cos\theta_k - x_0^k\Psi_2^{(i),(e)}(r_k, z_k)\sin\theta_k\right). \tag{2.82}$$

From [43], we can write the interior and exterior solutions, which satisfy these boundary conditions, as,

$$\Psi_j^{(i)}(r, z) = \frac{B_0^j}{2}\frac{r}{a} + \sum_{q=1}^{\infty} B_q^j \frac{I_1(\beta_q r)}{I_1(\beta_q a)}\cos(\beta_q z) \tag{2.83a}$$

$$\Psi_j^{(e)}(r, z) = C_0^j \frac{H_1(k_0 r)}{H_1'(k_0 a)} Z_0(z) + \sum_{q=1}^{\infty} C_q^j \frac{K_1(k_q r)}{K_1'(k_q a)} Z_q(z), \tag{2.83b}$$

where B_q^j and C_q^j are the new Fourier coefficients, which are different for each mode of motion. We refer the reader to Appendix C for explicit solutions of the Fourier coefficients. Further, it will be helpful to concisely define the radiation potential in our analysis of the wave-drift moment. Let the exterior radiation potential in surge and sway be described by,

$$\psi_j^{(e)}(r, \theta, z) = a\sum_{q=0}^{\infty} \check{Z}_q(z) H_q^j(r)\cos(\theta - \chi_j) \text{ for } j = 1, 2, \tag{2.84}$$

where

$$H_0^j(r) = C_0^j \frac{H_1(k_0 r)}{H_1'(k_0 a)} Q_o^{-1/2}, \tag{2.85a}$$

$$H_q^j(r) = C_q^j \frac{K_1(k_q r)}{K_1'(k_q a)} Q_q^{-1/2}, \text{ for } q > 0. \tag{2.85b}$$

Verification of the results presented in these sections is shown in Sec. 2.6 after the hydrodynamic quantities, such as the wave-exciting force and hydrodynamic added-mass and damping are explicitly defined.

Multiple, Interacting Cylinders

In this section we only take into account the effect of multiple, interacting cylinders as an additional term in the incident-wave potential. Therefore, only the diffraction potential is

updated with these effects. In order to simplify the analysis we assume that these waves emanating from the j^{th} cylinder result in plane waves at the k^{th} cylinder. Essentially, we assume that the distance between the cylinders is much larger than the wavelength of the incident-wave, $R_{jk} >> 2\pi/k_0$. We shall see that for many platforms this assumption may not be true, but still this type of analysis can lead to greater insight on the hydrodynamic forces on the body.

For the k^{th} cylinder, centered at (x_0^k, y_0^k), the velocity potential due to a regular wave propagating at an angle β with respect to the positive $x-$ axis, can be written in the local polar coordinate system by Eq. (2.62). Here, we present the main findings from [38] and refer the reader to this resource for more details on the derivation. The total incident-wave potential on the j^{th} cylinder to $\mathcal{O}(k_0 R_{jk}^{-3/2})$ is,

$$\begin{aligned}\psi^j_{I_{tot}} = -\frac{g}{\sigma_0}\cosh k_0 z \Bigg[&\frac{1}{\cosh k_0 h} P_j \sum_{m=0}^{\infty} \underbrace{\epsilon_m i^{m+1} J_m(k_0 r_j)\cos m(\theta_j - \beta_0)}_{\text{unperturbed incident wave}} \\ &+ \sum_{\substack{k=1 \\ k\neq j}}^{N_{col}} \underbrace{c_{jk} e^{-ik_0 r_j \cos(\alpha_{jk}-\theta_j)}}_{\text{scattered from } k^{th} \text{ cylinder}} \\ &+ \left(\sum_{\substack{k=1 \\ k\neq j}}^{N_{col}} \underbrace{P_k D_{jk}(r_j, \theta_j, \beta_0)}_{\text{incident wave correction}} + \sum_{\substack{\ell=1 \\ \ell\neq k}}^{N_{col}} \underbrace{c_{k\ell} D_{jk}(r_j, \theta_j, \alpha_{\ell k})}_{\text{back-scattered waves}} \right) \Bigg],\end{aligned} \tag{2.86}$$

where the approximating plane wave complex amplitude at the j^{th} cylinder due to the scattering from the k^{th} cylinder is,

$$c_{jk} = P_k S_{jk}(R_{kj}, \alpha_{kj}, \beta) + \sum_{\ell=1}^{N_{col}} c_{k\ell} S_{jk}(R_{kj}, \alpha_{kj}, \alpha_{\ell k}). \tag{2.87}$$

The amplitude of the equivalent plane wave that is scattered by cylinder k from an incident angle β is

$$\begin{aligned}S_{kj}(R_{jk}, \alpha_{jk}, \beta) = S_{kj}(\beta) = \sum_{m=0}^{\infty} \Bigg\{ &\frac{C_0^{(m)} Q_0^{-1/2}}{H_m'(k_0 a_j)} \\ &- \frac{\epsilon_m i^{m+1} J_m'(k_0 a_j)}{\cosh m_0 H_m'(k_0 a_j)} \Bigg\} H_m(k_0 R_{jk}) \cos m(\alpha_{jk} - \beta),\end{aligned} \tag{2.88}$$

and the non-planar correction term is

$$\begin{aligned}D_{kj}(\beta) = \frac{i}{k_0 R_{jk}} \Bigg\{ &S_{kj}(\beta) \sum_{\ell=0}^{\infty} (-i)^\ell \ell^2 J_\ell(k_0 r_k) \cos \ell(\alpha_{kj} - \theta_k) \\ &- T_{kj}(R_{jk}, \alpha_{jk}, \beta) \sum_{\ell=0}^{\infty} \epsilon_\ell (-i)^\ell \ell J_\ell(k_0 r_k) \sin \ell(\alpha_{kj} - \theta_k) \Bigg\},\end{aligned} \tag{2.89}$$

in which

$$T_{kj}(R_{jk},\alpha_{jk},\beta) = T_{kj}(\beta) = \sum_{m=0}^{\infty}\left\{\frac{C_0^{(m)}Q_0^{-1/2}}{H_m'(k_0a_j)} - \frac{\epsilon_m i^{m+1}J_m'(k_0a_j)}{\cosh m_0 H_m'(k_0a_j)}\right\} H_m(k_0R_{jk})m\sin m(\alpha_{jk}-\beta). \tag{2.90}$$

Thus, we can setup a linear system of equations for c_{jk}, for $j,k = 1,2...N_{col}$ (where N_{col} is the number of columns of the platform) using Eq. (2.87) and use standard matrix techniques to solve for the plane wave amplitudes c_{jk}.

The zero-speed, first-order wave-exciting force in surge and sway (p=1,2) on the j^{th} column due to the interaction effect among other columns is given in Eq. (F.4). Of course, the interacting cylinders will have an effect on the cylinder's added-mass and damping. For this effect, we refer the reader to Zhong [42], but include a figure in Sec. 2.6 from that work for discussion.

2.4.2 The double-body velocity potential φ_{01}

The slow-drift velocity potential describes the fluid velocity surrounding a truncated cylinder drifting in calm water. The problem is similar to the radiation problem described in 2.4.1, except with the body motion being described by the slow-drift velocities. Again, we use the method of domain decomposition to represent this potential in the areas around the cylinder and below the cylinder as,

$$\phi_{01}(r_k,\theta_k,z_k) = \mathrm{Re}\left[\sum_{j=1,2,6}\bar{\psi}_j(r_k,\theta_k,z_k)U_j\right], \tag{2.91}$$

with

$$\bar{\psi}_j^k(r_k,\theta_k,z_k) = \bar{\psi}_j^{k(i)} + \bar{\psi}_j^{k(e)}, \tag{2.92}$$

$$\bar{\psi}_j^{k(i),(e)}(r_k,\theta_k,z_k) = -a\bar{\Psi}^{(i),(e)}(r_k,z_k)\cos(\theta_k-\chi_j) \quad j=1,2 \tag{2.93a}$$

$$\psi_6^{k(i),(e)} = y_0^k\bar{\psi}_1^k(r_k,z_k)\cos\theta_k - x_0^k\bar{\psi}_2^k(r_k,z_k)\sin\theta_k. \tag{2.93b}$$

The same condition for the slow-drift yaw radiation potential holds as the zero-speed yaw radiation potential, which is given in Eq. (2.82).

The interior and exterior potentials are well known and are reproduced in summation form from [29] as,

$$\bar{\Psi}^{(i)}(r,z) = \frac{\bar{A}_0}{2}\left(\frac{r}{a}\right) + \sum_{q=1}^{\infty}\bar{A}_q\frac{I_1(\beta_q r)}{I_1(\beta_q a)}\cos(\beta_q z), \tag{2.94a}$$

$$\bar{\Psi}^{(e)}(r,z) = \frac{\bar{B}_0}{2}\left(\frac{a}{r}\right) + \sum_{q=1}^{\infty}\bar{B}_q\frac{K_1(\beta_q \bar{d}r)}{K_1(\beta_q \bar{d}a)}\cos(\beta_q \bar{d}z). \tag{2.94b}$$

Notice that $\bar{\Psi}^{(i)} = \Psi_1^{(i)}$ with newly defined Fourier coefficients.

To solve for the Fourier coefficients we utilize Eqs. (2.67) and the body-boundary condition in Eq. (2.49a), which can be rewritten using the current notation as

$$\frac{\partial \bar{\Psi}^{(e)}(r_k, z_k)}{\partial r_k} = 1 \text{ on } r_k = a, d \leq z_k \leq h \tag{2.95}$$

Again, we explicitly solve for the interior and exterior slow-drift Fourier coefficients $\bar{A}_q$ and $\bar{B}_q$ in Appendix D.

Let the exterior slow-drift potential in surge and sway be described by,

$$\bar{\psi}_j^{(e)}(r, \theta, z) = -a \sum_{q=0}^{\infty} \cos(\beta_q z) L_q(r) \cos(\theta - \chi_j) \text{ for } j = 1, 2 \tag{2.96}$$

where L_q can be found by examination of Eq. (2.94). It turns out that the unknown coefficients for this velocity potential $\bar{B}_q, \bar{C}_q$ velocity can be ill-defined for certain values of d/h (namely, $h/d \in \mathbb{Z}$). Thus we solve for the double-body potential added-mass ($\bar{\mu}_{jk}$, to be defined explicitly in Sec. 2.5), by solving for zero-frequency limit of the first-order added-mass $\mu_{jk}^{(0)}$. The results are shown in Sec. 2.6.

2.4.3 The interaction potential between body and slow-drift motion φ_{11}

In this section, we solve for the interaction potential (between body and slow-drift motion), which takes into account the slow-drift velocity of the platform as well as the incident waves. First, we reexamine the body boundary conditions in Eq. (2.49c) in light of the greater detail of ϕ_{01}. Thus, we can explicitly write the m' terms as

$$\begin{bmatrix} m_1' \\ m_2' \\ m_6' \end{bmatrix} = \begin{bmatrix} \partial^2 \varphi_{01} / \partial r \partial x \\ \partial^2 \varphi_{01} / \partial r \partial y \\ x_o \partial^2 \varphi_{01} / \partial r \partial y - y_o \partial^2 \varphi_{01} / \partial r \partial x \end{bmatrix} \tag{2.97}$$

As we are only interested in the surge, sway and yaw modes of motion, only the exterior potential is needed. Further, we have defined the velocity potential in separable cylindrical coordinates in Eq. (2.96). We have explicitly defined the m' terms in Appendix A.

Again, we decompose the potential φ_{11} into its diffracted and radiated components. However, the radiation potential is now proportional to the zeroth and first order motions of the k^{th} cylinder, $\dot{\xi}_j^{k(0)}$, $\dot{\xi}_j^{k(1)}$ as well as $\partial \xi_j^{k(0)} / \partial \beta$ as shown in Eq. (2.33) as,

$$\phi_{11}^k = \text{Re}\left[\left(A_o \check{\psi}_D^k - i\sigma_o \sum_{j=1,2,6} \check{\psi}_j^k \mathcal{A}_j^{k(0)} + \check{\psi}_j^{k(\beta)} \mathcal{A}_{j,\beta}^{k(0)} + \psi_j^k \mathcal{A}_j^{k(1)} \right) e^{-i\sigma_e t} \right] \tag{2.98}$$

where the subscript β refers to differentiation with respect to β (as seen in Eq. (2.34)). The superscripts ($\check{}$) are only used to differentiate these velocity potentials from the lower-order potentials. Note that the last term of Eq. (2.98) represents the radiation potentials ψ_j^k from the lower-order potential φ_{10}.

However, since the main focus of this analysis is to analyze the slow-drift motions, we quickly recognize that the time-average of this potential and hence, the forces, are null. Thus, this potential only contributes to the first- and second-order *time-harmonic* motions. In our time-domain hydrodynamic analysis we do not include the contribution from this potential but provide an outline of the solution to this potential in Appendix E.

2.4.4 The second-order zero-speed potential φ_{20}

We can describe the time-harmonic velocity potential, as

$$\phi_{20}(x,y,z,t) = \varphi_{20}(x,y,z)e^{-i2\sigma_o t} + \bar{\varphi}_{20}(x,y,z). \tag{2.99}$$

where the potentials are due to the sum and difference frequencies of the incident monochromatic waves. We neglect the sum frequency contribution since it is at a much higher harmonic than the slow-drift oscillations. Although this potential is extremely relevant for analysis of springing and ringing phenomena, especially coupled with the higher natural frequencies of taut mooring lines (such as those found on TLPs), which can lead to fatigue on the structure, we will neglect it in the current analysis. It is clear for the zero-speed problem (formulated in an inertial frame) that the contribution of $\bar{\varphi}_{20}$ to the pressure is $\mathrm{O}\left(\epsilon^3\right)$ (see the discussion in [44] and subsequent papers, such as [45] and [46]). Although the second-order wave-drift forces depend on this potential, as will be shown in Eq. (F.65), we can write these forces in terms of the lower-order potential by means of Stokes' and Green's Theorems, as done in [32]. Just as in the case of the diffraction problem of other potentials the body boundary conditions is homogeneous, that is,

$$\frac{\partial \bar{\varphi}_{20}^D}{\partial n'} = 0, \tag{2.100}$$

which was also found in [26].

2.5 Hydrodynamic Forces and Equations of Motion

In this section, we develop expressions for the surge, sway and yaw hydrodynamic forces and describe how they can be included in the platform's equations of motion.

2.5.1 Hydrodynamic Pressure

The hydrodynamic forces on a partially submerged body are equal to the pressure integrated over the wetted surface area of the body. The hydrodynamic pressure at the instantaneous

body position $\mathcal{P}$ can be expressed by expanding the pressure about the mean position of the body in slow-drift frame $\mathcal{S}_o$ in a Taylor series, as

$$\mathcal{P} \underset{\text{Re}}{=} p\big|_{\mathcal{S}_o} + (\boldsymbol{\xi} + \boldsymbol{\alpha} \times \boldsymbol{x}') \cdot \nabla p\big|_{\mathcal{S}_o} + ... \tag{2.101}$$

where $p\big|_{\mathcal{S}_o}$ is the hydrodynamic pressure on the body, evaluated at its slow-drift position. The total pressure in the fluid in the slow-drift frame of reference is given by Bernoulli's equation as,

$$p \underset{\text{Re}}{=} -\rho_o \left(\frac{\partial \phi}{\partial t} - \boldsymbol{s} \cdot \nabla \phi + \frac{1}{2} \nabla \phi \cdot \nabla \phi + gz \right), \tag{2.102}$$

where $\boldsymbol{s}$ is defined in Eq. (2.7). Expanding the pressure in terms of the double perturbation series in Eq. (2.20),

$$p(\boldsymbol{x}, t) = \underbrace{p_{00}(\boldsymbol{x}, t)}_{\text{O}(1)} + \underbrace{p_{10}(\boldsymbol{x}, t)}_{\text{O}(\epsilon)} + \underbrace{p_{11}(\boldsymbol{x}, t)}_{\text{O}(\tau\epsilon)} + \underbrace{p_{02}(\boldsymbol{x}, t)}_{\text{O}(\tau^2)} + \underbrace{p_{20}(\boldsymbol{x}, t)}_{\text{O}(\epsilon^2)} + \underbrace{p_{21}(\boldsymbol{x}, t)}_{\text{O}(\epsilon^2\tau)} + \text{O}\left(\epsilon\tau^2\right), \tag{2.103}$$

where p_{00} is the hydrostatic pressure p_{10} is the linear pressure and p_{02} is the non-zero pressure due to only the slow-drift motions (p_{01}, which is related to only the slow-drift velocity is null). In order of the perturbation series the pressures are,

$$\text{O}(1): \qquad p_{00} = -\rho_o g z, \tag{2.104a}$$

$$\text{O}(\epsilon): \qquad p_{10} \underset{\text{Re}}{=} i\rho_o \sigma_o \varphi_{10} e^{-i\sigma_e t}, \tag{2.104b}$$

$$\text{O}(\epsilon\tau): \qquad p_{11} \underset{\text{Re}}{=} \rho_o \left(i\sigma_o \varphi_{11} + \mathcal{L}_e[\varphi_{10}] + \boldsymbol{s} \cdot \nabla \varphi_{10} - \nabla \varphi_{10} \cdot \nabla \varphi_{01} \right) e^{-i\sigma_e t}, \tag{2.104c}$$

$$\text{O}\left(\epsilon^2\right): \qquad p_{20} \underset{\text{Re}}{=} -\frac{\rho_o}{2} \nabla \varphi_{10} \cdot \nabla \varphi_{10}, \tag{2.104d}$$

$$\text{O}\left(\tau^2\right): \qquad p_{02} \underset{\text{Re}}{=} -\rho_o \left(\sum_j \dot{U}_j \bar{\psi}_j - \boldsymbol{s} \cdot \nabla \varphi_{01} + \frac{1}{2} \nabla \varphi_{01} \cdot \nabla \varphi_{01} \right), \tag{2.104e}$$

$$\tag{2.104f}$$

$$\begin{aligned} \text{O}\left(\epsilon^2\tau\right): \qquad p_{21} &\underset{\text{Re}}{=} -\rho_o \left[\frac{\partial \phi_{21}}{\partial t} - \boldsymbol{s} \cdot \nabla \phi_{20} + \nabla \phi_{20} \cdot \nabla \phi_{01} + \nabla \phi_{11} \cdot \nabla \phi_{10} \right], \\ &= -\rho_o \left[-U_6 \frac{\partial \bar{\varphi}_{20}}{\partial \beta} - \boldsymbol{s} \cdot \nabla \bar{\varphi}_{20} + \nabla \bar{\varphi}_{20} \cdot \nabla \varphi_{01} + \frac{1}{2} \nabla \varphi_{11}^* \cdot \nabla \varphi_{10} \right], \end{aligned} \tag{2.104g}$$

We take into account the third-order pressure term $\text{O}(\epsilon^2\tau)$ in order to find the wave-drift damping of the structure, which is proportional to the wave-drift velocity (as well as the square of the incident-wave amplitude).

2.5.2 Hydrodynamic Forces and Moments

As in previous sections, we only consider motions, forces, and moments in the horizontal plane. The forces and moments in the slow-drift frame of reference can be described by the

integrals,

$$\boldsymbol{F} = \int_{\mathcal{S}_B} \mathcal{P}\boldsymbol{n} dS, \tag{2.105a}$$

$$\boldsymbol{M} = \int_{\mathcal{S}_B} \mathcal{P}\boldsymbol{x} \times \boldsymbol{n}\ dS, \tag{2.105b}$$

where $\mathcal{S}_B$ is the instantaneous position of the body. Let the force/moment vector in the horizontal plane be represented by $\boldsymbol{F_b} = (F_1, F_2, F_6)$, where $F_6 = M_3$ denotes the yaw moment on the body. Since the hydrostatic force does not contribute to $\boldsymbol{F_b}$, we expand the force vector into its perturbation series as,

$$F_j(t) = \underbrace{F_j^{(10)}(t)}_{\mathrm{O}(\epsilon)} + \underbrace{F_j^{(11)}(t)}_{\mathrm{O}(\tau\epsilon)} + \underbrace{F_j^{(02)}(t)}_{\mathrm{O}(\tau^2)} + \underbrace{F_j^{(20)}(t)}_{\mathrm{O}(\epsilon^2)} + \underbrace{F_j^{(21)}(t)}_{\mathrm{O}(\epsilon^2\tau)} + \mathrm{O}\left(\epsilon\tau^2\right),\ j = 1, 2, 6. \tag{2.106}$$

The instantaneous wetted surface area of the body is known from Taylor expansion of η at $z = h$ and consists of the body surface under the calm water line $\mathcal{S}_o$ and a surface wetted by the wave elevation η. The contour of the intersection of the calm water line with the body is denoted by $\mathcal{C}_o$. The linear forces directly follow from Eq. (2.105), such that,

$$F_j^{(k\ell)} \underset{\mathsf{Re}}{=} \int_{\mathcal{S}_o} p_{k\ell} n_j' dS \text{ for } k = 1, \ell = 0, 1 \text{ or } k = 0, \ell = 2, \tag{2.107}$$

where, as defined before, $n_6' = (\boldsymbol{x}' \times \boldsymbol{n}') \cdot \hat{e}_3$. The forces that are second-order in wave steepness come from [20] and are given as,

$$\begin{aligned} F_j^{(20)} \underset{\mathsf{Re}}{=} & \int_{\mathcal{S}_o} (\overline{p_{20}} + \overline{\left[\boldsymbol{\xi}^{(0)} + \boldsymbol{\alpha}^{(0)} \times \boldsymbol{x}'\right] \cdot \nabla p_{10}}) n_j' dS \\ & + \int_{\mathcal{S}_o} \overline{p_{10}\left[\boldsymbol{\xi}_b^{(0)} \times (n_1', n_2', 0)\right]} \cdot \hat{e}_j dS \\ & + \frac{\rho_o g}{2} \int_{\mathcal{C}_o} \overline{(\eta_{10} \cdot \eta_{10})} n_j' dl, \end{aligned} \tag{2.108}$$

where the $\overline{\mathrm{o}}$ denotes the time average, as defined in Eq. (2.41). For $y_j = \hat{y}_j e^{-i\sigma_o t}, \hat{y}_j \in \mathbb{C}^1$, it is easy to show that

$$\mathrm{Re}\left[y_1\right] \mathrm{Re}\left[y_2\right] \underset{\mathsf{Re}}{=} \frac{\hat{y}_1 \hat{y}_2}{2} e^{-2i\sigma_o t} + \frac{\hat{y}_1 \hat{y}_2^*}{2}, \tag{2.109}$$

where $(^*)$ denotes the complex conjugate, so that

$$\overline{\mathrm{Re}\left[y_1\right] \mathrm{Re}\left[y_2\right]} \underset{\mathsf{Re}}{=} \frac{\hat{y}_1 \hat{y}_2^*}{2}. \tag{2.110}$$

Thus can rewrite each of the terms in Eq. (2.108) as,

$$\begin{aligned} F_j^{(20)} = \underset{\mathsf{Re}}{} & \int_{\mathcal{S}_o} (\underbrace{p_{20}}_{(a)} + \underbrace{\frac{1}{2}\left[\boldsymbol{\xi}^{(0)} + \boldsymbol{\alpha}^{(0)} \times \boldsymbol{x}'\right] \cdot \nabla p_{10}^*}_{(b)}) n_j' dS \\ & + \frac{1}{2} \int_{\mathcal{S}_o} \underbrace{p_{10}^* \left[\boldsymbol{\xi}_b^{(0)} \times (n_1', n_2', 0)\right]}_{(c)} \cdot \hat{e}_j dS \\ & + \frac{\rho_o g}{4} \int_{\mathcal{C}_o} \underbrace{(\eta_{10} \cdot \eta_{10}^*)}_{(d)} n_j' dl. \end{aligned} \tag{2.111}$$

Similarly for the highest order force considered in this report, the forces and moment (also from [20]) are,

$$\begin{aligned} F_j^{(21)} = \underset{\mathsf{Re}}{} & \int_{\mathcal{S}_o} (\underbrace{p_{21}}_{(a)} + \underbrace{\frac{1}{2}\left[\boldsymbol{\xi}^{(0)} + \boldsymbol{\alpha}^{(0)} \times \boldsymbol{x}'\right] \cdot \nabla p_{11}^*}_{(b)}) n_j' dS \\ & + \frac{1}{2} \int_{\mathcal{S}_o} \underbrace{p_{11}^* \left[\boldsymbol{\xi}_b^{(0)} \times (n_1', n_2', 0)\right]}_{(c)} \cdot \hat{e}_j dS \\ & + \frac{1}{2} \int_{\mathcal{S}_o} \underbrace{\left(\left[\boldsymbol{\xi}^{(1)} + \boldsymbol{\alpha}^{(1)} \times \boldsymbol{x}'\right] \cdot \nabla p_{10}^*\right)}_{(d)} n_j' dS \\ & + \frac{1}{2} \int_{\mathcal{S}_o} \underbrace{p_{10}^* \left[\boldsymbol{\xi}_b^{(1)} \times (n_1', n_2', 0)\right]}_{(e)} \cdot \hat{e}_j dS \\ & + \frac{\rho_o g}{2} \int_{\mathcal{C}_o} \underbrace{(\eta_{10} \cdot \eta_{11}^*)}_{(f)} n_j' dl. \end{aligned} \tag{2.112}$$

The forces are decomposed, in their usual manner, into components that are independent from the body's motions, as well as dependent on the body's velocity and acceleration. We refer to these components as the wave-exciting force, damping, and added-mass, if they are proportional to the high-frequency oscillatory motion. If the forces are proportional to the slow-drift motions, the terms are known as slow-drift added-mass (double-body added-mass) and the slow-drift damping, which has been studied extensively in the hydrodynamics field (for yaw slow-drift damping see [19, 47, 24, 32, 48, 19]). As noticed in [19], the wave-drift damping in low-frequency motions is also strongly influenced by viscous effects, since separation occurs for most bodies in the Reynolds number regime. As in [20], let us separate the time-dependency of the oscillatory forces, such that

$$F_j^{(k\ell)} = \begin{cases} \mathrm{Re}\left[\bar{F}_j^{(k\ell)} e^{-i\sigma_e t}\right], \text{ for } k = 1, \ell = 0, 1, \\ \bar{F}_j^{(k\ell)} \text{ otherwise,} \end{cases} \tag{2.113}$$

since the time-independent forces are already real-valued.

The forces and moments can be written as,

$$\mathrm{O}\left(\epsilon\right):\bar{F}_j^{(10)} = A_o\mathcal{X}_j^{(0)} + \mathcal{A}_i^{(0)}\left(\sigma_o^2\mu_{ji}^{(0)} + i\sigma_o\lambda_{ji}^{(0)}\right), \tag{2.114a}$$

$$\mathrm{O}\left(\epsilon\tau\right):\bar{F}_j^{(11)} = A_o\mathcal{X}_j^{(1)} + \mathcal{A}_{i,\beta}^{(0)}\left(\sigma_o^2\mu_{ji}^{(\beta)} + i\sigma_o\lambda_{ji}^{(\beta)}\right) + \sum_{\substack{k,\ell=0\\ \ell\neq k}}^{1}\mathcal{A}_i^{(k)}\left(\sigma_o^2\mu_{ji}^{(\ell)} + i\sigma_o\lambda_{ji}^{(\ell)}\right), \tag{2.114b}$$

$$\mathrm{O}\left(\epsilon^2\right):\bar{F}_j^{(20)} = A_o^2\bar{\mathcal{X}}_j^{(2)} + A_o\mathcal{A}_i^{(0)}\bar{\kappa}_{ji} + \mathcal{A}_i^{(0)}\sum_{k=1,2,6}\mathcal{A}_k^{(0)*}\left(\sigma_o^2\bar{\mu}_{jik}^{(2)} + i\sigma_o\bar{\lambda}_{jik}^{(2)}\right), \tag{2.114c}$$

$$\mathrm{O}\left(\tau^2\right):\bar{F}_j^{(02)} = -\bar{\mu}_{ji}\dot{U}_j, \tag{2.114d}$$

$$\mathrm{O}\left(\epsilon^2\tau\right):\bar{F}_j^{(21)} = -A_o^2\bar{\lambda}_{ji}U_j + A_o^2\bar{\mathcal{X}}_j^{(3)} + \ldots, \tag{2.114e}$$

where we use the slow-drift velocities and accelerations as defined in the slow-drift frame of reference. Here, we have used the conventions of [20] and [35]. The zero-speed linear added-mass and damping are represented by $\mu_{ij}^{(0)}$ and $\lambda_{ij}^{(0)}$, respectively. The 'interaction' added-mass and damping are represented by $\mu_{ij}^{(1)}$ and $\lambda_{ij}^{(1)}$, respectively. The double-body flow added-mass and wave-drift damping coefficients are $\bar{\mu}_{ij}$ and $\bar{\lambda}_{ij}$, where we have neglected products (but not derivatives) of slow-drift velocities as done in [22]. The time-harmonic, wave-exciting forces for each order of the perturbation series are $\mathcal{X}_j^{(k)}$, for $k = 0, 1$, respectively. The steady hydrodynamic wave-exciting forces and moments are given by $\bar{\mathcal{X}}^{(k)}$ for $k = 2, 3$, since we have ignored the higher harmonics in this analysis. A few other interesting terms come out, such as $\bar{\kappa}_{ij}$, which is a steady force/moment on the platform proportional to the complex amplitude of the first-order oscillations. Further, terms related to the product of these complex amplitudes of oscillations are given by the tensor $\bar{\mu}_{jik}^{(2)}$ and $\bar{\lambda}_{jik}^{(2)}$. These represent the forces in the j^{th} direction, due to the product of complex amplitude oscillations of the body in the i^{th} and k^{th} directions. We note that the forces $\mathrm{O}\left(\epsilon^2\tau\right)$ will include products such as $U_jA_o\mathcal{A}_k^{(0)}$. However, we only consider this order of magnitude to derive expressions for the wave-drift damping, $\bar{\lambda}_{ji}$ and will neglect the highest-order steady forces/moments.

All of these hydrodynamic coefficients are fully derived in Appendix F. However, we amplify the results from this study by repeating the original findings shown in Appendix F. To the author's knowledge, the second-order, steady slow-drift forces and moment had not been previously investigated using the direct pressure integration technique. Most other derivations use some sort of momentum conservation principle over a control surface, such as described in [20]. Thus, for a *multi-column platform, whose centroid of waterplane area is aligned with the center of rotation*, we show that

$$\boxed{\sum_{k=1}^{N_{col}}\bar{\mathcal{X}}_6^{k(2)} = 0} \tag{2.115}$$

and that for the k^{th} column,

$$\boxed{\sum_{i=1,2,6} \mathcal{A}_i^{(0)} \sum_{j=1,2,6} \mathcal{A}_j^{(0)*} \sigma_o^2 \bar{\mu}_{6ij}^{(2)} + i\sigma_o \bar{\lambda}_{6ij}^{(2)} = 0.} \tag{2.116}$$

Thus the only surviving term in Eq. (2.114c) is the second one. In Appendix F we show that this moment on the platform can be represented as,

$$\begin{aligned}\boxed{\sum_{i=1,2,6} \mathcal{A}_i^{(0)} \frac{\bar{\kappa}_{6i}}{\rho_o g \pi a^2} =} & \mathcal{A}_1^{(0)} \sum_k^{N_{col}} \left(-\frac{y_0^k}{a} \bar{\kappa}_{11}^k + \frac{x_0^k}{a} \bar{\kappa}_{21}^k + \frac{\bar{\mathcal{X}}_2^{k(0)*}}{2} \right) \\ & + \mathcal{A}_2^{(0)} \sum_k^{N_{col}} \left(\frac{x_0^k}{a} \bar{\kappa}_{22}^k - \frac{y_0^k}{a} \bar{\kappa}_{12}^k - \frac{\bar{\mathcal{X}}_1^{k(0)*}}{2} \right) \\ & + \mathcal{A}_6^{(0)} \sum_k^{N_{col}} \left(-\frac{1}{2} \left[x_0^k \bar{\mathcal{X}}_1^{k(0)*} + y_0^k \bar{\mathcal{X}}_2^{k(0)*} \right] \right. \\ & \left. + 2\frac{x_0^k y_0^k}{a} \bar{\kappa}_{12}^{k(t)} - \frac{y_0^k y_0^k}{a} \bar{\kappa}_{11}^{k(t)} - \frac{x_0^k x_0^k}{a} \bar{\kappa}_{22}^{k(t)} \right)\end{aligned} \tag{2.117}$$

where

$$\begin{aligned}\boxed{\frac{\bar{\kappa}_{j\ell}^k}{\rho_o g a_k \pi} = -i\frac{P_k^*}{2} \left\{ \sum_{q=0}^{\infty} G_q^{(2)*} \cos[2\beta - (\chi_j + \chi_\ell)] \right.} & \\ \left[\underbrace{\check{D}_q}_{(b)} + \sum_{p=0}^{\infty} H_p^\ell(a_k) \left(\underbrace{\bar{E}_{pq}^D + \frac{\bar{F}_{pq}^D (k_q a_k)(k_p a_k)}{2}}_{(a)} + \underbrace{(\nu_o a_k) \check{Z}_p(h) \check{Z}_q(h)}_{(d)} \right) \right] & \\ \left. + G_q^{(0)*} \cos(\chi_j - \chi_\ell) \sum_{p=0}^{\infty} H_p^\ell(a_k) \left(\underbrace{\bar{F}_{pq}^D (k_q a_k)(k_p a_k)}_{(a)} + \underbrace{(\nu_o a_k) \check{Z}_p(h) \check{Z}_q(h)}_{(d)} \right) \right\} &\end{aligned} \tag{2.118}$$

with the $G_q^{(m)}$ terms related to the first-order scattering potential, defined in Eq. (2.78) and the H_p^ℓ terms related to the radiation potential defined in Eq. (2.85). The terms related to the integration of the vertical functions $\check{D}_q$, $\bar{E}_{pq}^D$ and $\bar{F}_{pq}^D$ are defined in Appendix F.3. The term $\bar{\kappa}_{j\ell}^{k(t)}$ is equivalent to $\bar{\kappa}_{j\ell}^k$ minus the contribution from the $\check{D}_q$ term.

2.5.3 Conservation of Momentum

We continue with a more general formulation that is not restricted to the analysis of a multi-column platform. As stated by [35], the conservation of linear momentum in the

inertial frame can be written as

$$m_b \frac{d^2}{dt^2}[\boldsymbol{X}_o + S^T(\Theta_o)\boldsymbol{\xi}] = S^T(\Theta_o)\boldsymbol{F} + \boldsymbol{f}_m \tag{2.119}$$

where m_b is the mass of the body and we have formulated the hydrodynamic forces $\boldsymbol{F}$ in the slow-drift frame. The mooring forces are represented by the vector $\boldsymbol{f}_m$ and are discussed in Sec. 2.5.4. We have assumed that the origin of the slow-drift frame and the center of gravity of the body are coincident (i.e., the center of rotation and the center of gravity lie on the same vertical axis). The expansion of the time derivative transforms the above equation into,

$$m_b \left(\dot{\boldsymbol{U}}_{\boldsymbol{o}} + \ddot{S}^T(\Theta_o)\boldsymbol{\xi} + 2\dot{S}^T(\Theta_o)\dot{\boldsymbol{\xi}} + S^T(\Theta_o)\ddot{\boldsymbol{\xi}}\right) = S^T(\Theta_o)\boldsymbol{F} + \boldsymbol{f}_m \tag{2.120}$$

where we will consider the smallness of these quantities in the next section.

The total angular velocity of the body $\boldsymbol{\Omega_b}$ is

$$\boldsymbol{\Omega_b} = S(\xi_6)\boldsymbol{\Omega_o} + \dot{\boldsymbol{\alpha}} = \boldsymbol{\Omega_o} + \dot{\boldsymbol{\alpha}} \tag{2.121}$$

where the second equality is due to only considering horizontal plane motion, such that $\xi_3 = \xi_4 = \xi_5 = 0$.

The conservation of angular momentum is

$$[I]\frac{\partial \boldsymbol{\Omega_b}}{\partial t} + \boldsymbol{\Omega_b} \times [I]\boldsymbol{\Omega_b} = S(\xi_6)\boldsymbol{M} + \boldsymbol{M}_m, \tag{2.122}$$

where $[I]$ is the inertia matrix of body and the hydrodynamic moments are $\boldsymbol{M} = (F_4, F_5, F_6)$. The mooring moment is represented by the vector $\boldsymbol{M}_m$. Again, only considering the yaw mode of motion, the equation of motion is simply,

$$I_b\left(\dot{U}_6 + \ddot{\xi}_6\right) = F_6 + f_6^m \tag{2.123}$$

where I_b is the yaw moment of inertia (I_{66}) and the yaw moment relating to the mooring system is given by f_6^m.

2.5.4 Mooring Forces

We assume that the effect of the mooring system on the platform can be represented by uncoupled linear stiffness terms, related to the first-order motions, such that

$$\boldsymbol{f}_m = -[k]\boldsymbol{\xi}^{(0)}, \tag{2.124}$$

where $k_{11} = k_{22} = k_m$, which is a spring stiffness related to the material and size of the mooring line. The mooring system consists of a inextensible single-point mooring line with a universal joint, which allows free motion in the yaw direction . The stiffness of the lines was not scaled properly from the full-size model due to the strict sway requirements in the towing tank. The platform spanned nearly two-thirds of the width of the tank and a fragile viewing

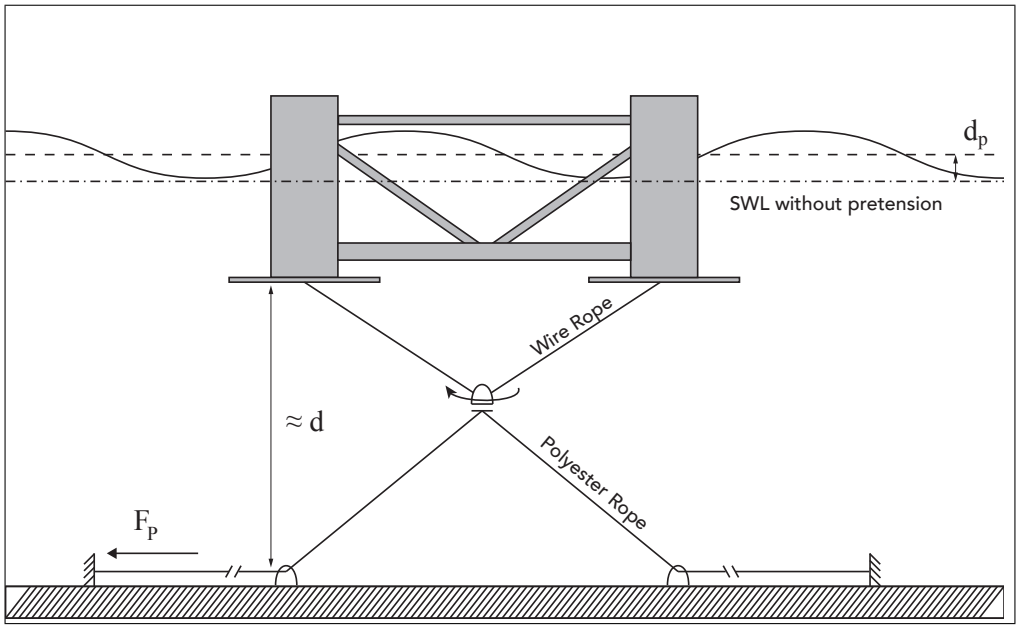

Figure 2.5: Diagram showing single-point mooring system with multiple touchdown points to prevent torsion in the ropes.

window was located less than a foot from the end of the heave plate. It was determined that the safety of the tank was of the highest priority. The system was pretensioned by pulling on the polyester ropes before fixing it to their respective mooring points. The amount of pretension in the ropes F_P can be determined by the increase in draft of the platform d_p, as shown in Fig. 2.5, by

$$F_P = \rho_o g A_{wp} d_p. \tag{2.125}$$

If the line is assumed to be inextensible, and neglecting terms $\mathrm{O}\left((|\xi_j|/d)^2\right)$, the stiffness is related to the horizontal displacements by,

$$f_j^m = -\frac{F_P}{d}\xi_j^{(0)} = -\left(\frac{\rho_o g A_{wp} d_p}{d}\right)\xi_j^{(0)} = -k_m \xi_j^{(0)}, \text{ for } j = 1, 2. \tag{2.126}$$

We neglect any damping in the mooring line due to the pretensioning of the mooring system after the platform was installed. Thus, we only take into account the damping of the universal joint in both the slow-scale and fast-scale yaw motions, where we assume that the friction in the joint is independent of the speed of rotation such that,

$$f_6^m = -b_{66}\dot{\xi}_6 - b_{66}U_6. \tag{2.127}$$

Here, we have assumed no stiffness in the universal joint and we have disregarded the roll and pitch motions (which are heavily influenced by the mooring design and stiffness). Since we had no way to disassociate the viscous damping and the damping due to the universal joint once the platform was in the water, we add the damping due to the universal joint into the empirically determined drag coefficient, which is discussed in further detail in Sec. 2.9.2.

2.5.5 Fast and Slow-Scale Equations of Motion

The equations of motion for the body, where only the hydrodynamic forces are considered, can be split into fast and slow timescales, referring to the small-amplitude motions of the body excited by the incident waves as well as the slow-drift motion, respectively.

Fast-scale Equations of Motion

We can expand the external force into its perturbation series in Eqs. (2.120) and multiply it with $S^T(\Theta_o)$ to obtain a time-harmonic equation of motion, given as,

$$\mathrm{O}\left(\epsilon, \epsilon\tau\right): \quad m_b\left[\frac{d^2}{dt^2}\left(\boldsymbol{\xi^{(0)}}+\boldsymbol{\xi^{(1)}}\right)+2U_6S^T(\Theta_o)R^T(\Theta_o)\frac{d\boldsymbol{\xi^{(0)}}}{dt}+...\right]=\boldsymbol{F}^{(10)}+\boldsymbol{F}^{(11)}+\boldsymbol{f}_m, \tag{2.128a}$$

where $\dot{S}(\Theta_o) = U_6R(\Theta_o)$ and the terms that include products or derivatives of slow-drift velocities are neglected. Focusing our attention on terms of $\mathrm{O}\left(\epsilon\right)$ and substituting the formulations for the wave forces given in the previous section, we find that

$$\sum_j^{1,2,6}\mathcal{A}_j^{(0)}\left[\sigma_o^2(\mu_{ij}^{(0)}+M_{ij}^b)+i\sigma_o(\lambda_{ij}^{(0)}+b_{ij})-k_{ij}\right]=-A_o\mathcal{X}_i^{(0)},\ \text{for } i=1,2,6 \tag{2.129}$$

where $[M^b]$ is the 2D mass matrix with $M_{11}^b = M_{22}^b = m_b$, $M_{33}^b = I_b$ and the off-diagonal terms are null since there is no coupling between modes of motion in the horizontal plane. For terms of $\mathrm{O}\left(\tau\epsilon\right)$, we can cancel the time dependency, which yields

$$-m_b\left[\sigma_o^2\boldsymbol{\mathcal{A}^{(1)}}+2\sigma_ok_o(U_1\cos\beta+U_2\sin\beta)\boldsymbol{\mathcal{A}^{(0)}}-2i\sigma_oU_6S^T(\Theta_o)R^T(\Theta_o)\boldsymbol{\mathcal{A}^{(0)}}+2i\sigma_oU_6\boldsymbol{\mathcal{A}^{(\beta)}}\right]=\bar{\boldsymbol{F}}^{(11)} \tag{2.130}$$

Let the i,j^{th} element of the matrix $S^T(\Theta_o)R^T(\Theta_o) = T_{ij}$. Substituting the representations of $\bar{\boldsymbol{F}}^{(11)}$, gives

$$\begin{aligned}\mathcal{A}_j^{(1)}&\left[\sigma_o^2(\mu_{ij}^{(0)}+m_b)+i\sigma_o\lambda_{ij}^{(0)}\right]=-A_o\mathcal{X}_i^{(1)}\\&-\mathcal{A}_j^{(0)}\left(2im_b\sigma_o\left(ik_o(U_1\cos\beta+U_2\sin\beta)+U_6T_{ij}\mathcal{A}_i^{(0)}\right)+\left(\sigma_o^2\mu_{ij}^{(1)}+i\sigma_o\lambda_{ij}^{(1)}\right)\right)\\&-\mathcal{A}^{(\beta)}\left(2im_b\sigma_oU_6+\left[\sigma_o^2\mu_{ij}^{(\beta)}+i\sigma_o\lambda_{ij}^{(\beta)}\right]\right)\ \text{for } j=1,2,\end{aligned} \tag{2.131}$$

which agrees with Eq. (4.23) of [35] for $\xi_4 = \xi_5 = 0$ and neglecting mooring restoring forces rather than Eq. (4.24) of [20], who omits the T_{ij} term. For the rotational modes, the formulation is the same, except that the T terms does not exist. Thus, we can T by $\boldsymbol{t}$, where $\boldsymbol{t}_{ij} = T_{ij}$ for $j = 1, 2$ and null otherwise. Rewriting Eq. (2.131) for the horizontal modes of motion $j = 1, 2, 6$,

$$\begin{aligned}\mathcal{A}_j^{(1)}&\left[\sigma_o^2(\mu_{ij}^{(0)}+M_{ij}^b)+i\sigma_o\lambda_{ij}^{(0)}\right]=-A_o\mathcal{X}_i^{(1)}\\&-\mathcal{A}_j^{(0)}\left(2iM_{ij}^b\sigma_o\left(ik_o(U_1\cos\beta+U_2\sin\beta)+U_6\boldsymbol{t}_{ij}\mathcal{A}_i^{(0)}\right)+\left(\sigma_o^2\mu_{ij}^{(1)}+i\sigma_o\lambda_{ij}^{(1)}\right)\right)\\&-\mathcal{A}^{(\beta)}\left(2iM_{ij}^b\sigma_oU_6+\left[\sigma_o^2\mu_{ij}^{(\beta)}+i\sigma_o\lambda_{ij}^{(\beta)}\right]\right)\ \text{for } j=1,2,6.\end{aligned} \tag{2.132}$$

In order to determine the equation of motion for $\mathcal{A}^{(\beta)}$, we have

$$\mathcal{A}^{(0)}_{j,\beta}\left[\sigma_o^2(\mu^{(0)}_{ij}+M^b_{ij})+i\sigma_o\lambda^{(0)}_{ij}\right]=-A_o\frac{\partial\mathcal{X}^{(0)}_i}{\partial\beta},\ \text{for } j=1,2,6. \tag{2.133}$$

Slow-Drift Equations of Motion

Likewise collecting higher-order terms, we can solve for the slow-drift translations and rotations,

$$\mathrm{O}\left(\epsilon^2,\tau^2,\epsilon^2\tau\right): \qquad m_b\,\frac{d^2}{dt^2}\boldsymbol{X_o}=S^T(\Theta_o)\left(\boldsymbol{F}^{(02)}+\boldsymbol{F}^{(20)}+\boldsymbol{F}^{(21)}\right), \tag{2.134a}$$

$$\mathrm{O}\left(\epsilon^2,\tau^2,\epsilon^2\tau\right): \qquad I_b\,\dot{\boldsymbol{\Omega}}_{\boldsymbol{o}}=\left(\boldsymbol{M}^{(02)}+\boldsymbol{M}^{(20)}+\boldsymbol{M}^{(21)}\right), \tag{2.134b}$$

Let us define a 2x2 matrix representing the upper-left of the rotational matrix $S^T(\Theta_o)$ as $s(\Theta_o)$. Then the translational slow-drift added-mass and damping, $i,j=1,2$, can be transformed into the inertial frame as

$$\bar{A}_{ij}=s^T(\Theta_o)\begin{bmatrix}\bar{\mu}_{11}&\bar{\mu}_{12}\\ \bar{\mu}_{21}&\bar{\mu}_{22}\end{bmatrix}s(\Theta_o) \tag{2.135a}$$

$$\bar{B}_{ij}=s^T(\Theta_o)\begin{bmatrix}\bar{\lambda}_{11}&\bar{\lambda}_{12}\\ \bar{\lambda}_{21}&\bar{\lambda}_{22}\end{bmatrix}s(\Theta_o)+s^T(\Theta_o)\begin{bmatrix}\bar{\mu}_{11}&\bar{\mu}_{12}\\ \bar{\mu}_{21}&\bar{\mu}_{22}\end{bmatrix}[\dot{s}]_\Theta \tag{2.135b}$$

$$\bar{K}_{ij}=s^T(\Theta_o)\begin{bmatrix}\bar{\kappa}_{11}&\bar{\kappa}_{12}\\ \bar{\kappa}_{21}&\bar{\kappa}_{22}\end{bmatrix}\ \text{for } i,j=1,2 \tag{2.135c}$$

whereas for the rotational slow-drift added-mass and damping,

$$\bar{A}_{i3}=s^T(\Theta_o)\begin{bmatrix}\bar{\mu}_{16}\\ \bar{\mu}_{26}\end{bmatrix},\quad \bar{A}_{3i}=\begin{bmatrix}\bar{\mu}_{61}&\bar{\mu}_{62}\end{bmatrix}s(\Theta_o), \tag{2.136a}$$

$$\bar{B}_{i3}=s^T(\Theta_o)\begin{bmatrix}\bar{\lambda}_{16}\\ \bar{\lambda}_{26}\end{bmatrix},\quad \bar{B}_{3i}=\begin{bmatrix}\bar{\lambda}_{61}&\bar{\lambda}_{62}\end{bmatrix}s(\Theta_o)+\begin{bmatrix}\bar{\mu}_{61}&\bar{\mu}_{62}\end{bmatrix}[\dot{s}]_\Theta \tag{2.136b}$$

$$\bar{K}_{i3}=s^T(\Theta_o)\begin{bmatrix}\bar{\kappa}_{16}\\ \bar{\kappa}_{26}\end{bmatrix},\quad \text{for } i,=1,2 \tag{2.136c}$$

$\bar{A}_{33}=\bar{\mu}_{66}$, $\bar{B}_{33}=\bar{\lambda}_{66}$, $\bar{K}_{33}=\bar{\kappa}_{66}$. Thus we can write the slow-drift equations of motion as

$$\ddot{\boldsymbol{X}}_{\boldsymbol{b}}\left([\bar{A}]+[M^b]\right)+A_o^2[\bar{B}]\dot{\boldsymbol{X}}_{\boldsymbol{b}}=S^T(\Theta_o)\left(A_o^2(\bar{\boldsymbol{\mathcal{X}}}^{(\mathbf{2})}+\bar{\boldsymbol{\mathcal{X}}}^{(\mathbf{3})})\right)+A_o[\bar{K}]\boldsymbol{\mathcal{A}_b}^{(0)}+\sigma_o^2\mathcal{A}_i^{(0)}[\mathcal{K}^{(j)}]\boldsymbol{\mathcal{A}_b}^{(0)} \tag{2.137}$$

In these equations, we have not explicitly shown the transformations for the tensor $[\mathcal{K}^{(j)}] = \mathcal{L}[\bar{\mu}_{jik}]$, due to the variety of different possibilities, depending on the rotational or translation velocities. However, they can be solved for in a similar manner to the $\bar{K}_{ij}$. It is important to note that there is two-way coupling between the slow-modes and the fast modes. This has been predicted by previous authors, (see Eq. (2.60) in [35] where the dependency is given in $\vec{n}_{10}$, which is defined in Eqs. (2.34) and (2.36) of [35]), although it seems that no previous authors have written it explicitly. If we consider $U_1 = U_2 = 0$ and are only interested in the yaw motion, then Eq. (2.137) becomes,

$$(I_b + \bar{\mu}_{66})\ddot{\Theta}_o + (A_o^2\bar{\lambda}_{66} + b_{66})\dot{\Theta}_o = A_o^2(\mathcal{X}_6^{(2)} + \mathcal{X}_6^{(3)}) + \sum_j A_o\bar{K}_{3j}\mathcal{A}_j^{(0)} + \sum_i \sigma_o^2\mathcal{K}_{ji}^{(6)}\mathcal{A}_i^{(0)}\mathcal{A}_j^{*(0)}. \tag{2.138}$$

Equation (2.129) provides the solution to the response-amplitude operator (RAO) of the complex amplitude of the first-order motion $A_j^{(0)}/A_o$, for a given wave heading β_o and wave frequency σ_o. In Appendix F.5, it will be shown that the terms in the summation of Eq. (2.138) are related to the first-order hydrodynamic terms, which are also dependent on the relative, unsteady wave heading β and incident-wave frequency σ_o. Thus, we can calculate the RAO's a-priori to create a database to solve for the instantaneous slow-drift position and velocity in time-domain simulations.

2.6 Verification of Frequency Domain Results

We verify the numerical procedure described in the previous sections against published data for truncated cylinders.

2.6.1 Verification for a Single, Isolated Cylinder

A verification of the numerical code used in this work for an isolated cylinder is shown in Figure 2.6 by comparing the results with those from an in-house numerical software, documented in [18]. The real and imaginary parts of the heave wave-exciting force are plotted as a function of the nondimensional wavenumber k_0a for a cylinder with dimensions $a/h = 0.1$, $d/h = 0.3$. Over a wide range of cylinder dimensions, the two codes agree to 4 decimal places.

2.6.2 Verification for Multiple, Interacting Cylinders

A simple verification of the author's code is shown in Figure 2.7 for the ISSC-TLP platform. The modeled platform simply has 4 columns with dimensions $a/h = .042$, $d/h = .825$, $R/h = .431$. The yaw wave-exciting moment ($\beta_0 = 22.5°$), is verified against the similar formulation of Williams in [38] and the 3D panel method of [49] in Fig. 2.7. There are two explanations for the discrepancies for the hydrodynamic coefficients between the present method and the previous published results: first, we do not make approximations for the

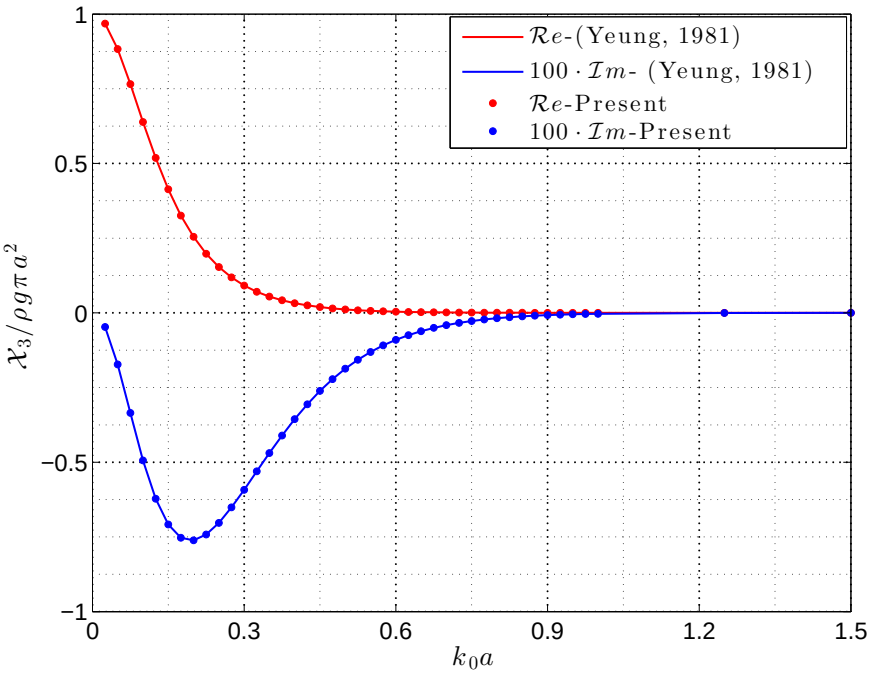

Figure 2.6: Verification of present code using results from [18] for heave wave-exciting force of an isolated, truncated cylinder with $a/h = 0.1$, $d/h = 0.3$.

Hankel functions as in the previous literature; second, we found a few critical typos in the derivations published and are unsure if the previous authors coded those mistakes. Zhong employs a similar method in [42], but exploits the fast decay of the evanescent modes, which was done for a truncated cylinder interacting with a channel's walls in [50]. Related to this work, she studied the effect of cylinder spacing distance R on the zero-speed, first-order added-mass and damping on an array of three cylinders in a configuration of an equilateral triangle. Their dependency on the nondimensional frequency of oscillation of the cylinders are shown in Figs. 2.8 and 2.9. The added-mass and damping of other configurations are included in [42].

2.6.3 Verification of Double-Body Added Mass

We solve for the double-body added mass of the truncated cylinder by letting the incident-wave frequency approach zero for the first-order problem. As Yeung points out in [18], the limit as $a \gg h$ is

$$\lim_{a/h \to \infty} \bar{\mu}_{11} = \frac{1 - d/h}{1 + d/h}. \tag{2.139}$$

For other values of a/h, we compare the low-frequency results from [18] with the results from the code developed in the present study in Fig. 2.10. Indeed, the results approach the asymptotic values (shown with the dashed lines) for $a \gg h$. Interestingly, for $a \ll h$, the results approach the limit for a bottom-seated cylinder ($d/h = 0$). The results shown are

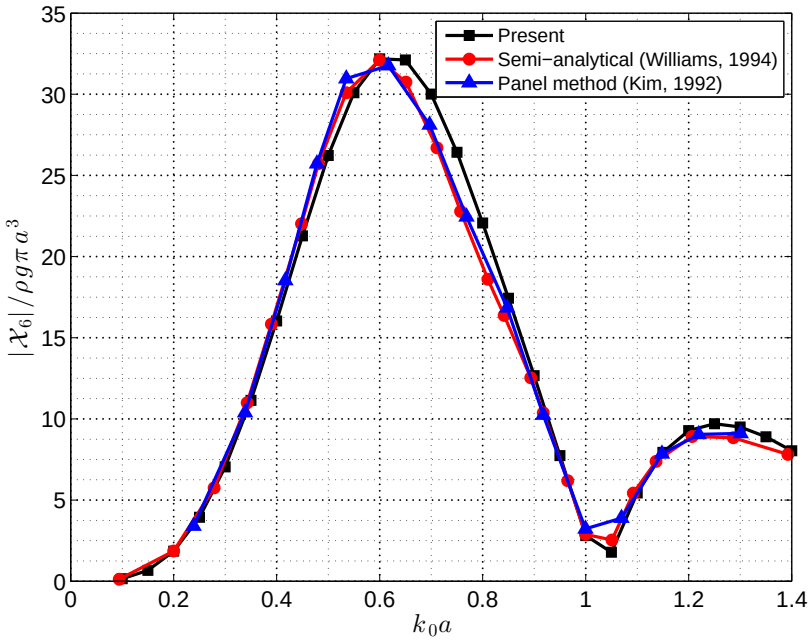

Figure 2.7: Verification of yaw wave-exciting moment for the ISSC TLP platform for β_o=22.5° with results from a similar formulation in [38] and the panel method in [49].

for $k_o a = 0.0025$, however, the results showed good convergence for values approaching this frequency.

2.7 Case Study: Isosceles-shaped Semi-Submersible Platform

In this section, we show the results for the hydrodynamic model developed in the frequency domain. These results are necessary so that we can simulate the model in the time-domain. The specifications of the platform are shown in Table 2.1 and their definitions are in plan view in Fig. 2.11.

The surge and sway hydrodynamic coefficients are identical due to circumferential symmetry. The surge added-mass and damping are shown in Fig. 2.12 and the surge response amplitude operator (RAO), which can be found in Eq. (2.129), is plotted in Fig. 2.13. The large peak at $k_o a = 0.021$ corresponds to the surge resonant frequency of the platform, which is highly dependent on the stiffness of the mooring cables. Around this frequency, the response amplitude operators are non-physical since this analysis assumes that the fluid is inviscid. It can be shown that resonance occurs when the term inside the square brackets in Eq. (2.129) approaches null. In a real fluid the drag forces will dampen out these large oscillations (see Sec. 2.8). The other dashed line in Fig. 2.13 corresponds to half of the

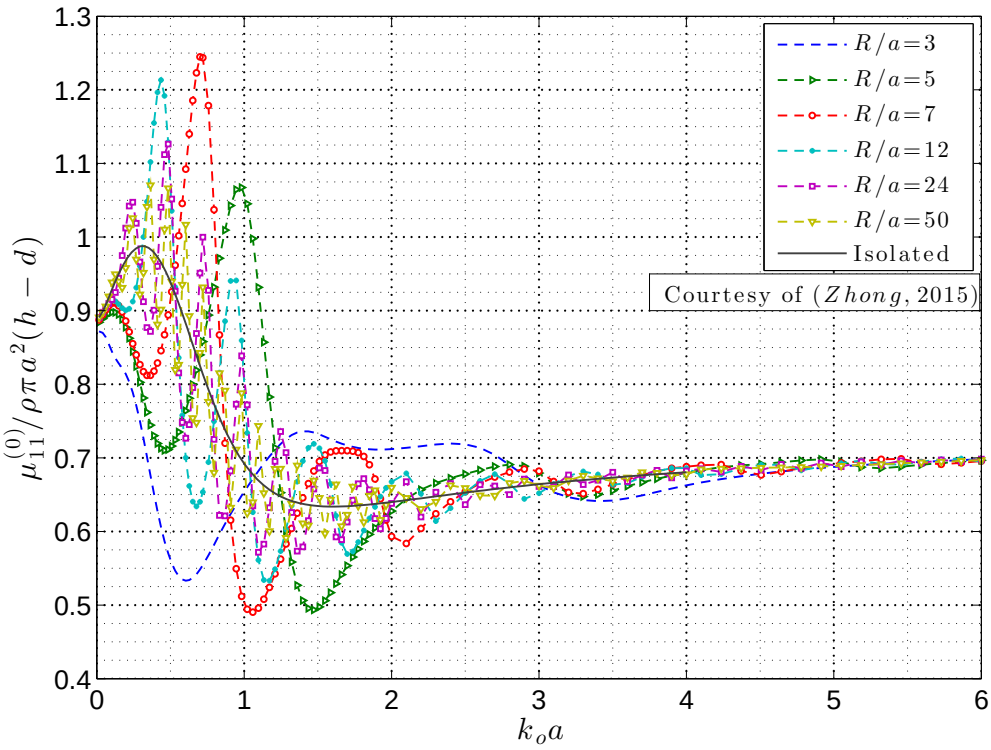

Figure 2.8: Zero-speed, first-order, surge-surge hydrodynamic added-mass of a cylinder in a three-cylinder array including interaction effects, courtesy of Zhong [42]. The spacing between the cylinders in an equilateral triangle is varied and the results compared to the case of an isolated cylinder.

Parameter	Value
N_c	3
$\bar{a} = a/h$	0.047
$\bar{d} = d/h$	0.729
$\bar{R}_{12} = R_{12}/h$	0.904
$\bar{R}_{23}, \bar{R}_{31}$	0.769
d_p/d	0.068
$(k_o a)_{res,surge}$	0.021

Table 2.1: Geometry and mass properties of the tri-column semi-submersible built and simulated in this study.

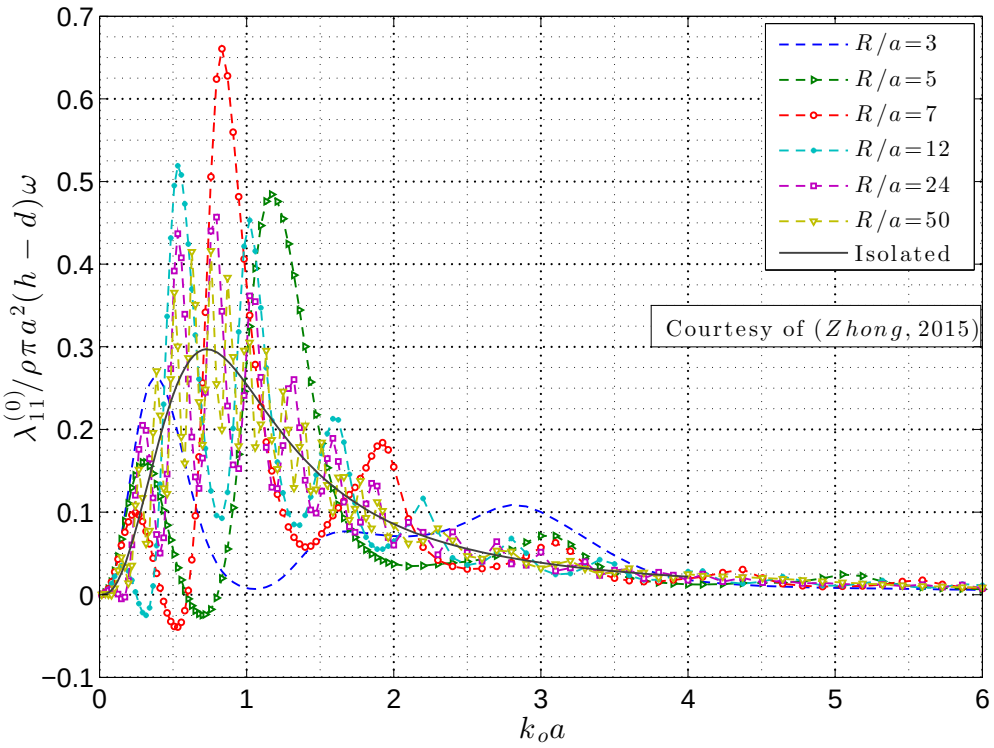

Figure 2.9: Zero-speed, first-order, surge-surge hydrodynamic damping of a cylinder in a three-cylinder array including interaction effects, courtesy of Zhong [42]. The spacing between the cylinders in an equilateral triangle is varied and compared to the case of an isolated cylinder.

nondimensional distance of one of the sides of the platform. When $\beta = 54°$, the wave is heading perpendicular to the vector described by R_{23} in Fig. 2.11. Thus, the surge RAO is a local minimum when the wavelength of the incident is exactly one half of h_2, which is also defined in Fig. 2.11.

The yaw radiation and damping and wave-exciting moment are shown in Figs. 2.14 and 2.15, respectively. As shown in Fig. 2.16, the yaw RAO depends on the relative incident-wave angle β. Although not shown in the figure, the limit for RAO_6 as $k_o a \to 0$ is finite. In this long-wave limit, the yaw response of the platform is proportional to the wave slope.

2.7.1 Second-Order Steady Moment

As mentioned previously, it will be shown that the steady, second-order wave exciting moment due to the summation of the drift forces in surge and sway on each column is null. This result comes from the fact that the drift forces are *temporally* and *spatially* independent. Thus, irrespective of the incident wave angle, the moment due to these forces is null. It will also be shown in Appendix F that the moment related to the product of the linear motion amplitudes (the last term in Eq. (2.114c)) is also null. Thus the only term that

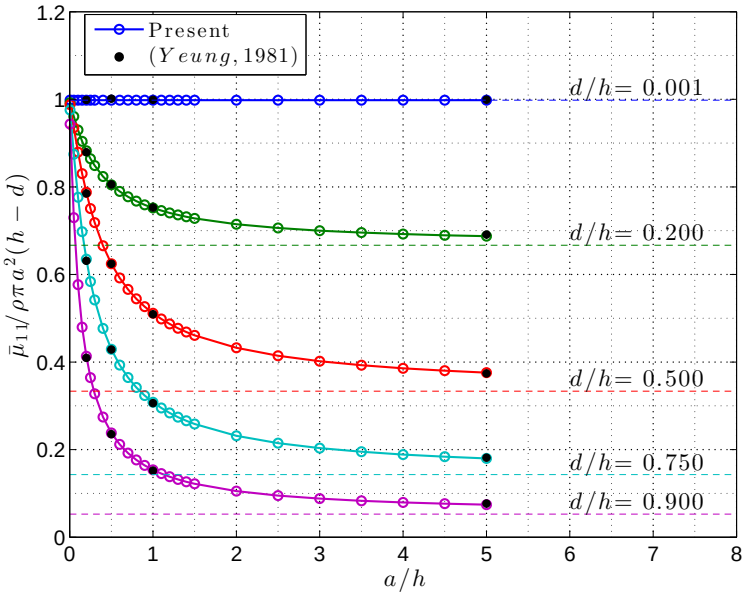

Figure 2.10: Low-frequency approximation of surge, double-body added-mass coefficients $\bar{\mu}_{11}$ of a truncated cylinder.

remains in Eq. (2.114c) is linearly proportional to the motion amplitudes *and* the incident wave amplitude. This moment is given explicitly in Eq. (F.57), which depends on the newly derived surge and sway forces, given in Eq. (F.29). The moment depends on the first-order response amplitude operators in surge, sway and yaw, which are all dependent on the fluid damping on the system. Thus, we show results from the RAO's shown in Figures 2.13 and 2.16, which are determined using only inviscid assumptions.

The steady, second-order moments on the MIST platform are shown in Figures 2.17 and 2.18 as functions of incident wave frequency and platform heading, respectively. The *stable* equilibrium positions occur when the platform exhibits symmetry ($\Theta_o = 0°, 60°, 120°$, etc), when the moment crosses the x-axis with a downward slope.

2.8 Effect of Viscosity

The platform considered in this study has moving in a Reynolds regime where the effect of viscosity on the motion of the platform may be important. Generally, the Reynolds number, denoted by Re is a non-dimensional ratio indicating the effect of viscosity over inertial effects. It is defined as,

$$Re = \frac{UL}{\nu}, \tag{2.140}$$

where U and L are the characteristic velocity and length of the object and ν is the kinematic viscosity of the fluid. Thus, for a column of the platform that is undergoing pure yaw, $Re_j = 2a_j\dot{\theta}_0 R_j/\nu$. For the vertical cylinders considered in this study at model-scale the

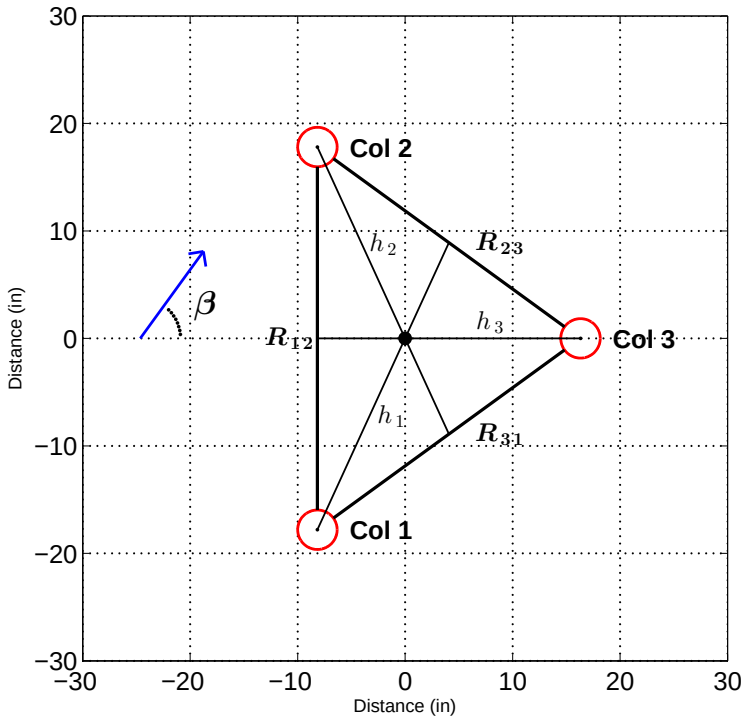

Figure 2.11: Plan view of MIST platform in the slow-drift frame, with definitions of distances between columns.

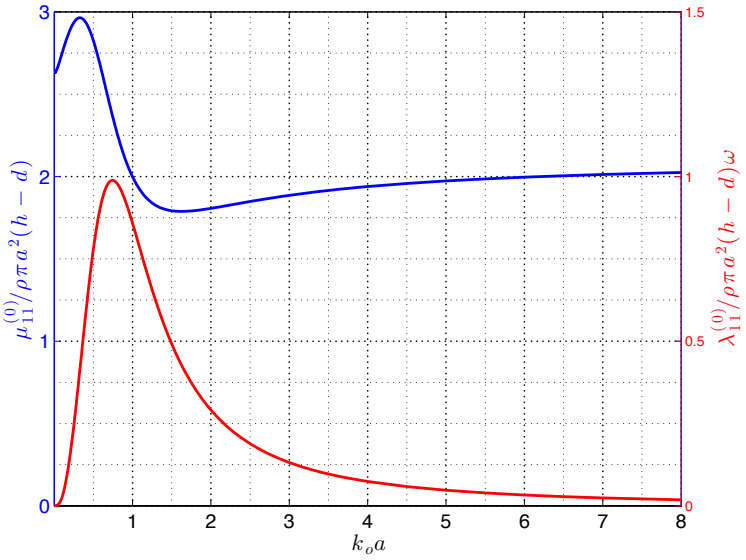

Figure 2.12: First-order surge-surge, hydrodynamic added-mass and damping for MIST platform.

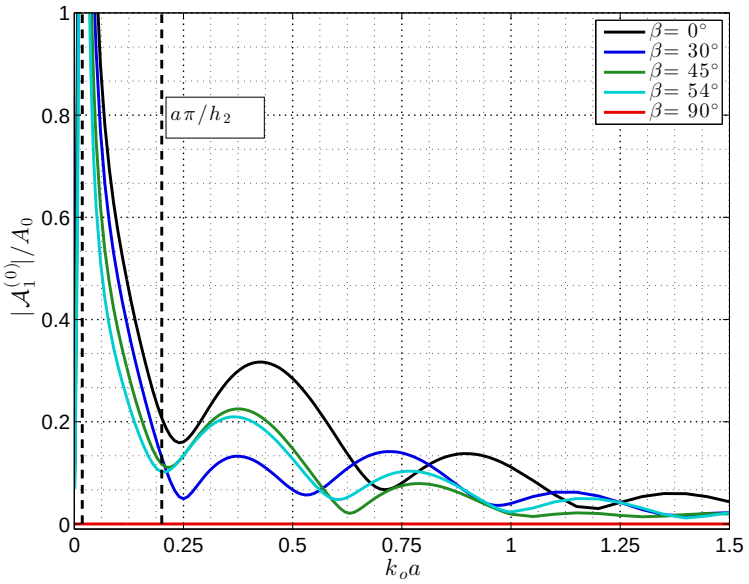

Figure 2.13: First-order surge response-amplitude operator for MIST platform. First dashed line corresponds to resonant frequency (highly dependent on mooring stiffness).

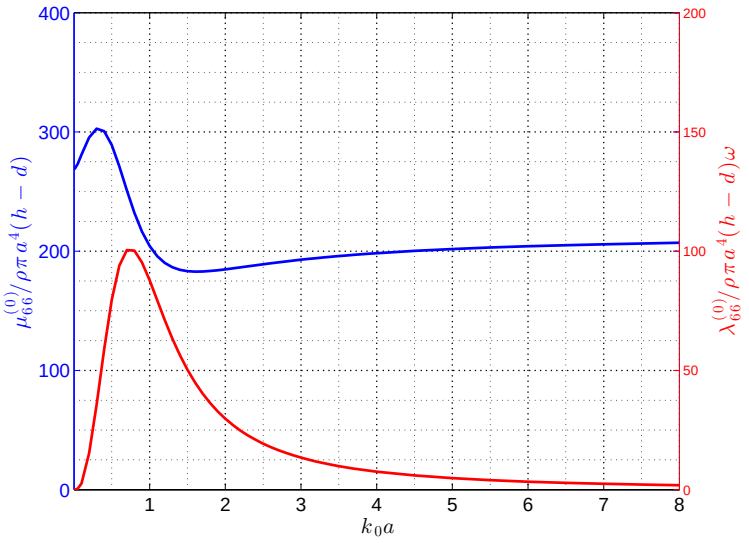

Figure 2.14: First-order yaw-yaw, hydrodynamic added-mass and damping for MIST platform.

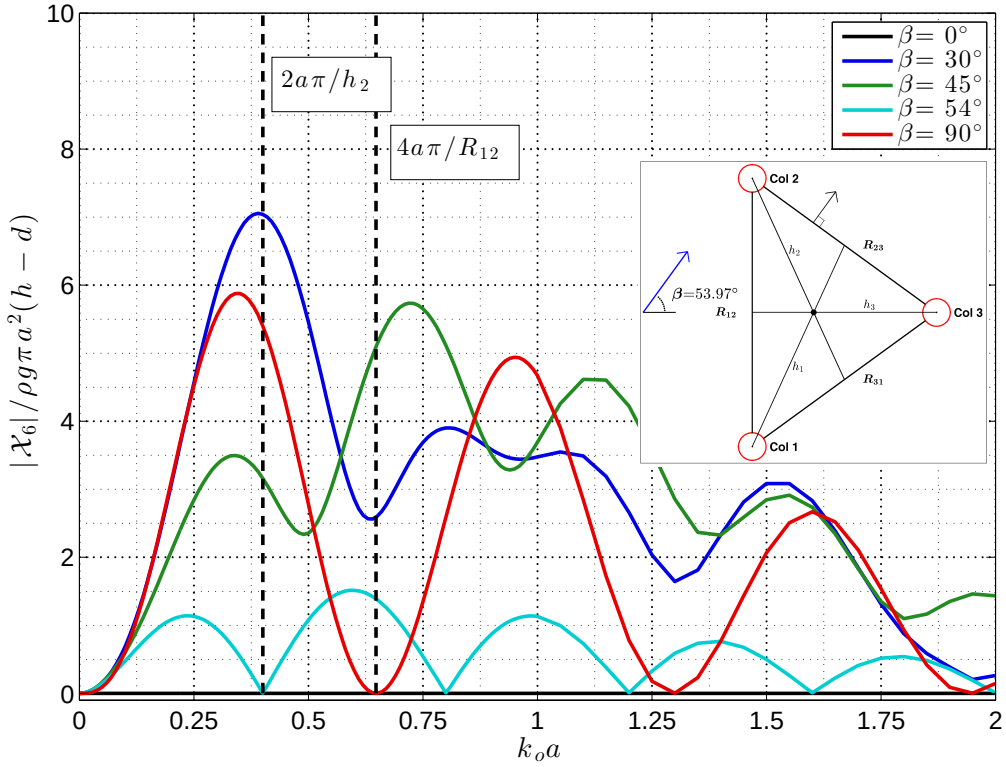

Figure 2.15: First-order yaw wave-exciting moment for MIST platform.

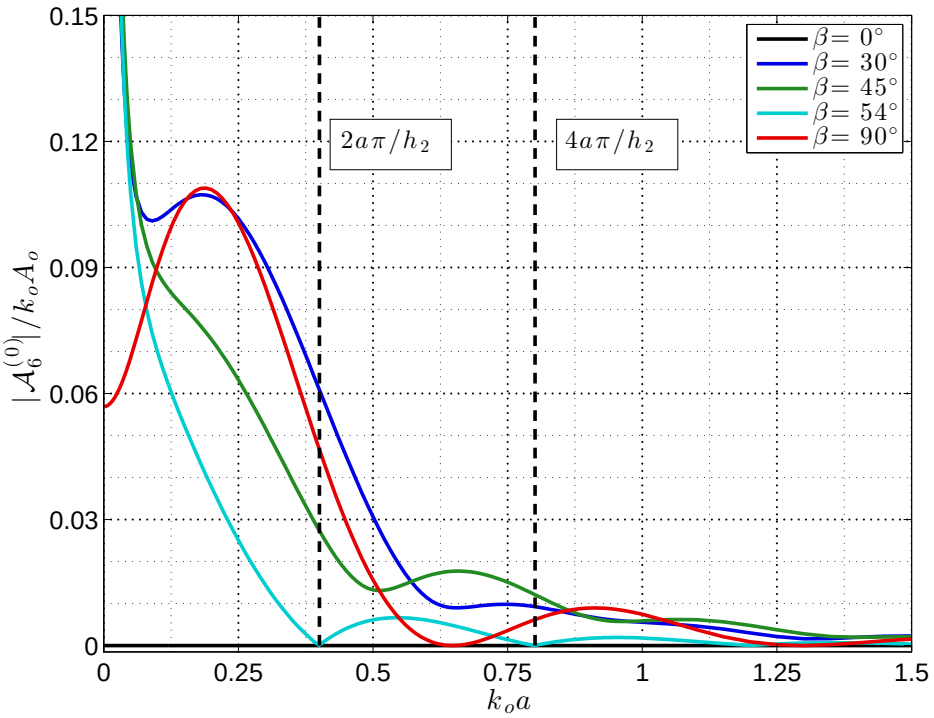

Figure 2.16: First-order yaw response-amplitude operator for MIST platform.

maximum $Re_j \approx 2.1 \cdot 10^3$. The other important parameter when considering viscosity and drag forces in oscillatory flow is the Keulegan-Carpenter number, which relates the drag force to the inertial forces.

$$KC = \frac{U}{fL}. \tag{2.141}$$

As shown by the frequency of oscillations in Fig. 2.2, the KC number for the fast-scale motion is an order of magnitude smaller than for the slow-scale motions. The KC number on the j^{th} column for the fast-scale motion is is $KC_j = \pi\dot{\theta}|r_j|/\sigma_0 a_j \approx 0.075$. At such a low Kc number, many authors have shown that the drag on cylinders can increase drastically [51], [52]. A frequency parameter is often used to relate the Kc and Re as,

$$\Gamma = \frac{Re}{Kc}. \tag{2.142}$$

We reproduce the experimental data performed by Troesch and Kim in 1991, since it is very close to the Re and Kc used in this study. From this experimental data, it is clear that is prudent to separate the drag coefficients for the fast and slow motions, K_D^f and K_D^s, respectively since the forces can differ by nearly an order of magnitude depending on the Kc number. The authors of [22] also mention the necessity of separating the slow and fast-scale velocities when computing the sectional viscous force on a cylinder (see Eq. (8) in [22]).

Normally, the effect of viscosity on submerged or partially submerged bodies is taken into account by using a quadratic drag or Morison-type equation (sometimes referred to as MOJS equation) [53]. This force takes into account the flow separation on the bodies due to

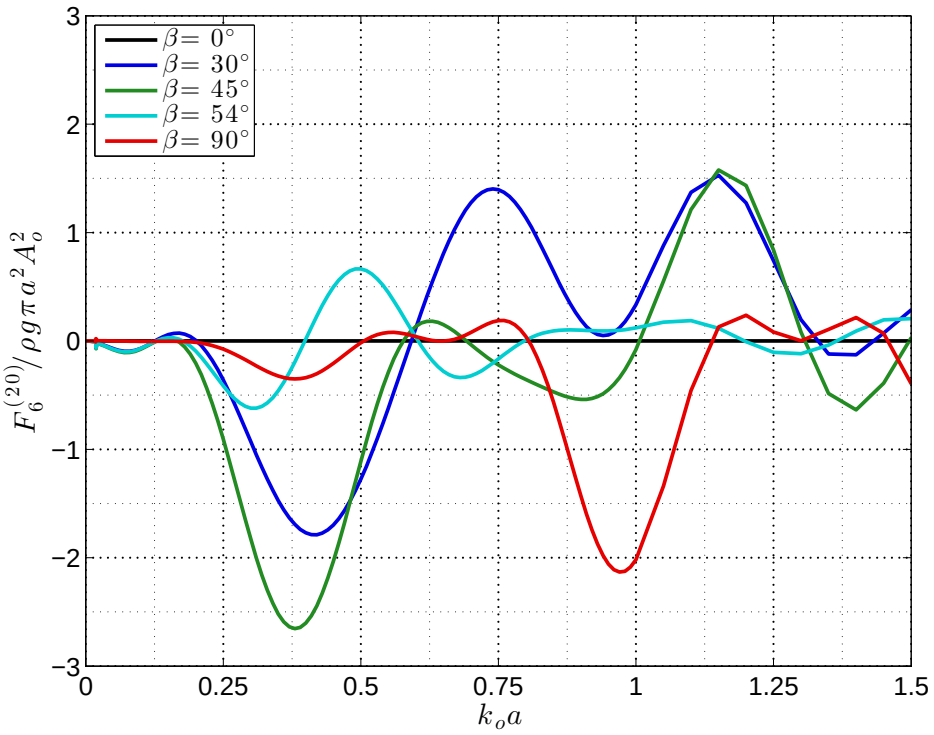

Figure 2.17: Steady, second-order moment on the MIST platform as function of the incident wave frequency and incident wave angles.

effect of the adverse pressure gradient causing the flow about the bluff body to separate. In the linear hydrodynamic analysis we assume that all streamlines about the body follow the body contours. Empirically it was determined that this drag force is generally proportional to the square of the velocity of the body. For our linear response analysis in the frequency domain, it is helpful to convert the quadratic damping into a linear damping, such as in [54] and [55]. As done by [56], we estimate this linear damping due to the viscous effects on the *fast-scale* motions by matching the experimental RAOs (in yaw) with the numerical results. In [55], the author makes an energy conservation argument, equating the energy dissipated by the quadratic and linear dampers. Thus, the linear damping coefficient is a function of the quadratic damping coefficient along with other parameters, such as the motion amplitude and frequency. However, the conversion of a quadratic damping term into a linear damping term for the *slow-scale* motions is more difficult since we cannot assume a time-harmonic response. We were never able to run the experiments long enough to see a cyclic response in the slow-drift motion of the platform (only 35 s are shown in Fig. 2.2, but is representative of the length of time before back-scattered waves interfere with the experiment). Thus, estimating the viscous moment on the slow-drift motion remains an open question and is discussed further in Sec. 5.7.

For now, we separate the viscous forces on the slow-drift motions and the higher-frequency motions, since they are operating in different fluid regimes. On the platform, the drag forces

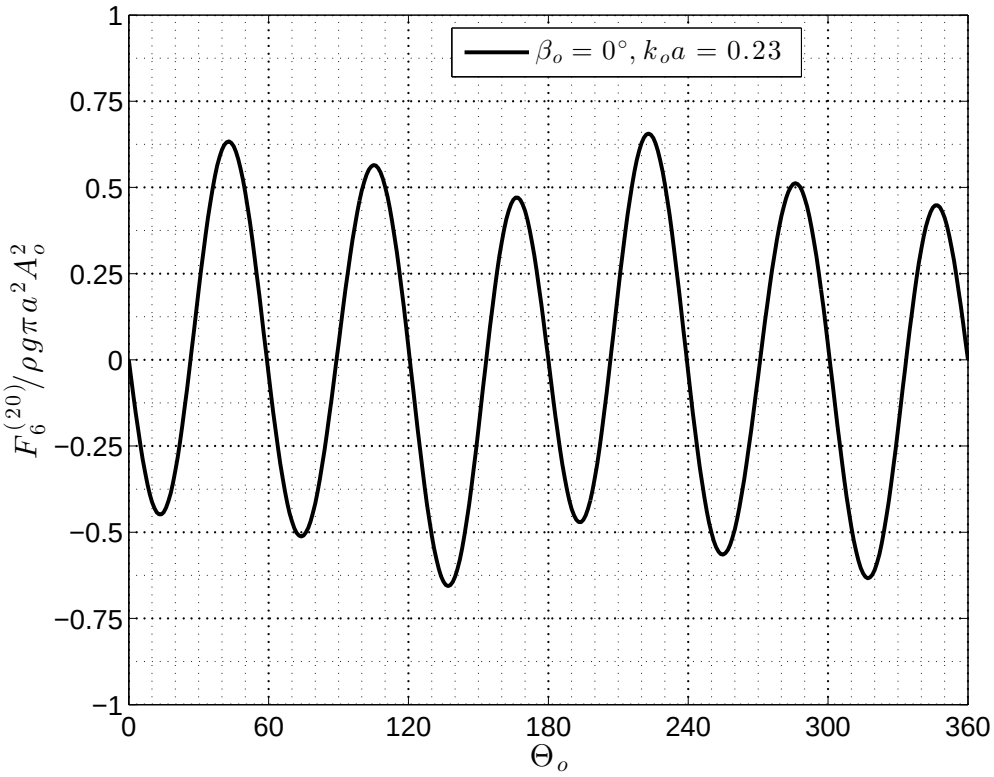

Figure 2.18: Steady, second-order moment on the MIST platform as function of the slow-drift position of the platform.

are

$$\boldsymbol{f}_v = -\sum_j^{N_{col}} \begin{bmatrix} 1 & 0 & -y_0^j & 0 \\ 0 & 1 & x_0^j & 0 \\ -y_0^j & x_0^j & R_j^2 & 0 \\ 0 & 0 & 0 & R_j^2 \end{bmatrix} \begin{bmatrix} K_D^f \dot{\xi}_1 \\ K_D^f \dot{\xi}_2 \\ K_D^f \dot{\xi}_6 \\ K_D^s U_6 \end{bmatrix} \tag{2.143}$$

where K_D^f and K_D^s are the linear drag coefficients for the fast and slow motions, respectively. For a rotating platform whose center of rotation is aligned with the geometric centroid of the waterplane area (here, only the main columns are considered in this analysis while the truss structure is ignored), the off-diagonal terms will sum to 0.

2.9 Time-Domain Study

In order to validate the analysis in Secs. 2.4.2-2.8, we can use experimental data in the time-domain from model tests. If we assume that the mooring system keeps the center of rotation relatively fixed while having little effect on the platform in the yaw direction, the only forces

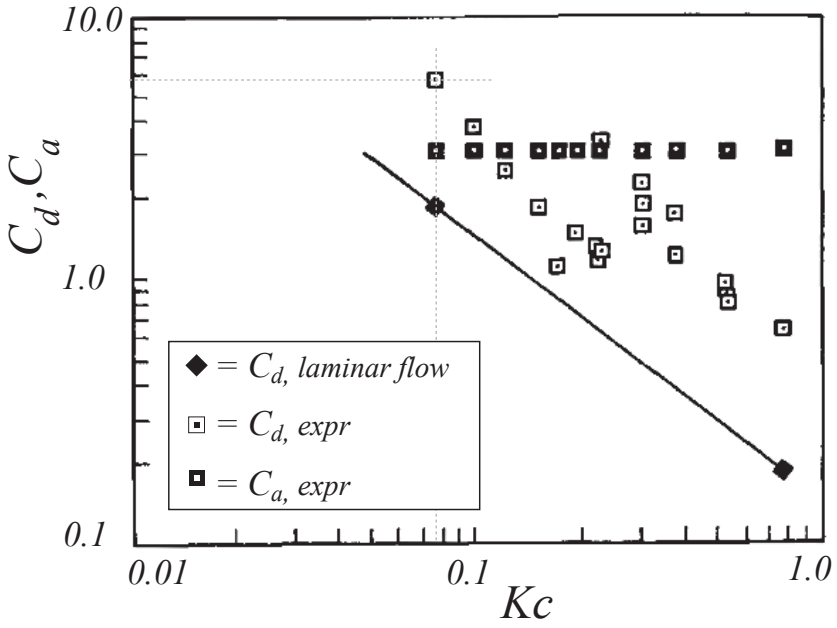

Figure 2.19: Drag and Added-Mass coefficients for oscillating cylinder with $\Gamma = 23,200$ (Adapted from [52])

on the platform will be due to the incident-wave and other hydrodynamic forces. We consider only four degrees of freedom in the time-domain, since we are considering horizontal plane motion only where $U_1 = U_2 = 0$. Upon examination of Eqs. (2.129) and (2.138), which detail the equations of motion for the fast-scale and slow-scale motions of the body, respectively, we first focus on the fast-scale motions, which have been developed previously in the literature [57, 58].

2.9.1 Fast-Scale Motions in Time-Domain

The total equations of motion for the fast-scale motions are

$$M_b \ddot{\boldsymbol{\xi}}_b(t) = \boldsymbol{f}_e(t) + \boldsymbol{f}_r(t) + \boldsymbol{f}_v(t) + \boldsymbol{f}_m(t) \ , \tag{2.144}$$

where f_e are the wave-exciting forces/moment and f_r are the wave radiation forces/moment, f_v are the non-linear viscous forces/moment and f_m are the forces/moment due to the mooring system. For the analysis in the current section, we neglect the influence of the generators/wind turbines and only consider hydrodynamic forces. We will consider the entire system in Chapter 5.

The hydrodynamic forces in the j^{th} direction can be described in the time domain using

integrals to describe the memory-effects of the fluid,

$$f_j^e(t) = \int_{-\infty}^{\infty} K_j^e(t-\tau)\eta_o(0,\tau)\,d\tau\ , \tag{2.145}$$

$$f_{ij}^r(t) = -\mu_{ij}(\infty)\ddot{\xi}_j(t) - \lambda_{ij}(\infty)\dot{\xi}_j(t) - \overbrace{\int_{-\infty}^{t} K_{ij}^r(t-\tau)\dot{\xi}_j(\tau)d\tau}^{\tilde{K}_{ij}(t)}, \tag{2.146}$$

where K_{ij}^r is the radiation impulse response function and can be solved for by applying an inverse-Fourier transform to the frequency-domain hydrodynamic coefficients:

$$K_{ij}^r(t) = \frac{2}{\pi}\int_0^{\infty}[\lambda_{ij}(\sigma) - \lambda_{ij}(\infty)]\cos\sigma t d\sigma\ . \tag{2.147}$$

We only use the first-order representation of the free-surface η_{10} in this analysis. The wave-exciting moment kernel can be expressed as,

$$K_e(t) = \frac{1}{\pi}\int_0^{\infty}[\mathrm{Re}\left[\mathcal{X}_6(\sigma)\right]\cos\sigma t - \mathrm{Im}\left[\mathcal{X}_6(\sigma)\right]\sin\sigma t]d\sigma\ . \tag{2.148}$$

However, the integrals in Eqs. (2.145) and (2.146) are time-consuming to compute in the time-domain. Thus, we represent it as a set of ordinary differential equations that can be represented by a state-space model, as was formulated first by [59]. In general,

$$\dot{\chi}_{ij} = A_{ij}^r\chi_{ij} + B_{ij}^r\dot{\xi}_j, \tag{2.149}$$

$$\tilde{K}_{ij} = C_{ij}^r\chi_{ij} + D_{ij}^r\dot{\xi}_j. \tag{2.150}$$

This transformation was state-space represented in [57], and adapted by Tom and Yeung in [56], where a balanced reduction formulation was used to reduce the number of states in the vector χ_{jj}, (*balmr* in MATLAB), without sacrificing the accuracy of the solution. We assume that the wave-exciting moment kernel is causal such that,

$$f_j^e(t) = A_o|\mathcal{X}_j(\beta,\sigma)|\,\mathrm{Re}\left[e^{i(\varphi_j-\sigma t)}\right]. \tag{2.151}$$

In this way we have represented all of the forces on the right-hand side of Eq. (2.144) and can solve for the instantaneous position of the fast-scale motions about the slowly-varying drift position using well-proven time integration techniques such as those found in built-in MATLAB libraries.

2.9.2 Slow-Drift Motions in Time-Domain

We only consider a single degree of freedom of the slow-drift motions (yaw) in this analysis. Like the previous subsection, the second-order equation of motion is,

$$(I_b + \bar{\mu}_{66})\ddot{\Theta}_o = \mathcal{f}_e - A_o^2\bar{\lambda}_{66}\dot{\Theta}_o + \mathcal{f}_v(t) + \mathcal{f}_m(t), \tag{2.152}$$

where the wave-exciting force does not have an explicit dependence on time. This steady wave-exciting force can be found from Eq. (2.138) as

$$f_e = A_o^2(\mathcal{X}_6^{(2)} + \mathcal{X}_6^{(3)}) + \sum_j A_o \bar{K}_{3j} \mathcal{A}_j^{(0)} + \sum_i \sigma_o^2 \mathcal{K}_{ji}^{(6)} \mathcal{A}_i^{*(0)} \mathcal{A}_j^{(0)}. \tag{2.153}$$

Note that all terms in Eq. (2.153) are dependent on the instantaneous yaw orientation of the platform $\Theta_o(t)$. It will be shown in Appendix F that for a platform that is rotating about the centroid of its waterplane area, $\mathcal{X}_6^{(2)}$ is null. Furthermore, it will also be shown that $\mathcal{K}_{ji}^{(6)}$ is null. We will neglect $\mathcal{X}_6^{(3)}$ since it is of higher order than we are considering. When we solve this equation in the time-domain in Chapter 5, we assume that the yaw velocity is small, such that we can use the previous instantaneous position of the platform to calculate the forces on body at each time step.

In the previous subsection we described how we treat the first-order motions $\xi_j(t)$ as unknowns and solve for them with a time-stepping algorithm. We expect the motion to be time-harmonic with a frequency related to the incident wave frequency, as described in Eq. (2.30). However, it is clear that the amplitude $|\mathcal{A}_j(t)|$ and phasing $\angle\mathcal{A}_j(t)$ of the motion is changing with respect to time. Thus, our assumption in the frequency domain analysis, where we consider the complex amplitude of motion as a constant, does not hold in the time-domain. Utilizing Eq. (2.108) as a guide we rewrite Eq. (2.153) reflecting the above information as,

$$\boxed{f_e(t) = \frac{A_o}{T} \int_{t-T}^{t} \sum_j \mathrm{Re}\left[\bar{K}_{3j} e^{-i\sigma\tau}\right] \dot{\xi}_j^{(0)}(\tau) d\tau.} \tag{2.154}$$

The other forces, including the mooring and viscous forces are dealt with in the same manner as the fast-scale motions (albeit with a different drag coefficient due the change in KC number).

In later chapters we refer to the total hydrodynamic yaw moment on the platform Q_e, as

$$I_b \ddot{\Theta}_o = Q_e = -\bar{\mu}_{66} \ddot{\Theta}_o - \mathcal{B}_{66} \dot{\Theta}_o + f_e(t) \tag{2.155}$$

where $\mathcal{B}_{66}$ is the total slow-drift drag coefficient on the platform, which is the sum of the wave-drift damping, linear viscous drag and friction from the mooring system, which can be represented as from Eq. (2.143) as,

$$\bar{\mathcal{B}}_{66} = \frac{\mathcal{B}_{66}}{\rho_o g A_0^2 a^2/\sigma_o} = \underbrace{\frac{\bar{\lambda}_{66}}{\rho_o g a^2/\sigma_o}}_{wave-drift} + \underbrace{\frac{\bar{b}_{66}}{\rho_o g A_0^2 a^2/\sigma_o}}_{mooring} + \underbrace{\frac{K_D^s}{\rho_o g A_0^2/\sigma_o} \sum_j^{N_{col}} \left(\frac{R_j}{a_j}\right)^2}_{viscous}. \tag{2.156}$$

We will discuss this coefficient in further detail when discussing the results of the hydrodynamic simulations in Sec. 5.7.1.

Chapter 3

Aerodynamics of Vertical-Axis Wind Turbines

In this chapter, the aerodynamics of vertical-axis wind turbines are investigated. We surmise that one of the reasons there are widespread failures in the structural integrity of vertical-axis wind turbines is a misunderstanding or mischaracterization of the *magnitude* and *frequency* of the forces on the turbines as they circumnavigate the central column. For example, one of the few public investigations of commercial vertical-axis turbines is documented in [60], which resulted in failures of the welding and strut attachments. We hope to elucidate some of these features by using a state-of-the-art Large-Eddy Simulation (LES) technique, known as high-order, discontinuous-Galerkin Implicit LES (ILES). Before introducing this method we discuss general considerations of simulating vertical-axis wind turbines and then discuss a blade element momentum theory, which is widely used in the industry today. Thus, we include simulations using a low-fidelity (low computational cost) method as well as a high-fidelity CFD method. The examination would be more complete if we had re-performed the analysis using a middle-fidelity method such as the Unsteady Reynolds-Averaged Numerical Simulations (URANS), using open-source software such as OpenFOAM[1]. The same argument could be made, however, for using even higher-fidelity methods such as Detached Eddy Simulation (DES) or Direct Numerical Simulation (DNS) techniques. Since great effort had already been put into writing the LES code used in the current analysis by [61], we analyzed the turbines using only this technique.

3.1 General Considerations

A plan view of a straight-bladed vertical-axis wind turbine is shown in Fig. 3.1. The reader is referred to Fig. 4.1 for an isometric view of a straight-bladed turbine. However, the diagram can be used to illuminate the aerodynamics of the turbine with a two-dimensional slice. For a straight-bladed turbine, with uniform incident wind, the problem reduces to two-dimensions. We implemented three-dimensional analysis to include blade curvature as well as wind shear in the blade element momentum theory, which is discussed in Sec. 3.2. From the analysis in Sec. 3.3, it is clear that three-dimensional analysis must be used in some circumstances when simulating turbines. Thus, we include a small spanwise extrusion in Sec. 3.4 with periodic boundary conditions on the top and bottom to simulate the three-dimensional effects. In the diagram in Fig. 3.1, the incident wind U_∞ is blowing from right to left. The azimuthal angle of the blade θ varies from 0 to 2π, although in many plots, we show the variation from $-\pi/2$ to $3\pi/2$. The radius of the turbine is R, the chord of the airfoil c, the blade mount position c_0, and the blade pitch angle α_0. As the turbine rotates, the relative wind velocity (to an observer on the airfoil) U_R varies as well as the instantaneous angle of attack α. The

[1] www.openfoam.com/

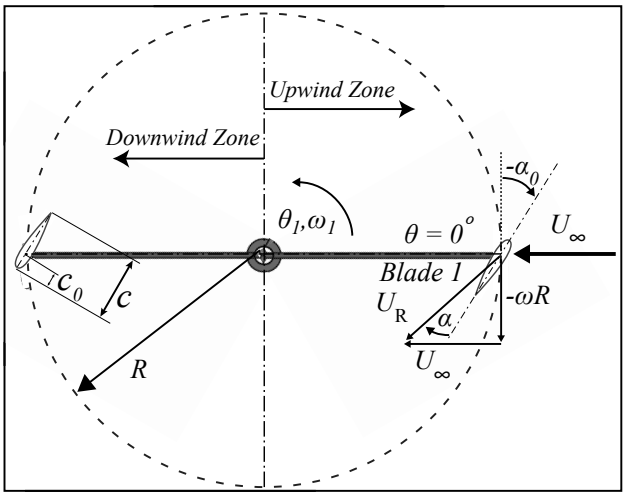

Figure 3.1: Plan view of two-bladed vertical-axis turbine with various parameters.

variation in the angle of attack and the local Re number of the upwind zone is shown in Fig. 3.2. The angle of attack is negated in the downwind zone.

The efficiency of the turbine is highly dependent on its tip-speed ratio, which is the ratio of the speed of the airfoil to that of the wind, that is

$$\lambda = \frac{\omega_1 R}{U_\infty} \tag{3.1}$$

As depicted in Fig. 3.1, once blade enters the 'upwind' zone, the incident wind is unaltered. However, in the 'downwind zone' the incident wind has been retarded by airfoils passing through the 'upwind' zone. This effect will be easier to see in the flow visualizations of the CFD method in Sec. 3.4.

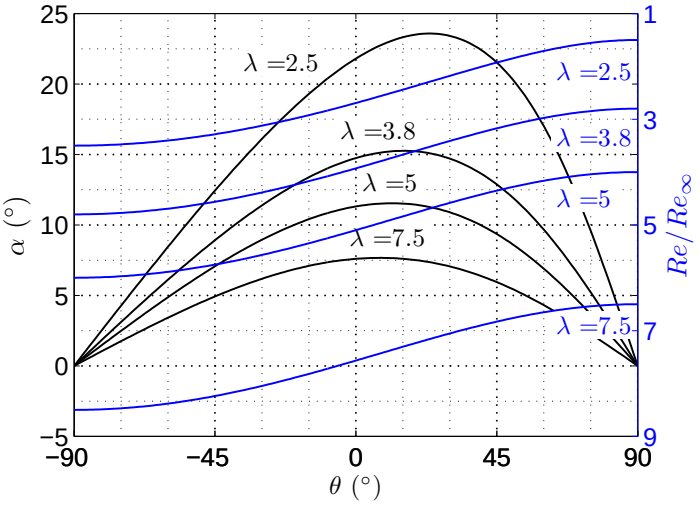

Figure 3.2: Variation of angle of attack and chord Re of a straight-bladed VAWT as it completes one half rotation.

3.2 Double-Multiple Streamtube Method

The first aerodynamic model considered is a blade element momentum model (BEM) known as the Double-Multiple Streamtube Method (DMST). BEM methods consider the transfer of momentum from the incident wind particles to the rotating airfoils. In order to estimate the instantaneous aerodynamic torque at a specific rotor position, the Double-Multiple Streamtube Method (DMST) was implemented. This methodology breaks down the problem into an upwind and downwind zone (hence, 'double'), and each of these zones into many azimuthal sections denoted by θ_1 (hence, 'multiple streamtubes'). The flow within a single streamtube is retarded by the blade by a factor of u and u', in each of these zones, respectively. The amount of momentum transfer for the blades in the upwind and the downwind zones must be solved iteratively. However, this model assumes that the fluid pressure completely recovers in the equilibrium zone in the middle turbine, as shown in Fig. 3.3. This specific formulation comes from pages 158-162 of [3], where we assume that the rotor speed, $\omega_1 = \dot{\theta}_1$ is constant. For a more detailed description of this method see [3].

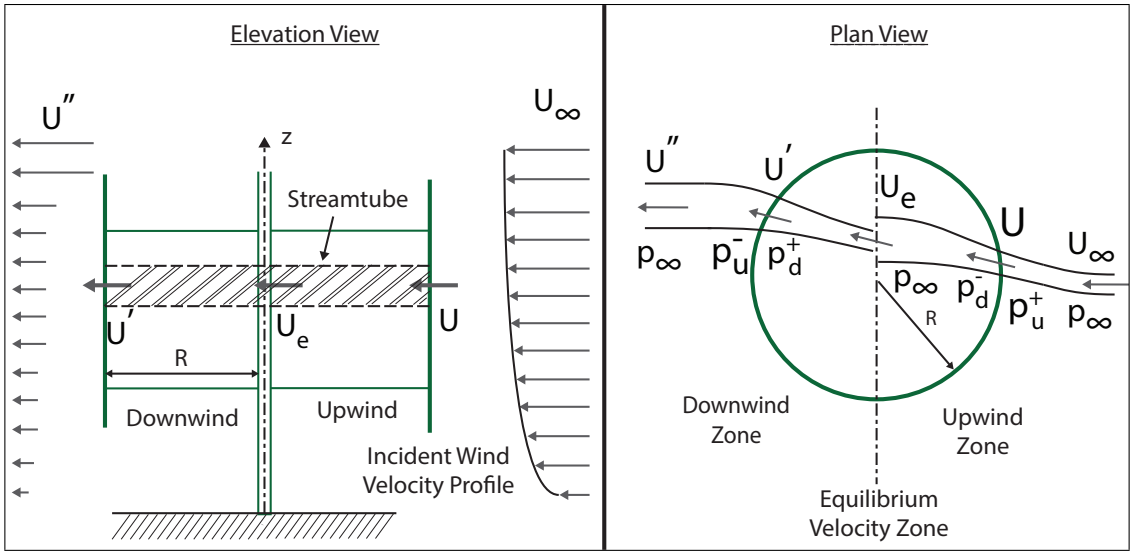

Figure 3.3: Elevation and plan views of the Double-Multiple Streamtube Method.

Upwind Aerodynamics

In order to find the induction factor u in the upwind zone, the following iterative algorithm was used until $||u^{(k+1)} - u^{(k)}|| < u_{tol}$:

$$U = u^{(k)} U_\infty \tag{3.2a}$$
$$W^2 = U^2 \left((X - \sin\theta_1)^2 + \cos^2\theta_1 \cos^2\delta \right) \tag{3.2b}$$
$$\text{where } X = R\omega_1 / U \tag{3.2c}$$
$$\alpha = \arcsin\left(\frac{\cos\theta_1}{\sqrt{(X - \sin\theta_1)^2 + \cos^2\theta_1 \cos^2\delta}} \right) \tag{3.2d}$$
$$[C_L, C_D] = f\left(\alpha, Re[W]\right) \text{ lookup table} \tag{3.2e}$$
$$C_N = C_L \cos\alpha + C_D \sin\alpha \tag{3.2f}$$
$$C_T = C_L \sin\alpha - C_D \cos\alpha \tag{3.2g}$$
$$f_{up} = \frac{Nc}{8\pi R} \int_{-\pi/2}^{\pi/2} \left(C_N \frac{\cos\theta}{|\cos\theta|} - C_T \frac{\sin\theta}{|\cos\theta| \cos\delta} \right) \left(\frac{W}{U} \right)^2 d\theta \tag{3.2h}$$
$$f_{up} u^{(k+1)} = \pi (1 - u^{(k+1)}) \tag{3.2i}$$

Downwind Aerodynamics

In order to find u' in the downwind zone, which leads to the calculation of α' and W' in the downwind zone the following iterative algorithm was used until $||u'^{(k+1)} - u'^{(k)}|| < u'_{tol}$:

$$U' = u'^{(k)} (2u - 1) U_\infty \tag{3.3a}$$
$$W'^2 = U'^2 \left((X' - \sin\theta_1)^2 + \cos^2\theta_1 \cos^2\delta \right) \tag{3.3b}$$
$$\text{where } X' = R\omega_1 / U' \tag{3.3c}$$
$$\alpha' = \arcsin\left(\frac{\cos\theta_1}{\sqrt{(X' - \sin\theta_1)^2 + \cos^2\theta_1 \cos^2\delta}} \right) \tag{3.3d}$$
$$[C'_L, C'_D] = f\left(\alpha', Re[W']\right) \text{ lookup table} \tag{3.3e}$$
$$C'_N = C'_L \cos\alpha' + C'_D \sin\alpha' \tag{3.3f}$$
$$C'_T = C'_L \sin\alpha' - C'_D \cos\alpha' \tag{3.3g}$$
$$f_{down} = \frac{Nc}{8\pi R} \int_{\pi/2}^{3\pi/2} \left(C_N \frac{\cos\theta}{|\cos\theta|} - C_T \frac{\sin\theta}{|\cos\theta \cos\delta|} \right) \left(\frac{W'}{U'} \right)^2 d\theta \tag{3.3h}$$
$$f_{down} u'^{(k+1)} = \pi (1 - u'^{(k+1)}) \tag{3.3i}$$

3.2.1 Verification for a Single Turbine

The DMST code was verified by comparing the results of the current study with published results. Figure 3.4 shows the tangential force coefficients C_T for the Sandia 5m turbine described in [62] by using the DMST in the present study (lines, various λ) as well as

the DMST coded by [3] (circles). The discrepancies in the two codes may be caused by

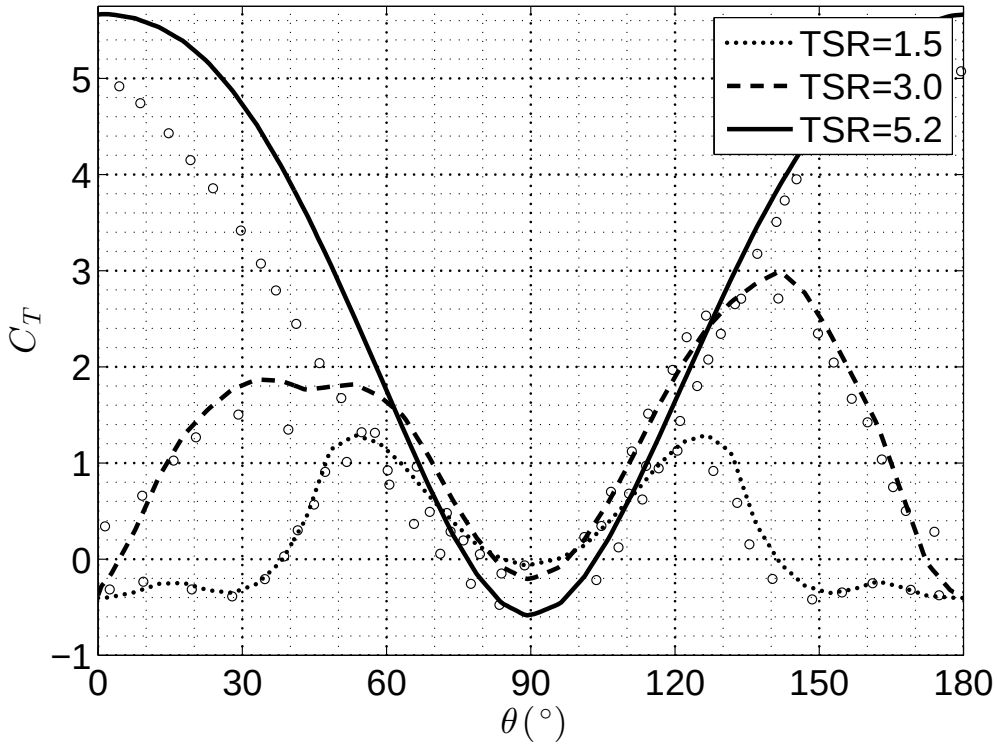

Figure 3.4: Tangential force coefficient for the Sandia 5m turbine described in [62]. Circles represent published DMST data in Fig. 6.16 in [3].

the choice in the number of streamtubes, C_L, C_D data, interpolation methods, convergence criteria, among other things.

3.3 LES of Static Airfoil at Low-Re and Large AOA

The airflow over streamlined bodies at low to moderately low Re (i.e., $10^3 \leq Re \leq 10^5$) has been examined thoroughly by means of experimental, analytical and computational techniques by many researchers in the modern era (see review papers, for instance, [63, 64, 65, 66]). This Re range presents unique challenges to researchers who have to deal with separated, highly unsteady transitional flow. Though early wind tunnel tests of the NACA0012 were plagued by inaccuracies [67], many recent experimental studies have used state-of-the-art pressure and force measurements as well as flow visualization techniques (see, for instance, [68, 69, 70, 71, 72]).

However, experimental studies will always be limited by the amount and type of data that can possibly be collected from such tests. Recent growth in computational power and

parallel computing techniques has led to increasingly higher-fidelity computational analyses, such as large-eddy simulation (LES) and direct numerical simulation (DNS), (see [73, 74, 75, 76, 77, 78, 79, 80, 81, 82]). While DNS can solve for the flow field at Kolmogorov scales, it requires prohibitively fine meshes for the Reynolds numbers considered, even for high-performance computers. Thus, researchers are actively seeking numerical schemes that could model the flow structures at a wide range of spatial and temporal scales and could accurately predict the magnitude and frequency of forces on the airfoil with lower computational cost. In LES simulations, element sizes are significantly larger than the Kolmogorov scale. This reduces the computational cost drastically, and the effect of the unresolved scales are incorporated through subgrid models. In our work, we use the so-called implicit LES model which assumes that this subgrid model is the inherent dissipation of the numerical scheme. In most cases these flow structures are inherently three-dimensional and require full 3D simulation techniques, although in this work we will compare the 3D results with corresponding 2D simulations to highlight the differences.

3.3.1 Governing Equations and Computational Domain

We shall briefly introduce the governing equations and the computational domain in this section, although more details can be found in [83].

Governing Equations

The in-house software used in the current analysis was first described in [84]. This numerical code solves the compressible Navier-Stokes equations using a higher order, discontinuous Galerkin discretization. For the current analysis, the Mach number (Ma) is set, such that the flow is essentially incompressible. In indicial form, the compressible Navier-Stokes equations are

$$\frac{\partial \rho_a}{\partial t} + \frac{\partial}{\partial x_j}(\rho_a u_j) = 0, \tag{3.4a}$$

$$\frac{\partial}{\partial t}(\rho_a u_i) + \frac{\partial}{\partial x_j}(\rho_a u_i u_j + p\delta_{ij}) = \frac{\partial}{\partial x_j}\tau_{ij} \qquad \text{for } i = 1, 2, 3, \tag{3.4b}$$

where $\rho_a u_j$ is the fluid momentum in the j^{th} direction, p is the pressure, and the viscous stress tensor is

$$\tau_{ij} = \mu\left(\frac{\partial u_i}{\partial x_j} + \frac{\partial u_j}{\partial x_i} - \frac{2}{3}\frac{\partial u_k}{\partial x_k}\delta_{ij}\right). \tag{3.5}$$

To reduce the number of unknowns in the system, we assume all processes happen isentropically (i.e., entropy is constant). Hence,

$$p = s\rho_a^{\gamma}. \tag{3.6}$$

where $\gamma = C_p/C_v$, the adiabatic gas constant s is a constant. We can use the isentropic model of the Navier-Stokes equations, since it converges to the solution of the incompressible Navier-Stokes equations as the Mach number goes to 0, (so long as suitable assumptions about the

domain, boundary conditions, initial conditions, etc, are made) [61]. Thus, for a 3D domain, we have four equations and four unknowns ρ_a, u_j given in the non-linear system of equations in Eqs. (3.4), (3.5), (3.6) and can use a time-stepping algorithm once a discretized domain is defined.

High-Order Discontinuous Galerkin Discretization

The domain is discretized into structured and unstructured elements, which can be represented by basis functions of arbitrary order. A first-order basis function, $p = 1$ uses a linear basis function to represent the solution on the nodes of the element. Higher-order basis functions use higher-order polynomials (quadratic: $p = 2$, cubic: $p = 3$, etc) to define these basis functions, which are defined between the nodes of the element. The convective operator (left hand side of Eq. (3.4b)) is discretized using a discontinuous Galerkin method, which produces a stable discretization irrespective of the polynomial order. The viscous terms are discretized using a compact discontinuous Galerkin representation, described in [84], which leads to optimal order accuracy and generates sparser matrices than the alternative existing methods.

Computational Domain

The computational domains for static NACA0012 airfoils at arbitrary angle of attack is shown in Figs. 3.5. Mesh 1 represents the coarsest mesh, while Mesh 2 represents a much finer mesh. After some initial simulations, it was determined that the solution was fairly independent of these mesh sizes and a mesh size in between these two was created for the 3D simulations. The airfoil is a standard NACA0012 section and, for the 2-D simulations, we use an outer square size of 25 chord lengths. The 2D meshes have 1,613 and 7,482 high-order elements, respectively, corresponding to 16,130 and 74,820 high-order nodes, or about 48,000 and 224,000 degrees of freedom. We measure the resolution length of the first layer of elements around the airfoil by dividing the element height by the polynomial degree, $h_{\min}/p$, which is a natural choice for high-order methods. For our two meshes this quantity is $5 \cdot 10^{-4}$ and $5 \cdot 10^{-5}$, respectively.

For the 3D domain, we extrude the 2D airfoil section to a span length of 0.4 chord lengths, and use periodic conditions between the two ends. The 3-D domain has an outer box of three chord lengths above, below, and upstream from the airfoil; and it has five chord lengths in the wake. This leads to a mesh with 151,392 high-order tetrahedral elements, or about 3 million high-order nodes, which correspond to above 12 million degrees of freedom. The first layer of elements has $h_{\min}/p = 2.5 \cdot 10^{-4}$. In Fig. 3.5(a), the stretched elements in the boundary layer can be seen. After a small distance, this structured mesh transitions to an unstructured mesh of triangles or tetrahedrals (in the case of the 3D mesh). The 3D meshes are obtained by prismatic extrusion of the triangular elements. All triangular and tetrahedral meshes are produced using the DistMesh mesh generator [85]. In addition, high-order methods require meshes with curved elements, which are particularly difficult to generate for meshes with boundary layers. We use the elasticity-based approach proposed

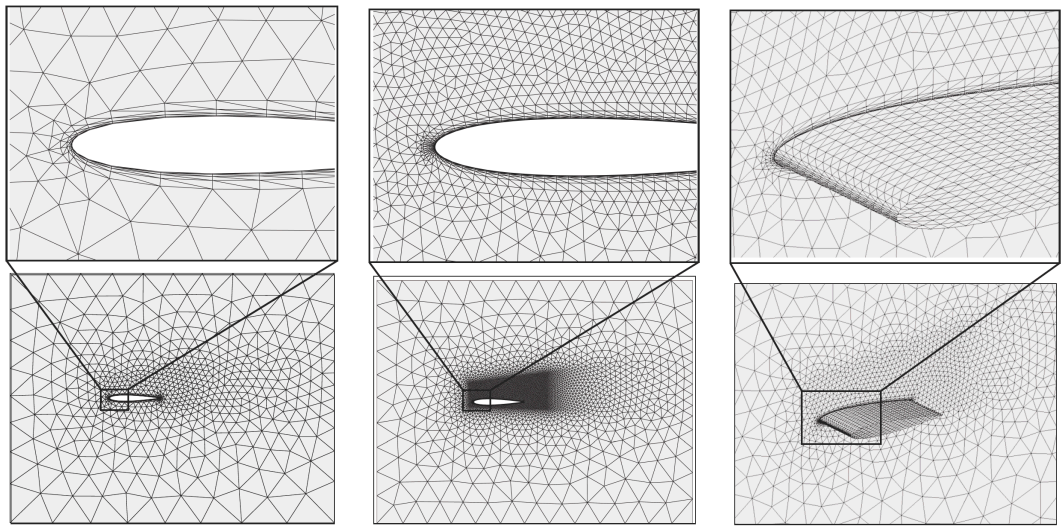

(a) Mesh 1, 2D (b) Mesh 2, 2D (c) 3D Mesh

Figure 3.5: Computational domain in 2D and 3D for the static NACA0012 airfoil at a wide range of angles of attack.

in [86], which tends to produce well-shaped meshes with globally curved elements.

3.3.2 Lift and Drag Forces

In this section, we present the average magnitude and frequency content for NACA0012 airfoils over a range of angle of attacks.

Magnitude of Forces

The forces on a stationary NACA0012 airfoil over a range of angles of attack ($0° \leq \alpha \leq 55°$) were obtained and decomposed into the stream-wise and cross-stream directions (F_D and F_L, respectively). These results were compared to experimental and computational data from a variety of previous studies at similar Re.

The lift coefficients from a variety of experiments and numerical simulations at low Re ($5{,}300 \leq Re \leq 20{,}700$) are shown in Fig. 3.6. Similar to experimental procedures, these results are calculated by time-averaging the solution after a short transient period (usually $t^* = tU_\infty/c = 5$). The simulations ran for $t^* = 40 - 80$. The rectangular box is amplified and shown in Fig. 3.6(b). The 2D results from the present simulation are displayed with open and filled circles for Mesh 1 and Mesh 2, respectively (no appreciable difference at this level). Experimental data from [70], [72], and [87] are shown. Many different high-quality experimental tests are shown in these figures due to the difficult nature of obtaining reliable results at such Re. Results from the inviscid linear-vorticity panel method code XFoil [88] are also plotted for comparison. At this Reynolds number, the 2D ILES predicts the lift coefficient of the NACA0012 fairly well up to about α=8°. Above this α the 2D ILES drastically overpredicts the lift force. As the flow becomes detached, cross-stream structures

have a significant impact on the lift and drag forces on the airfoil. At The XFoil code, however, captures the relatively linear behavior of this airfoil over a larger range, though underpredicts the lift from $3° \leq \alpha \leq 12°$ as shown in Fig. 3.6(b). The 3D ILES simulations at α= 10°, 12°, 15° and 30° are close to the experimental data. Interestingly, the value at α= 10° is close to the values obtained by XFoil, though the computational cost of obtaining such a datum are orders of magnitude higher for the CFD software compared to the potential flow solver.

The lift coefficients for the NACA0012 at higher Re ($40.0 \cdot 10^3 \leq Re \leq 360 \cdot 10^3$) are shown in Fig. 3.7 up to α=55° and up to α=12° in Fig. 3.7(b). The results show similar trends to the ones described in Fig. 3.6, with the 2D ILES simulations overpredicting the lift values at $\alpha > 10°$. Experimental data from [89] and the data from Sheldahl and Klimas' seminal airfoil testing [90] at large angle of attacks are plotted as well. The LES simulations performed by Lehmkuhl, documented in [76] are shown in Fig. 3.7(b). Again, the XFoil code, captures the behavior of this airfoil fairly well. The 3D ILES simulations at 30° and 50° are close to the experimental data.

The drag coefficients for NACA0012 at $5 \cdot 10^3 \leq Re \leq 360 \cdot 10^3$ are shown in Fig. 3.8(a) for $\alpha \leq 55°$ and for $\alpha \leq 12°$ in Fig. 3.8(b). The trend of increasing Re coinciding with decreasing $C_D(\alpha = 0)$ was shown experimentally in [90]. Both XFoil and the ILES simulations follow the experimental data well for $\alpha \leq 12°$. A similar LES simulation was run for NACA0012 by Pagnutti [91] for $\alpha = 0$ and is shown in Fig. 3.8(b). The 3D simulations also provide accurate results under post-stall conditions.

Frequency Content of Forces

In order to analyze the frequency content of the ILES simulations, a Fourier transform could be used to analyze the time history of the lift and drag forces. However, since the total simulation time was never greater than 80 s due to time and storage constraints, a desired frequency resolution of 0.01 Hz could not be obtained. Thus, the peaks of the signals were obtained by finding the zero-slope and the dominant frequency of the lift force was obtained through the averaging of these periods. The data obtained from this procedure are shown in Fig. 3.9. These results are compared to the dominant frequencies in the lift signal experimentally determined by Alam in [70]. They are also compared to dominant vortex shedding frequencies found in the DNS simulations of a NACA0012 at $\alpha = 9.25°, 12°$ by Rodriguez in [82] as well as the dominant vortex shedding frequencies found in the experiments performed by Huang and reported in [69]. In the literature, when the frequency of the vortex-shedding is discussed, the length scale is generally related to the width of the wake. However, these aforementioned authors use slightly different length scales for the length parameter of the Strouhal number. To simplify, we re-normalized all of the results by the same length scale (c), so that the results from our study can be compared to the previous studies. From the agreement in Fig. 3.9 over the large range of angles of attack, it is evident that the oscillations in the force signal are due to the shedding vortices. Interestingly, our results showed that the shedding frequencies at $\alpha = 12°$ and 15° are quite similar. However, the standard deviations of the periods for the lift and drag forces are on the order of 10% of the

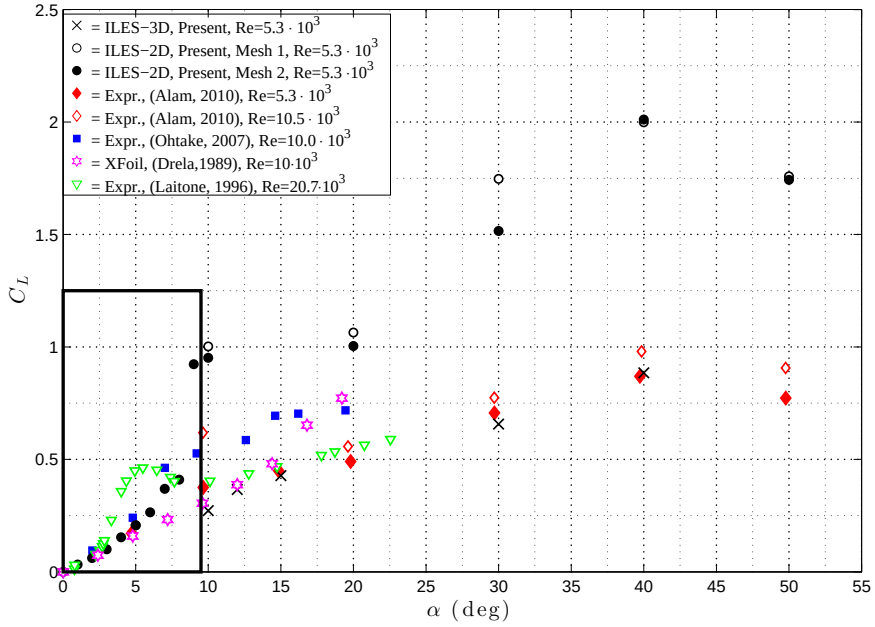

(a) Lift coefficient at large angle of attack.

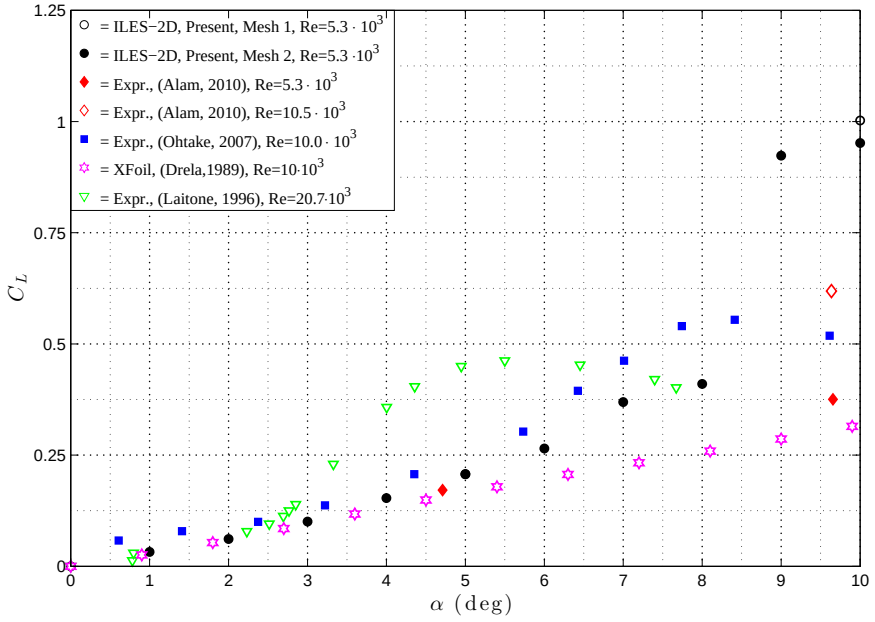

(b) Lift coefficient at small angle of attack.

Figure 3.6: Lift coefficient of NACA 0012 at $5{,}300 \leq Re \leq 20{,}700$.

period. The dominant frequencies in the drag force were similar to those of the lift force as experimentally determined in [70] and are not reproduced here.

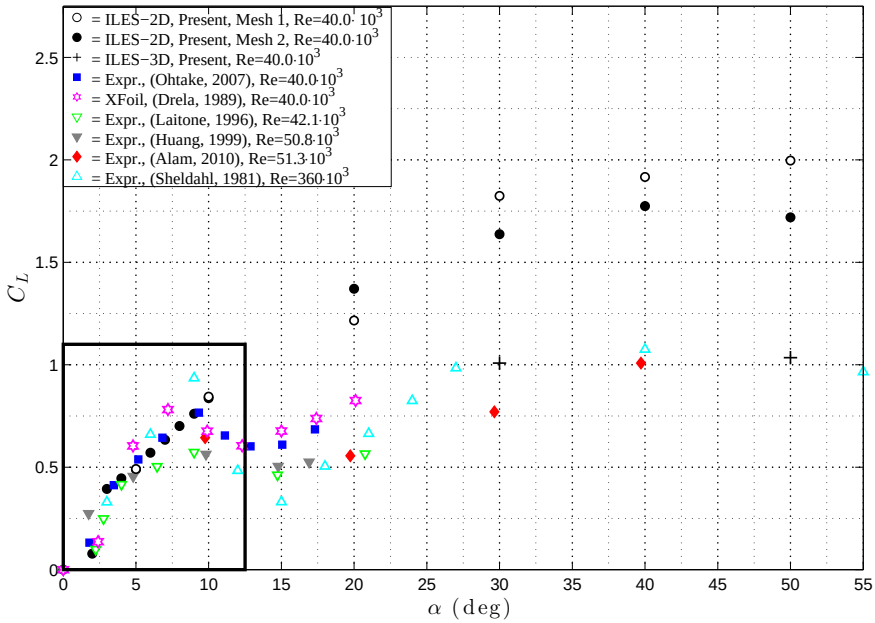

(a) Lift coefficient at large angle of attack.

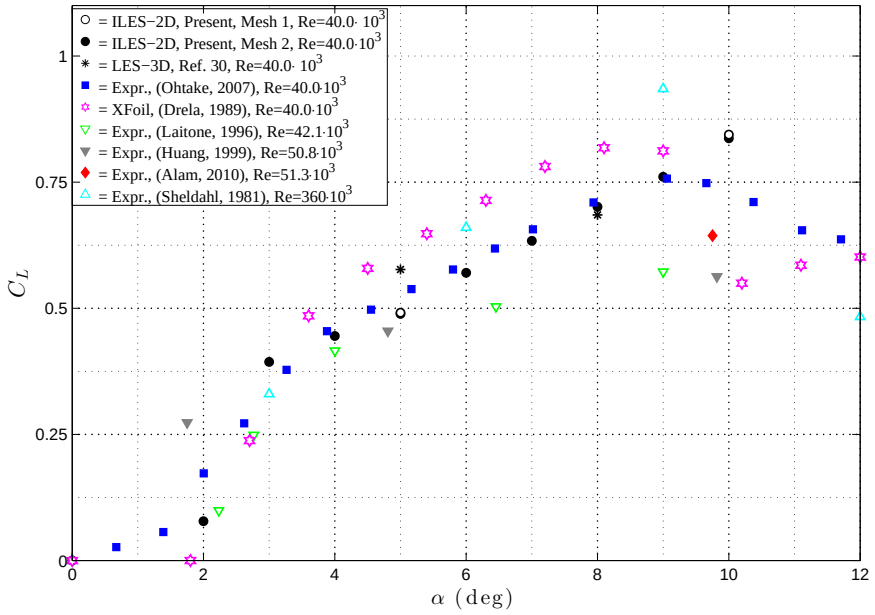

(b) Lift coefficient at small angle of attack.

Figure 3.7: Lift coefficient of NACA 0012 at *Re* 40,000 and above.

3.3.3 Flow Visualization

To analyze the fidelity of the unsteady flow structures in the 3D ILES simulation, two comparisons with experimental data were performed: the first was with a dye injection the second was with interpolated PIV data.

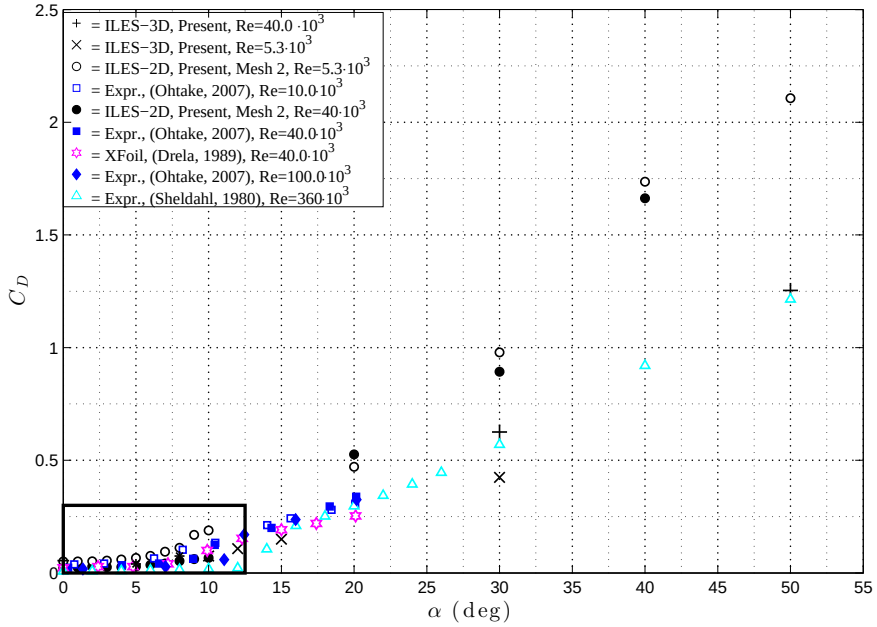

(a) Drag coefficient at large angle of attack.

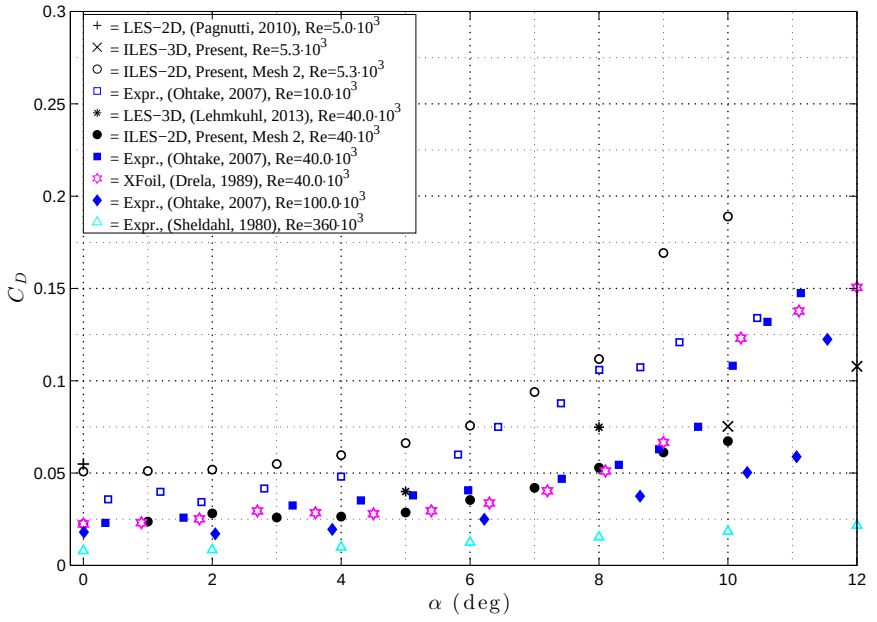

(b) Drag coefficient at small angle of attack.

Figure 3.8: Drag coefficient of NACA 0012 at $5 \cdot 10^3 \leq Re \leq 360 \cdot 10^3$.

Dye-Injection

In the experiments reported in [70], flow visualization was performed using a dye-injection technique. The dye was injected with a 1 mm nozzle at three different sites along the midspan of the airfoil: the nose of the airfoil and 0.1 chord lengths from the nose on the

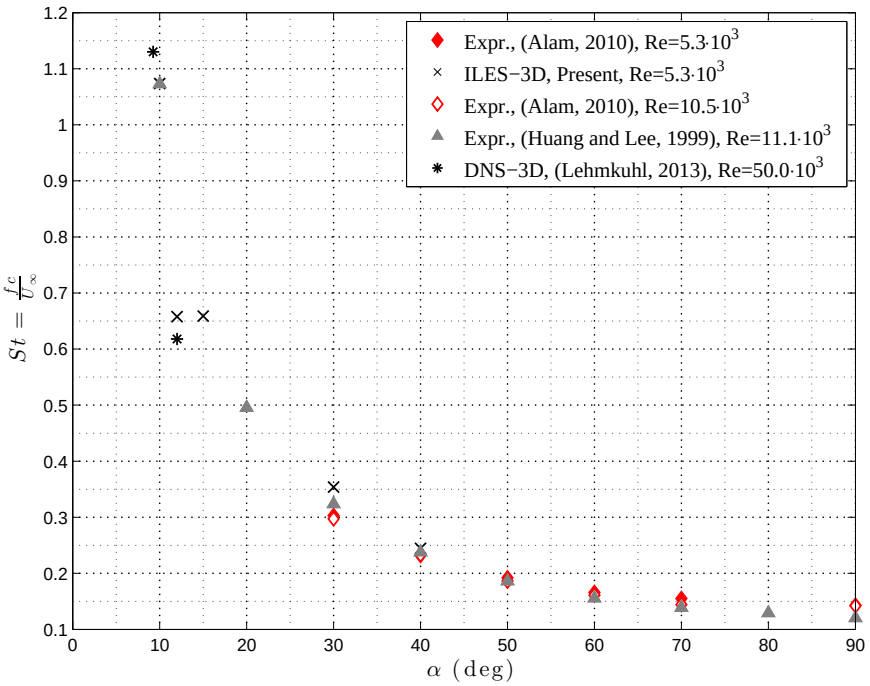

Figure 3.9: Comparison of dominant non-dimensional frequencies, fc/U_∞, of lift force or vortex shedding over a large range of angle of attack at low Re.

suction and pressure sides of the airfoil. To compare with the images from this study, a particle-tracing algorithm in the ParaView visualization open-source software [92] was employed. The particle-tracer algorithm is quite computationally expensive since the velocity of each particle is interpolated from the entire 3D solution at each time-step. In the particle-tracer simulation, only the nose and suction side injection sites were chosen to minimize computational cost, since many of the particles originating at the nose ended up on the pressure side of the airfoil. This post-processing algorithm took approximately 24 hours on a desktop computer. One instant of this simulation ($t^* = 4.05$) is shown for $\alpha = 10°$ and $Re = 5.3 \cdot 10^3$ in side view in Fig. 3.10 and compared to the image shown in [70] for the same flow parameters. Although the particle-tracer technique neither includes the effect of the input velocity of the dye nor its diffusion properties, the images show relatively good agreement.

Vortical Structures

Though it is not possible to see the time evolution of the vortical structures in this particle tracer simulation, the time evolution of the vorticity at $\alpha = 10°$ is shown in Fig. 3.11. The images on the right are cross-sectional instances of the streamwise vorticity from the 3D ILES simulations at midspan. These snapshots are compared to the sketches of 'Regime C' that Huang describes in [68]. Although the time-evolution of streamlines are sketched in Fig. 3.11a), it is clear that the seeds of these streamlines change in time for purposes

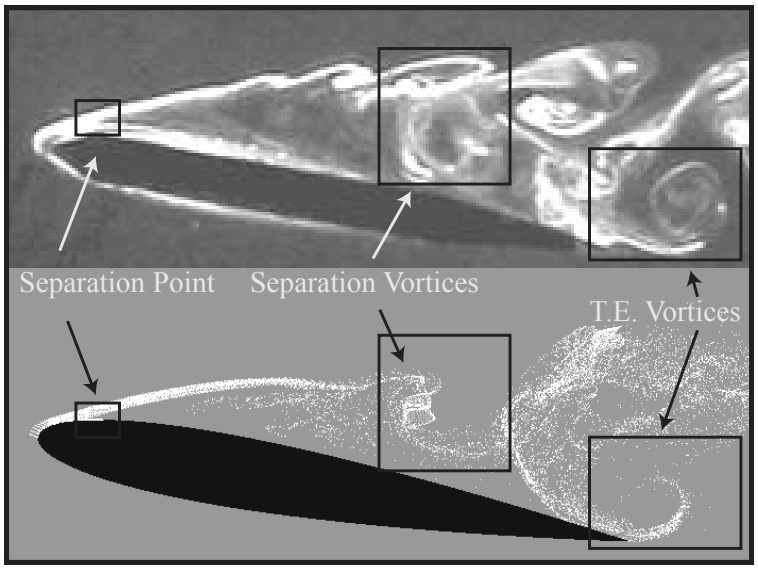

Figure 3.10: Comparison of dye-injection visualization experiment at $\alpha = 10^\circ$ and $Re = 5.3 \cdot 10^3$ (top image from [70]) and particle-tracer post-processing from 3D ILES simulation.

of clarity. Thus, in order to visually compare the present simulations the vorticity was plotted instead. As the authors of [68] describe, once the separation point moves upstream, a surface vortex is formed in the separated boundary layer around the mid-chord (middle panel of Fig. 3.11). As the counter-clockwise rotating vortex rolls down the suction side of the airfoil and is shed into the surrounding fluid, a trailing-edge vortex (clockwise-rotating) rolls up from the pressure side to the suction side. Huang attributes this effect to the low pressure region immediately behind the counter-clockwise rotating vortex. The vortices are shed in an alternating fashion, with a counter-clockwise rotating one generated from the trailing-edge and clockwise-rotating generated in the separated boundary region and rolling down the suction side of the airfoil.

Vorticity PIV Data

In [68], Huang and colleagues impulsively started a NACA0012 airfoil at various angles of attack in a water tank. The PIV images were obtained from a CCD camera that was mounted on a small moving carriage below the tank (see Fig. 1 in [68] for experimental setup). The water was seeded with polyamide particles to reflect the laser light and the airfoil was towed such that $Re = 1.2 \cdot 10^3$. Once the original velocity field was calculated from the PIV data, the data were enhanced by interpolating at points with a weighting distance of $1/r^2$. The vorticity was calculated from a central difference scheme from this interpolated data. These contours lines with labels showing the magnitude of the vorticity are shown in Fig. 3.12. This data is superimposed with the filled contour data from the midspan of the 3D ILES simulations at $Re = 5.3 \cdot 10^3$. The results show remarkably good agreement for the spatial and temporal evolution of the vortical structures despite the different flow parameters ($Re = 1.2 \cdot 10^3$ versus $Re = 5.3 \cdot 10^3$). From this comparison, we can conclude

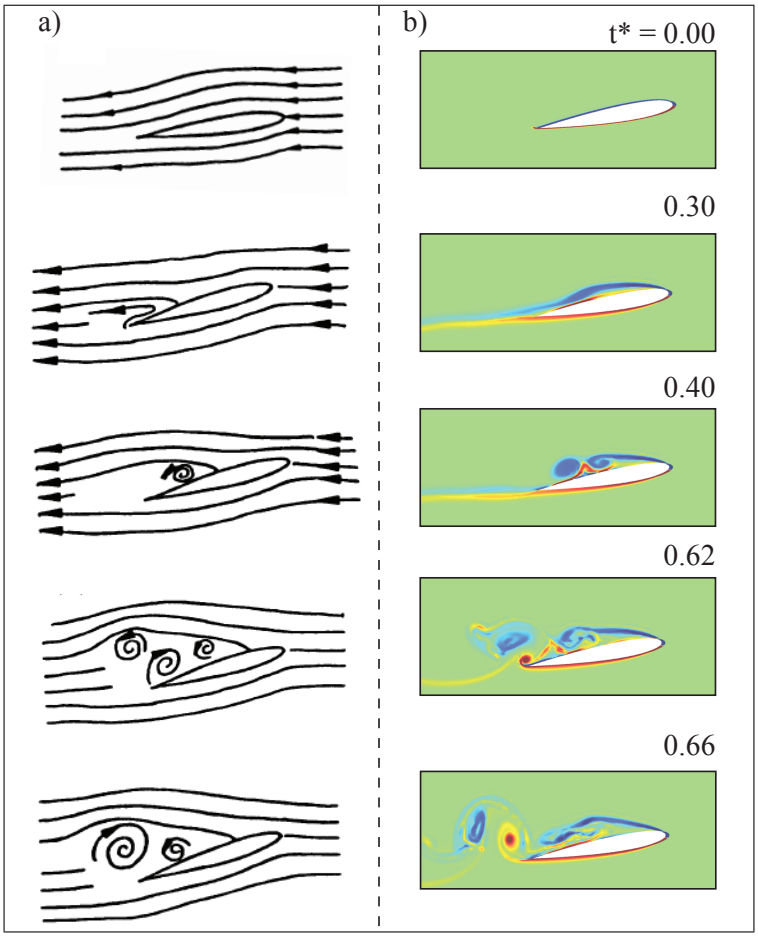

Figure 3.11: a) Streamline sketches of 'Regime C' defined in [68] compared with b) time-evolution of vorticity for ILES simulation at $\alpha = 10°$ and $Re = 5.3 \cdot 10^3$.

that at such high angles of attack the flow is relatively insensitive to small changes in Re in this regime. As Huang describes in [68], at this large angle of attack, a starting vortex is generated from the leading-edge ($t^* < 1.0$). As this vortex rolls down the suction side of the airfoil ($1 < t^* < 2.67$), it induces a trailing-edge vortex in its stead (much like the evolution shown in Fig. 3.11 at lower α). Eventually this leads to alternative shedding of a surface vortex and trailing-edge vortex.

After obtaining results simulating a single static NACA0012 airfoil in 2D and 3D at $Re \leq 50 \cdot 10^3$, under a range of α that matched a wide array of experimental data, we surmised that this methodology could be applied to a straight-bladed, low-Re VAWT.

3.4 LES of a Vertical-Axis Wind Turbine

The VAWT chosen for this study was the one built and tested by Strickland and reported in [93] as well as in [94]. Since the model VAWT was actually tested in a tow-tank, the

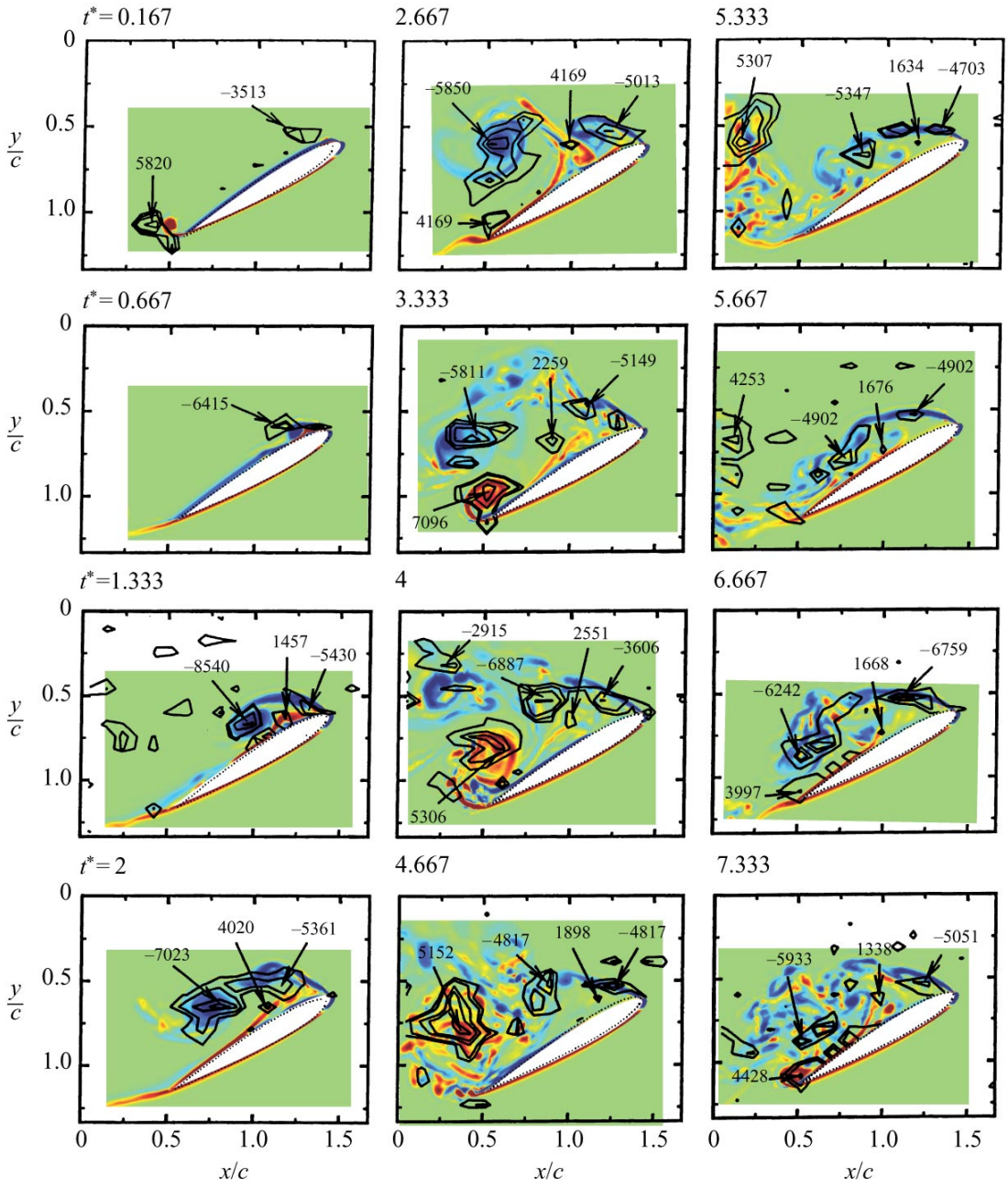

Figure 3.12: Comparison of vorticity at various normalized time instances, at $\alpha = 30°$ from interpolated PIV data (Fig. 14 from [68]) at $Re = 1.2 \cdot 10^3$ in black contours and labels with the 3D ILES simulations from this study at $Re = 5.3 \cdot 10^3$ in a jet colormap.

average chord Reynolds number for turbine blades is approximately $40 \cdot 10^3$. A schematic of the experimental test setup is shown in Fig. 3.13. The width of the tow tank was 5 m, so the effect of the side walls on the turbine blades is negligible. However, the bottom of the blades were only approximately 35 cm away from the bottom of the tank, so the proximity

of this boundary on the blades could have a significant effect on the flow around the blades. The physical parameters of the VAWT are shown in Table 3.1. The definitions of these parameters are shown in Fig. 3.1 where the 2-bladed VAWT is shown in plan view. A plot of the variation of the angle of attack as well as the chord Reynolds number for various tip-speed ratios λ is shown in Fig. 3.2.

In [93], the authors do not explicitly report the blade offset distance c_0, which is the distance from the leading edge of the airfoil to the blade mounting point, along the chord line of the airfoil. However, from the discussion on pages 57 and 59 of [93] on the measurement of the moment about the quarter-chord, we infer that $c_0 = c/4$. From this section, we also infer that the intended blade offset pitch angle α_0, as shown in Fig. 3.1, to be 0°. Yet, the authors report uncertainty in the measurement of the azimuthal angle on the order of 1°. The determination of the actual α_0 used in the experiments is discussed in Sec. 3.4.3. The authors also do not report the temperature of the fluid T when performing the experiments, which we explore in further detail in Sec. 3.4.4. In the tow tank experiments, the forces were averaged over a particular time step, which corresponded to a change of azimuthal angle $\theta \approx 15°$. Thus, maximum errors for the azimuthal angle could be $\pm 15°$. In [94], when the authors compared their experimental data to the results from their vortex code, they also encountered a phase shift between the numerical and experimental data, especially for $\lambda = 7.5$ (see Fig. 17 in [94]). In the present study, we found that if we shifted θ of the experimental results by -15° only for λ of 2.5 and 7.5 then we found the best agreement with our numerical results. All of the following plots include this offset in the azimuthal angle for λ of 2.5, 7.5. Unless otherwise noted, the data from the ILES simulations are the averages over all of the passes of the simulations (usually 2 passes for the 3D simulations and 3-4 passes for the 2D simulations) for Blades 1 and 2 at each of the azimuthal positions. Considering the turbine is started impulsively at $t^* = 0$, the results from the first rotation are discarded since the simulation has not yet reached a near-periodic solution.

Parameter	Value	Unit
c	9.14	cm
R	0.61	m
ω_1	1.56	rad/s
H	0.85	m
α_0	-2	deg
c_0	$0.25c$	m

Table 3.1: Geometry and turbine parameters for the VAWT simulated in this study.

In the following sections the sectional tangential force coefficient, C_T is displayed as a function of azimuthal angle θ as defined in 3.1. The sectional tangential force coefficient on

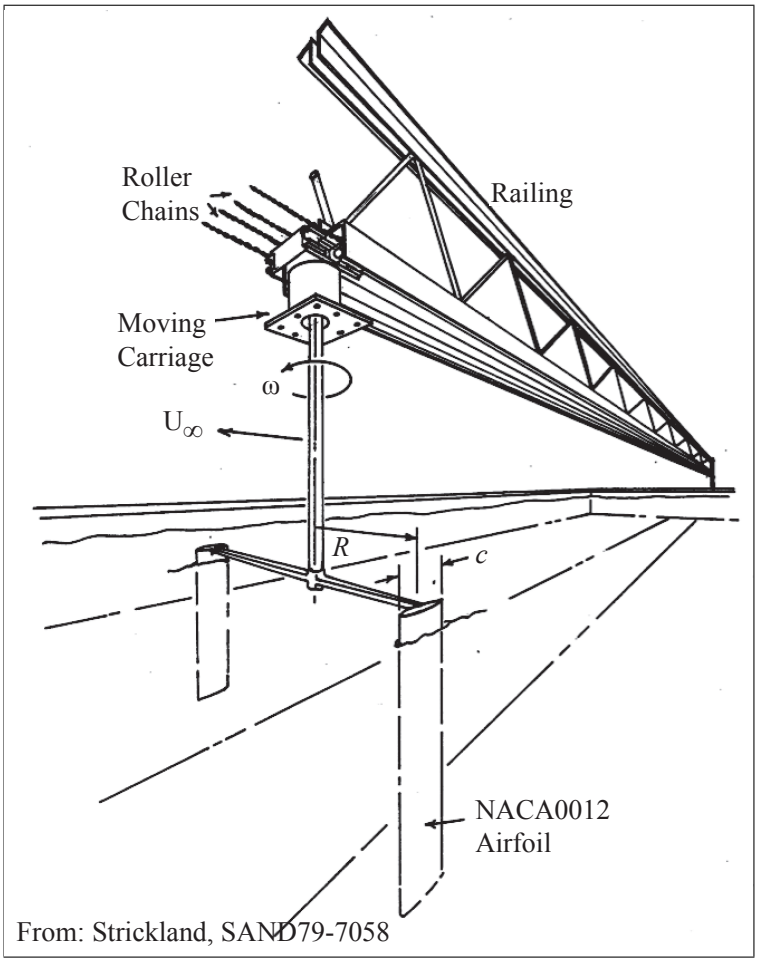

Figure 3.13: Schematic of tow tank experiment of low Re VAWT performed by Strickland in [93] and [94].

the j^{th} blade is usually defined as,

$$C_{Tj} = \frac{F_{Tj}}{1/2\rho_a U_\infty^2 c} \tag{3.7}$$

where F_{Tj} is the sectional tangential force on the j^{th} blade. In the 3D simulations, C_{Tj} is the average tangential force coefficient over the entire section of the blade so it is normalized by the spanwise length of the blade ($0.65c$). For a straight-bladed VAWT, the power coefficient is a function of the sum over the number of blades N_b of the averages of C_{Tj} over one revolution, $\bar{C}_{Tj}$ and other parameters, such that

$$C_P = \sum_j^{N_b} \frac{\frac{\omega_1}{2\pi}\int_0^{2\pi} F_{Tj}(\theta) R d\theta}{1/2\rho_a U_\infty^3 2R} = N_b \frac{\lambda \bar{C}_T}{2}\frac{c}{R} \tag{3.8}$$

where $\bar{C}_T$ is representative of the average tangential force of all blades.

3.4.1 Deforming Computational Domain

The method described in Sec. 3.3.1 is extended to a spinning turbine by using an Arbitrary Lagrangian Eulerian (ALE) formulation. With this methodology, we define a fixed, 'reference' domain as well as a moving 'physical' domain and use a smooth mapping to transform between the two domains. In our case, we can simply use a rotating framework to model the spinning turbine. Thus, we are performing decoupled Fluid-Structure Interaction (FSI) simulations, since we prescribe the motion of the physical bodies (in this case, airfoils) and then measure the fluid properties around them, much like in the forced motion of the experiments described in [94]. In future work, we can implement a coupled FSI simulation where the displacement of the airfoils at each time step depends on the forces on the airfoil.

Arbitrary Lagrangian Eulerian Formulation

For the turbine simulations, we account for the moving and deforming domains by the Arbitrary Lagrangian-Eulerian (ALE) formulation proposed in [95]. It is accurate to arbitrary orders in both space and time. The so-called Geometric Conservation Law (GCL) is satisfied using an additional equation that is used to compensate for numerical integration errors. We analytically compute the deformation gradient and the grid velocity and formulate the ALE equations directly in the reference domain. For details on this procedure, see [95].

Computational Domain

The computational domain for the VAWT is shown in Fig. 3.14. We use a boundary layer similar to the one in the static simulations, and we use a finer-mesh resolution in the near wake of the airfoils. The 3-D mesh is again generated by extruding the 2-D mesh, with a span of 0.65 chord lengths. The resulting size of the 2-D mesh is 11,630 elements, or 116,300 high-order nodes and about 350,000 degrees of freedom. The size of the 3-D mesh is 139,560 elements, or about 2.8 million high-order nodes and about 11 million degrees of freedom. The time step chosen for this study is $\Delta t^* = 5 \cdot 10^3$.

3.4.2 Comparison of 2D and 3D ILES

Most of the parameterization study for the ILES simulations were performed in 2D due to the high computational cost of the 3D simulations. In this section, however, we show that the 3D simulations generally follow their 2D counterparts, especially for high TSR. In Fig. 3.15, the 2D and 3D simulations are compared for $\alpha_0 = -2^\circ$ and $\lambda = 5.0$. Generally, the results of the 2D simulations exhibit the same behavior as the results from 3D cases, albeit with some higher frequency harmonics. In Fig. 3.16, the results from the 2D and 3D simulations for $\lambda = 2.5$, $T = 25^\circ C$ are shown for different α_0. Here, there are discrepancies between the 2D and 3D simulations, especially for $0^\circ \leq \theta \leq 45^\circ$ Thus, we can safely infer that the dominant features that appear in the upwind and downwind zones in the 2D simulations will also appear in the 3D simulations. However, for low TSR, when α is in a post-stall region, the 2D simulations will generally not closely follow their 3D counterparts.

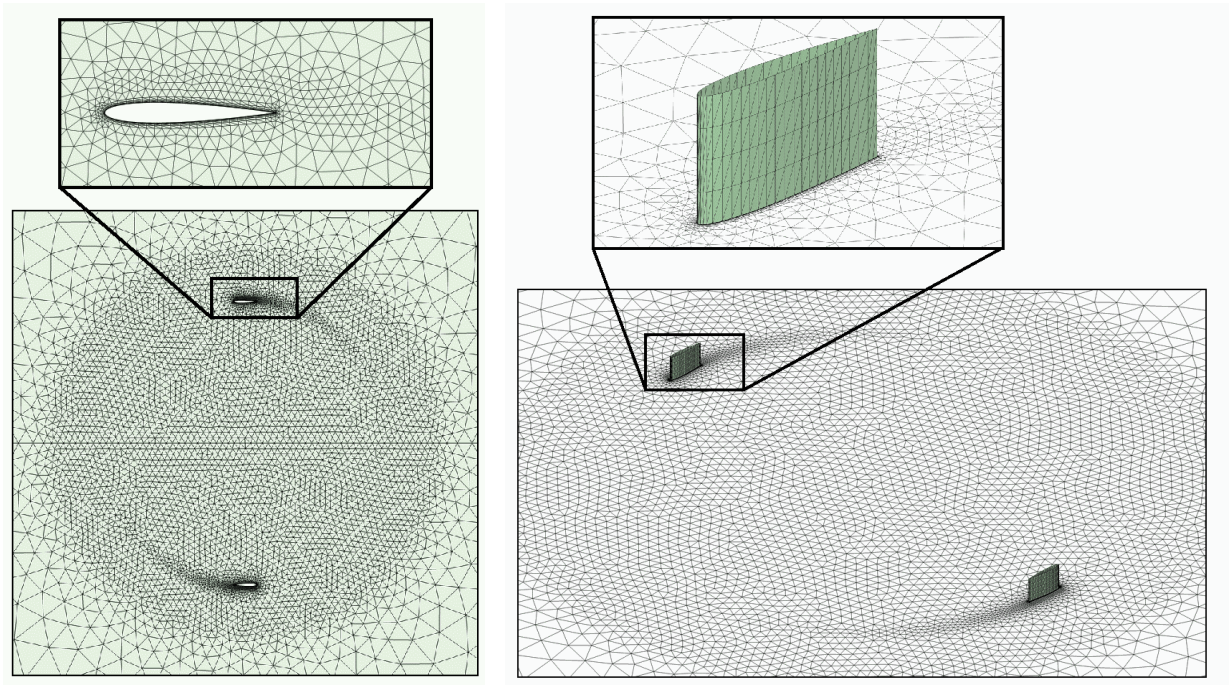

(a) 2D Mesh

(b) 3D Mesh

Figure 3.14: The two high-order computational meshes used for 2D and the 3D simulations of the VAWT considered in this study.

3.4.3 Parameterization Study: Pitch Angle Offset

In order to recreate the experiments performed in [94], parameterization studies were performed for the experimental parameters that were not reported or reported with a certain degree of uncertainty. The authors report that discrepancies in the experimental data, *"may be due to misalignment errors in the blade mounting... on the order of* 1° *in the blade angle of attack"*. In order to determine the pitch angle offset of the experimental turbine, relatively low-cost 2D ILES simulations were performed for $-5^\circ \leq \alpha_0 \leq +5^\circ$, in increments of 1° for $\lambda = 5.0$ and $T = 20^\circ C$. As mentioned previously, the mounting point of the airfoil was taken to be a distance of $c/4$ from the leading edge. The blades were then rotated about this point by an angle of α_0. In these simulations, we found that any toe-in angle ($\alpha_0 > 0^\circ$) of the airfoil decreased the efficiency of the turbine and led to a high variability in blade forces. Thus, in Fig. 3.17, we only show the tangential force coefficient of the VAWT as a function of the azimuthal angle for $\alpha_0 \leq 0^\circ$ to improve readability. From Fig. 3.17, it is clear that $\alpha_0 = -3^\circ$, denoted by '+' markers, has the largest maximum value of any of the simulations. However, $\alpha_0 = -2^\circ$, shown with open squares, has the largest power coefficient of the simulations ($C_p = 0.27$). This finding follows the trend observed by Klimas and colleagues for their 5 m experimental VAWT [96]. In these experimental tests, which were performed at various λ for a Darrieus turbine with curved blades, the overall maximum power coefficient was achieved for $\alpha_0 = -2^\circ$, ($C_p = 0.32$). Further, this pitch angle offset had the largest

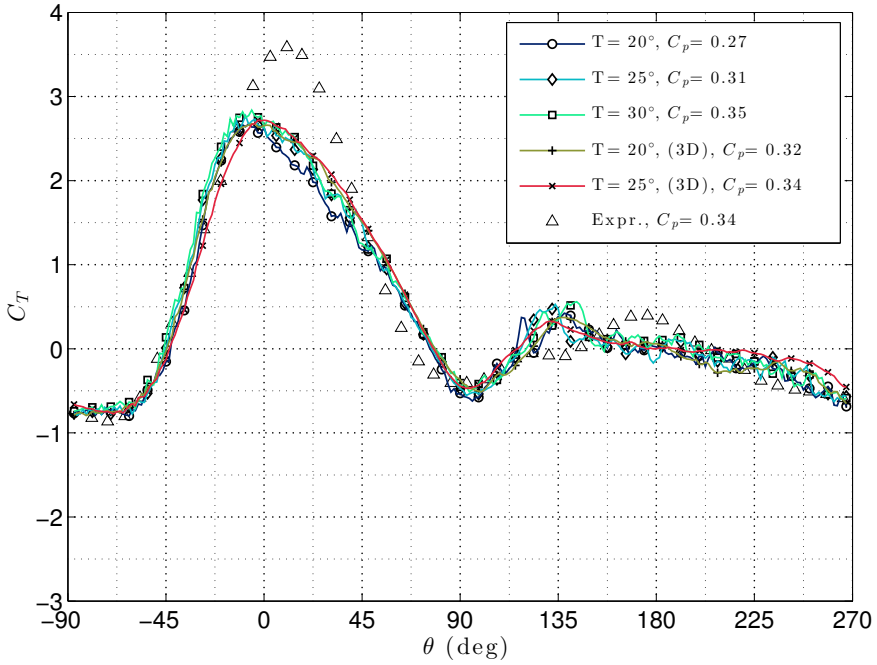

Figure 3.15: Tangential force coefficient of a VAWT blade as a function of azimuthal position for simulations in 2D and 3D $\alpha_0 = -2°$ at $\lambda = 5.0$ for various temperatures.

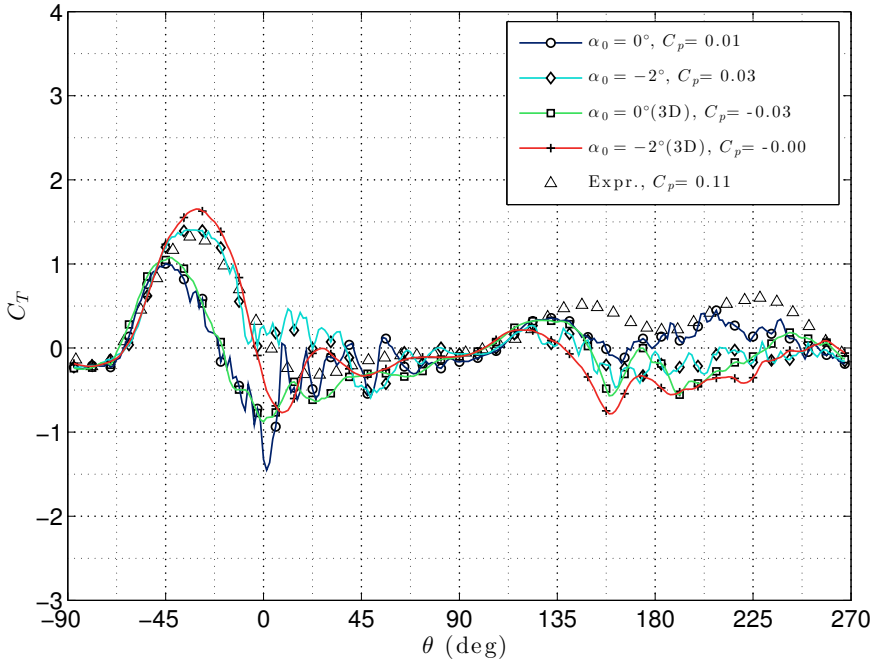

Figure 3.16: Tangential force coefficient of a VAWT blade as a function of azimuthal position for simulations in 2D and 3D $\alpha_0 = 0, -2°$ at $\lambda = 2.5$.

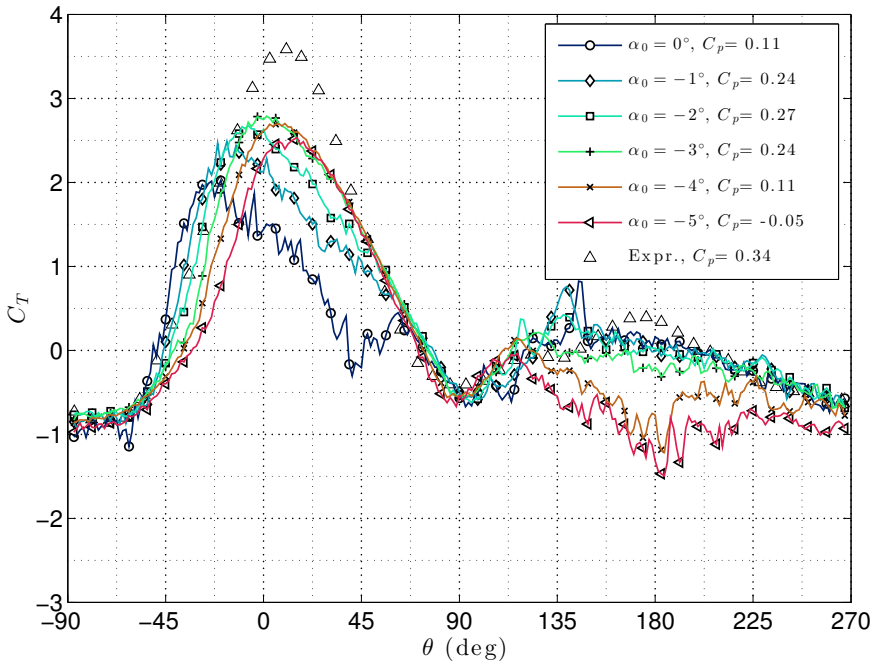

Figure 3.17: Tangential force coefficient of a VAWT blade as a function of azimuthal position for various α_0 at $T = 20°C$, $\lambda = 5.0$.

C_p for $3.5 \leq \lambda \leq 6.0$. Although the parameterization study for the pitch angle offset was only performed in 2D, it is encouraging that the results follow the trend found by previous experimental studies.

3.4.4 Parameterization Study: Temperature of Fluid

After analyzing the ILES simulations of the single NACA airfoil, it became clear that the dynamic fluid structures around the airfoil at high angle of attack were sensitive to the local Re number of the airfoil. Further, the experiments were undertaken at a tow tank at Texas Tech University in Lubbock, Texas, where the temperature of the fluid could realistically vary by 5-10° depending on the building, insulation, season, etc. We varied the temperature on the order of $5°C$, to slightly change the Re of the flow and examined the numerical results. Though the simulations matched most closely for higher Re (corresponding to higher temperatures), we only thought it was reasonable to assume water temperature of at most $T = 25°C$. The data for the kinematic viscosity of water as function of the temperature was found in [97]. Figure 3.15 shows the tangential force coefficient as a function of azimuthal angle at $\lambda = 5.0$ and $\alpha_0 = -2°$ for various fluid temperatures $(20, 25, 30°C)$. Clearly, there is not a large change in the trend of the force as the temperature changes by 5° or 10°. However, for these small temperature changes, we were not expecting such a large change in the turbine power coefficient, C_p. Figure 3.15 shows that a 5° increase in the temperature, which corresponds to a 10% increase in the Re number (due to the change in the kinematic viscosity of water), yields a 5% increase in power production. However, this increase is within

the margin of variation of the torque variation from various passes of the turbine of blade. The 2D results, also plotted in Fig. 3.15, show a similar trend but to even a higher degree.

For a wind turbine exposed to environmental conditions the temperature of the fluid cannot be modified. However, this analysis shows that it is critical for researchers to report the temperature of the working fluid in controlled model tests (especially if they are performed in water) so that the conditions can be recreated in such numerical simulations.

3.4.5 Validation for a Single Turbine

Besides simulating the VAWT with ILES methods, two analytical codes were used to estimate the aerodynamic torque on the blades for comparison. A blade-element methodology called the Double Multiple Streamtube Method described in [3] was used along with a dynamic stall model of Berg [98]. This formulation uses a momentum method to model the streamwise wake deficit both in the 'upwind zone' and 'downwind zone' of the rotor (see Fig. 3.1 for depiction of zones) by iteratively solving for an induction factor. Once this factor is known in the upwind zone for all azimuthal angles, the force on the blades in the downwind zone can be determined. Also, a vortex method developed at Sandia National Laboratories called Code for Axial and Cross-flow TUrbine Simulation (CACTUS) [2] was used to simulate the aerodynamic torque. As of 2013, this numerical method was made available to public as an open-source software. In this model, the data from the twentieth revolution of the turbine was used in order to allow the code to reach a steady-state solution. After corresponding with the authors of the code, the number of blade elements was increased to 10, which slightly improved the accuracy of the code. The sectional lift and drag coefficients for both of the codes came from the experimental data of [70] and [72]. For these codes, the angle of attack was calculated at the mid-chord, as recommended in [94].

The experimental data of the tangential force coefficient shown as triangles in Figs. 3.18, 3.19 and 3.20 was taken as a blade swept over the first half of its fourth revolution (the only tabular data provided in [94]). Due to the computational intensity of the ILES, the data from the ILES 2D and 3D simulations were taken from the forces on 'Blade 2' as it made its first pass from $-90° \leq \theta \leq 270°$ after starting from $\theta(t = 0) = -270°$. However, subsequent revolutions exhibited similar behavior, which was in agreement with the experimental data. The data from CACTUS was taken at 32 instances on the twentieth revolution of the simulation. The DMST only estimates the torque on the blades as an average for a single revolution (no unsteady effects) but the resolution can be increased by increasing the number of streamtubes.

Figures 3.18, 3.19 and 3.20 show that the ILES simulation can approximate the experimental data very well at high TSR, especially in the downwind section. At λ=2.5, the CACTUS model utilizing the Leishman-Beddos dynamic stall model (described in [99]) recreates the experimental data the best. However, at higher TSR the accuracy of the analytical models drops drastically resulting in highly inaccurate predictions for the power coefficients.

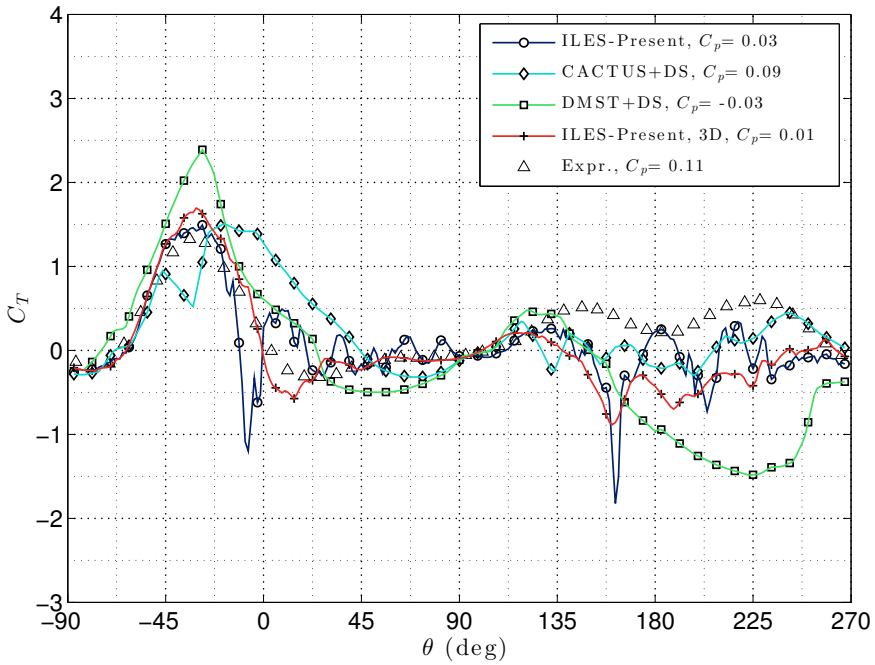

Figure 3.18: Tangential force coefficient of a VAWT blade from ILES simulation as a function of azimuthal position for λ=2.5, compared with vortex code 'CACTUS' [2] and BEM model, 'DMST' described in [3].

3.4.6 Flow Visualization

Iso-surfaces of the q-criterion are frequently used to visualize the unsteady 3D flow structures in the fluid domain. The q-criterion physically represents areas where rotation dominates the strain of the flow. In the core of a columnar vortex, $q > 0$ since vorticity increases as the radial distance to the core decreases [75]. In Fig. 3.21, iso-surfaces of the q-criterion, where $q = 100$, are shown in 3D for various azimuthal angles of Blade 1 when $\lambda = 2.5$. As shown in the top row of Fig. 3.21, the azimuthal angle θ is 0° and columnar vortices are present in the downwind zone of the turbine. These vortices were shed in the wake of Blade 2 from its previous pass and then convected downstream due to the incident wind. The image to the right is a more detailed depiction of the iso-surfaces formed around Blade 1. At this instant in time, the angle of attack α is greater than 20°, excluding dynamic effects (see Fig. 3.2). Clearly, there are instantaneous vortical structures forming on the suction side of the airfoil. At $\theta = 60°$ these disturbances have formed into a more coherent structure, labeled 'Vortex A'. The location of Vortex A moves from the upwind zone into the downwind zone due to the influence of the incident wind throughout the time instances in Fig. 3.21. As the vortex continues to be convected downstream, the vortex core coalesces, while the other vortical structures on the periphery are dissipated. Interestingly, the vortex cores are convected too slowly to directly interfere with the flow field around Blade 1 when $120° \leq \theta \leq 180°$.

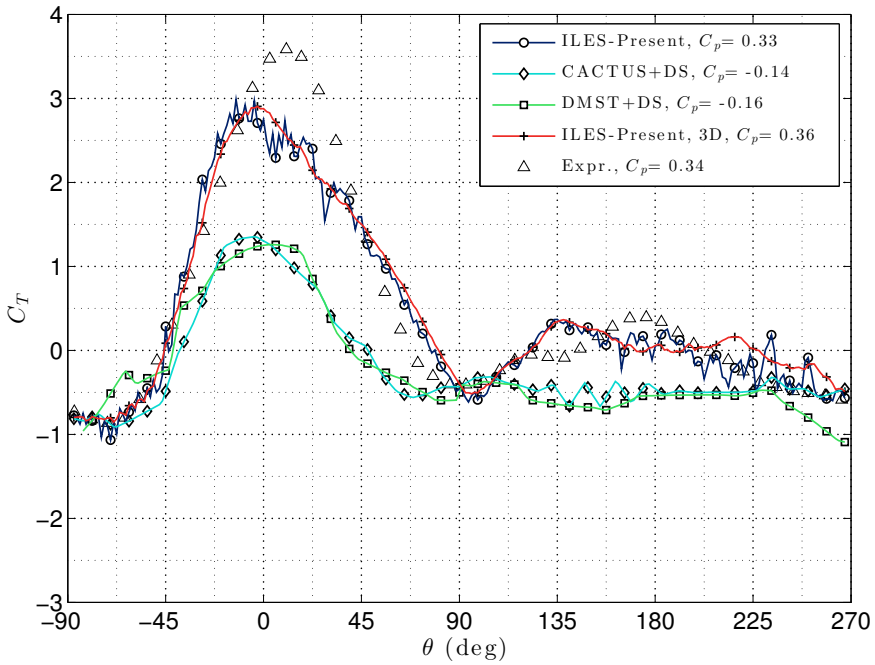

Figure 3.19: Tangential force coefficient of a VAWT blade on a straight-bladed turbine from ILES simulation as a function of azimuthal position for λ=5.0, compared with vortex code 'CACTUS' [2] and BEM model, 'DMST' described in [3].

3.5 LES of Counter-Rotating Vertical-Axis Wind Turbines

The ILES method described in Secs. 3.3 and 3.4 was extended to capture the complex aerodynamics of two, closely-spaced, counter-rotating vertical-axis wind turbines. A novel technique had to be developed for this application since the domain includes moving interfaces. That is, there are three domains that must be spliced together using complex moving meshing techniques: the outer static boundary that includes the area around and in between the spinning turbines (labeled region (III) in Fig. 3.22); two, rotating domains that include the spinning turbines, each spinning the opposite direction as the other (labeled regions (I) and (II), respectively). The dashed lines in Fig. 3.22 signify the interfaces that must be dealt with specially. The turbine-to-turbine spacing is denoted by $\bar{D}$, which is nondimensionalized by the VAWT diameter.

3.5.1 Computational Domain and Element Flipping Technique

A novel technique for element flipping on high-order domains was developed by L. Wang as part of a collaboration on this research. His technique is described in greater detail in [100]. For now, we introduce some of the basic concepts to get an idea for how the technique works.

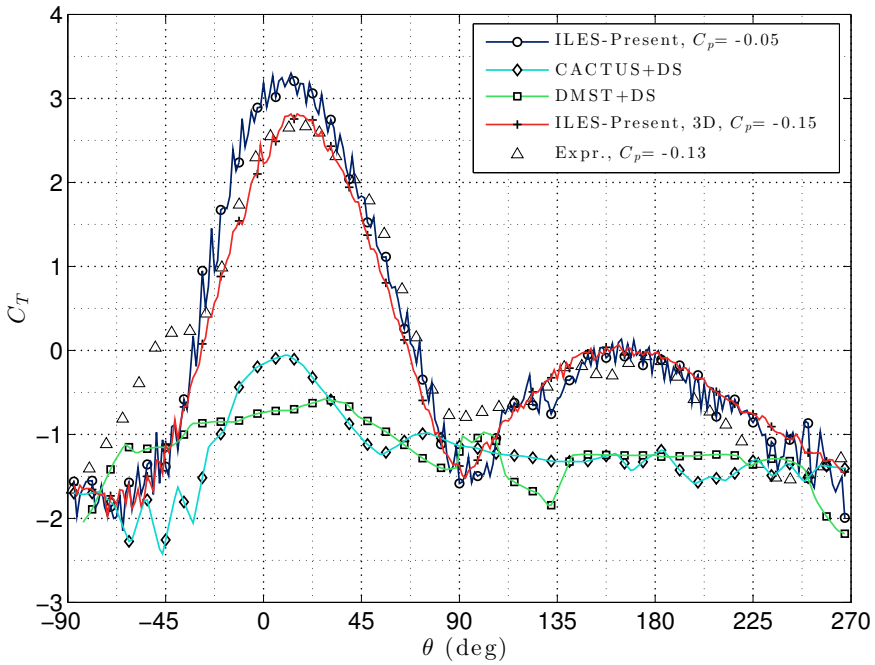

Figure 3.20: Tangential force coefficient of a VAWT blade from ILES simulation as a function of azimuthal position for λ=7.5, compared with vortex code 'CACTUS' [2] and BEM model, 'DMST' described in [3].

Element Flipping Technique

Figure 3.23 shows the computational domain for the LES simulations of the counter-rotating vertical-axis wind turbines. We use the same turbine as in Sec. 3.4 to ensure that the results are consistent under various simulation techniques. For instance, if we freeze one of the turbines and rotate the other, we generally recover the results found in Sec. 3.4. There is a higher density of elements in between the two turbines, since we are interested in the fluid behavior between the turbines. The yellow box is shown in greater detail in three figures, each at a different time step in the simulation. The figures show how the orientation of the band of elements that represent the 'sliding interface' between the rotating meshes and the static mesh, shaded in red in Fig. 3.23, can vary depending on the time step. In order to determine when an element should be flipped, the algorithm approximates the quality of each element at each time step. For all elements under a certain threshold, the algorithm performs an element flipping operation between elements that share an edge, as shown in Fig. 3.24.

This topological change requires a projection of the solution from the polynomials on the old elements, to polynomials on the new element. However, the old and new elements can be partitioned such that the solution can be projected without introducing errors that sacrifice the order of the solution. For more detail, the reader is referred to the L. Wang's thesis [100].

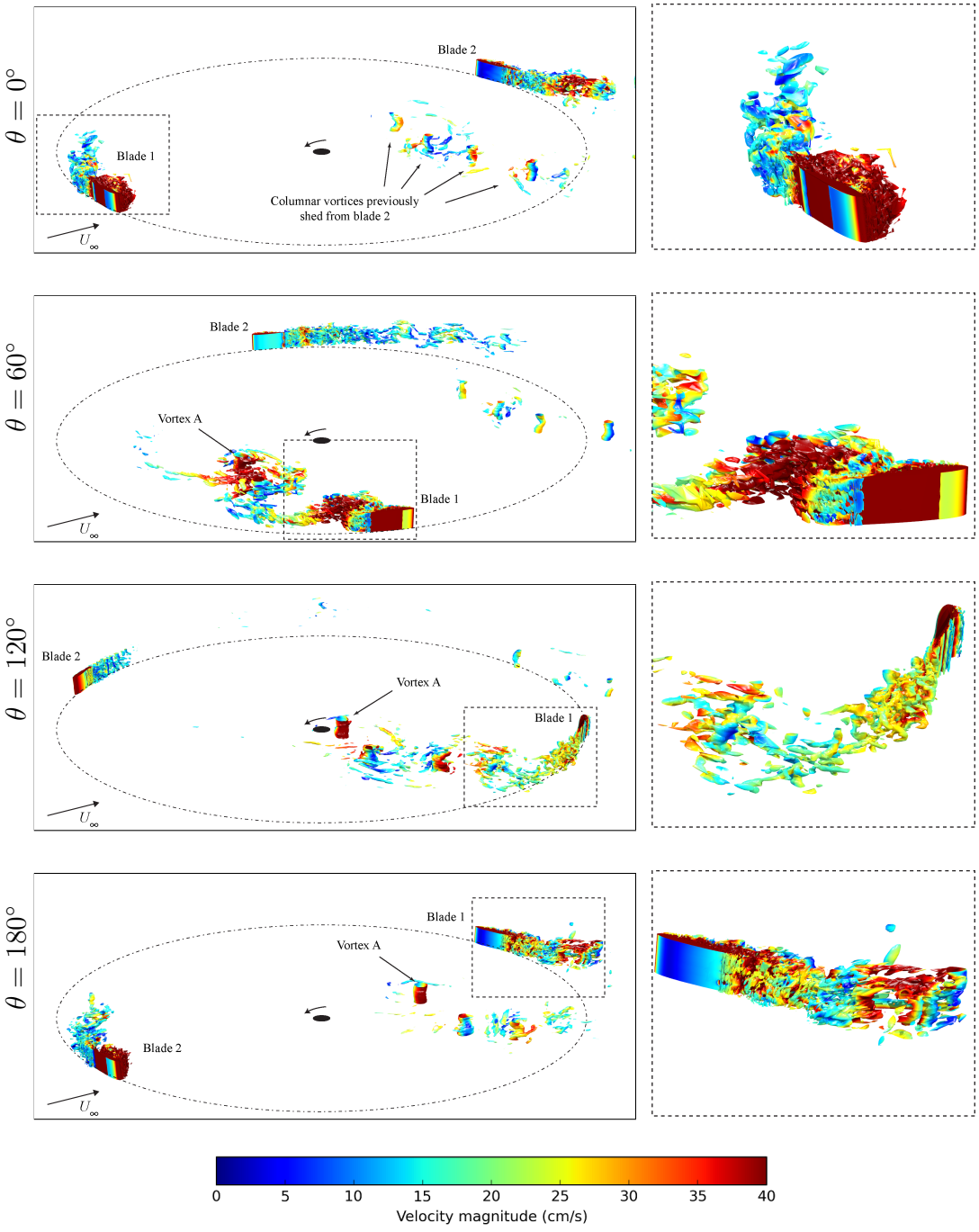

Figure 3.21: Iso-surfaces of the q-criterion for $q = 100$ at various azimuthal angles of Blade 1 at $\lambda = 2.5$. Images on right are magnified views of Blade 1. The time evolution of 'Vortex A' is discussed in the text. The isosurfaces are colored according to the magnitude of the velocity, as indicated by the colorbar at the bottom of the figure.

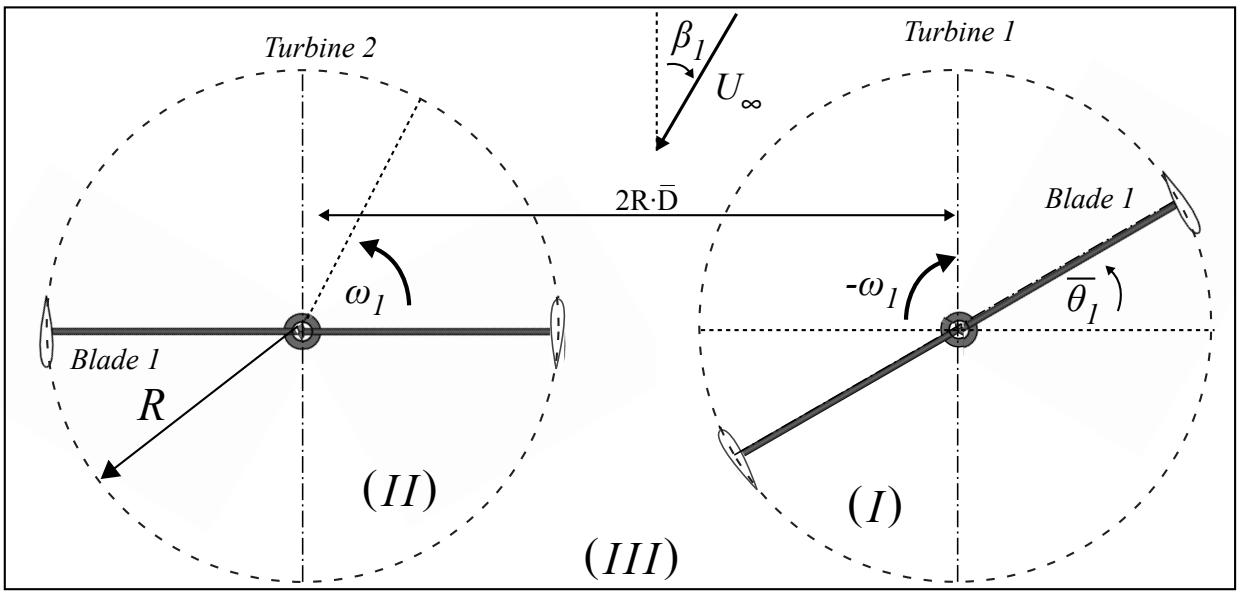

Figure 3.22: Plan view of counter-rotating, two-bladed vertical-axis wind turbines with non-dimensional spacing $\bar{D}$, static offset azimuthal angle $\bar{\theta}_1$ and incident wind direction β_1.

3.5.2 Parameter Study: Distance Between Turbines

In the following section we define an average power coefficient for the turbine pair as

$$C_p^* = \frac{C_p^{(1)} + C_p^{(2)}}{2\bar{C}_p} \tag{3.9}$$

where $\bar{C}_p$ is the average power coefficient of an isolated turbine. To calculate this baseline value, we freeze one of the turbines, such that $\dot{\theta}_2 = 0$ and ran the same simulations. Varying which turbine was frozen and the incident wind direction resulted in less than 5% variation of the power coefficient of the isolated turbine.

In order to study the synergistic effect between the counter-rotating turbines, the distance between the centers of rotation of the turbines was varied to determine the optimal distance between the turbines. The results from these simulations for various incident wind directions β_1 are shown in the polar plot in Fig. 3.25. These plots were created to mimic the polar plot created by J. O. Dabiri in Figure 4a in [4] from data taken from his experimental wind farm, which is reproduced in Fig. 3.26. It must be stated that the computational domain studied here is not equivalent to the experimental study performed in [4]. The turbines in [4] were purchased from Windspire Energy$^{\text{TM}}$, with a proprietary airfoil shape. Furthermore, the Re number used in the computational study is orders of magnitude lower than the experimental conditions. Thus, a direct comparison of the results presented in the section and the results in [4] is not possible from the current study.

The circumferential direction represents the direction the incident wind originates from. The radial direction represents the normalized power coefficient C_p^*. For $\beta_1 = 90°,\ 270°$, $C_p^* < 0$ due to the shadowing effect from the upwind turbine, which can be seen in Sec. 3.5.4.

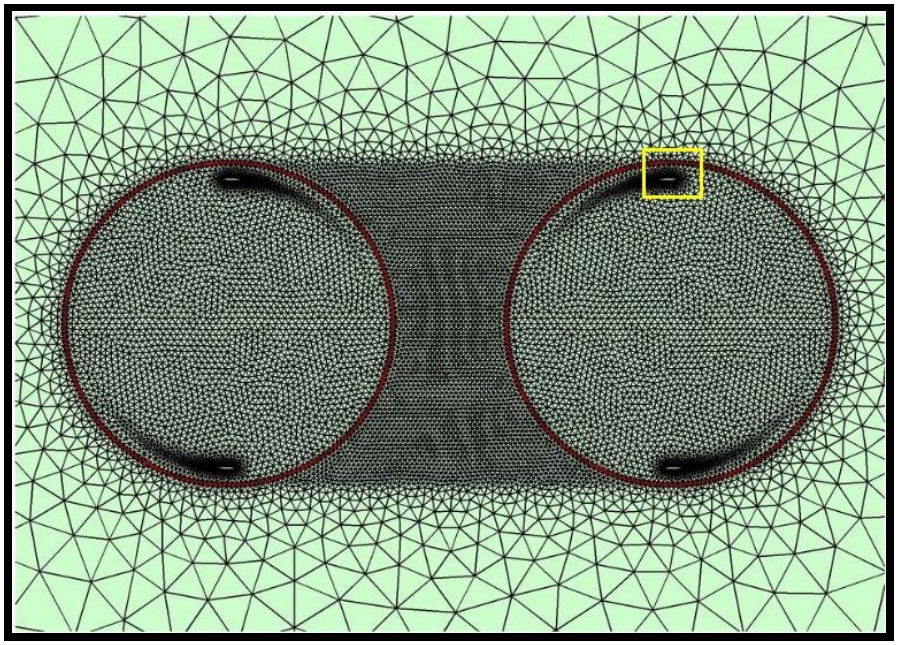

Computational domain used for counter-rotating simulations.

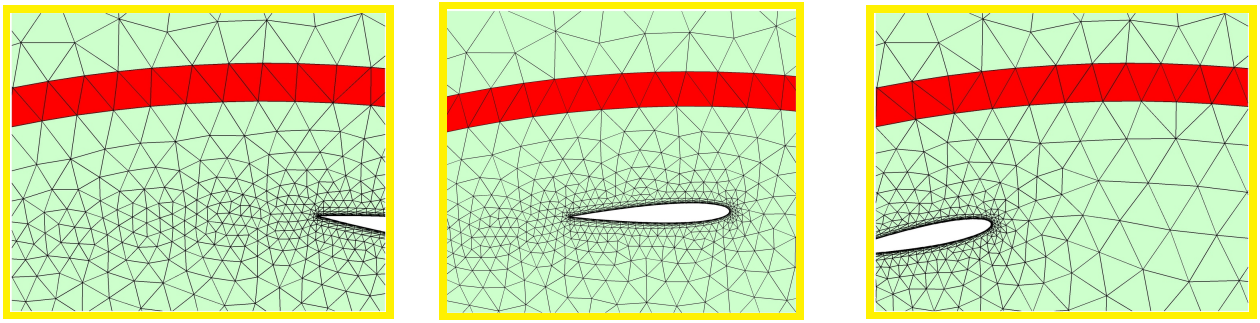

Figure 3.23: Unstructured mesh for counter-rotating VAWTs. The region where all the edge flipping operations occur is colored in red. The area outlined by the yellow box is shown in greater detail in the three figures below at various time steps in order to show the mesh motion. (All figures courtesy of L. Wang [100].)

This effect was not seen in the experimental study reported in [4], who even saw a slight jump in the efficiency around $\beta_1 = 105°$ (which is 195° in their figure since their orientation of β_1 is offset by 90°). The figure from the experimental data in [4] is reproduced in Fig. 3.26 for comparison.

The differences between the reported effects of counter-rotating turbines at close distance studied using an experimental wind farm, reported in [4], and the present results, shown in Fig. 3.25, deserve further discussion. There are many reasons that may explain these discrepancies. Namely, the turbine simulated is a two-bladed turbine with NACA0012 airfoils, while the Windspire$^{\text{TM}}$rotor, used in [4] is a three-bladed rotor with a proprietary airfoil shape. Furthermore, the simulation is only in 2D and does not take into account vertical

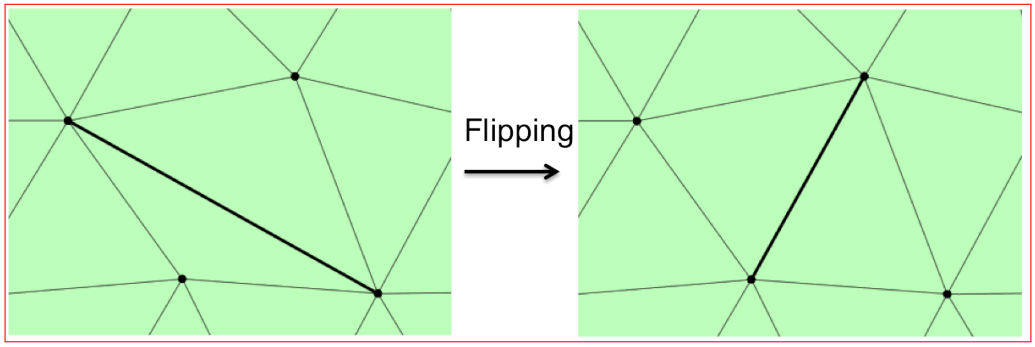

Figure 3.24: Element flipping technique showing local topology change between two triangular elements. (Courtesy of L. Wang [100].)

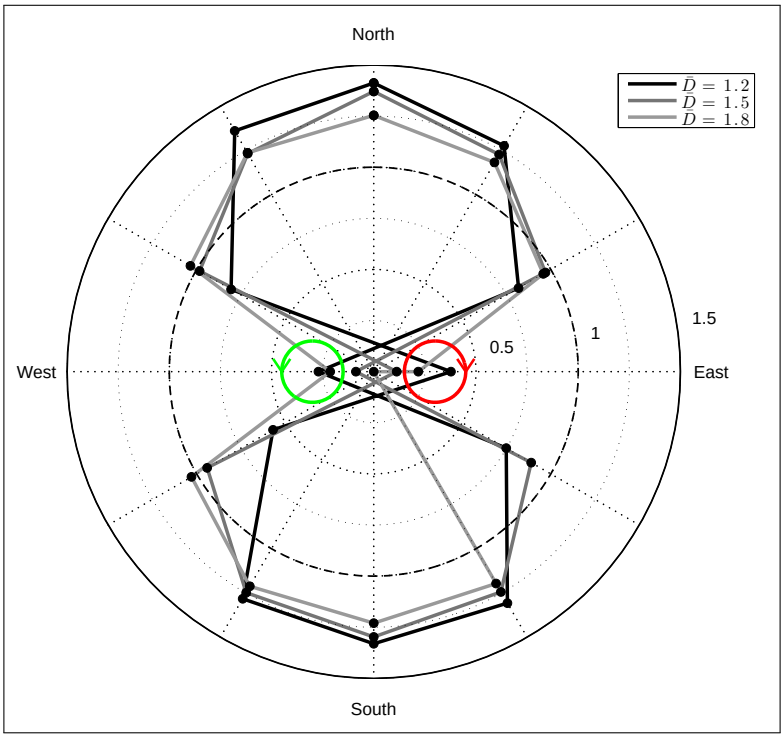

Figure 3.25: Normalized power coefficient C_p^* of 2D simulations of counter-rotating turbines as a function of wind-speed direction and turbine spacing $\bar{D}$.

momentum fluxes, which may be where the additional kinetic energy flux originates from, as reported in [101]. Since the simulations occur in 2D, we neither take into account the vertical variation of the incident wind field nor any turbulence. In fact, the simulation of a real wind field is quite an open question in the computational fluid dynamics community. Finally, the results shown in Fig. 3.25 are shown for $\lambda = 5.0$, which is larger than the tip-speed ratios reported for the experimental turbines. For all of these reasons, we may see discrepancies between the data shown here and previously published work.

Independent of this work, a discrete vortex-code was written for the study of vertical-axis

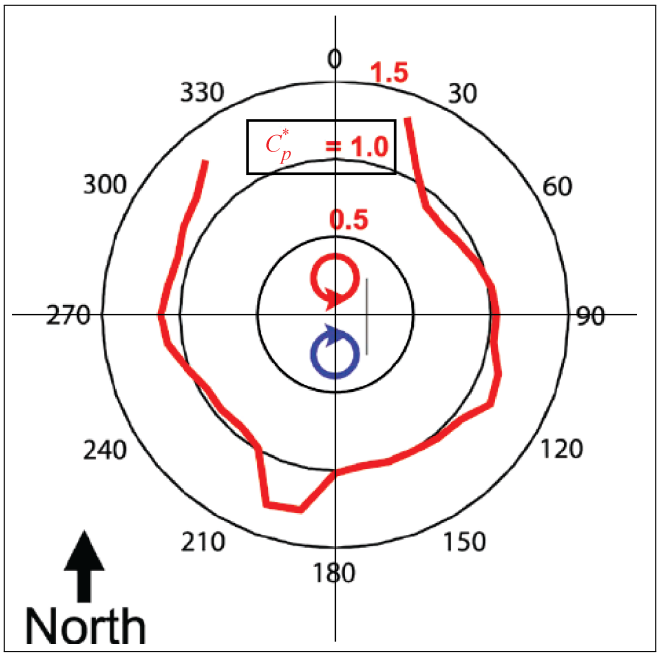

Figure 3.26: Normalized power coefficient C_p^* of experimental counter-rotating turbines as a function of wind-speed direction for $\bar{D} = 1.6$ (Adapted from [4]).

wind turbines [102] as an M.S. thesis. Using the method of images, Leclercq was able to extend this vortex method to study three-bladed counter-rotating turbines, with the wind originating from the 'North' as shown in Fig. 3.25. He noted a 13% in the total power production at a best separation-to-distance ratio $\bar{D}$ of 2.0. To our knowledge, this is one of the few lower fidelity studies of counter-rotating turbines that somewhat substantiate these computational results.

We use the vocabulary developed for counter-rotating cylinders studied in [103], such that when the wind comes from the 'North' ($\beta_1 = 0°$) the configuration is 'doublet-like', while when the wind comes from the 'South' ($\beta_1 = 180°$), it is 'reverse doublet-like'. From Fig. 3.25, it is clear that the turbines are most efficient in the 'doublet-like' configuration, gaining nearly 30% total power from their isolated counterparts. This synergistic effect is almost as large in the 'reverse doublet-like' configuration.

3.5.3 Parameter Study: Turbine Angular Offset

In Chapter 4, the MIST platform is described, which uses a timing belt to force the turbines to counter-rotate at the same speed, in order to control the platform orientation. Thus, the angular offset of the turbines, denoted as $\bar{\theta}_1$ and portrayed in Fig. 3.22, is fixed for a given platform configuration. Figure 3.27 shows the variation of the average power coefficient when the angular offset of the turbines is changed to 30° and 90°. The plot shows that the power coefficient is fairly insensitive to this variation.

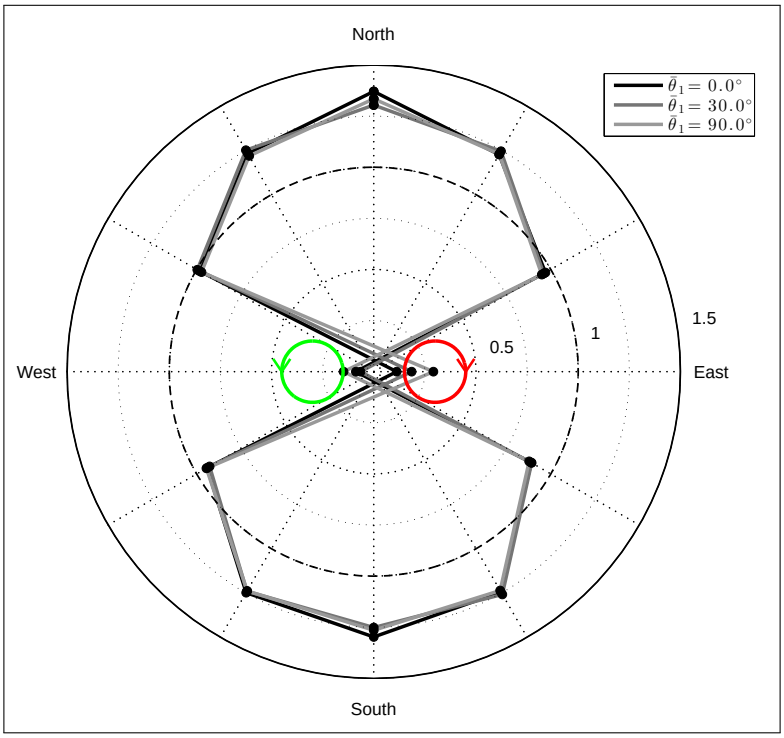

Figure 3.27: Normalized power coefficient of 2D simulations of counter-rotating wind turbines as a function of wind direction and turbine offset angle $\bar{\theta}_1$.

3.5.4 Flow Visualization

To further explore the results, we can visualize the fluid velocity at certain time instants $u = [u, v]$. Figure 3.28 shows time instances of the domain with the color representing the magnitude of the fluid velocity in the direction of the incident wind speed.

$$u^*(\boldsymbol{x}, t) = \frac{u(\boldsymbol{x}, t) \cdot \boldsymbol{\beta}_1}{|U_\infty|} \tag{3.10}$$

Clearly, in the 'doublet-like' configuration, the flow is accelerated between the turbines by over 50%. However, when β_1 is orthogonal to the orientation of the platforms, the upstream turbine retards the incident flow to such a degree that the power produced by the downstream turbine is actually negative, which means that the turbine needs power to spin. Hence, the polar plots in Figs. 3.25 and 3.27 show negative total power produced by the turbine pair.

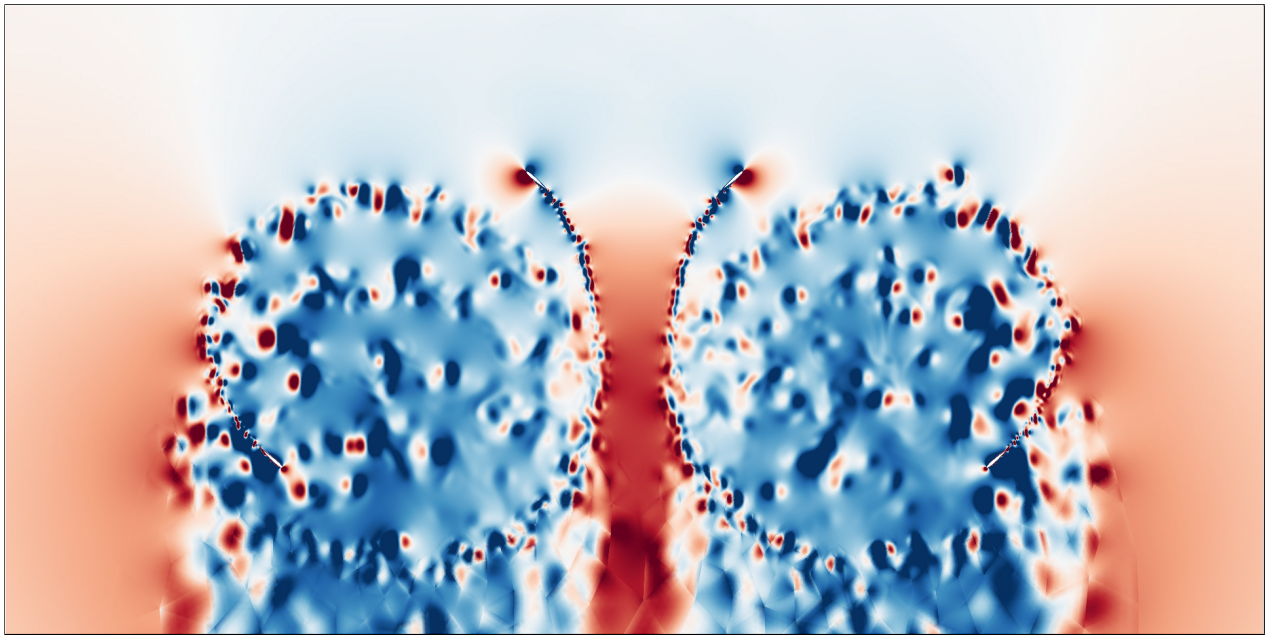

(a) $\bar{D}$=1.2, $\beta_1 = 0°, \bar{\theta}_1 = 0°$

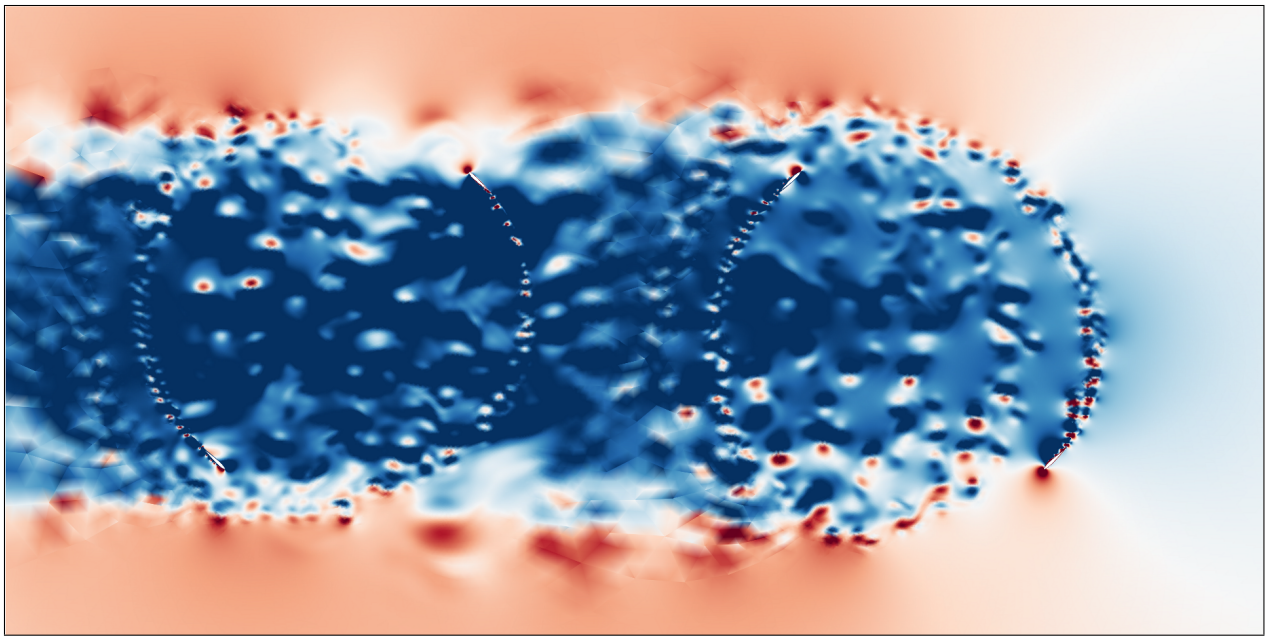

(b) $\bar{D}$=1.5, $\beta_1 = 90°, \bar{\theta}_1 = 0°$

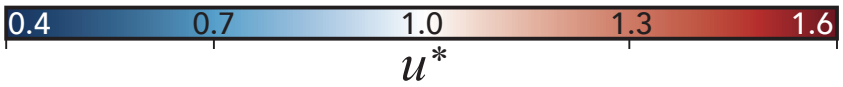

Figure 3.28: Snapshots of the normalized fluid speed, u^* in the direction of the incident wind with $\alpha_0 = -2°$, $\lambda = 5.0$.

Chapter 4

Hybrid Testing of MIST Platform in Model Scale

The Multiple Integrated and Synchronized Turbines (MIST) Platform is a technology that has potential to reduce the cost of offshore wind by using unconventional turbines on a floating platform. Conventional turbines, also known as Horizontal-Axis Wind Turbines (HAWTs), must be spaced far apart so that the wakes of the turbines do not interfere with each other. Typically, the turbines are placed around 5 turbine diameters away from each other in the cross-stream direction and at least 7 turbine diameters away in the down-stream direction [104]. Most offshore turbines have diameters of at least 100m. This spacing makes placing more than one HAWT on a platform prohibitively expensive because of size of the platform. Still, some companies are trying to develop these types of platforms because of the inherent cost-savings per turbine, from shared moorings, electrical connections and other sources. Recent research on unconventional turbines, also known as Vertical-Axis Wind Turbines (VAWTs), shows that the aforementioned spacing requirement need not apply to these types of turbines. In fact, there may even be a synergistic effect between the counter-rotating VAWTs (see Sec. 3.5). For these reasons, the MIST platform was designed to support two, counter-rotating VAWTs to optimize the power extracted from the wind. In Sec. 4.1, we detail how the turbines are connected to the platform and each other. In Sec. 4.2, we discuss the construction of the platform and all materials that were used. Section 4.3 introduces the simulation technique, known as hybrid simulation, or hardware-in-the-loop simulation, that was implemented to prove the concept experimentally. The technique requires a network of interconnected sensors and actuators that can estimate the state of the model and respond appropriately. Using these sensors, we implemented a control algorithm that can optimize the power produced from the combined turbine system by controlling the relative incident wind heading on the platform, as discussed in Sec. 4.4. Section 4.5 describes the onboard communication systems that enable the control system to operate robustly. Finally, experimental results are shown in Sec. 4.6, which illustrate a successful reorientation of the platform.

4.1 Description of MIST Platform

The main components of the technology are the floating platform itself, the counter-rotating turbines, a connecting mechanism and electrical generators housed within the platform, all of which are shown in Fig. 4.1. Not depicted in the rendering is the mooring system with a universal joint which was described in Sec. 2.5.4 and shown in Fig. 2.5.

The MIST platform is designed very similarly to the WindFloat floating platform that supports a single HAWT [105]. This platform is a semi-submersible with three columns in order to increase the hydrostatic stability of the platform. Unlike the WindFloat, however,

the platform is shaped is like an isosceles triangle, instead of an equilateral triangle. We postulated that the length of the side between the turbines had to be a certain distance apart (depending on the radius of the VAWT), but that the other lengths could be shorter to save on material costs. The merits of the design choice are discussed in Sec. 6. Like the WindFloat, the platform has diagonal trusses to increase the stiffness of the platform in torsion and heave plates to suppress the heave and pitch motions of the platform. Unlike the MIST platform, however, the WindFloat uses an active ballast system to move weight (in the form of ballast water) around the platform in order to keep the platform at even keel when the wind direction and thrust force from the turbine changes direction. As described in Sec. 2.5.4 the MIST platform is implemented with a Single Point Mooring (SPM) system in order to allow free yaw motion so that the proper yaw orientation can be obtained.

The wind turbines depicted in Fig. 4.1 are known as straight-bladed Darrieus (or H-type) VAWT. The blades on the red turbine are oriented such that it will spin clockwise, while they are reversed on the green turbine so that it will spin counter-clockwise, as shown in Fig. 4.2. The main advantage of straight blades are the ease of manufacturing and simplicity of design. Recently, the rise of computer-aided manufacturing has led to an increase in the complexity and size of HAWT blades. The straight-bladed VAWTs have horizontal struts in order to support the weight of the blades. The design of these struts is critical because they can decrease the efficiency of the turbine when the blades are in the downwind section. Other designs attach the blades to the central column in different ways and may use guy wires to support the column.

The 'connecting mechanism' mechanically connects the turbines so that they are forced to rotate in equal and opposite directions. That is, the angular displacement of one turbine is equal and opposite the displacement of the other. This feature is achieved through the use of gears, pulleys and a timing belt. Essentially, the turbines are both connected to the main timing belt. A timing belt is simply a chain or elastic band (like in many automotive drive trains) that connect a driving element to its driven counterpart. Here, however, one turbine is connected to this timing belt through a gear system, while the other is connected through a simple pulley system. Depending on the instantaneous aerodynamic torque one turbine may be 'driven' while the other is 'driving' or vice-versa. Since the single gear pair reverses the direction of rotation, the turbines rotate opposite to each other. Many other ideas were considered for connecting the turbines in such a way, but we believe this method is a simple, reliable way. The belts and gears increase the frictional force between the turbines and platform, which reduces the power available in the generators. The generators are also shown in Fig. 4.1 and are connected to the turbines through gearboxes. The planetary gearboxes used in the experimental model were used to increase the rotational speed of the shafts so that the generators could operate near their optimal efficiency. In the prototype-scale platform, the gearboxes may not be necessary and instead, a 'direct-drive' power generation system may be possible. In Chapter 5, we show how the choice of gear ratio has a huge impact on the control of the platform orientation.

The mooring system for this platform is relatively simple: three wire ropes connect each column of the platform to a universal joint. The universal joint allows the platform to rotate without effecting the main anchor line. For the prototype-scale platform, where electrical

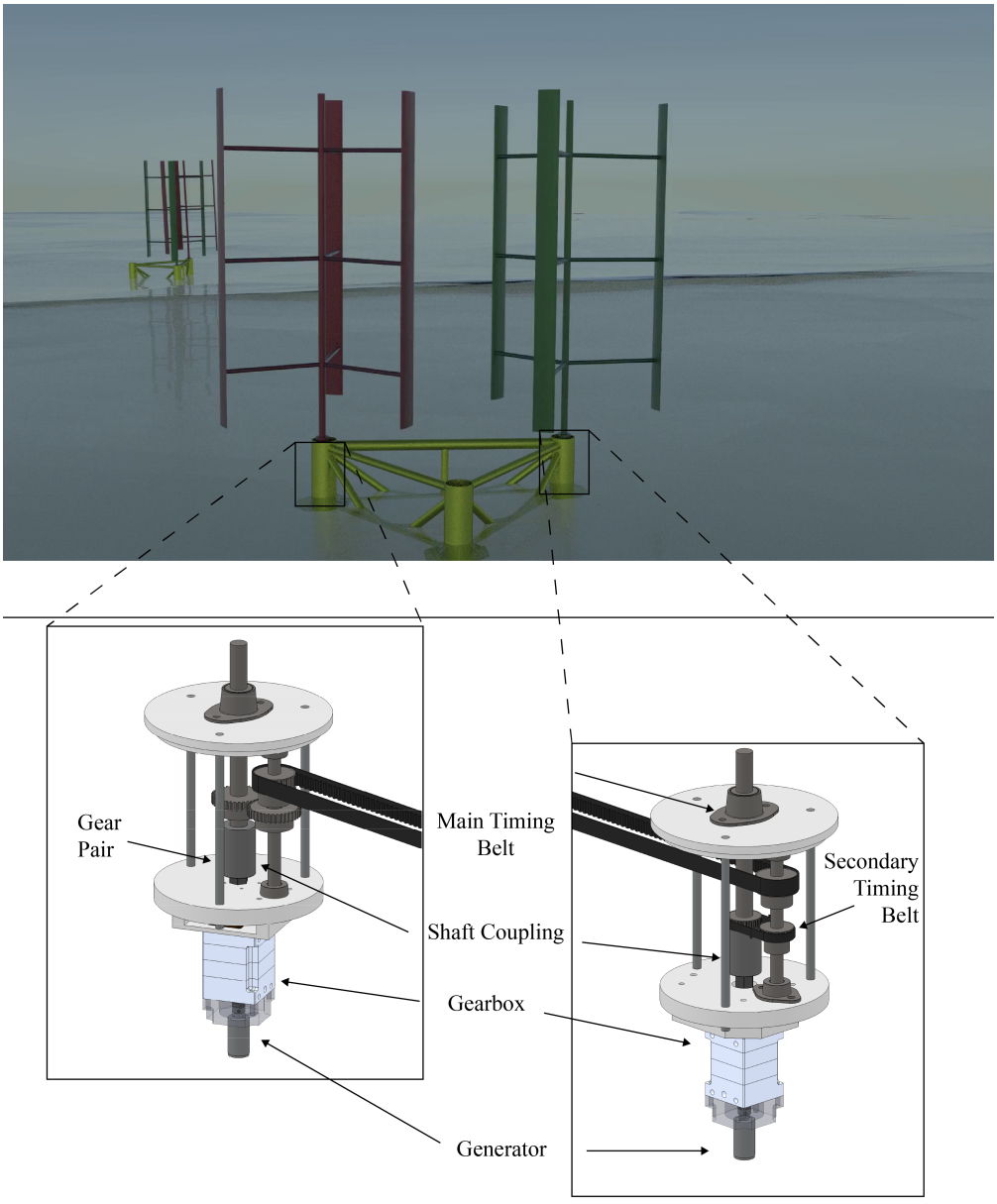

Figure 4.1: Computer-aided drawing of MIST platform, with details of the connecting mechanism shown in greater detail in the inset figures.

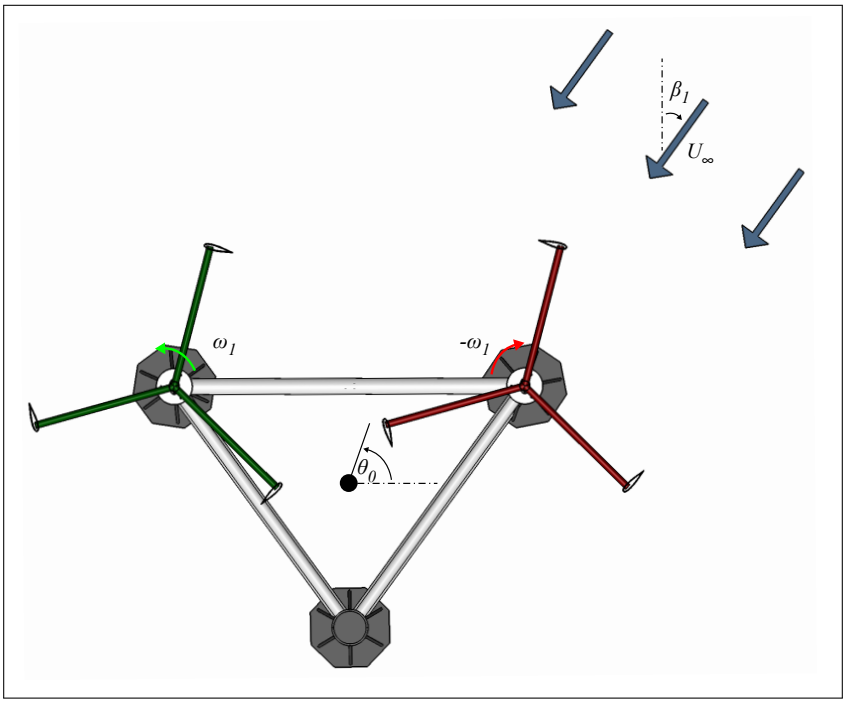

Figure 4.2: Computer-aided drawing of MIST platform, in plan view with the incident wind, turbine rotation speed and platform orientation.

power will be exported, the electrical umbilical will also need to be connected to the platform in such a way that can allow free rotation of the platform, probably through the use of slip rings. However, these types of connections are quite common now, especially in the turret systems of FPSOs, which can rotate in order to position themselves above the drilling well or to prevent large loads on the structure. The turret system can be designed for the harsh, offshore environment since all bearings and electrical connections can be housed above the sea level in watertight compartments.

The goals of the testing were as follows:

1. Under various relative wave-heading and wave-amplitude conditions, demonstrate that the yaw orientation of the platform can be controlled simply by changing the power absorbed in the generators.

2. Demonstrate that hybrid testing can be used to simulate the periodicity and magnitude of the aerodynamic torque on a vertical-axis wind turbine.

3. Determine the effect of the vertical center of gravity of the turbines on the platform motion.

The achievement of these goals is discussed in Sec. 4.6. Sections 4.2-4.5 are dedicated to describing the components of the model platform.

4.2 Physical Model

A physical model of the MIST platform was built in order to test the hypothesis that simply by modifying the parameters of the electrical generators, we can control the platform orientation as well as the turbine rotation rate to maximize the power absorbed by the turbines. In order to prove this concept, the control system needs to perform adequately in a variety of realistic environmental conditions, such as different sea states and wind conditions. In this section, we describe the physical model that was built and tested at $\lambda_m = 1/82.3$ so that other researchers can use the lessons learned from this testing campaign when designing their own experimental tests. Though clearly not exhaustive, we seek to highlight the interesting products used in this study to help future researchers with their own applications by using bullet points for quick reference.

It should be noted that a lot of the decisions regarding the manufacturer, model and material choices were made with cost and turnaround time as the main priorities. Thus, many parts were machined with the help of undergraduate researchers (namely, S. Paiva). The decisions made herein can be debated, but the total cost of the platform and all related components was around $3,000. For more details on the cost of the wind-input generators, see [1].

The main components of the MIST platform that was constructed for this study are shown and labeled accordingly in Fig. 4.3.

The components in Fig. 4.3 are:

1. Heave plates to reduce heave, pitch and roll motions
2. LiPo Batteries to power microprocessors, sensors and wireless modules
3. Microprocessor to control generators and send signals to and from other microprocessors
4. MIST Platform
5. Generator circuits including LEDs to indicate power production of generators
6. Generators with planetary gearbox (located inside columns 1 and 2)
7. Wind Input Generators (acting as Vertical-Axis Wind Turbines)
8. Motor/Propeller units to actuate the 'turbines'

The particulars of the full-scale platform are shown in Table 4.1. Clearly the column-to-column distance is much larger than the current semi-submersible platforms considered for single HAWTs. For instance, the newest generation of the WindFloat platform that can support at least a 6 MW turbine has a column spacing of around 50m[1]. However, the column spacing on the MIST platform is largely driven by the minimum VAWT turbine

[1]Personal communication with Dr. D. Roddier

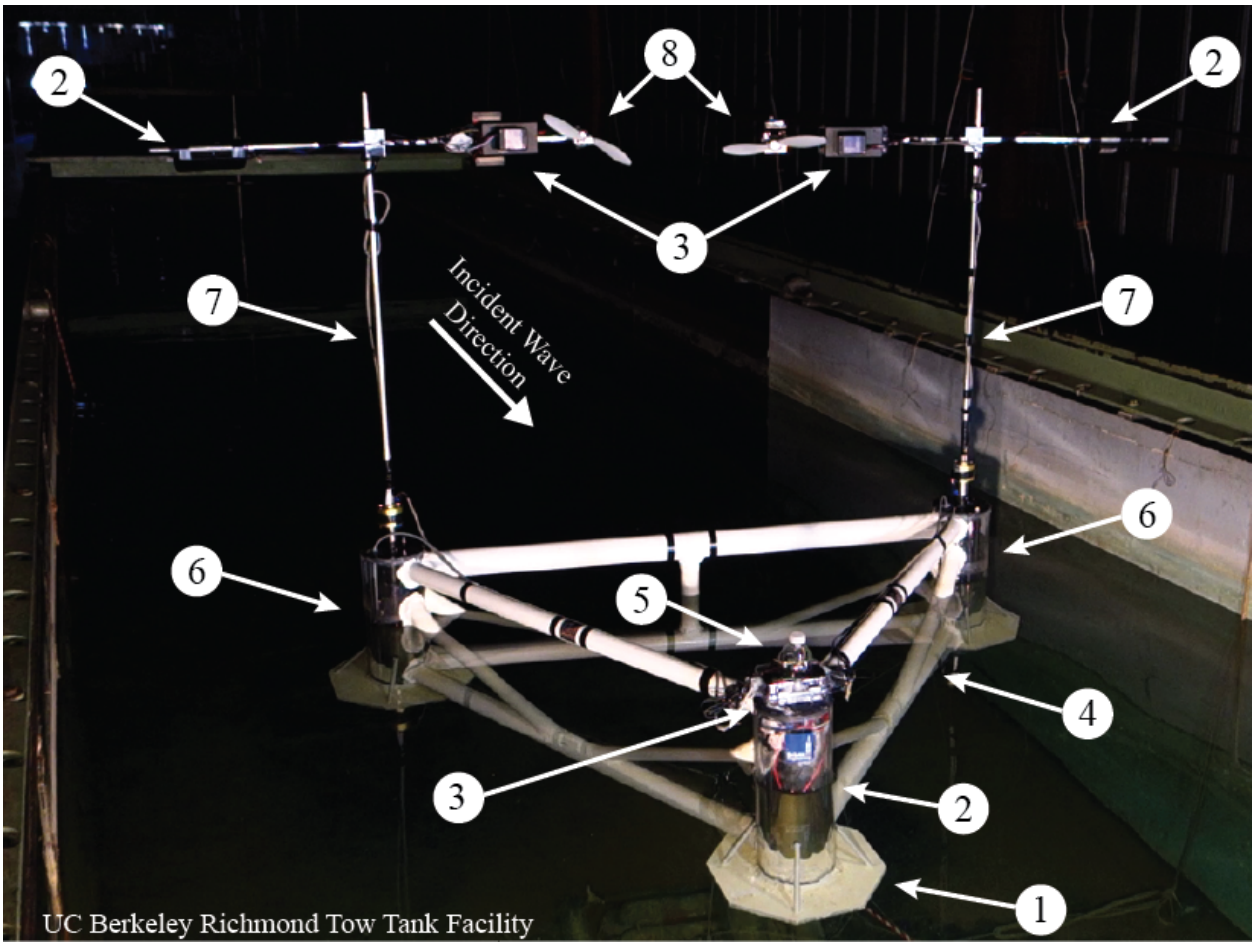

Figure 4.3: Main components of hybrid testing MIST platform, at 1:82.3 scale, labeled by number, in the UC Berkeley Physical-Model Testing Facility.

spacing that will still produce a large synergistic effect. In [4] the turbine spacing $D/2R$ is 1.6. We showed in the CFD simulations in Chapter 3, however, that this spacing can be reduced without reducing the synergistic effect of the turbines. The distance may be able to reduced down to 1.2, though experimental data would be needed to verify this claim. Perhaps the planform area of the platform could be drastically reduced, especially using connected turbines that are overlapping, (much like a Chinook tandem rotor helicopter, see discussion in Chapter 6 and Fig. 6.1).

The particulars of the full-scale turbine considered in this study are shown in Table 4.2. The centers of gravity and draft are defined relative to the final waterline position (after pretension of the mooring lines), and the mass moments of inertia I_j are defined relative to the axis of rotation of the body. The mass properties of the turbine tower were informed by the 5 MW NREL offshore HAWT turbine described in [106]. The yaw mass moment of inertia of the platform includes the effect of the mass of the drivetrain system. Most of the values for this 5 MW rotor are within 10-20% of the 5MW conceptual VAWT designed in [107], except for the rotor inertia (about 50% too low). However, the inertia in the drivetrain

Parameter	Value	Unit
λ_m	1/82.3	-
$2a$	11.5	m
R_{12}	111.5	m
R_{23}, R_{13}	89.2 ($0.8 \cdot R_{12}$)	m
h	123	m
$h - d$	30	m
COG_z	-13.5	m
I_b	34.7	t-km^2
m_b	12.9E3	t

Table 4.1: Geometry and particulars of the full-scale platform (including embedded drivetrain system and ballast) considered in this study. See Figures 2.4 and 2.11 for definitions of geometric variables.

Parameter	Value	Unit
c	6.0	m
R	42.9	m
$\bar{D}$	1.3	-
λ	3.5-5.0	-
N_b	2	-
H	146	m
m_{vawt}	1.08E3	t
COG_z	74.6	m
I_r	0.46	t-km^2
U_{rated}	11.4	m/s
C_p	0.36	-
P_{rated}	5.0	MW

Table 4.2: Geometry of the full-scale VAWT considered in this study. See Figures 3.1, 3.22, and 1.2 for definitions of geometric variables for counter-rotating turbines.

was not taken into account (planetary gearboxes, spur gears, etc), which drastically increases the inertia of the spinning turbines.

4.2.1 Construction of Platform

The platform was constructed of PVC and clear acrylic pipe:

- Acrylic pipe: 5.5" OD, 1/4" thickness, (McMaster-Carr)
- PVC Pipe: Schedule 40, Sizes 2 and 3, (McMaster-Carr)
- PVC Plate, 3x 12"x12"x1/2", (McMaster-Carr)

The clear acrylic pipe was chosen so that the drivetrain inside the sealed platform could be monitored and troubleshooted if necessary. The 5.5" acrylic pipe was machined into 3 equal sections of length 20". The Schedule 40 PVC pipes formed the trusses of the platform. The bottom horizontal members were of size pipe 3 (2-3/8" OD). The rest of the trusses were size pipe 2 (1-2/3" OD), except for the horizontal member housing the timing belt, which was

size pipe 3. The ends of the trusses were cut using a circle saw whose diameter was equivalent to the mating PVC pipe diameter. Due to the brittle nature of PVC, the diagonal trusses were the most difficult to form. Nearly 6 attempts to machine the trusses on a mill resulted in fractured or chipped pipes that were discarded. The heave plates were 1/2" PVC plates cut in an octagonal shape with diagonal connecting rods of 3/8". All joints were chemically welded together with JB-Weld (an epoxy that chemically bonds the mating materials), and were allowed to set for over 24 hours before sealing and painting. The joints were then sealed with 3M Marine Sealant and then painted with a marine paint. The chemical weld and the sealant worked extremely well and no leaks were ever detected for the 4 months the platform was in the water.

4.2.2 Mooring System

A schematic of the mooring system is shown in Fig. 2.5. The most critical portion of the mooring system is the universal joint that allows the platform to spin freely. This joint consists of two shackles that spin independently. A stainless steel universal joint was purchased from a local marine supply store. Wire rope was used to attach each heave plate to the universal joint. The wire rope was bent around a thimble and clamped down with wire rope clips as suggested in Ref. [108]. The other components of the mooring system are listed below.

- Wire Rope: 7x7 strand core, 1/8" diameter (McMaster-Carr)
- Wire Rope Clip: Type 304 stainless steel for 1/8" rope diameter (McMaster-Carr)
- Wire Rope Thimble: Type 304 stainless steel for 1/8" rope diameter (McMaster-Carr)
- Rope Pulley: Stainless steel (Local marine supply shop)
- Universal joint: Stainless steel (Local marine supply shop)
- Polypropylene rope: 3/8" thick (Home Depot)

4.2.3 Drivetrain and Generators

The drivetrain consists of a nearly identical pair of generators and gearboxes connected by a timing belt and is shown in the bottom of Fig. 4.1. On the left column the generator and gearbox are connected to the main timing belt through a gear pair, while on the left column it is through a secondary timing belt. In this way, the generators and the turbines are forced to rotate in opposite directions, while keeping the setup of the system relatively symmetric. Thus, even if the turbines have an asymmetric applied torque, both turbines and generators will spin at the same speed. After much consideration, a high-quality brush DC Motor from Portescap was chosen to act as a generator. Communicating with engineers at this company confirmed that it was suitable for power generation (< 5W). Furthermore, it

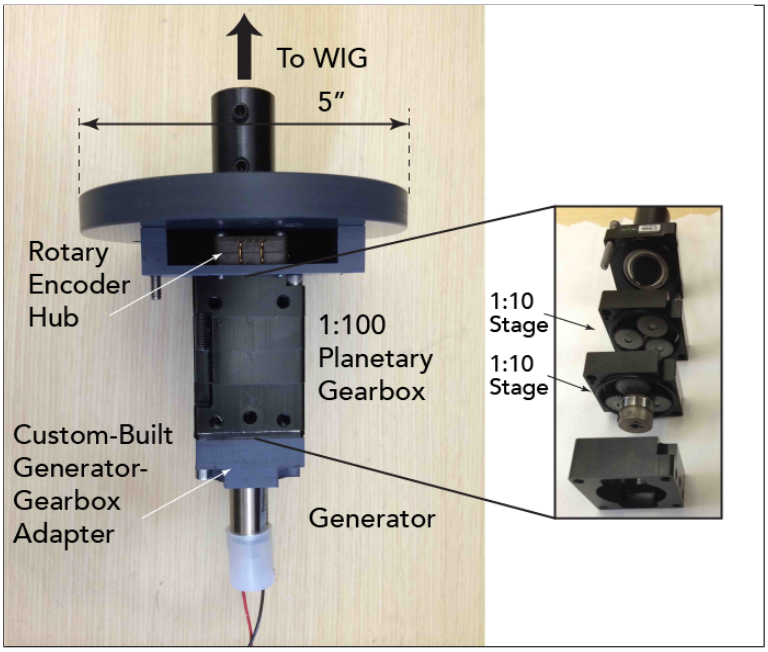

Figure 4.4: Pictures of generator and planetary gearbox that was used for drivetrain system.

was readily available from the supplier DigiKey[2] for a reasonable price. However, a gearbox was purchased separately in order to step up the speed of the motor/generator closer to its optimal operating conditions. A custom built adapter (machined from PVC) shown in Fig. 4.4 was used to link the motor and the gearbox. It was evident that the gearbox was extremely more efficient when used on its side (as shown in Fig. 4.4) than upright (as oriented once inside the column). Gravity caused the stages to bump against the bottom of the frame, resulting in increased friction. We attempted to change the length of the adapter to reduce the friction, but it was not successful. In retrospect, it may have been better to go with the motor/gearboxes we were considering at first from Maxon Motors[3]. After placing the order, the company installs the gearbox directly on to the motor at the factory. In the end, we did not go with this option due to cost and turnaround time (delivery approximately 2 months after the initial order). Other options were pursued in the initial design phase including slip-clutches and magnetic particle brakes from Stock-Drive Products[4]. However, we decided a visual cue of the damping provided by the dampers was important and also allowed for more realistic simulation. Furthermore these types of control strategies have been proposed for parking VAWTs [109]. Pictures of the actual generator and gearbox used are shown in Fig. 4.4. The components of this sub-assembly are:

- Athlonix Portescap Motor, 6V, 0.64V/1000 rpm, 16N78212P1001
- VEX Robotics VersaPlanetary Gearbox, 2x1:10 stages

[2] www.digikey.com
[3] www.maxonmotorusa.com
[4] www.sdp-si.com

The 1:100 gearbox was chosen since the target rotational speed of the turbines was around 100 rpm. Thus, the generators would produce a voltage near its nominal voltage during the operational conditions. The sensors, including the optical encoder and current sensors will be discussed in Sec. 4.3.1.

Dry Testing of Drivetrain

The dry testing of the frictional loss of the drivetrain system consisted of four stages, each depicted in a different panel in Fig. 4.5. The stages of the testing were:

1. Motor-Generator Set ($M \rightarrow G$) to determine the coil losses in the generators
2. Motor-Gearbox-Gearbox-Generator Set ($M \rightarrow Gb \rightarrow Gb \rightarrow G$) to determine the losses in the planetary gearboxes
3. Motor-Gearbox-Gearbox-Generator Set with a solid-state relay to determine the resistive nature of the relay
4. Motor-Gearbox-Timing Belt-Gearbox-Generator Set ($M \rightarrow Gb \rightarrow Dt \rightarrow Gb \rightarrow G$) to determine the frictional losses in the belts and gears.

The losses for each additional element in the drivetrain system are shown in Table 4.3. The

Source	%
P_{coil}	15
P_{gb}	10
P_{dt}	10

Table 4.3: Summary table of power losses in drivetrain

solid-state relay will be discussed further in Sec. 4.4.

4.3 Implementation of Hybrid Simulation Technique

The hybrid simulation technique combines experimental and computational techniques to maximize the accuracy of the tests given the physical constraints of model testing. Historically, this technique has been used in earthquake engineering, as described in [110]. The linear motion of the earthquake is easier to model using theory and actuators, while the nonlinear response of the structure can be studied experimentally. At first, this type of technique was only used in open-control scenarios where the displacements (of the ground, for instance) were known a-priori and the response of the model was studied. More recently,

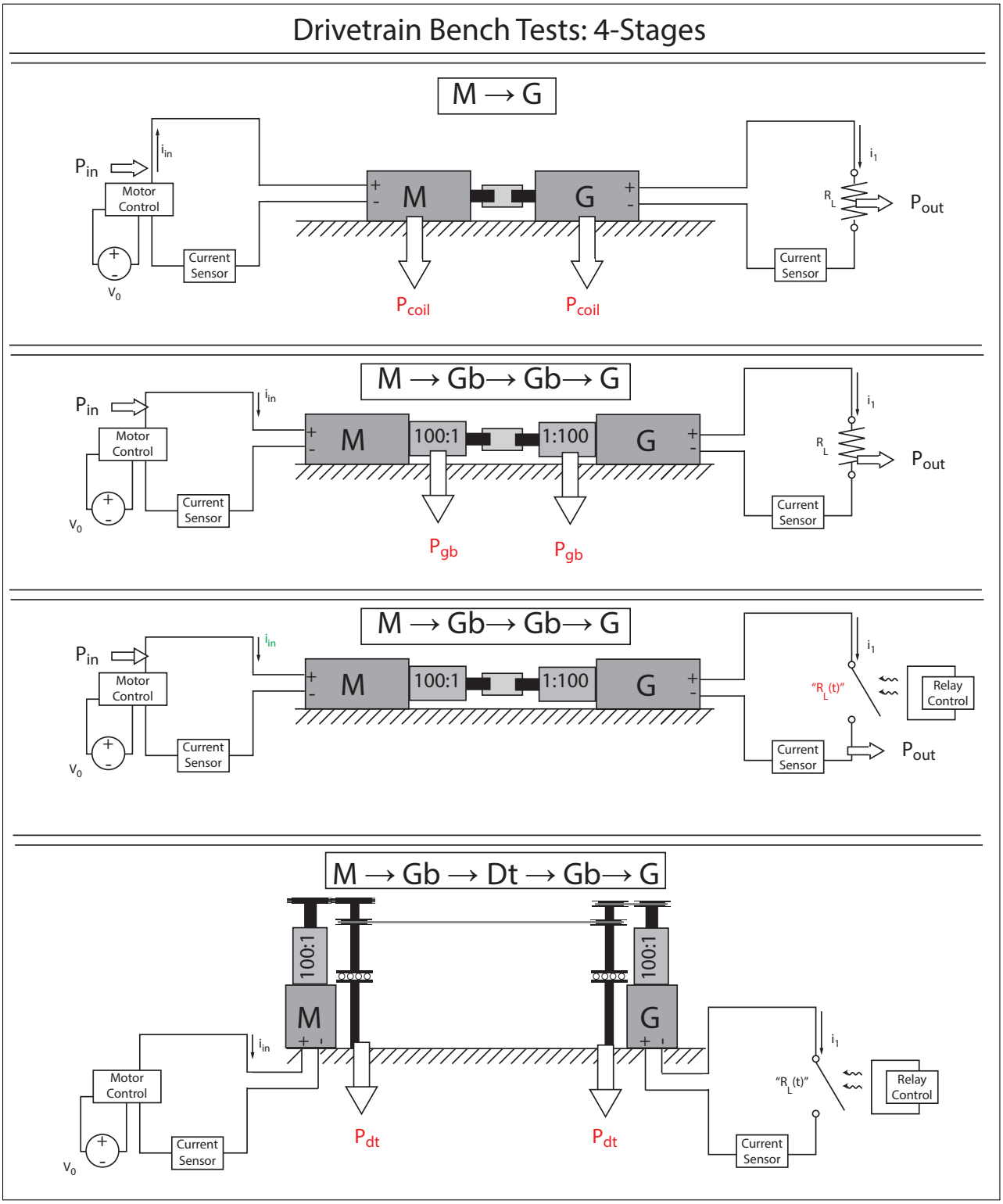

Figure 4.5: Four stages of 'dry testing' for drivetrain, with downward white arrows showing power losses.

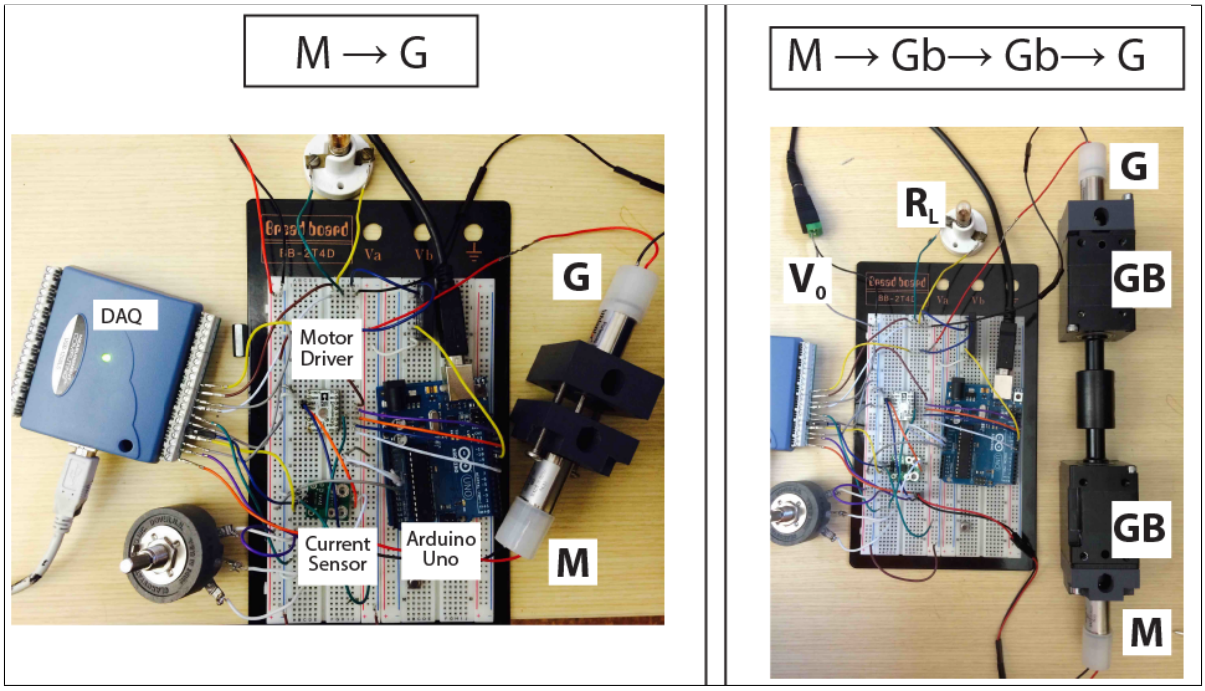

Figure 4.6: First two stages of drivetrain 'dry testing' setup.

however, these experiments have been extended to 'real-time' hybrid simulations where the response of the model is (nearly) instantaneously analyzed and fed back into the actuator controller. In the field of ocean engineering, Hall et al. [16] showed that for a floating platform with a wind turbine, large displacements can occur on many different time scales on account of the fluid and structural dynamics. These phenomena make it challenging for an actuator to be flexible enough to comply with large displacements but rigid enough to respond over short time-scales. Thus, for the hybrid simulation of the MIST platform, these challenges are circumvented by actuating only the critical forces with respect to operation of the platform.

In the experimental setup used for hybrid testing of the MIST platform, the physical model is the floating platform, which is tested in a wave tank. The effect of the wind turbines on the platform are simulated by actuators, known as Wind-Input Generators (WIGs), which are described in further detail in Sec. 4.3.3. Thus, part of the simulation is done in the 'physical world', while another part of the simulation is performed computationally (either a-priori or in real-time), as depicted in Fig. 4.7.

The goal of the hybrid simulations is to seamlessly the missing piece of the physical model with actuators that can accurately mimic the necessary physics of the system. When implementing this type of technique, the choice of the type of the actuator is critical so that it can respond in the necessary amount of time (known as the latency of the system) with adequate force without negatively altering the dynamics of the system. This challenge was described in detail in [16], who showed that, without sacrificing accuracy, it appeared nearly impossible to mimic the entire turbine with current technology. This strict requirement was

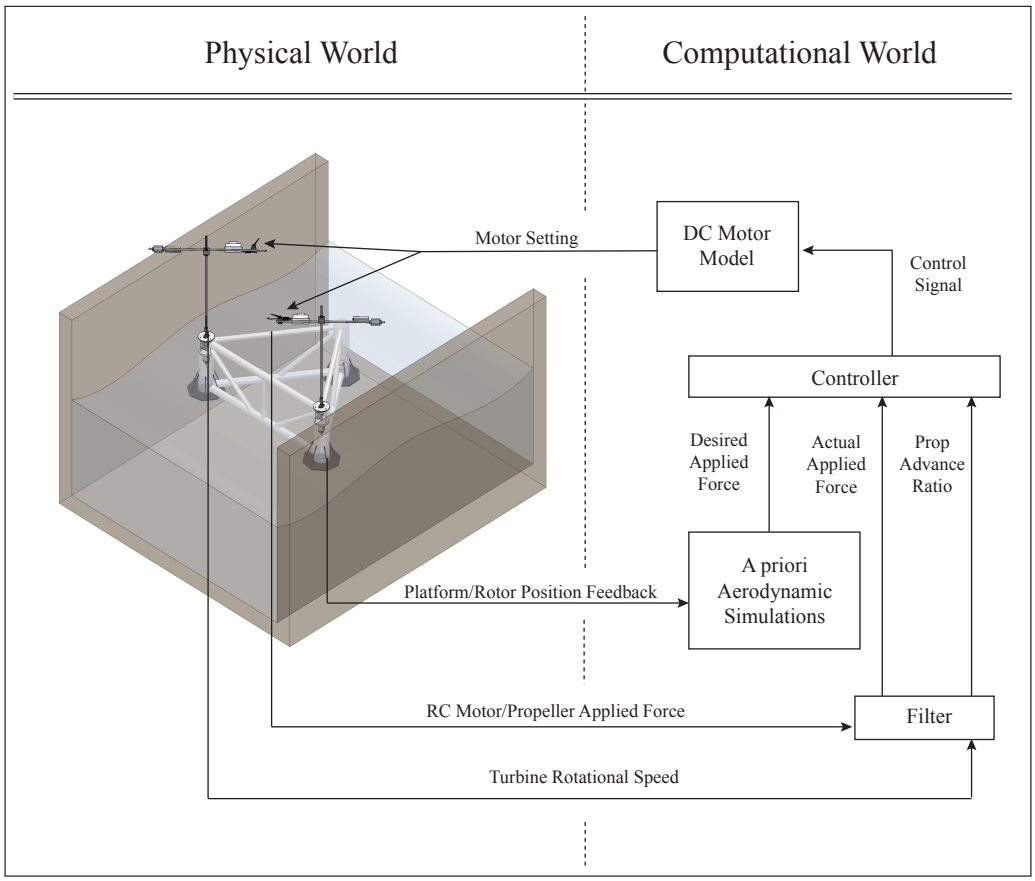

Figure 4.7: Schematic of hybrid simulation testing technique for MIST platform, with experimental model in the 'physical world' and aerodynamic simulations performed in 'computational world'.

partly due to the fact that actuator frame has to be mounted to the earth frame while the actuator, itself, needs to be connected to the platform. Here, however, we can mount the actuator, which is a remote-controlled plane motor/propeller, directly to the model. When powered, the motor applies a torque to the model, which causes the model to pitch and roll. However, the pitch and roll moment from the incident waves is generally orders of magnitude higher than this artificially applied moment. Thus, unlike the actuator proposed in [16], which must be able to traverse a relatively large distance (equivalent to the global motions of the platform in waves), but still have an extremely accurate position sensor, the motor simply needs to respond to a control signal based on the circumferential position of the turbine. In this way, we relax the requirements of the actuator but we restrict our hybrid simulation to only actuating in one degree-of-freedom (DOF). The motor/propeller actuator only applies a force in the tangential direction of the 'blade' as depicted by the vectors F_1 and F_2 in Fig. 4.8. Therefore, we neglect the aerodynamic force in the normal direction, which is significant for the structural design of the turbine, but not for the power production.

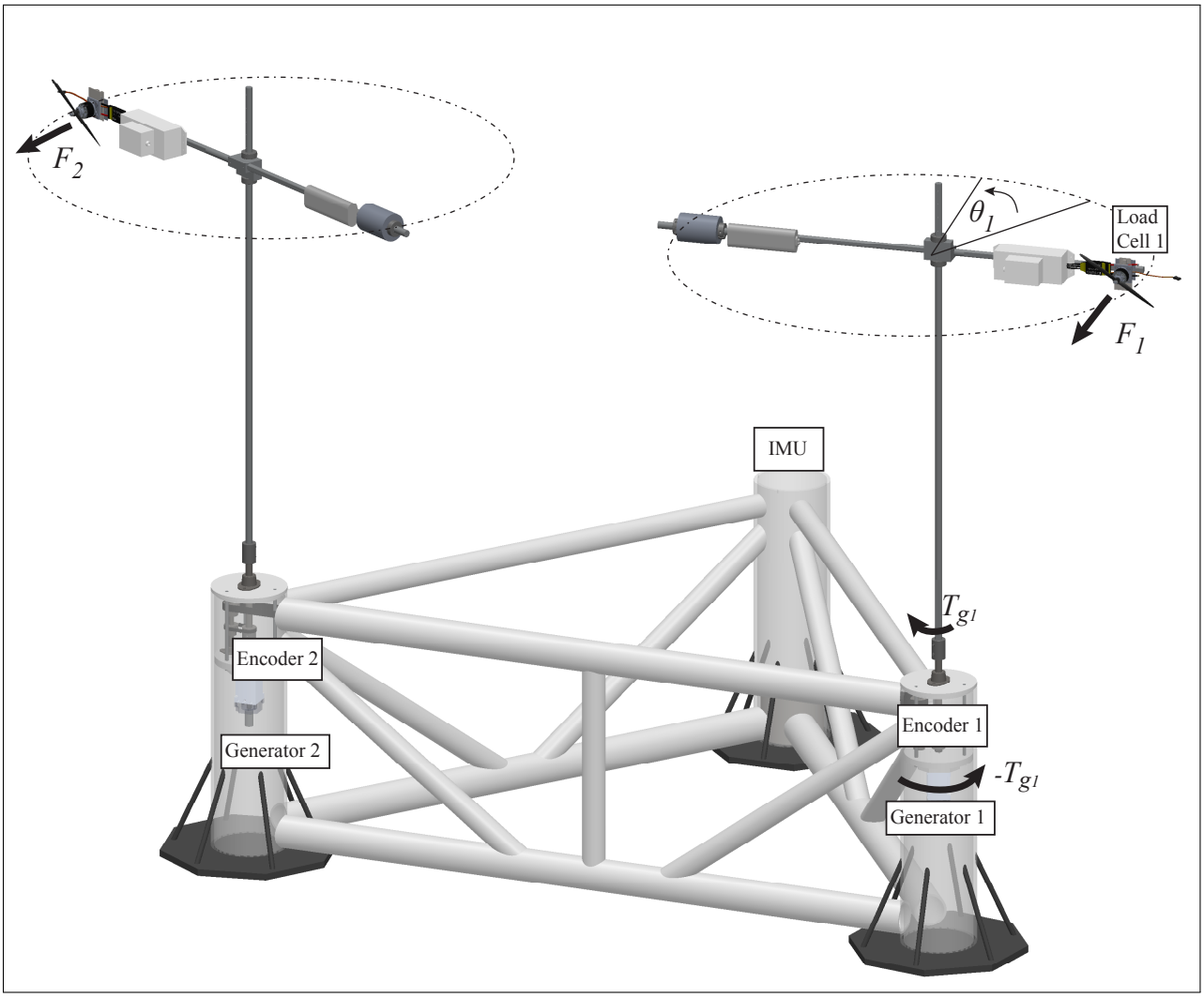

Figure 4.8: Schematic of sensors and actuators on the MIST platform.

4.3.1 Sensors and Actuators

The MIST platform employed a host of sensors and actuators as well as microprocessors in order to implement the hybrid simulation technique. The main components of the system are shown in Fig. 4.8. Two rotary encoders were used:

- US Digital Hubwheel, attached rigidly to the rotating shaft, HUBDISK-2-500-500-NE
- US Digital Optical Encoder Module, fixed to the platform, EM-2-500-N

They were rigidly attached to the columns of the 'turbines' inside the sealed columns. Theoretically, by attaching two rotary encoders with outputs EN_j to the system, the position

of the platform and the 'turbines' could be found by the following equations,

$$EN_1 = \theta_1 - \theta_0 \tag{4.1a}$$
$$EN_2 = \theta_2 - \theta_0, \tag{4.1b}$$

where θ_0 is the total yaw displacement of the platform, taking into account the slow-drift motions and the wave-induced oscillatory motions. Since $\theta_1 = -\theta_2$ because of the drivetrain, the angular displacement of the platform and the turbines are

$$\theta_1 = \frac{EN_1 - EN_2}{2} \tag{4.2a}$$
$$\theta_0 = -\frac{EN_1 + EN_2}{2} \tag{4.2b}$$

In practice, however, the encoders had too high a resolution (500 counts per revolution for the rotor that was operating near 100 rpm) for the microprocessor to capture every single on/off signal. Thus, small inaccuracies in the angular measurement of the rotor compounded and resulted in large errors in the position of the platform. The measurement of the speed of the turbines was relatively unaffected by these smaller errors in position, especially after taking a running average of the speed over a second. An inertial measurement unit (IMU), which uses an accelerometer, a gyrometer and a magnetometer was installed on third column to measure the absolute yaw angle of the platform (as well as pitch and roll motions).

4.3.2 Angular Position Measurement

A '9DOF' sensor stick (SEN-10724) was purchased from SparkFun Electronics[5] in order to measure the yaw, pitch and roll of the platform. This IMU, shown in Fig. 4.9 had three different sensors embedded in the small chip:

- Accelerometer: Analog Devices 3-axis digital accelerometer (up to 16g), ADXL345
- Gyrometer: InvenSense 3-axis angular rate sensor (14.375 LSBs per °/sec), ITG-3200
- Magnetometer: Honeywell 3-axis magnetoresitive sensor (1-2○ accuracy), HMC5883L

The IMU was located underneath the cap of column 3, as shown in Fig. 4.9. An open-source code[6], known as an altitude, heading and reference system (AHRS) was written by Peter Bartz, from TU Berlin using the formulation of [111] for an Arduino microprocessor in order to calibrate the sensors as well as obtain an accurate measurement of the yaw, pitch, and roll from the sensors. The code is based on the directional cosine matrix theory that was described in [112]. Essentially, the code uses the gyrometer data to detect the pitch and roll velocity of the sensor. When errors begin to accumulate on account of gyrometer drift as well as time integration, data from the accelerometer (for the pitch and roll) and

[5] www.sparkfun.com
[6] https://github.com/ptrbrtz/razor-9dof-ahrs

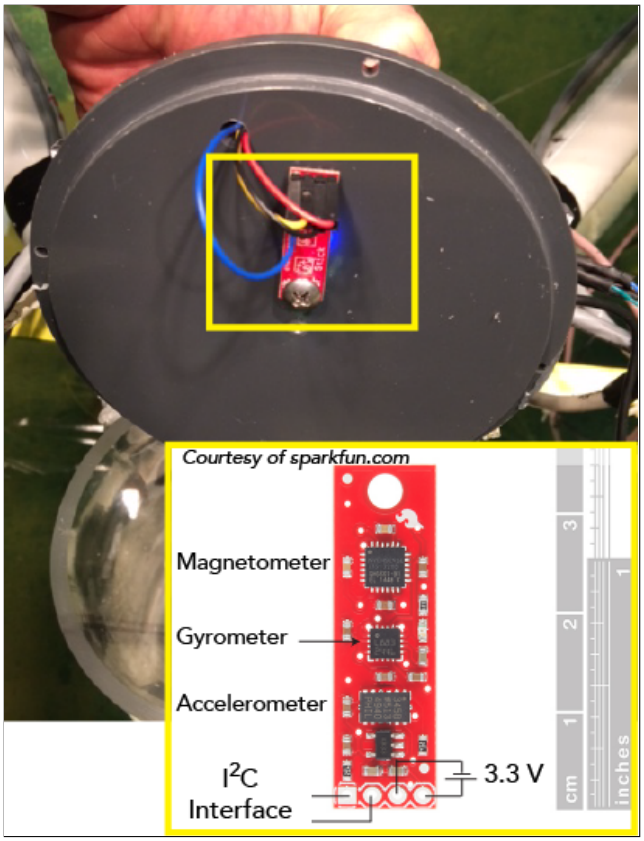

Figure 4.9: Picture of IMU located below the cap of column 3 on MIST platform along with detailed view of sensor stick.

the magnetometer (for yaw) can dissipate the errors by utilizing a PI controller. Because of the recent exponential growth in the interest of recreational and commercial unmanned aerial vehicles (UAVs), the cost of these types of sensors has dropped while the accuracy has increased.

4.3.3 Actuation: Wind-Input Generators [1]

The first of the two Wind-Input Generators (WIGs) were built by Elena Koukina for her M.S. project, which concerned the closed-loop control of these actuators. The WIG consisted of two 1/2" aluminum rods connected in a 'T' with block that allowed the vertical height of the horizontal member to be changed. At one of the end of the horizontal members was a motor that was rigidly attached. The necessary components for this assembly:

- Motor: Turnigy Aerodrive SK3 - 3530, 1150 rpm/V, 28T Brushless Outrunner
- Propeller: 9" Diameter x 4.7" Pitch
- Electronic Speed Controller, Afro ESC, 30 Amp
- Lithium-Polymer Battery, 20C, 3S, 11.1V 6400mAh

In her work, Koukina [113] details the load cell and the seventh-order filtering technique used to obtain reliable measurements for the thrust force from the motor/propeller unit. The load cell was simply extracted from a kitchen scale with 0.01g precision. Further, in her M.S. Thesis [1], she details how to upload open-source software to the ESC so that the motor can be controlled by a pulse-width modulated signal from an Arduino using built-in (Servo motor) libraries. The reader is referred to this document for further information.

The instantaneous force applied by the WIG should follow the tangential force curves developed in Chapter 3 (and shown in Figs 3.15-3.20, for an isolated turbine). Obviously, these simulations were performed at much lower Reynolds number than a full-scale turbine, due to limitations of the present numerical method described in Chapter 3. However, publicly released data from large-scale VAWTs, such as the Sandia 34m turbine in [6] show a similar variation of the thrust force and C_p. In fact, the maximum C_p can be found at $\lambda = 6.0$ and is around 0.40, which is promising for the commercialization of VAWTs. In the experiments

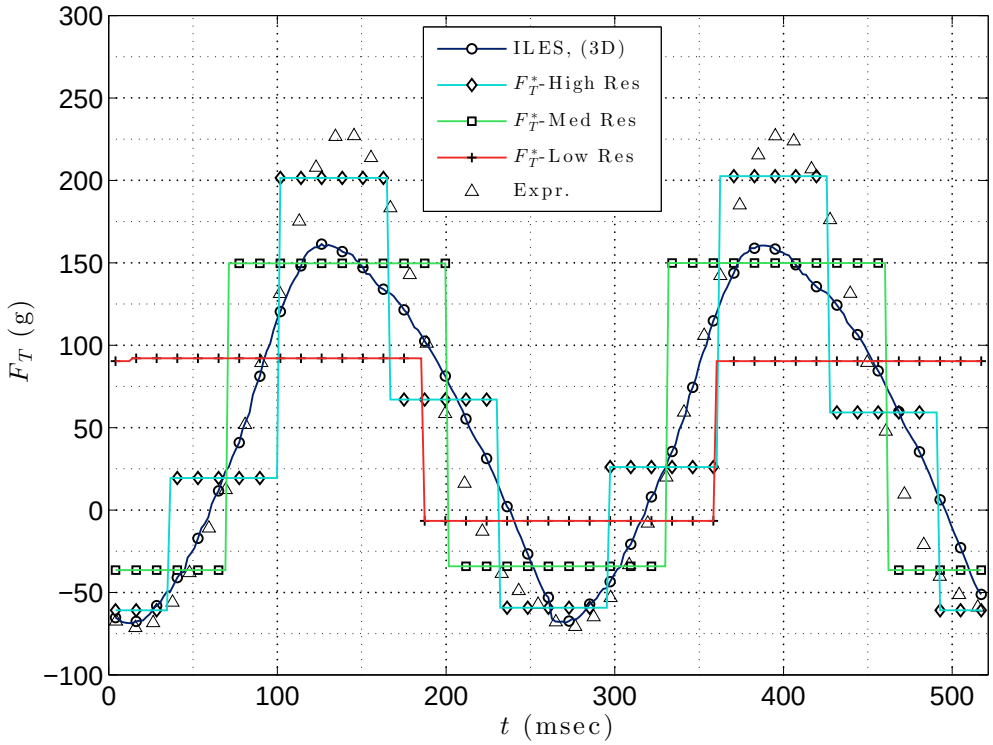

Figure 4.10: Instantaneous tangential force the actuators should apply depending on the desired resolution for one revolution (λ = 3.5). CFD simulations (ILES) are for λ =5.0, $\alpha_0 = -2°$.

we attempted to meet the 'Medium' resolution curve in Fig. 4.10, which was near the limits of the hardware used in the study. In order to get the major effect of the turbines on the platform, the torque should exhibit a number of peaks per revolution equal to the number of blades (which was 2 in this case). This frequency is achieved in the implemented control algorithm shown in Algorithm 2.

4.3.4 Microprocessors

Microprocessors are widely used in control settings to analyze the output of various sensors, perform certain calculations and send signals or data to actuators or other microprocessors. In modern microprocessors, communication among the sensors, actuators and user(s) can occur with different analog and digital protocols, including analog voltages, two-wire interfaces (TWI), such as Serial Peripheral Interface (SPI) or Inter-integrated Circuit (I^2C), or even wireless protocols such as the IEEE 802.15.4. The recent 'Maker' movement has led to a proliferation of inexpensive, easy-to-use microprocessors, such as the Arduino and Raspberry Pi products. Generally, an algorithm is written in a computer language, such as C++, uploaded to the microprocessor. Once the microprocessor is provided with adequate power, it will continually loop through the algorithm until the power is removed. Since the authors had prior experience using Arduino microprocessors for data acquisition, control and communication operations, it was decided to continue using this line of products.

The microprocessors used in this study were the Arduino *Due*s because of the large number of analog inputs that was required of the 'Master'. However, many libraries were not updated for the ARM-based flash microcontroller (MCU) since the *Due* was released in 2012. The Xbee wireless modules required multiple Serial ports, which were available on this board. Once we decided to go with the *Due* for the 'Master' controller, we decided it was apt to make all of four of our MCUs identical.

- Arduino Due: ATMEL SAM3X MCU, 2x256 kbFlash-based memory, 84 MHz

In this report, we interchange 'Arduino', 'Microprocessor' and *Due* freely. The circuits connected to the 'Master' MCU are shown in Fig. 4.11. A picture of the actual breadboard on top of the Arduino, inside of the waterproof container, which is affixed to the top of column 3, is shown in Fig. 4.12.

4.4 Control Implementation

Two main control schemes were implemented on the MIST platform. The first concerns the application of the thrust force by the WIGs, while the second concerns the strategies to regulate the 'turbine' speed as well as the platform yaw orientation. Both of these control algorithms are shown in Fig. 4.13.

4.4.1 Wind-Input Generator Control

The control strategy that concerns the application of a desired thrust force (and hence, torque) by the WIGs is discussed in greater detail in [1] but we will highlight some of the challenges and successes in this section. It is well known that the thrust force supplied by a motor and propeller not only depends on the particulars of the motor and propeller and the power supplied to the motor, but also the advance ratio of the propeller. In the current study, the advance ratio of the propeller is proportional to the rotational speed of the WIGs.

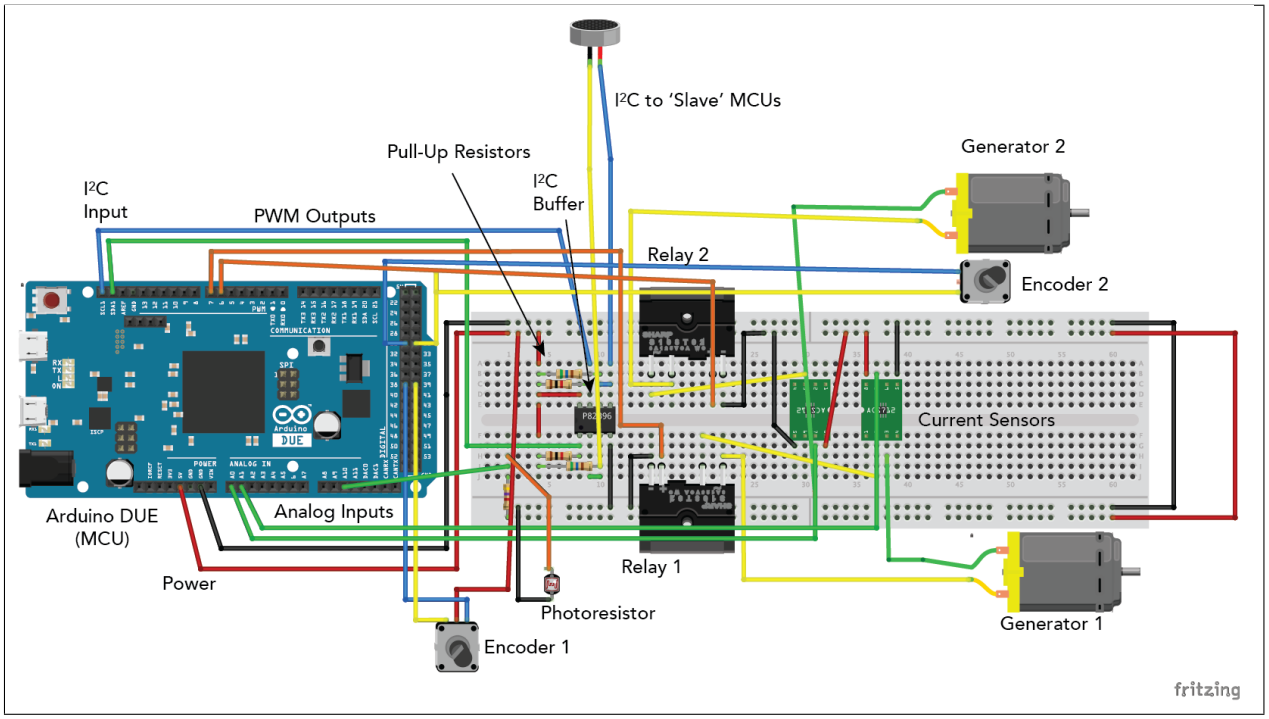

Figure 4.11: Schematic showing wiring of 'Master' MCU, including inputs and outputs, I^2C, relays and generators.

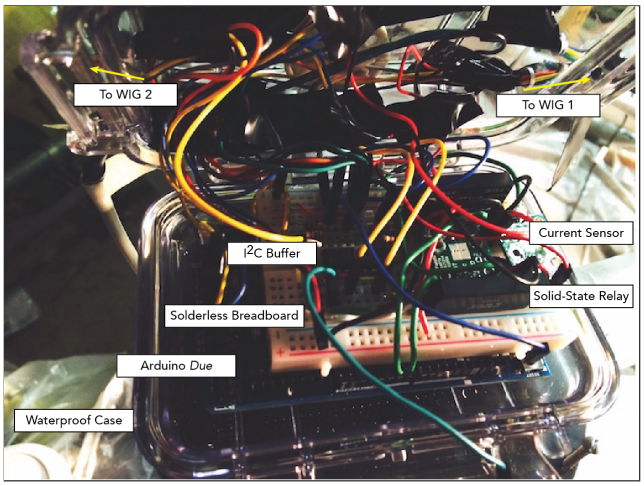

Figure 4.12: Breadboard on top of 'Master' MCU, both of which are housed inside of a waterproof casing on top of Column 3.

That is, the faster the WIGs spin, the less thrust force produced by the motor/propeller for a given motor setting. Ideally, the control algorithm for the WIGs would be the one shown in Algorithm 1. In practice, however the latency of the system made it such that the last step was not possible. Furthermore, the effect of the orientation of the turbines relative to the 'incident wind' was not taken into account. This effect was not taken into account

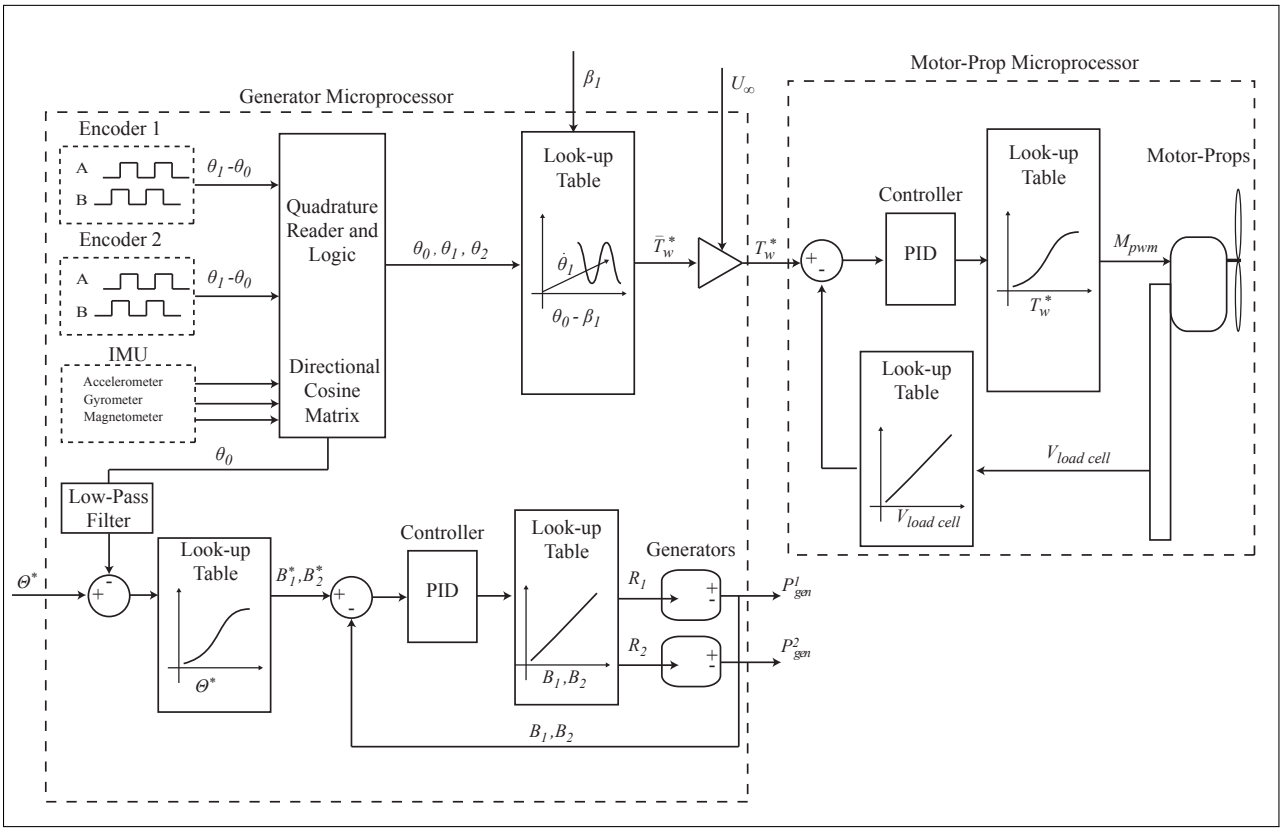

Figure 4.13: Diagram of control strategy for platform orientation and hybrid simulation technique.

Algorithm 1 Ideal Desired Thrust Force Control from WIGs

```
while Simulation is occurring do
    Obtain the yaw heading of the platform, Θ_o
    Obtain the rotational speed of the turbines, ω_1
    Use a lookup table (i.e., Fig. 4.10) to determine desired force, F_T^*
    Based on calibration, determine the proper motor setting
    Measure the actual load applied, F_T
    if sufficient time exists then
        Run PID loop to reduce F_T^* − F_T
    end if
end while
```

partially because at the time of the experiments, the simulations of the counter-rotating turbines presented in Chapter 3 had not been completed. The only data for counter-rotating turbines based on wind direction was found in [4], but the asymmetry of the data seemed non-physical.

Practically, the large variations in the desired thrust force made it impossible to start the turbine spinning (much like a non self-starting turbine). Thus, when the turbine was first turned on a constant desired force was sent to the controller. Once the WIG reached its operating speed, the simulation was initiated (by the sending of waves down the wave tank) and the controller would receive a signal to start the oscillatory thrust.

Another issue that arose was the difference in voltages of the batteries supplying each of the motors. Unfortunately, E. Koukina only had time to build one WIG with a load cell that could measure the applied force before she graduated. Since all parts of the WIGs were identical, we hypothesized that if the settings of the two motors were the same, then they should produce the same force. In practice, we believe the LiPo batteries drained at slightly different rates, which caused the voltages of the batteries to vary. Future iterations of this technique should utilize a voltage regulator so that each of the motors receive the same power. Such an addition would simplify the control effort significantly. To get around this issue in these experiments, the motors were calibrated before each run by setting them to an equal value (with the generators turned off) and then slightly varying them until the yaw velocity of the platform settled to 0. In this way, there were three different states of the WIGs for startup, calibration and operation, respectively. The 'Master' Arduino received commands from the human operator at the base station, who then relayed the commands to the 'Slaves'. The algorithm for control of the thrust force that was implemented in the Arduino *Due* on the 'Slaves' is shown in Algorithm 2. In this way, the speed of the turbines was not controlled instantaneously, but the motor controls signal MTR was pre-determined after initial tests to a level that caused the turbines to rotate near the desired rotation rate.

4.4.2 Desired Heading Control

To control the platform yaw orientation, the power taken off from the generators can be varied to provide a differential torque on the platform. That is, the torque provided by the

Algorithm 2 Implemented Desired Thrust Force Control on 'Slave' Microprocessors

```
if TurbineState==Constant then
    Set motor to achieve desired force, with value MTR
else if TurbineState==Calibrate then
    if '+' signal received then
        MTR=MTR+1
    else if '-' signal received then
        MTR=MTR-1
    end if
else if TurbineState==Oscillatory then
    Obtain period of revolution T_rev from 'Master'
    if  mod (t, T_rev/2) < T_rev/4 then
        Set motor to 2·MTR
    else
        Set motor to OFF
    end if
end if
```

generator can be varied by changing the power-take-off resistance R_j in the circuit. For instance, if $R_j \to \infty$, no current will be produced in the circuit and hence no mechanical power will be converted into electrical power. On the other hand, if $R_j = 0$, the generator is shorted and the maximum current will be developed in circuit. The voltage developed in the circuit is directly proportional to the speed of rotation of the generator rotor. Thus the generator was chosen to operate at a speed near its operating voltage to ensure efficient electrical power generation. The resistance in the circuit was varied by using a solid-state relay that can open and close the circuit with a switch frequency up to 500 Hz as shown in Fig. 4.14.

The actual circuit employed in the tests is shown in the bottom of Fig. 4.14, as well as an approximation of the DC generator in the gray box. Here the voltage induced in the circuit is denoted as V_g, the terminal inductance is L_g and terminal resistance is R_g. Thus, the entire generator circuit is simply a voltage source with two resistors in series. From the specification sheet of the motor the rotor inductance is small (0.10 mH) and is ignored for this discussion. In order to relate the generator damping with the resistance of the circuit, the mechanical power is equated with the electrical power dissipated by the generator as,

$$P_j^{(mech)} = B_j(\gamma\dot{\theta}_j - \dot{\theta}_0)^2 \tag{4.3a}$$

$$P_j^{(elec)} = \frac{V_j^2}{R_g + R_j} = \frac{k_e^2(\gamma\dot{\theta}_j - \dot{\theta}_0)^2}{R_g + R_j} \text{ for } j = 1, 2 \tag{4.3b}$$

where k_e is the motor constant, which is dependent on the type of magnets, number of windings, number of poles, etc. Thus, from Eq. (4.3), the controllable rotary damping, $B_j(t)$ can easily be found as,

$$B_j(t) = \frac{k_e^2}{R_g + R_j(t)} \tag{4.4}$$

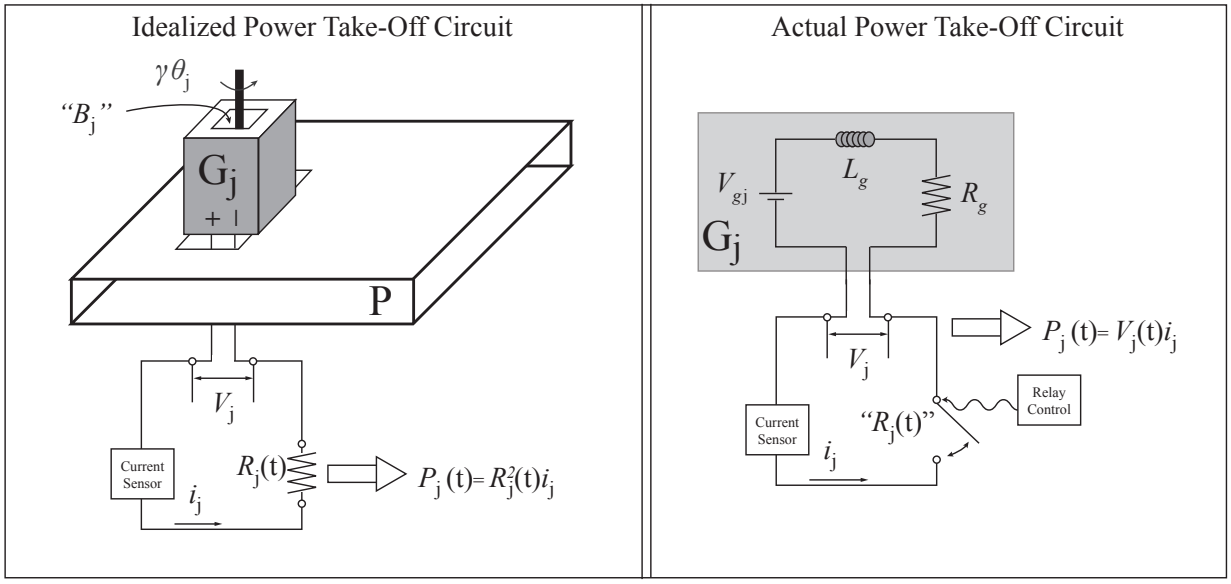

Figure 4.14: Diagram showing the idealized circuit of the j^{th} generator and the actual circuit implemented to control platform orientation by varying R_j.

For $R_j = 0$, we reach the maximum damping that can be provided by the generator. In this case, the duty cycle is set to 100%, the circuit is shorted and the maximum current is produced. Likewise, if the duty cycle is set to 0%, the circuit is open, $R_j \to \infty$ and the minimum damping is provided only due to the friction in the drivetrain system and generator bearings. In this way the damping provided by the generator is controlled by a PWM signal sent from the 'Master' MCU. The solid-state relay used is:

- Crydom CN024D05 3.5 A, 24VDC, Maximum 500 Hz PWM (DigiKey)

Before the experimental campaign, a robust controller using a Linearization Feedback technique was devised in SIMULINK. The controller will be discussed in greater detail in Chapter 5. This type of control was implemented in the 'Master' Arduino. Like any control effort, the technique requires a suitable approximation of the external forces on the platform. At the time of the experimental campaign the slow-drift formulation introduced in Chapter 2 had not been formalized yet. Thus, the motion of the platform due simply to waves could not be accurately predicted. For this reason and on account of the noisy sensor data, a simpler algorithm was implemented on the 'Master' MCU and is shown in Algorithm 3. This algorithm uses information about the positional error and how fast the platform is approaching the desired heading to calculate the difference in the settings of the generator. Thus, it is essentially a P-D controller with saturation and a non-constant derivative gain.

Algorithm 3 Control of Platform Orientation with 'Master'

Require: Instantaneous yaw position measurement $\theta_b(t)$ from IMU
Require: Running average yaw speed $\dot{\theta}_0(t)$
Require: Desired yaw position θ_0^*
  Calculate position error $e_\theta(t) = \theta_0(t) - \theta_0^*$
  Estimate difference in generator settings Δ_g based on desired speed of turbines, ω_1^*
  if $e_\theta(t) > 0°$ **then**
    if $e_\theta(t) < 15°$ **then**
      Estimate an approach speed factor ϵ_θ based on $\dot{\theta}_0(t)$,
      Generator 1 = HIGH/2 + $\epsilon_\theta \Delta_g$
      Generator 2 = HIGH/2 - $\epsilon_\theta \Delta_g$
    else
      Generator 1=HIGH, generator 2=OFF
    end if
  else if $e_\theta(t) < 0°$ **then**
    if $e_\theta(t) > -15°$ **then**
      Estimate a speed factor ϵ_θ based on $\dot{\theta}_0(t)$
      Generator 1 = HIGH/2 - $\epsilon_\theta \Delta_g$
      Generator 2 = HIGH/2 + $\epsilon_\theta \Delta_g$
    else
      Generator 1=OFF, generator 2=HIGH
    end if
  end if

4.5 Communication Systems

The communication systems that were implemented on the platform ended up being some of the most time consuming facets of the project. In order to have reliable and repeatable testing outcomes, the communication systems must be designed and implemented to be as robust as possible. At first the communication system consisted entirely of wired connections between microprocessor. It became quickly evident that the cable transferring data from the onboard processor to the 'base station' for data storage was having a large effect on the motion (especially yaw displacement) of the platform (as found in [114] as well). After initial testing, it was determined that wireless modules should be installed between the 'Master' microprocessor (see Fig. 4.15) and the 'base station' so that this data cable could be removed. After the wireless modules were installed on these microprocessors, it was evident that the system could be made more robust by installing them on all the microprocessors used in the study, including 'Slave 1' and 'Slave 2'.

4.5.1 I^2C Protocol

In order to communicate between Arduinos the simplest serial two-wire interface communication system, known as I^2C, or Inter-Integrated Circuit was implemented. This protocol

was created by Philips Semiconductor in 1982 and is still used widely today. The interface uses two bidirectional open-drain lines: a serial clock line (SCL) and a serial data line (SDA). The I^2C protocol is most suitable for communication systems with relatively short transmission distances (<10 m) that are not subject to noise. The I^2C protocol was first implemented between the 'Master' and 'Slave' microprocessors as shown in Fig. 4.15. In

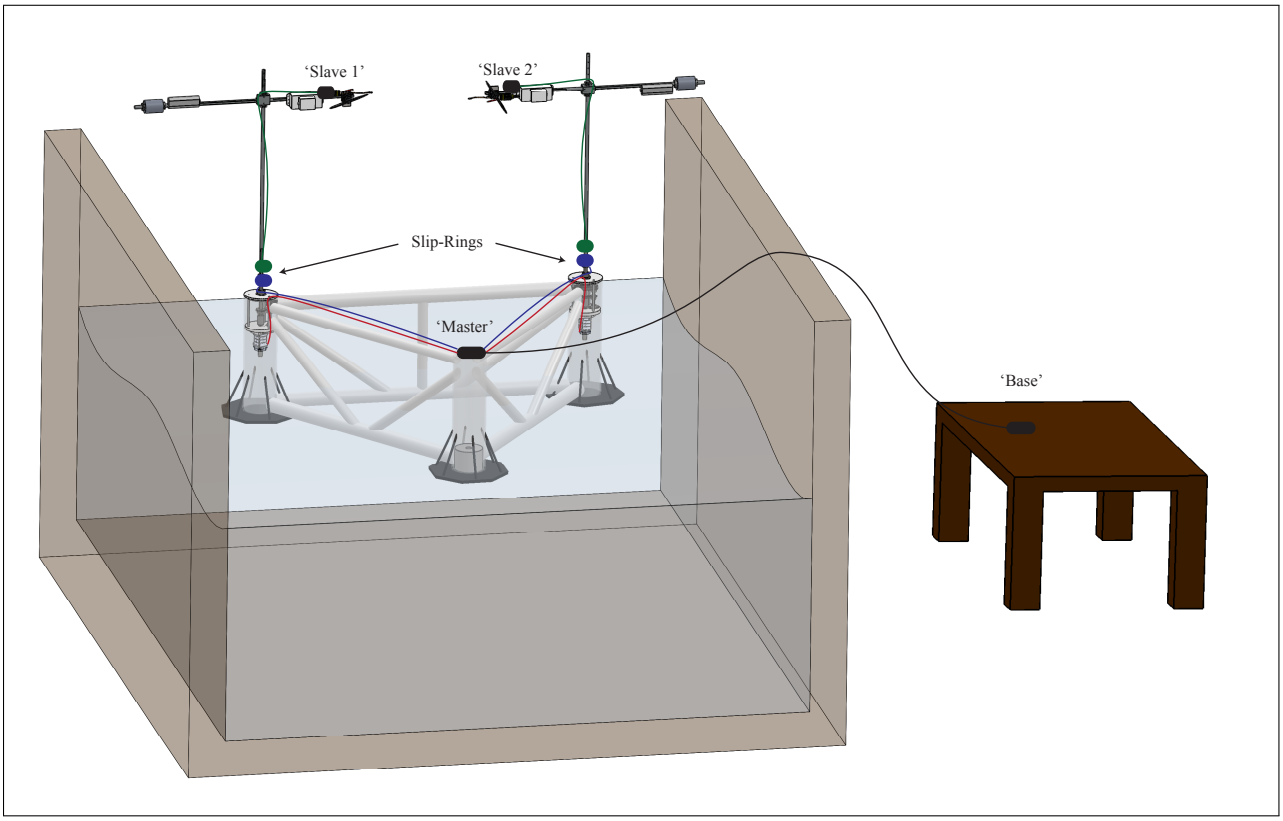

Figure 4.15: Schematic showing wired connections between microprocessors using I^2C.

between these microprocessors, a slip ring allows WIGs to freely rotate, while maintaining electrical connection. The slip rings chosen for the model were:

- MOFLON Slip Ring, 6 conductor 10 A, through bore-1/2"

The slip rings were guaranteed to produce variations $< 5m\Omega$ per revolution. However, even these small variations in the resistance resulted in voltage changes in the SCL lines that caused transmission errors to occur. We utilized the built-in two-wire interface library that comes pre-installed with the Arduino software, which has features including designating multiple 'slaves' on the same has a I^2C network as well as automatically creating the transmission packet that uses the appropriate checksums. However, if a data transmission error occurs, the software hangs and can only be reset by cycling the power to the Arduino board. Thus, building a resilient communication network was of the utmost importance. To do so, we utilized a bus buffer and raised the voltage of the high voltage line to increase the network's noise immunity. The bus buffer purchased from DigiKey was:

- Philips Semiconductor P82B96 IC Dual, Bi-directional Bus Buffer

The most unclear aspect of implementing the I^2C system was the selection of the pull-up resistors. Even though multiple application notes were written (see, e.g., [115]), we never found a clear way to calculate the necessary resistance in the circuit based on the rise time and the estimated capacitance of the circuit. The normal operation of the I^2C protocol operates at 100 kHz, so that too much added resistance can cause the rise time of the signal to increase beyond the limits of the built-in logic. Too little resistance does not damp the noise in the system. The final circuit that was implemented with Arduino *Due*'s is shown in Fig. 4.16.

Although the system was tested successfully for long periods of time (> 5 min) before the platform was deployed in the wave tank, it proved difficult to obtain reliable results once two 'slaves' were operating on the same I^2C network. During the initial stages of the testing it became clear that the communication link between the 'Master' MCU and the 'Base' MCU shown in Fig. 4.15 was having an undue effect on the system dynamics. This link was a Serial line that was used to record data from the 'Master' MCU as well as send commands to initiate testing. This issue is a well known problem with wave-tank testing where data recorded by an MCU located on a floating body must be transferred off the floating body. Researchers participating in the DeepCWind consortium that performed extensive model testing of horizontal-axis wind turbines with various floater designs noted this issue in [114]. In Figure 1 of [114], the reader can notice a large amount of cabling that is connected to the turbine. Especially in the case of testing the MIST platform, where the yaw motion was the most critical to simulate, the cable prevented free rotation of the platform. Thus, the decision was made to transition to a wireless data communication system, at first between 'Master' and 'Base' and later as redundant link between 'Master' and 'Slaves'.

4.5.2 Wireless Communication

A wireless communication system was setup between the four MCU's used in these experiments. Each MCU was located on a different body: the two turbines, the floating platform and the Earth. Five Xbee wireless units were installed, with one on each of the MCU's and two on the 'Master' as shown in Fig. 4.18.

Four of the Xbee units are shown in Fig. 4.17, along with the 'Xbee Explorer' (red unit), which allows the modification of the Xbees using open-source software. The rationale for utilizing two units on a single MCU is explained herein. The wireless communication units were:

- Xbee Series 1, 1 mW chip antenna (Amazon)
- Xbee Explorer USB Stick (Sparkfun)

The Xbee can either be programmed to be used in 'Transparent' mode (AT) or application programming interface mode (API). In 'Transparent' mode, the unit is continuously transmitting and listening for wireless packages on the designated frequency. In the API mode,

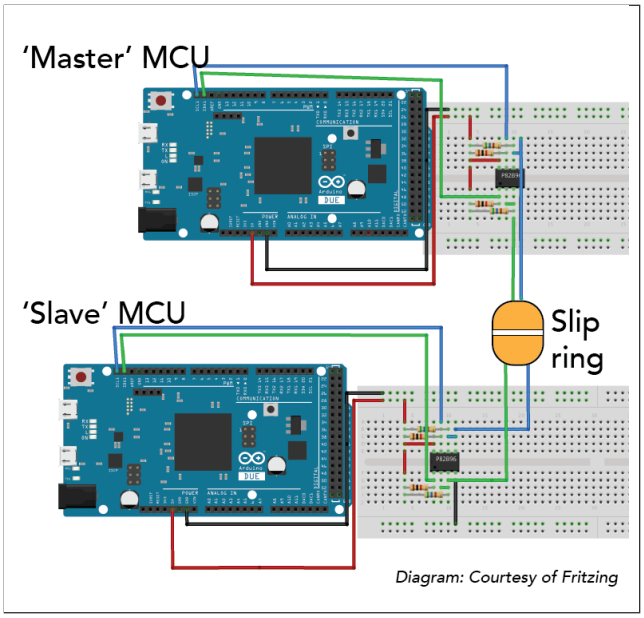

Figure 4.16: Schematic showing wiring diagram for I^2C circuit.

one unit is designated as a 'master,' while others are designated 'slaves'. These 'slave' units only transmit information over the network when requested to do so by the 'master.' After initial testing with the Arduino *Due* and multiple Xbee units using the built-in library, it became clear that the AT mode was able to send and receive data faster. Since the priority

Figure 4.17: Picture of Xbee units deployed on MIST platform, with Xbee Explorer (for programming the units) in red. See Fig. 4.18 for location of units on model.

of the link between the 'Master' and 'Slave' MCUs was to record data as fast possible, this

link (shown by the blue wifi symbols in Fig. 4.18) was set to 'transparent'. However, since the 'Master' MCU needed to be able to address each slave MCU individually, these link were set to the API mode. Since an Xbee can only be configured to either API mode or AT mode at one time, five Xbees were needed to create this system. An excellent resource

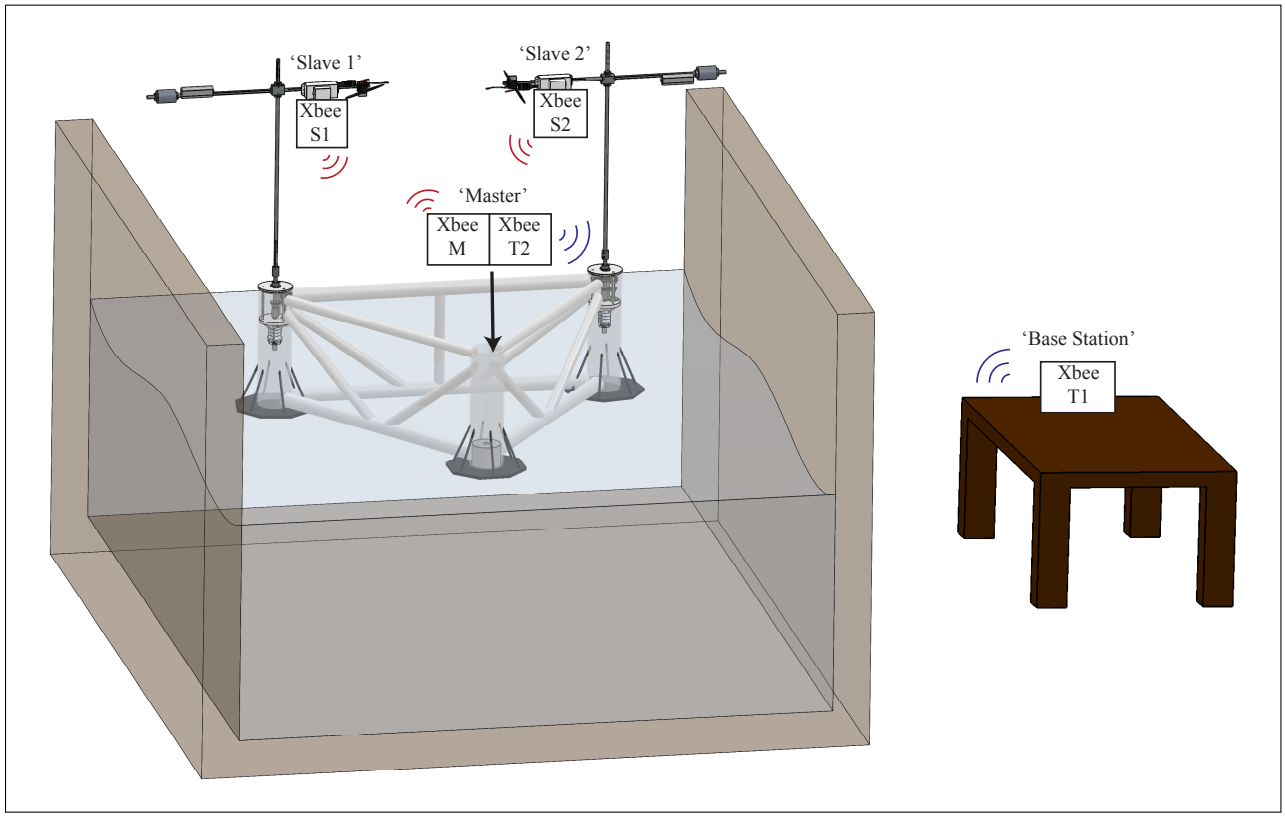

Figure 4.18: Schematic showing Xbee wireless modules used to communicate between microprocessors used in study.

on explaining the fundamentals of designing wireless networks, including using Xbees with Arduinos, is [116].

It became apparent during the tests that the size of the payload interfered with Xbee's ability to two-way communicate in 'Transparent' mode. That is, since the 'Master' Xbee was sending data to the 'Base' Xbee as quickly as possible ($\approx 50ms$), it was only able to receive commands if the payload it was sending was small (around 20 32-bit floats). However, during the tests, around 40 32-bit floats were sent to the 'Base Station' for recording. Thus, during calibration and start-up only a small payload was sent for data recording. After the yaw heading was sent and the platform was acting autonomously, a command was sent to the 'Master' to send the full payload. Thus, in the data recording there is no data for the first few seconds after the platform started behaving autonomously.

4.6 Experimental Results

A number of experiments were undertaken in early March 2015 at the UC Berkeley Physical-Model Testing Facility, which is described in other publications, such as [58]. The tank is only 2.5 m wide, so the mooring system was pretensioned such that the model would not impact the side walls of the tank. A test matrix of desired model-scale wind and wave conditions is shown in Table 4.4. However, due to limitations of the wave-maker used in the study, wave testing under extreme and shutdown conditions was not possible. Thus, we only considered operational conditions, but increased the wave amplitude to test the limits of our ability to control the yaw orientation.

Condition		Operational (Normal)	Operational (Extreme)	Shutdown
Variable	Unit	Wind/Turbine		
$\max F_T^*(t)$	kgf	0.20	0-2.5	3.75
ω_1	rpm	75.1-125.2	177	0
		Ocean/Platform		
A_0	in	2.2	12.2	12.2
T_0	s	1.1	1.9	1.9
β	deg	0	0	0
$\theta_0(0)$	deg	[0:30:180]	90	90

Table 4.4: Model-scale test matrix.

4.6.1 Successful Control Tests

Many tests were undertaken at various initial yaw angles $\theta_0(t=0) = \theta_0(0)$. The success of the control scheme largely depended on the initial and desired yaw headings relative to the incident-wave direction. The time history of one such successful test is shown in Fig. 4.19. Due to limitations such as the length of the tank (and hence reflection of waves from the beach back to the floating platform) and battery capacity, the duration of tests were limited to 1-2 minutes. Thus, only a 45 sec period is shown in Fig. 4.19. Once the WIGs were powered and calibrated and the platform was oriented at the proper $\theta_0(0)$, a train of regular waves were sent down the tank and the desired yaw orientation was set to $\theta_0^* = \theta_0(0) \pm 30°$. As described at the end of Sec. 4.5, there was a time delay from the setting of the desired heading to the beginning of the data collection. This delay can be seen in Fig. 4.19, since $e_\theta(0) = \theta_0 - \theta_0^*$ at the beginning of the data collection is only $-20°$ (rather than its original

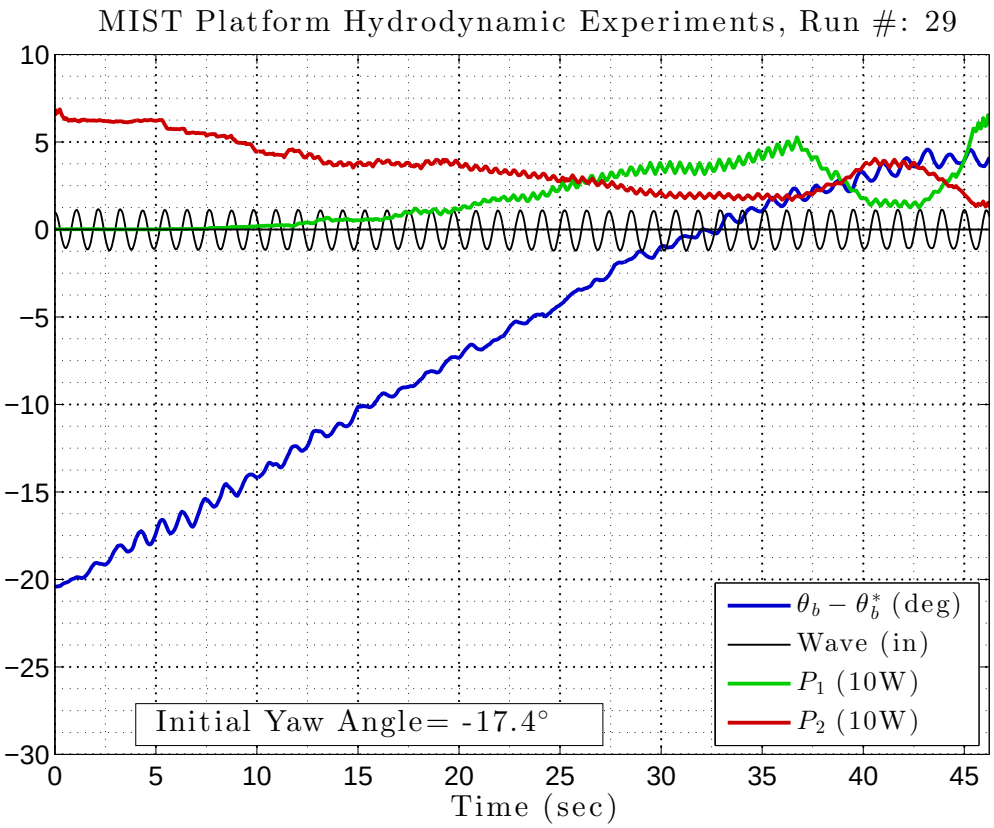

Figure 4.19: Yaw error and power generated during successful control of yaw heading of the MIST platform in regular waves.

value of $-30°$). Although the error is approaching $0°$ (albeit, with a small overshoot), it is unclear whether the main contribution is steady, hydrodynamic moment, or the moment generated by the imbalanced power conversion in the generators. This uncertainty will be addressed in greater detail in Sec. 5.8.

4.6.2 Applied Aerodynamic Torque

The force applied by a vertical-axis wind turbine at model scale is shown in Fig. 4.10, along with three different resolutions. As described in Sec. 4.4.1 and Algorithm 2, the goal was to apply a cyclic torque with a frequency twice that of the rotating turbine. This represents the torque from a two-bladed vertical-axis wind turbine. The actual applied thrust force is shown by the blue curve with circle markers in Fig. 4.20. The fastest achieved tip-speed ratio at model scale was $\lambda = 3.5$. The motor/propeller inertia was too large to try turn the motor on/off faster than 400 ms. From these curves it is clear we achieved a period for the applied force of about 450 ms. This frequency corresponds to a tip-speed ratio of $\lambda = 3.5$ at the rated wind speed and operating conditions given in Table 4.2. The figure also shows how data was only recorded by the 'Base' MCU every 50-60 ms. However, the 'Slave' MCUs were controlling and sensing the applied force at a much higher rate, probably

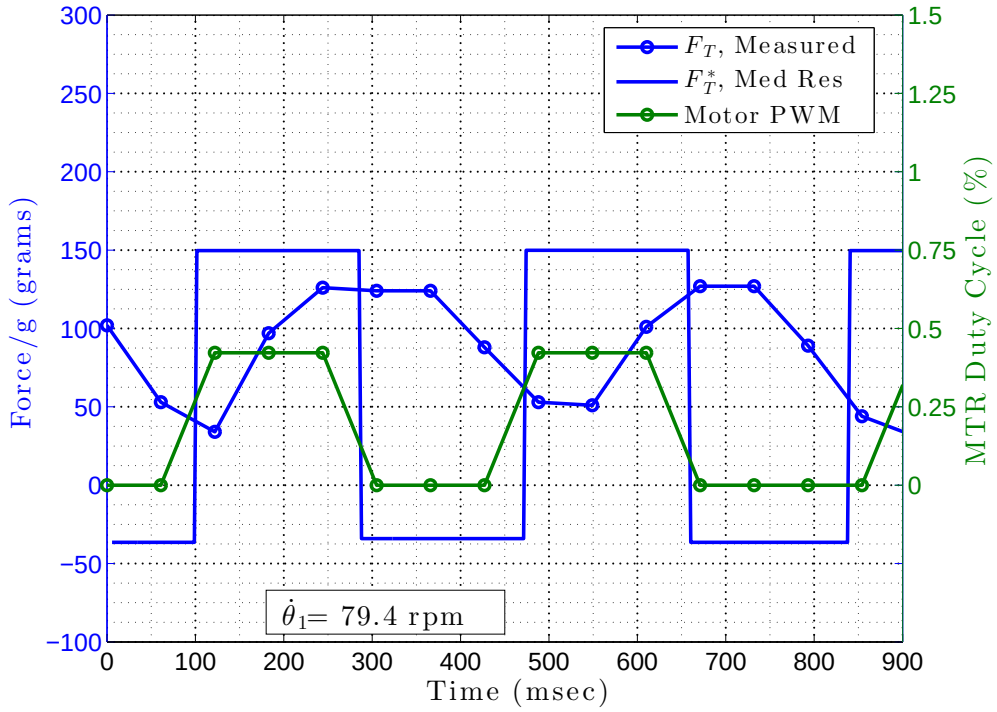

Figure 4.20: Comparison of applied thrust force F_T from the Wind-Input Generator (WIG) against the desired thrust force F_T^* at medium resolution with $\lambda = 3.5$ as a function of time.

on the order of 10-20 ms. The discrepancy is due to the fact that the Xbees on the 'Slave' MCUs were in 'API' mode, which has a much slower maximum speed than the Xbee's in 'Transparent' mode. Although the MCUs were sensing and modifying the thrust force much more frequently, the Xbees could only send data every 50 ms in 'API' mode.

Another interesting feature of Fig. 4.20 is the time lag between the motor setting (in green) and the applied force. We surmise that this time delay is due to the inertia of the motor/propeller unit. After the motor is energized at (for instance, at $t = 500$ msec in Fig. 4.20), the applied force does not begin increasing for about 100 ms. The propeller dominates the rotational inertia of the system as the motor, itself, was quite light and compact (5.5kg-mm^2) while the propeller's moment of inertia is 130 kg-mm^2. The phase lag between the desired and actual force curves is not an issue for these simulations because physically it only represents a different starting position of the turbine. If future researchers want to follow a specific time history of forces that is not simply oscillatory, they would have to take this effect into account.

Interestingly, as shown in Fig. 4.20, the applied force never reaches 0 or negative values. During the 'off' periods the motor was set to 0% of its duty cycle. However, the inertia in the rotor kept the propeller spinning. Although the electronic speed controller (ESC) was reprogrammed in such a way that allowed for bi-directional control of the propeller (i.e., forward and reverse depending on the motor setting), we never set the motor to a negative value for fear of damaging the controller or motor. However, for higher fidelity

hybrid simulations the motor/propeller must be able to operate in reverse. For more details about reprogramming ESCs, see [1].

The measurement of the applied force by a load cell on a spinning WIG assumes that the rotor is spinning at a constant speed. If the rotor is accelerating the force measured by the load cell will be larger than the actual applied force, since the motor/propeller's acceleration is in the same direction as the applied force. Likewise, if the rotor is decelerating, the force measured by the load cell will be smaller than the actual applied force. Again, this will not have a large effect on the absolute minimum or maximum values achieved by the WIGs; it will only introduce a phase lag in the actual force. Furthermore, the inertia of the rotor is quite large (compared to the thrust force), around 0.25 kg-m^2, so the rotor does not experience drastic changes in acceleration, once it is rotating near its operating speed.

4.6.3 Effect of Vertical Center of Gravity

As depicted in the photograph in Fig. 4.3, the cross-beam of the WIG is located near the top of the 'tower' or central column (shown as component # 7 in Fig. 4.3). However, for the start of the experiments, the horizontal cross-beams were lowered to a height halfway up the central columns, to ensure the WIGs were not deflecting too much and causing undue stress on the slip rings. By lowering the vertical center of gravity of the WIGs, however, we can examine the effect of changing the vertical center of gravity of the turbines on the pitch/roll motion floating body. Figure 4.21 shows a time series of the pitch motion motion

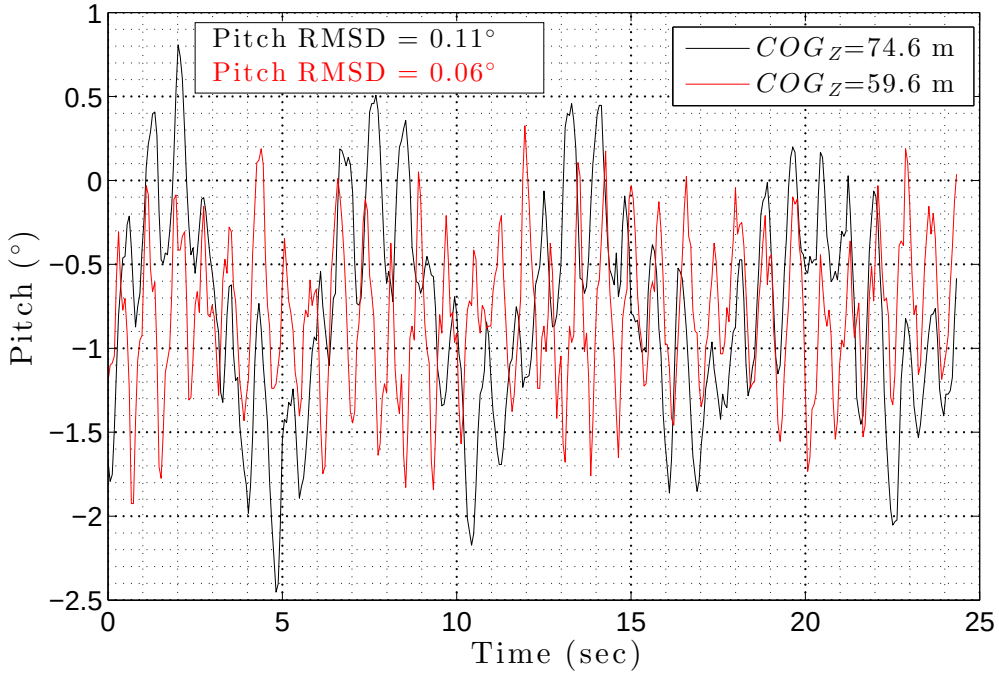

Figure 4.21: Pitch motion of platform with standard COG_z (black) and 20% reduction (red).

of the platform for two different vertical centers of gravity for the turbines. The black curve

represents the standard center of gravity (35.7 in model-scale corresponds to 74.6m full-scale, as shown in Table 4.2). The vertical center of gravity is measured from the still waterline. The red curve represents the time series of the platform subject to similar wind and wave conditions (with a similar starting yaw position) with a center of gravity that is lowered by 20%. As shown, the root-mean-square deviation is reduced by 40% for the platform with lowered center of gravity. The black curve exhibits a low frequency behavior (approximately 5x that of the incident-wave frequency), which may be due to non-linear effects, such as in the pretensioned mooring lines.

Chapter 5

Numerical Study of Floating Platform in Time Domain

In this chapter we describe the equations of motion in the time-domain for the main components of the MIST platform: the floating platform, the drivetrain and the turbines. First, we describe the components of the MIST platform which have not been examined mathematically thus far, including the drivetrain. We introduce a global overview of the Simulink model, which links the external forces, the controller, and the plant (platform and turbines). After the state vector is introduced, we describe the kinetics and the kinematics of each subsystem in greater detail. A brief discussion on the non-linear control implemented in the numerical model is presented. Next, the hydrodynamics are detailed using the theories developed in Chapter 2 and finally the implementation of the aerodynamics module using a simple lookup table is briefly described. The results of the simulations are reported and compared to the experimental data, which was obtained using the procedures detailed in Chapter 4.

5.1 Drivetrain Subsystem

In Fig. 5.1, a drivetrain system is shown that functions the same way the actual drivetrain on the MIST platform performs, such as the one detailed in Fig. 4.1. We have removed extraneous parts and only focus on the functionality of the drivetrain, which is to connect the rotors of the two turbines so they are forced to rotate in equal and opposite directions. Here, we assume the gearbox ('GB$_j$' with gear ratio, $\gamma_j > 1$) is frictionless and has no other losses. The summation of moments on the five different bodies (rotors 1 and 2, gearboxes 1 and 2 and platform) are shown in Eq. (5.1).

$$I_{gb1}\ddot{\theta}_1 = T_1^* + r_{p1}F_{21} - r_{gb11}F_{g1} \tag{5.1a}$$
$$I_{g1}\ddot{\theta}_{g1} = +r_{gb12}F_{g1} - T_{g1} \tag{5.1b}$$
$$I_{gb2}\ddot{\theta}_2 = T_2^* + r_{p2}F_{12} - r_{gb21}F_{g2} \tag{5.1c}$$
$$I_{g2}\ddot{\theta}_{g2} = +r_{g22}F_{g2} - T_{g2} \tag{5.1d}$$
$$I_b\ddot{\theta}_0 = +T_{g1} + T_{g2} + Q_e \tag{5.1e}$$

where Q_e denotes the external moment on the platform, namely from the hydrodynamic yaw moment and the mooring system, as given in Eq. (2.155). The aerodynamic torques T_1^* and T_2^* are denoted with superscripts * to convey the fact they are the *ideal* torques that would be applied to the system if they were vertical-axis turbines. The actual torques provided by the WIGs to the drivetrain are denoted without the superscripts. If the gears

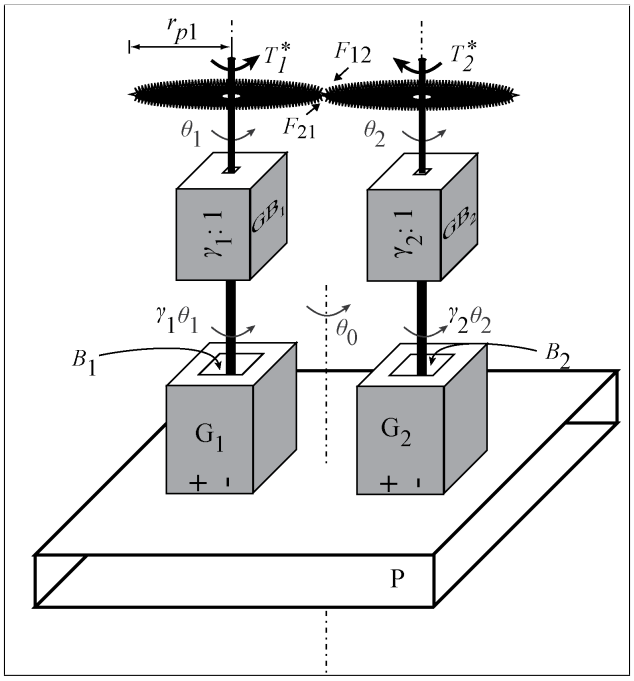

Figure 5.1: Simplified schematic of MIST platform drivetrain, where T_j^* are the aerodynamic VAWT torques and the flat plate represents the platform. The gearboxes G_j with gear ratio $\gamma_j > 0$ are shown as well as the electrical generators with linear damping coefficients B_j.

do not slip and we ignore the effects of backlash and other nonlinearities, then the following kinematic constraints hold (as well as their time derivatives)

$$r_{p1}\theta_1 = -r_{p2}\theta_2, \tag{5.2a}$$

$$\frac{r_{gbj1}}{r_{gbj2}} = \frac{\theta_{g1}}{\theta_1} = \gamma \tag{5.2b}$$

where θ_{g1} and θ_1 rotate the same direction in Eq. (5.2b) due to the nature of the planetary gearset. The generators are modeled as linear dampers, such that,

$$T_{g1} = +B_1\left(\dot{\theta}_{g1} - \dot{\theta}_0\right) \tag{5.3a}$$

$$T_{g2} = +B_2\left(\dot{\theta}_{g2} - \dot{\theta}_0\right) \tag{5.3b}$$

Isolating the generator forces F_{g1} in Eq. (5.1b) and F_{g2} in Eq. (5.1d), we find that,

$$F_{g1} = \frac{1}{r_{gb12}}\left(I_{g1}\gamma\ddot{\theta}_1 + B_1(\gamma\dot{\theta}_1 - \dot{\theta}_0)\right) \tag{5.4a}$$

$$F_{g2} = \frac{1}{r_{gb22}}\left(I_{g2}\gamma\ddot{\theta}_2 + B_2(\gamma\dot{\theta}_2 - \dot{\theta}_0)\right) \tag{5.4b}$$

Substituting these into Eqs. (5.1a) and (5.1c), we obtain,

$$I_{gb1}\ddot{\theta}_1 = T_1^* + r_{p1}F_{21} - \frac{r_{gb11}}{r_{gb12}}\left(I_{g1}\gamma\ddot{\theta}_1 + B_1(\gamma\dot{\theta}_1 - \dot{\theta}_0)\right) \tag{5.5a}$$

$$I_{gb2}\ddot{\theta}_2 = T_2^* + r_{p2}F_{12} - \frac{r_{gb21}}{r_{gb22}}\left(I_{g2}\gamma\ddot{\theta}_2 + B_2(\gamma\dot{\theta}_2 - \dot{\theta}_0)\right) \tag{5.5b}$$

From Newton's Third Law, the magnitudes of the internal forces between the two gears are equal, i.e., F_{21}=F_{12}, (we have already assumed they are in opposing directions in Fig. 5.1 and Eq. (5.1a) and (5.1c)). Further we assume that the gear ratio between the rotors is unity, $r_{p1} = r_{p2}$. Thus, we can combine Eqs. (5.5a) and (5.5b), using the kinematic constraints in Eq. (5.2), as

$$\left(I_{gb1} + I_{gb2} + (I_{g1} + I_{g2})\gamma^2\right)\ddot{\theta}_1 = T_1^* - T_2^* - \gamma^2(B_1 + B_2)\dot{\theta}_1 + \gamma(B_1 - B_2)\dot{\theta}_0 \tag{5.6}$$

Equation (5.1e) can be rewritten as,

$$I_b\ddot{\theta}_0 = +\gamma(B_1 - B_2)\dot{\theta}_1 - (B_1 + B_2)\dot{\theta}_0 + Q_e \tag{5.7}$$

In vectorized form Eqs. (5.6) and (5.7) become,

$$\begin{bmatrix} I_b & 0 \\ 0 & I_g \end{bmatrix} \frac{d}{dt} \begin{bmatrix} \dot{\theta}_0 \\ \dot{\theta}_1 \end{bmatrix} = \begin{bmatrix} -(B_1 + B_2) & \gamma(B_1 - B_2) \\ \gamma(B_1 - B_2) & -\gamma^2(B_1 + B_2) \end{bmatrix} \begin{bmatrix} \dot{\theta}_0 \\ \dot{\theta}_1 \end{bmatrix} + \begin{bmatrix} Q_e \\ T_1^* - T_2^* \end{bmatrix} \tag{5.8}$$

where $I_g = I_{gb1} + I_{gb2} + (I_{g1} + I_{g2})\gamma^2$. Thus, if $B_1 = B_2$, this system is decoupled and the rotors will not exert any net moment on the platform. That is, as long as $\dot{\theta}_0(0) = 0$, then $\dot{\theta}_0(t) = 0$. However, in some instances we want to couple the system so that $\dot{\theta}_0(t) \neq 0$. In this case, we can set $B_1 > B_2$, if we want $\dot{\theta}_0(t) > 0$ (assuming $\dot{\theta}_1(t) > 0$) or $B_1 < B_2$, if we want $\dot{\theta}_0(t) < 0$. The control of B_j in the experimental setup is described in Sec. 4.4.

5.1.1 Frictional Losses

During the dry testing of the model, described in Sec. 4.2.3, it became evident that there were major frictional losses between the drivetrain and the platform. That is, on top of the torque transferred from the rotors to the platform that is mediated by the generators, there is torque transferred through frictional contact with bearings, gearbox housings, etc. In order to recreate the experimental results, we model these frictional forces as function of the relative velocities of the rotor and platform *without* the influence of the gearbox. The frictional forces on the needle bearings, which allow the rotor to rotate relative to the platform, are not influenced by the gearbox. Thus, we model the frictional torque between the rotors and platforms, as

$$T_{Lj} = B_{Lj}\left(\dot{\theta}_j - \dot{\theta}_0\right) \text{ for } j = 1, 2. \tag{5.9}$$

We can rewrite Eq. (5.8) including these frictional forces as,

$$\begin{bmatrix} I_b & 0 \\ 0 & I_g \end{bmatrix} \frac{d}{dt} \begin{bmatrix} \dot{\theta}_0 \\ \dot{\theta}_1 \end{bmatrix} = \begin{bmatrix} \mathcal{B}_{00} & \mathcal{B}_{01} \\ \mathcal{B}_{10} & \mathcal{B}_{11} \end{bmatrix} \begin{bmatrix} \dot{\theta}_0 \\ \dot{\theta}_1 \end{bmatrix} + \begin{bmatrix} T_1^* - T_2^* \\ Q_e \end{bmatrix} \tag{5.10}$$

$$\mathcal{B}_{00} = -(B_1 + B_2 + B_{L1} + B_{L2}) \tag{5.11}$$

$$\mathcal{B}_{01} = \mathcal{B}_{10} = \gamma(B_1 - B_2) + (B_{L1} - B_{L2}) \tag{5.12}$$

$$\mathcal{B}_{11} = -\gamma^2(B_1 + B_2) - (B_{L1} + B_{L2}) \tag{5.13}$$

Moreover, it became clear that these frictional loss coefficients were directly related to the damping in the generators. That is,

$$B_{Lj} = f(B_j) \text{ for } j = 1, 2. \tag{5.14}$$

Essentially, the frictional losses are modeled as a damper between the rotor and the platform that is independent of the gearbox speed but depends on the back-torque generated in the drivetrain. For simplicity we write the loss coefficient as a linear function of the generator coefficient, as

$$B_{Lj} = c_b B_j + d_b \text{ for } j = 1, 2, \tag{5.15}$$

where the parameters c_b and d_b are experimentally determined.

5.2 Aerodynamic Forces on Platform

In this section, we describe how the aerodynamic forces on the turbines are transferred as (additional) moments to the platform. For now, we include the effect of the normal and tangential forces on each turbine's blade (labeled ($F_{Tj}^{(i)}$ and $F_{Nj}^{(i)}$ for the tangential and normal forces on rotor i, blade j, respectively) to describe how these forces influence yaw motion of the platform. These aerodynamic forces from each blade not only result in a moment on the turbine itself, which is described in the previous section, but also a linear acceleration of the rotors, which is transferred to the platform through the bearings that allow the rotors to yaw relative to the platform. The tangential force on rotor i blade j can be described as,

$$\boldsymbol{F_{Tj}}^{*(i)}(\theta_i) = |F_{Tj}^{*(i)}(\beta_1 - \theta_i)| \left(-\sin\left[\bar{\theta}_i + \theta_i + \frac{(j-1)N_b}{2\pi}\right] \hat{\imath} + \cos\left[\bar{\theta}_i + \theta_i + \frac{(j-1)N_b}{2\pi}\right] \hat{\jmath} \right) \tag{5.16}$$

where we have defined $\bar{\theta}_i$ relative to the inertial frame, as done in Chapter 3. Likewise, the normal forces can be represented as,

$$\boldsymbol{F_{Nj}}^{*(i)}(\theta_i) = |F_{Nj}^{*(i)}(\beta_1 - \theta_i)| \left(-\cos\left[\bar{\theta}_i + \theta_i + \frac{(j-1)N_b}{2\pi}\right] \hat{\imath} - \sin\left[\bar{\theta}_i + \theta_i + \frac{(j-1)N_b}{2\pi}\right] \hat{\jmath} \right) \tag{5.17}$$

Although the line of action of these aerodynamic forces act through the blades, themselves, the moment on the platform is developed through the linear bearings between the platform and the rotor (which should align with rotor's center of gravity for fatigue purposes). Therefore, the moment arm for the forces on the i^{th} rotor can be expressed as,

$$\boldsymbol{R}_i = |R_i| \left(\cos\left[\theta_0 + \alpha_i\right] \hat{\imath} + \sin\left[\theta_0 + \alpha_i\right] \hat{\jmath}\right) \tag{5.18}$$

The total moment on the platform is developed from summing all the individual moments

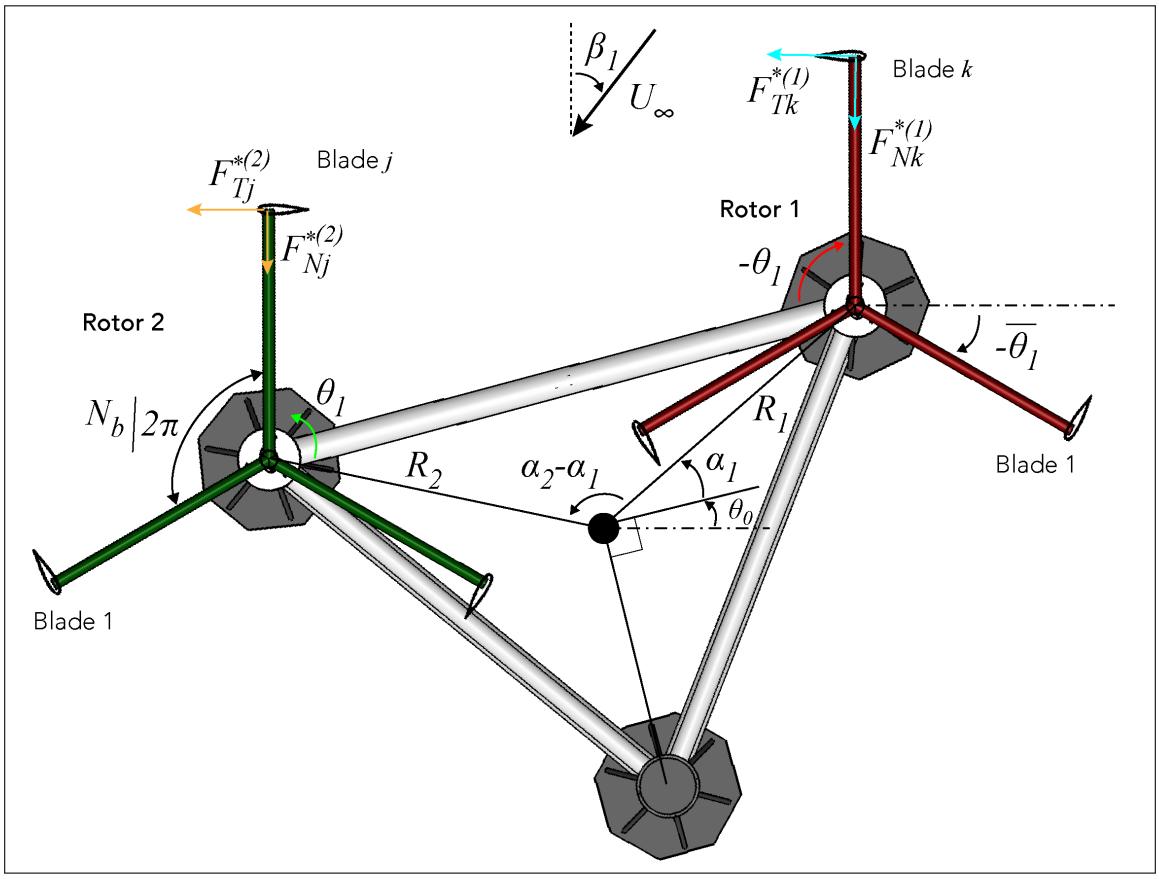

Figure 5.2: Schematic of MIST platform in plan view to describe how tangential and normal aerodynamic forces on rotor i, blade j, ($F^{*(i)}_{Tj}$ and $F^{*(i)}_{Nj}$, respectively) are transferred to a moment on the platform. Here, the turbines are depicted as three-bladed (N_b=3).

developed from each of the blades and their rotors as,

$$\begin{aligned} F_6^{T*}(t) &= \sum_i^2 \left(\boldsymbol{R_i} \times \sum_j^{N_b} \boldsymbol{F_{Tj}^{*(i)}}(\theta_i) \right) \cdot \hat{e}_3 \\ &= \sum_i^2 \sum_j^{N_b} |R_i| |F_{Tj}^{*(i)}(t)| \cos\left[(\theta_0 + \alpha_i) - \left(\bar{\theta}_i + \omega_i t + \frac{(j-1)N_b}{2\pi} \right) \right], \end{aligned} \tag{5.19}$$

where we have assumed the rotor velocity is constant ($\theta_i = \omega_i t$, for $i = 1, 2$). The reader is reminded that due to the constraints described in the previous section, $\omega_2 = -\omega_1$ and $\bar{\theta}_2 = \pi$, as shown in Fig. 3.22. Likewise, the moment on the platform developed from the normal forces can be expressed as,

$$\begin{aligned} F_6^{N*}(t) &= \sum_i^2 \left(\boldsymbol{R_i} \times \sum_j^{N_b} \boldsymbol{F_{Nj}^{*(i)}}(\theta_i) \right) \cdot \hat{e}_3 \\ &= -\sum_i^2 \sum_j^{N_b} |R_i| |F_{Nj}^{*(i)}(t)| \sin \left[(\theta_0 + \alpha_i) + \left(\bar{\theta}_i + \omega_i t + \frac{(j-1)N_b}{2\pi} \right) \right]. \end{aligned} \tag{5.20}$$

For $\bar{\theta}_1 = 0$, and $\bar{\theta}_2 = \pi$, the turbines are mere images of each other. If the turbines' power coefficients are equivalent, the net moments from each of the turbines will cancel (over one revolution of the turbines, $2\pi/\omega_1$), and only a cyclic surge/sway force on the platform will be applied. For the case of misaligned wind, we saw in the extreme case of Fig. 3.28(b), that the power coefficients will be different depending on the flow conditions. During the hybrid tests of the MIST platform, single actuators on each rotor were used to represent the thrust from two blades. In order to prevent unnecessary moments on the platform, we set their thrust forces to be equivalent and $\bar{\theta}_1 = 0°$. Thus, this moment F_6^{T*} was null for the experiments and will not be considered in the follow numerical analysis for this reason. However, in future studies it will be important to take these forces into account as they can have a large effect during start-up of the turbine, before the turbine has reached its rated speed (when, for instance, $\omega_1 << \sigma_o$). Furthermore, these forces will contribute to a time-varying surge and sway force on the platform, which must be considered when considering the fatigue life of the platform. Care must be taken to avoid large yaw excursions during the start-up period to prevent excessive loads on the mooring system.

5.3 Global SIMULINK Model

A depiction of the global Simulink model is shown in Fig. 5.3. In this model, there are subsystems such as the reference signal, controller and plant that make up a classical control problem. The signals include the output y, reference y_{des}, error e, control signal u and external forces $\hat{d}$. The external forces subsystems are shown explicitly since they are the main focus of the analysis and will be discussed in greater depth in the following sections. The user inputs to the system include the reference signals, which are the desired yaw heading θ_0^* and desired turbine speed ω_1^*. The controller for this numerical model is discussed in Sec. 5.4.

5.3.1 State Vector and Equations

In this section we develop the basic equations of motion for the platform and the spinning turbines. As mentioned in Chapter 2, we restrict our focus to simply three degrees of freedom

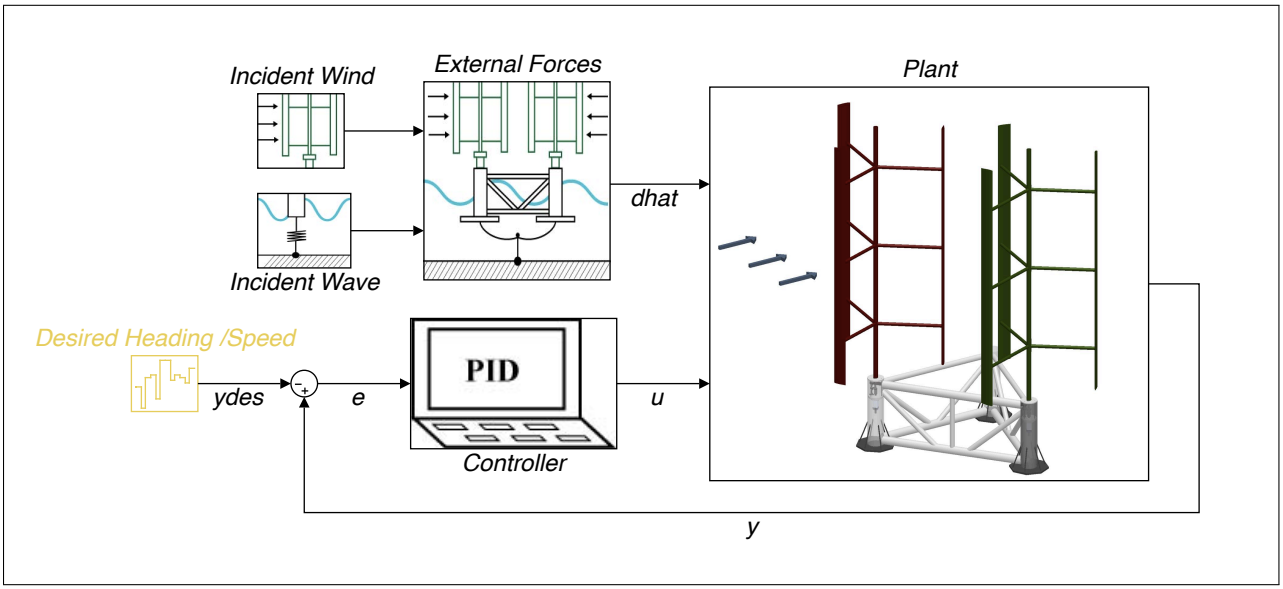

Figure 5.3: Global Simulink model, including controller, plant and external forces.

(DOFs) for the platform: surge, sway and yaw as well as two DOFs for the spinning turbine. These two DOFs have collapsed into one due to the constraint imposed by the 'connecting mechanism' as described in Sec. 5.1. We also consider the slow-drift yaw motion of the platform. For our system let us define the state vector as,

$$\boldsymbol{q} = \begin{bmatrix} q_1 \\ \vdots \\ q_{10} \end{bmatrix} = \left[\begin{array}{c} \xi_1 \\ \xi_2 \\ \xi_6 \\ \Theta_o \\ \theta_1 \\ \hline \dot{\xi}_1 \\ \dot{\xi}_2 \\ \dot{\xi}_6 \\ U_6 \\ \omega_1 \end{array}\right], q \in \mathcal{R}^{10x1} \tag{5.21}$$

The horizontal line is only for visual purposes and will be used in the forthcoming equations to denote the sub-matrices and sub-vectors, separating the displacements from the velocities. The plant, itself, is a relatively simple first-order plant. We use a discrete time-integrator because we are simulating the experimental model, whose controller can only be updated at discrete time instances defined by the sampling frequency of the MCU. The only non-standard term is the non-linear damping, which arises from the viscous terms, as shown

in Fig. 5.4. Thus, in continuous time, the dynamics can be state-space represented by the

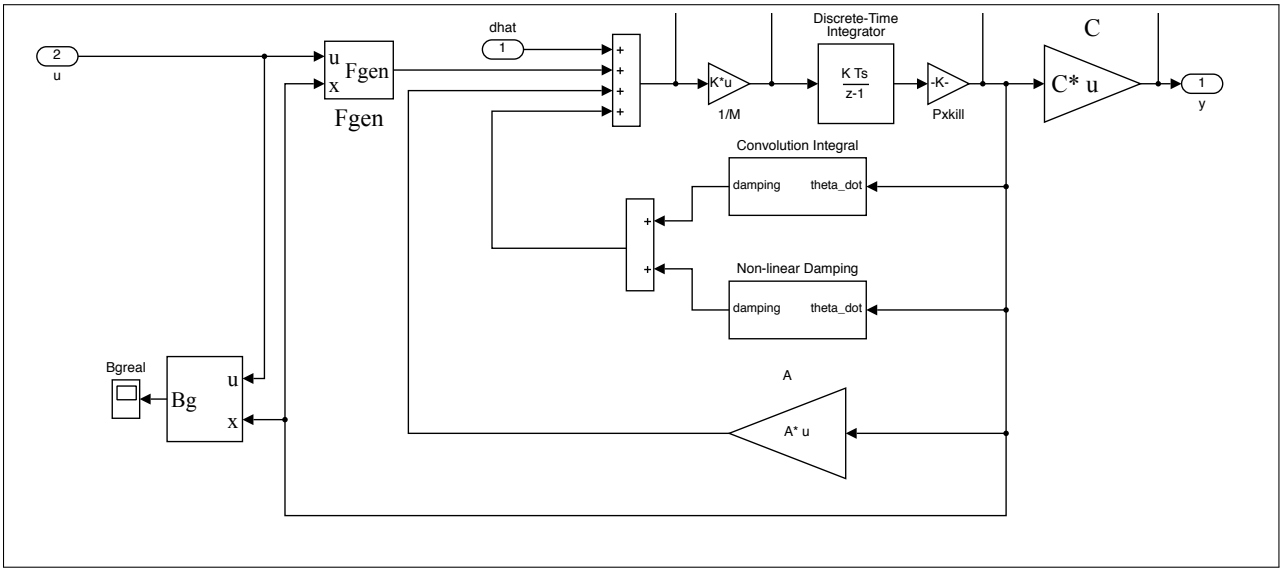

Figure 5.4: Simulink plant, including discrete time integrator and linear and non-linear damping terms.

multiple-input, multiple-output (MIMO) system, as

$$\dot{\boldsymbol{q}} = M^{-1}\left(A\boldsymbol{q} + \boldsymbol{d}(q,t) + \delta\boldsymbol{d}(t) + C_r\boldsymbol{\chi} + \boldsymbol{f_v}(|\boldsymbol{q}^T|)\boldsymbol{q} + \boldsymbol{g}(\boldsymbol{q})\boldsymbol{u}\right) \tag{5.22a}$$

$$\boldsymbol{y} = C\boldsymbol{q}, \quad \boldsymbol{u} \in \mathcal{R}^{2x1}, \boldsymbol{g} \in \mathcal{R}^{10x2}, \boldsymbol{y} \in \mathcal{R}^{2x1}, C \in \mathcal{R}^{2x10} \tag{5.22b}$$

The radiation state vector $\boldsymbol{\chi}$ is found from Eqs. (2.150) and is determined from the state vector $\boldsymbol{q}$. The non-linear function $f_v(|\boldsymbol{q}^T|)\boldsymbol{q}$ represents the viscous forces and can be inferred from Eq. (2.143). Here, the linear matrix A can be represented by,

$$A = \left[\begin{array}{ccc|ccc} 0 & \dots & 0 & 1 & \dots & 0 \\ & \ddots & & & \ddots & \\ 0 & \dots & 0 & 0 & \dots & 1 \\ \hline k_{11} & \dots & k_{15} & b_{11} & \dots & b_{15} \\ & \ddots & & & \ddots & \\ k_{51} & \dots & k_{55} & b_{51} & \dots & b_{55} \end{array}\right], \boldsymbol{d}(x,t) = \left[\begin{array}{c} 0 \\ \vdots \\ 0 \\ \hline A_o\boldsymbol{\mathcal{X}}_1^{(0)} \\ A_o\boldsymbol{\mathcal{X}}_2^{(0)} \\ A_o\boldsymbol{\mathcal{X}}_6^{(0)} \\ f_e \\ R(F_T^{*(1)} - F_T^{*(2)}) \end{array}\right] \tag{5.23}$$

where k_{ij} and b_{ij} are the linear spring and damping coefficients of the bodies. The steady second-order wave-exciting force is given in Eq. (2.153). As mentioned in Sec. 2.9, this wave-exciting force has no explicit dependence on time, but rather the relative wave incident-wave

heading β and hence, instantaneous position $\Theta_o(t)$ of the platform. For these simulations, we pre-calculate a database of f_e at various $\beta_o - \theta_0$ and then use a lookup table to find the instantaneous forces based on the position of the platform at the previous time step. The theoretical aerodynamic torques on the i^{th} rotor $RF_T^{*(j)}$ are simply the summation of the tangential forces on each blade as,

$$F_T^{*(i)} = \sum_j^{N_b} F_{Tj}^{*(i)}. \tag{5.24}$$

The mass matrix M is

$$M = \text{diag}\left(1 \quad \dots \quad 1 \;\middle|\; m_b \quad m_b \quad I_b \quad I_b \quad I_g + I_r\right), \tag{5.25}$$

where I_b, I_r, I_g are the moments of inertia about their centers of rotation of the platform, turbine and drivetrain, respectively.

5.4 Control of Platform Orientation and Turbine Speed

In this section we describe the control algorithms that were implemented numerically to optimize the power production. In the first part we describe a non-linear control technique described in [117]. Due to the complexity of this control scheme, we do not implement it in the microprocessor on the experimental platform.

5.4.1 Theoretical Control

In general we aim to control the system whose dynamics are governed by the following non-linear, 'square' MIMO system:

$$\dot{\boldsymbol{\zeta}} = \boldsymbol{f}(\boldsymbol{\zeta}) + \sum_{j=1}^{n} \boldsymbol{g_j}(\boldsymbol{\zeta}) u_j \tag{5.26a}$$

$$\boldsymbol{y} = \boldsymbol{h}(\boldsymbol{\zeta}) \tag{5.26b}$$

where $\zeta \in \mathcal{R}^{rx1}$ is the state vector we wish to control, and $\boldsymbol{y} \in \mathcal{R}^{nx1}$ is the measured output of the system, and u_j are the control variables. For our system $n = 2$. The plant can be described by

$$\boldsymbol{f}(\boldsymbol{\zeta}, t) = M_r^{-1}\left[A_r\boldsymbol{\zeta} + \hat{\boldsymbol{d}}(\boldsymbol{\zeta}, t) + \delta\boldsymbol{d}(t)\right] \tag{5.27}$$

where M_r contains the mass matrix that corresponds with the new state ζ, the linear plant dynamics are contained in the matrix A_r is $\mathcal{R}^{rxr}$, $\hat{d}(\zeta, t)$ is the modeled external disturbances to the system (such as aerodynamic and hydrodynamic loads) and $\delta\boldsymbol{d}$ is the error in the

modeling of the external loads. For simplicity, we have neglected the non-linear forces found in Eq. (5.22) in deriving the controller.

For the MIST platform, we consider the state space equations, shown in Eq. (5.8), such that $\boldsymbol{\zeta} \in \mathcal{R}^{4x1}$,

$$\boldsymbol{\zeta} = \begin{bmatrix} q_4 \\ q_5 \\ q_9 \\ q_{10} \end{bmatrix}. \tag{5.28}$$

Hence we are only seeking to control the slow-drift orientation of the platform and filter out the higher-frequency oscillations from the absolute yaw position of the platform. Then, the mass matrix M_r becomes

$$M_r^{-1} = \begin{bmatrix} 1 & 0 & 0 & 0 \\ 0 & 1 & 0 & 0 \\ 0 & 0 & I_b^{-1} & 0 \\ 0 & 0 & 0 & (I_g + I_r)^{-1} \end{bmatrix} \tag{5.29}$$

For clarity, let us define the lower right-hand corner of this matrix as $M_r' \in \mathcal{R}^{2x2}$. The vectors $\boldsymbol{g_j}$, $\boldsymbol{u}$ are chosen to represent the dynamics of the generators, which are modeled as linear dampers, as shown in Eqs. (5.3), such that $\boldsymbol{g_j} \in \mathcal{R}^{rx1}$, $\boldsymbol{u} \in \mathcal{R}^{nx1}$,

$$\begin{bmatrix} u_1 \\ u_2 \end{bmatrix} = \begin{bmatrix} B_1 \\ B_2 \end{bmatrix} \tag{5.30}$$

$$g_1 = M_r' \begin{bmatrix} -(1+c_b) & (\gamma + c_b) \\ (1+c_b) & -(\gamma^2 + c_b) \end{bmatrix} \begin{bmatrix} q_9 \\ q_{10} \end{bmatrix} = \begin{bmatrix} g_{11} \\ g_{12} \end{bmatrix}, \tag{5.31a}$$

$$g_2 = M_r' \begin{bmatrix} -(1+c_b) & -(\gamma + c_b) \\ -(\gamma + c_b) & -(\gamma^2 + c_b) \end{bmatrix} \begin{bmatrix} q_9 \\ q_{10} \end{bmatrix} = \begin{bmatrix} g_{21} \\ g_{22} \end{bmatrix}, \tag{5.31b}$$

where we have not shown the full vectors that are padded with $0 \in \mathcal{R}^{2x1}$ for clarity. We assume that we have full knowledge of the state vector and so the output of the system is simply the state variables we are seeking to optimize. Thus,

$$h(\zeta) = \begin{bmatrix} \boldsymbol{c_1} \\ \boldsymbol{c_2} \end{bmatrix} \zeta = \begin{bmatrix} q_4 \\ q_{10} \end{bmatrix} = \begin{bmatrix} \boldsymbol{e_1}^T \\ \boldsymbol{e_4}^T \end{bmatrix} \zeta, \tag{5.32}$$

where $\boldsymbol{c_j} \in \mathcal{R}^{1xr}$ are the output vectors, which are equal to unit vectors with $\boldsymbol{e_r}$ being the unit vector in the r direction. In this technique we attempt to find a transformation to transform the original nonlinear system into a linear system that can be controlled using state feedback. We follow the formulations found in [117] and [118]. In order to do so we define a new vector $\boldsymbol{v}$ such that,

$$\boldsymbol{v} = \begin{bmatrix} y_1^{(r_1)} \\ y_2^{(r_2)} \end{bmatrix} \tag{5.33}$$

where r_1 and r_2 are the relative degrees of the MIMO system. In order to find the relative degrees r_1, r_2 we continue taking time derivatives of the output $\boldsymbol{y}$ until the control $\boldsymbol{u}$ explicitly shows up. Here we make use of the Lie derivatives, such that

$$y_k^{(n)} = L_f^{(n)}(h_k) + \sum_{i=1}^{m} L_{g_i}^{(n)}(L_f^{(n-1)}(h_k))u_i \tag{5.34}$$

where the first-order Lie derivative is defined as,

$$L_f^{(1)}(h(x)) = \nabla h(x) \cdot f(x) = \sum_{i=1}^{N} \frac{\partial h}{\partial x_i} f_i. \tag{5.35}$$

An n^{th}-order Lie derivative is defined recursively as

$$L_f^{(n)}(h(x)) = \frac{\partial}{\partial x}\left[L_f^{(n-1)}(h(x))\right] \cdot f \tag{5.36}$$

with $L_f^{(0)}(h(x)) = h(x)$. Since $c_1 \cdot g_i = 0$ for $i = 1, 2$, we find that the relative degree of y_1 is 2, while $r_2 = 1$. Thus, the output of this system is

$$\begin{aligned} \boldsymbol{v} &= \begin{bmatrix} y_1^{(2)} \\ y_2^{(1)} \end{bmatrix} = F(q) + E(q) \begin{bmatrix} u_1 \\ u_2 \end{bmatrix} \\ \boldsymbol{v} &= \begin{bmatrix} L_f^{(2)}(h_1) \\ L_f^{(1)}(h_2) \end{bmatrix} + \begin{bmatrix} L_{g_1}(L_f^{(1)}(h_1(x))) & L_{g_2}(L_f^{(1)}(h_1(x))) \\ L_{g_1}(L_f^{(0)}(h_2(x))) & L_{g_2}(L_f^{(0)}(h_2(x))) \end{bmatrix} \begin{bmatrix} u_1 \\ u_2 \end{bmatrix} \end{aligned} \tag{5.37}$$

where we have assumed we have perfect knowledge of the external forces such that the error on the modeled loads δd is null. The matrix $E(q)$ can be found as

$$E(q) = \begin{bmatrix} -I_b^{-1}\left[(1+c_b)q_9 - (\gamma + c_b)q_{10}\right] & -I_b^{-1}\left[(1+c_b)q_9 + (\gamma + c_b)q_{10}\right] \\ (I_g + I_r)^{-1}\left[(\gamma + c_b)q_9 - (\gamma^2 + c_b)q_{10}\right] & -(I_g + I_r)^{-1}\left[(\gamma + c_b)q_9 + (\gamma^2 + c_b)q_{10}\right] \end{bmatrix}. \tag{5.38}$$

The vector $F(q)$ is,

$$F(q) = \begin{bmatrix} I_b^{-1} & 0 \\ 0 & (I_g + I_r)^{-1} \end{bmatrix} \left(\begin{bmatrix} -b_{44} & -b_{45} \\ -b_{54} & -b_{55} \end{bmatrix} \begin{bmatrix} q_9 \\ q_{10} \end{bmatrix} + \begin{bmatrix} f_e \\ RF_{T1}^* - RF_{T2}^* \end{bmatrix} \right), \tag{5.39}$$

where b_{55} is the linear damping coefficient between the spinning rotors and the earth fixed frame and b_{45} is the linear damping coefficient between the spinning rotors and the platform (such as friction in the bearings).

We isolate the terms in the matrix $E(q)$ that depend on the state, such that

$$E(q) = \begin{bmatrix} e_{11} & -e_{12} \\ e_{21} & -e_{22} \end{bmatrix} . \begin{bmatrix} q_9 & 0 \\ 0 & q_{10} \end{bmatrix} + \begin{bmatrix} e_{11} & e_{12} \\ -e_{21} & -e_{22} \end{bmatrix} . \begin{bmatrix} 0 & q_9 \\ q_{10} & 0 \end{bmatrix} \tag{5.40}$$

where

$$\begin{bmatrix} e_{11} & e_{12} \\ e_{21} & e_{22} \end{bmatrix} = \begin{bmatrix} -I_b^{-1}(1+c_b) & I_b^{-1}(\gamma + c_b) \\ (I_g + I_r)^{-1}(\gamma + c_b) & (I_g + I_r)^{-1}(\gamma^2 + c_b) \end{bmatrix} . \tag{5.41}$$

Here, we have set the partial derivative of the external forces vector with respect to the state vector as null. This assumption can be justified by the fact that the external forces are changing rather slowly with respect to these variables. To find the conditions when E^{-1} is ill-defined (for $c_b = 0$) we set $\det(E) = 0$ and obtain,

$$q_9 = \pm \gamma q_{10}. \tag{5.42}$$

Or, in other variables related to the speeds of the turbine and platform, the condition becomes

$$\gamma \dot{\theta}_1 = \pm \dot{\theta}_0 \tag{5.43}$$

which is nearly impossible to achieve since $\dot{\theta}_1 >> |\dot{\theta}_0|$. By definition, we have that

$$\boldsymbol{v} = \begin{bmatrix} \ddot{q}_4 \\ \dot{q}_{10} \end{bmatrix} = \begin{bmatrix} \dot{q}_9 \\ \dot{q}_{10} \end{bmatrix} . \tag{5.44}$$

To drive the error $\boldsymbol{e}$ to 0 we set

$$\boldsymbol{v} = -K_e \boldsymbol{e}, \tag{5.45}$$

where we have used the MATLAB function *place* to find the state-feedback gain K_e that sets the closed-loop poles of the system in the left-half plane. Thus, we can drive the state-space system

$$\dot{\boldsymbol{e}} = A_e \boldsymbol{e} + B_e \boldsymbol{v} \tag{5.46}$$

to the origin. The control variable $\boldsymbol{u}$ can be found from Eq. (5.37) and is,

$$\boldsymbol{u} = E^{-1} (\boldsymbol{v} - F) . \tag{5.47}$$

From $\boldsymbol{u}$ we can back-calculate the required damping of the generators B_j and can set the actuators (solid-state relays) to the appropriate setting.

5.4.2 SIMULINK Control Module

Feedback Linearization Implementation

The implementation of aforementioned control technique is shown in Fig. 5.5. Since there are no constraints on $\boldsymbol{u}$ in the feedback linearization technique, the algorithm can find the optimal damping coefficients B_1 or B_2 to be negative. Physically, this corresponds to energy being an input into the system, or running the generators as motors. This type of reactive control is well-known in the wave energy industry where the phase control of the device is extremely important. In this setting, however, a negative damping coefficient only serves to speed up the platform rotation. Thus we have inserted a saturation block that limits the values of B_j to physical limitations set by the generators, as described in Eq. (4.4). The E

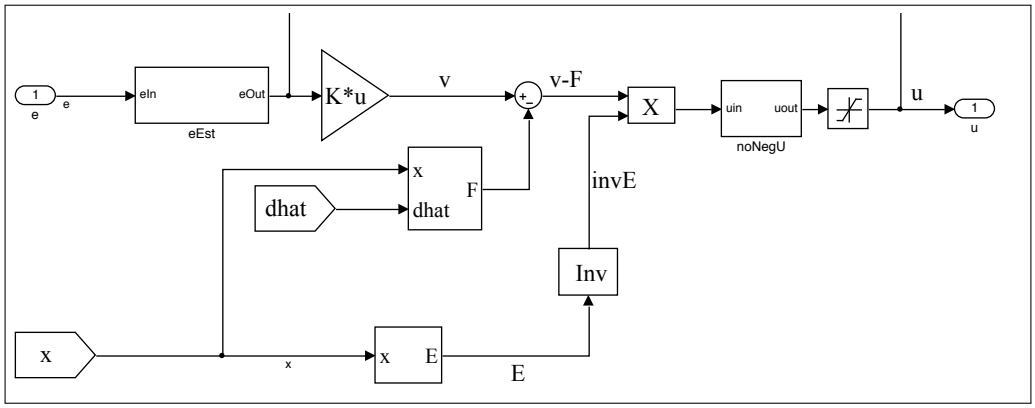

Figure 5.5: Simulink control module implementing Feedback Linearization technique.

block is determined by Eq. (5.40) and the F block is found in Eq. (5.39). We have also added a subsystem to estimate the velocity error of the platform, that is $\dot{\theta}_0 - \dot{\theta}_0^*$, which is essentially a time derivative of the position error of the platform over a predetermined time-horizon.

PD Controller Implementation

In the Simulink control module we also implemented the PD controller as described in Algorithm 3. Essentially, we estimate the total damping necessary on the turbines' rotors a priori to ensure that their rotational speed is near the target tip-speed ratio. Then, we divide up the damping between the two generators depending on the platform position. First, we check to see if the platform positional error is under a certain threshold. If it is not, then we turn one generator on at full strength, while turning the other generator off. If the platform is relatively close to the desired position, then we adjust the generator settings depending on the instantaneous platform speed. Taking into account the approach velocity prevents large overshoots in the platform position. This algorithm was implemented with 'If-Then' statements in Simulink, just as in the Arduino C++ code.

5.5 SIMULINK Hydrodynamics Model

The hydrodynamics module closely follows the potential-flow development in Chapter 2. We first discuss the external forces and then the terms proportional to the time-varying velocity and acceleration.

5.5.1 Hydrodynamic External Forces

The time-domain representation first-order wave exciting forces and the slow-drift moment constitute an external force vector, which can be applied to the state vector. The first-order time-domain forces were shown in Eq. (2.151) and the second-order forces in Eq. (2.154). Therefore the external force vector becomes,

$$\boldsymbol{F}_{ext,hydro} = A_0 \begin{bmatrix} 0 \\ \vdots \\ 0 \\ |\mathcal{X}_1(\beta,\sigma_o)|\cos(\varphi_1 - \sigma_o t) \\ |\mathcal{X}_2(\beta,\sigma_o)|\cos(\varphi_2 - \sigma_o t) \\ |\mathcal{X}_6(\beta,\sigma_o)|\cos(\varphi_6 - \sigma_o t) \\ \hline \sum \mathrm{Re}\left[\bar{K}_{3j}(\beta)e^{-i\sigma_o t}\right]\dot{\xi}_j^{(0)}(t) \end{bmatrix}, \boldsymbol{F}_{ext} \in \mathcal{R}^{10x1}. \tag{5.48}$$

In Simulink, we can use a two-dimensional interpolation look-up table (shown as green boxes in Fig. 5.6) in order to find the instantaneous values of $|\mathcal{X}_j^{(0)}(\beta,\sigma_o)|$ and $\bar{K}_{3j}$, as $\Theta_o(t)$ changes throughout the simulation. The time-averaging of the slow-drift moment occurs over one wave period. As shown in Fig. 5.6, the running time-averaging is performed by a discrete filter, whose window is defined as 1 wave period. In the simulations we ramp up the incident wave amplitude (over the first 15 periods), just as is done in the experimental wave tank. Thus, there are no issues simulating Eq. (2.154) in the time-domain, even though it is essentially undefined for $t < T$.

5.5.2 Hydrodynamic Damping

The time-domain representation of the first-order radiation damping is shown in Eqs. (2.150). For each coupled mode of motion of the platform, we must define separate state-space matrices. Each of the nonzero, coupled radiation state-space representations are shown in Fig. 5.7. The instantaneous velocity of the platform is taken from the state of the vector and used as an input to each of the state-space representations. These matrices are pre-calculated using the technique described in Sec. 2.9, before the simulation starts. The infinite-frequency added-mass and damping for each coupled mode of motion are added to the mass and damping matrices appropriately.

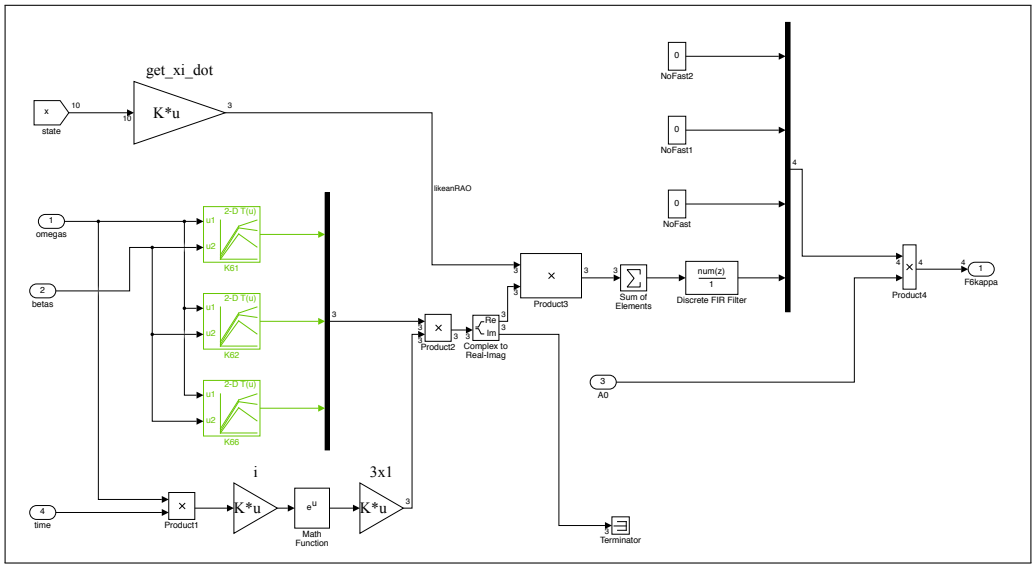

Figure 5.6: Simulink control module implementing the slow-drift moment on the platform.

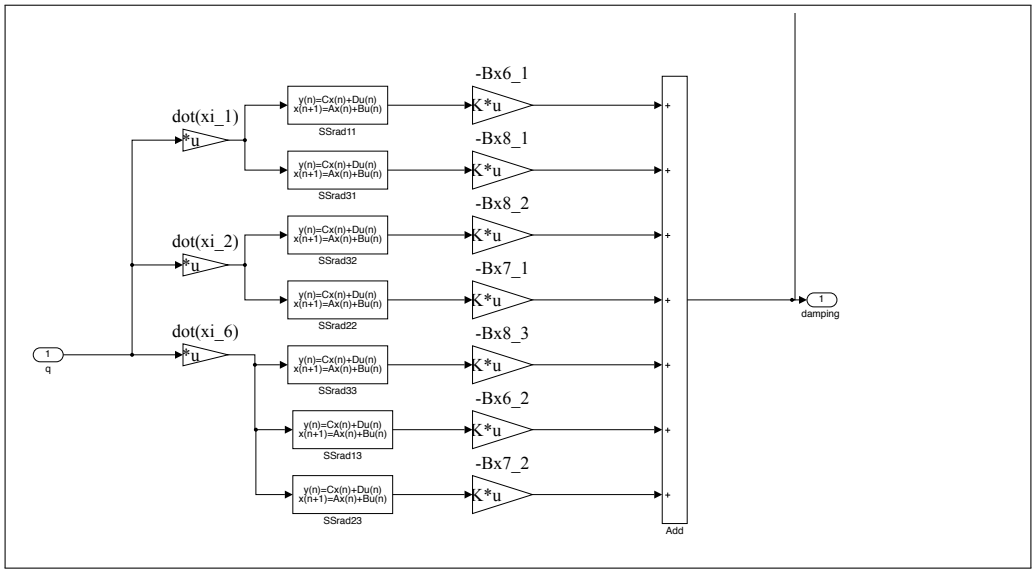

Figure 5.7: Simulink control module implementing convolution integrals for various modes of motion.

5.6 SIMULINK Aerodynamics Model

For fixed, counter-rotating vertical-axis wind turbines (i.e., the rotors only undergoes yaw motion) the instantaneous force on an airfoil is dependent on its azimuthal position, as well as the wind direction. In the simulations, we only take into account the effect of the platform yaw motion by using the relative wind direction in the lookup table for the torque on the turbines. We do not take into effect the added velocity of the blades due to the surging or swaying motion of the platform and turbines. However, these velocities are small compared

to the speed of the airfoils, especially at higher λ. Figure 5.8 shows the Simulink subsystem

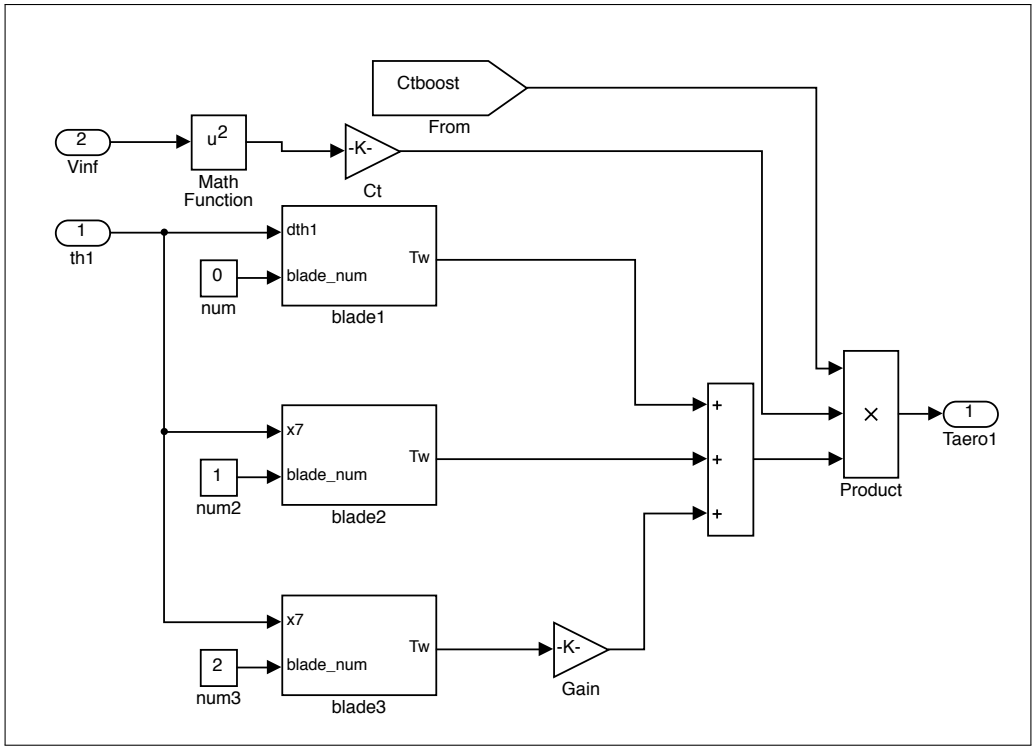

Figure 5.8: Aerodynamics module in Simulink used for emulating a vertical-axis wind turbine with variable incident wind speed and direction.

for calculating the instantaneous aerodynamic loads T_j^* for a three-bladed rotor. In the pre-processing script, the user can choose the number of equally-spaced blades of the turbine. Essentially, the blades instantaneous position is determined and then a torque coefficient is found from a lookup table, based on its position and the relative wind angle. The torque coefficient is then dimensionalized using the instantaneous wind speed. A more complex model would include the full effect of the turbine motion when calculating the aerodynamic loads.

5.7 Simulation Results

In this section, we compare the time-domain results from the model-scale experiments with the numerical model developed in the time domain.

5.7.1 Hydrodynamic-Induced Motion Comparison

The theory for transforming the potential-flow frequency domain results into the time domain was detailed in Sec. 2.9. We found a few experimental data sets that we could accurately

mimic after determining the proper value for the linear damping coefficient $\bar{\mathcal{B}}_{66}$. We nondimensionalize this linear damping coefficient as in [22], which was also shown in Eq. (2.156), where the authors report wave drift damping values for a 4-column barge. The determination of the 'best-fit' $\bar{\mathcal{B}}_{66}$ and its impact on the slow-drift motion of the platform are shown in Figs. 5.9, and 5.10, where we show time histories from experimental and numerical data. For instance, after iterating to find the damping value which led to the best agreement, it was determined that a value of 8200 for $\bar{\mathcal{B}}_{66}$ given the conditions depicted in Fig. 5.9 led to the best match. Another value for $\bar{\mathcal{B}}_{66}$, which is nearly 25% of the 'best-fit', is also used and the results from that simulation is shown simply to highlight the contribution of the linear damping coefficient.

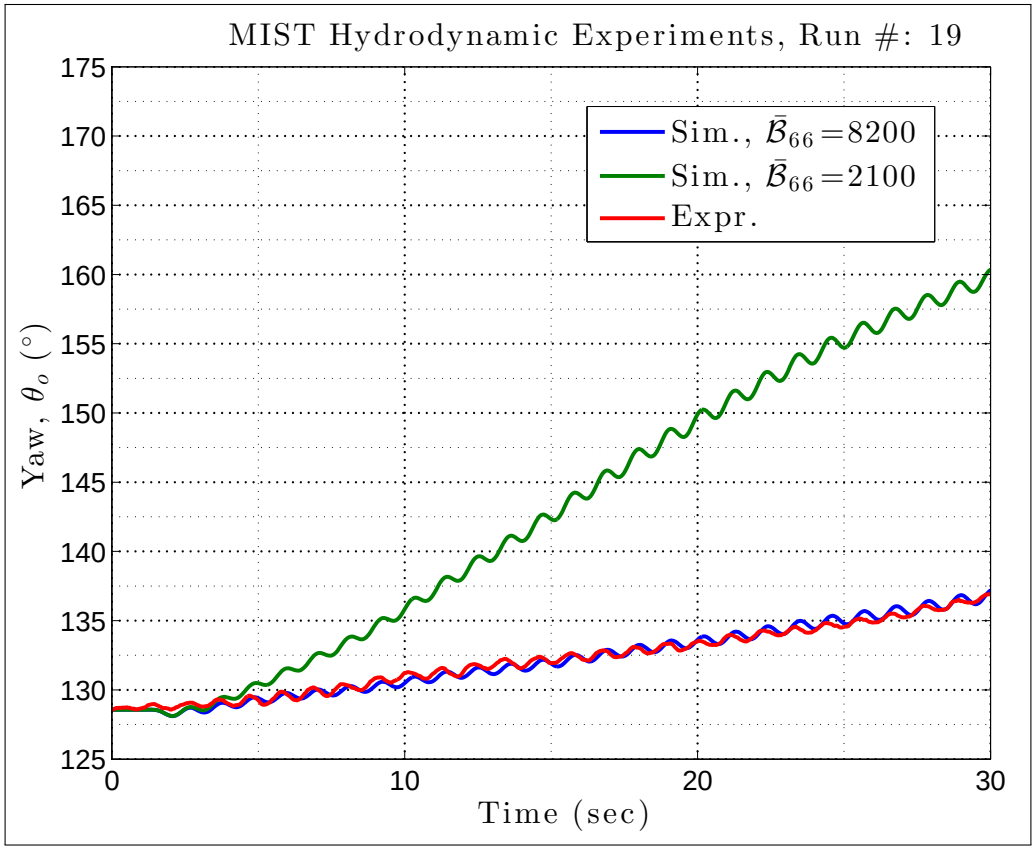

Figure 5.9: Time history of experimental platform motion (red curve) compared with two time histories of numerical simulations, each with different values of $\bar{\mathcal{B}}_{66}$ ($k_o a = 0.23$).

A similar methodology was used to come up with the values for the linear damping coefficient shown in Fig. 5.10. The values for $\bar{\mathcal{B}}_{66}$ that match most closely with both of the experiments are an order of magnitude higher than the highest wave-drift damping for a 4-column platform as reported in [22]. Thus, it seems like the flow separation and the effect of the universal joint have the largest influence on the damping of the slowly rotating platform. Further, it is clear from the best-fit $\bar{\mathcal{B}}_{66}$ values, shown in Figs. 5.9, and 5.10 that this coefficient depends on the incident-wave frequency and relative wave direction. From these

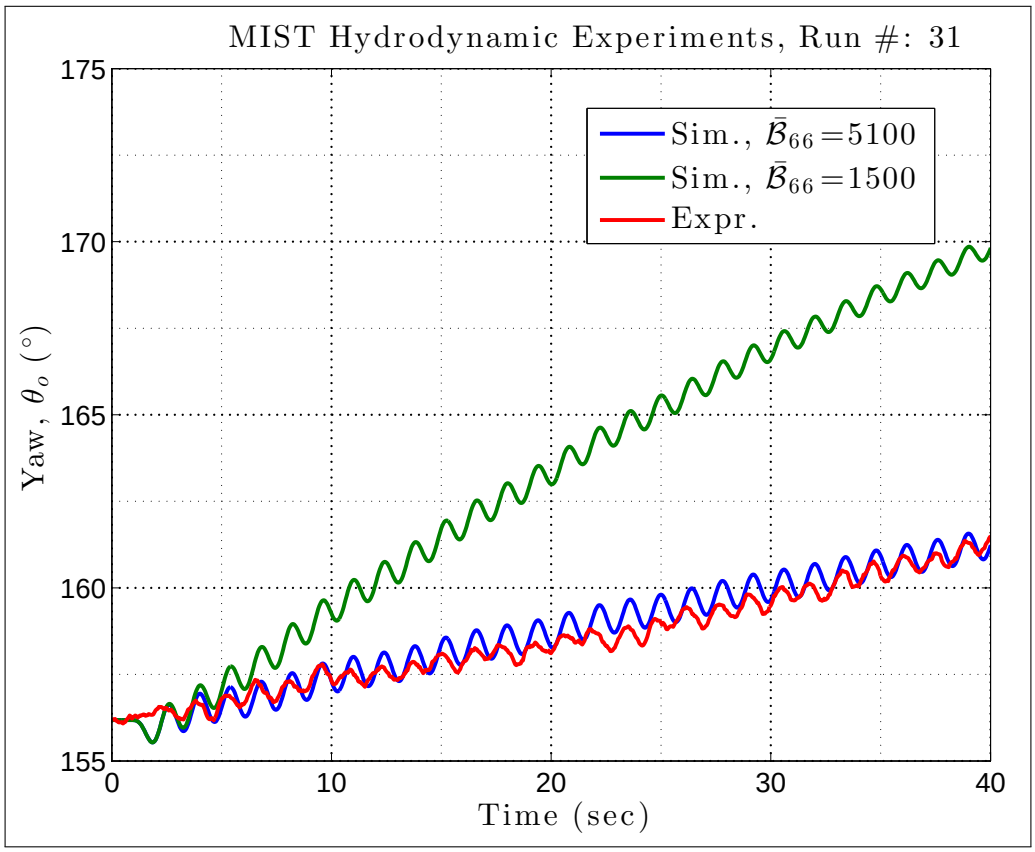

Figure 5.10: Time history of experimental platform motion (red curve) compared with two time histories of numerical simulations, each with different values of $\bar{\mathcal{B}}_{66}$ ($k_o a = 0.14$).

time-domain results, we conclude that the viscous forces dominate the slow-drift yaw motion of the platform, but it is difficult to estimate a quadratic drag coefficient from these tests. In general, it was difficult to find agreement between the experimental data and the numerical model for a few reasons. Namely, the universal joint had a large effect on the platform yaw motion. During some tests it was observed to 'seize' when the heave/pitch/roll motion was relatively large. At these moments, the joint is in tension and is no longer able to glide smoothly. Furthermore, it is difficult to estimate the linear damping coefficient $\bar{\mathcal{B}}_{66}$, which depends on this joint, the viscous effects and the wave-drift damping. The repeatability of the experimental data was also hard to achieve as well. Even if the water was quiescent, the platform tended to drift, since there is essentially no restoring moment in the yaw direction. Thus, it was difficult to position the platform in the correct position before each run. Some sort of magnetic locking device positioned above the water should be utilized in future tests to release the platform from a fixed position at the desired time.

5.7.2 Aerodynamic-Induced Motion Comparison

In order to prove that the control algorithm worked properly, we ran tests without the presence of waves. Essentially we used the water column as a medium that allowed us to freely rotate the platform relative to the Earth-fixed frame. The results of one of such tests are shown in Fig. 5.11 (red curve). The data are compared with that of the simulations

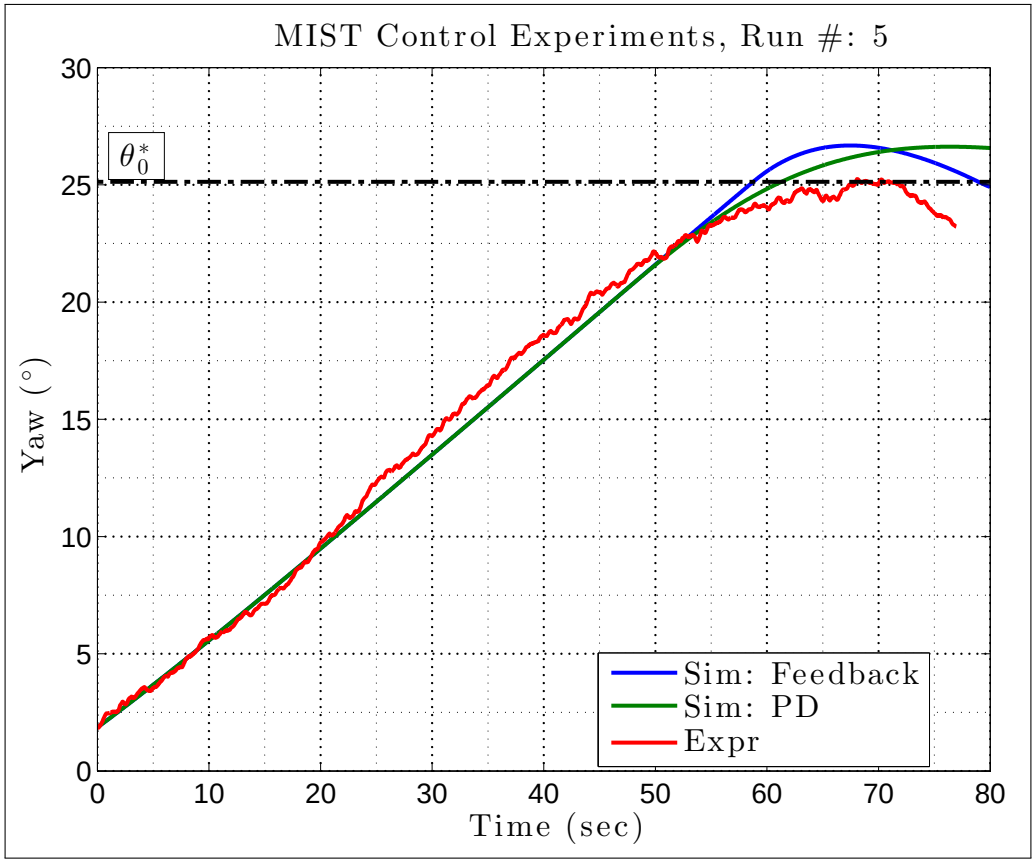

Figure 5.11: Time history of experimental platform motion (red curve) compared with two time histories of numerical simulations, each with a different type of control, without the presence of waves. In this simulation $\mathcal{B}_{66}$ is set to 1 N/rad/s (unable to nondimensionalize since A_o=0 in this simulation)

using two different control algorithms, as described in Sec. 5.4.2. The goal of the control effort is to reorient the platform such that its yaw orientation matches θ_0^*, as shown by the black dash-dot line in Fig. 5.11. A theoretical non-linear control technique, called Feedback Linearization ('Feedback', blue curve) assumes no foreknowledge of system, but was not used in the experiments while the Proportional-Derivative controller implemented ('PD', green curve) requires the total generator damping that is necessary to keep the rotors spinning at constant speed. As in the previous simulation, we varied the value of $\mathcal{B}_{66}$ until the time-constant of the simulations matched that of the experiments. For reference, $\mathcal{B}_{66} = 1$ N/(rad/s) corresponds to 2% and 7% of the damping used in the simulations shown in

Fig. 5.9. Once the linear drag of the platform is determined the simulation results agree well with the experimental results.

5.7.3 Aerodynamic and Hydrodynamic-Induced Motion Comparison

The aerodynamic, hydrodynamic and generator control modules were all used simultaneously to solve for the position of the platform in incident and regular waves. The results of these simulations are shown in Figs. 5.12 and 5.13.

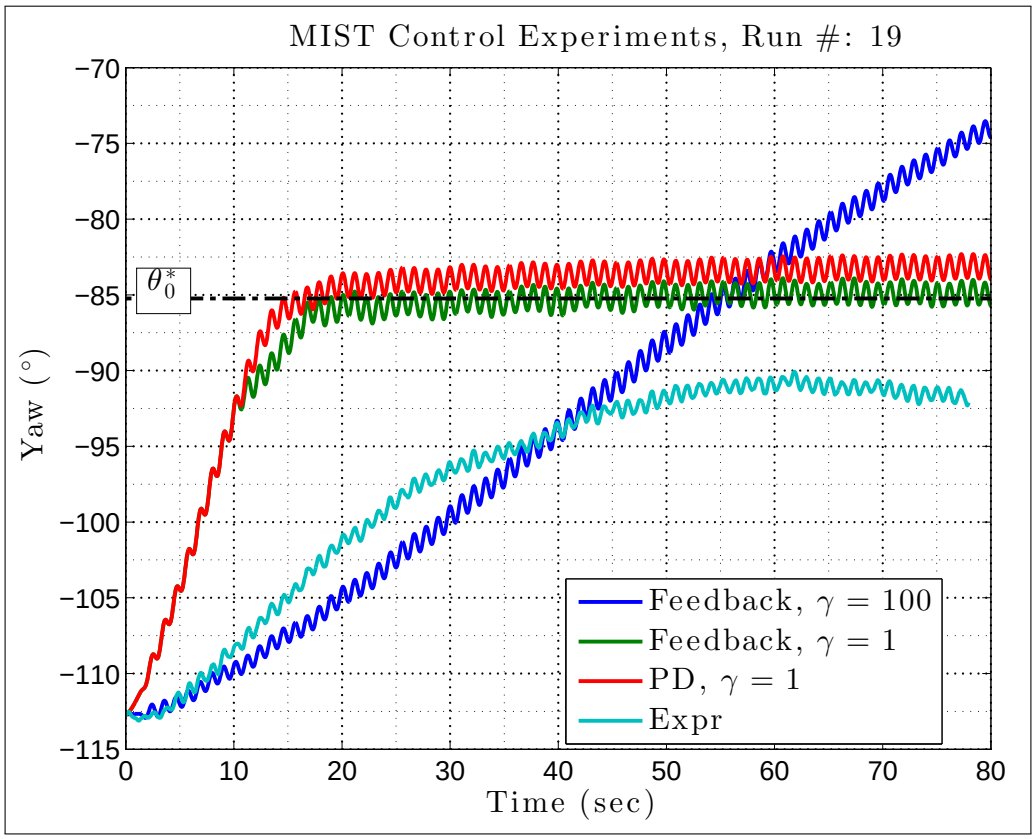

Figure 5.12: Time history of experimental platform motion (light blue curve) compared with time histories of numerical simulations, in the presence of waves. The gearbox ratio γ of the generators is varied.

In these figures the time series of the platform yaw motion $\theta_0(t)$ is shown (light blue curve), along with time series simulated by the SIMULINK model. The dark blue lines represent the best attempt to numerically recreate the experimental data. As the diverging light blue and dark blue curves in Fig. 5.13 show, the numerical model is not able to recreate the platform motion in all scenarios. However, if the gearbox ratio is changed to unity, which occurs in a direct-drive generator, then the control strategies are able to redirect the platform to the appropriate heading, θ_0^*, as shown by the red and green lines in Figs. 5.12

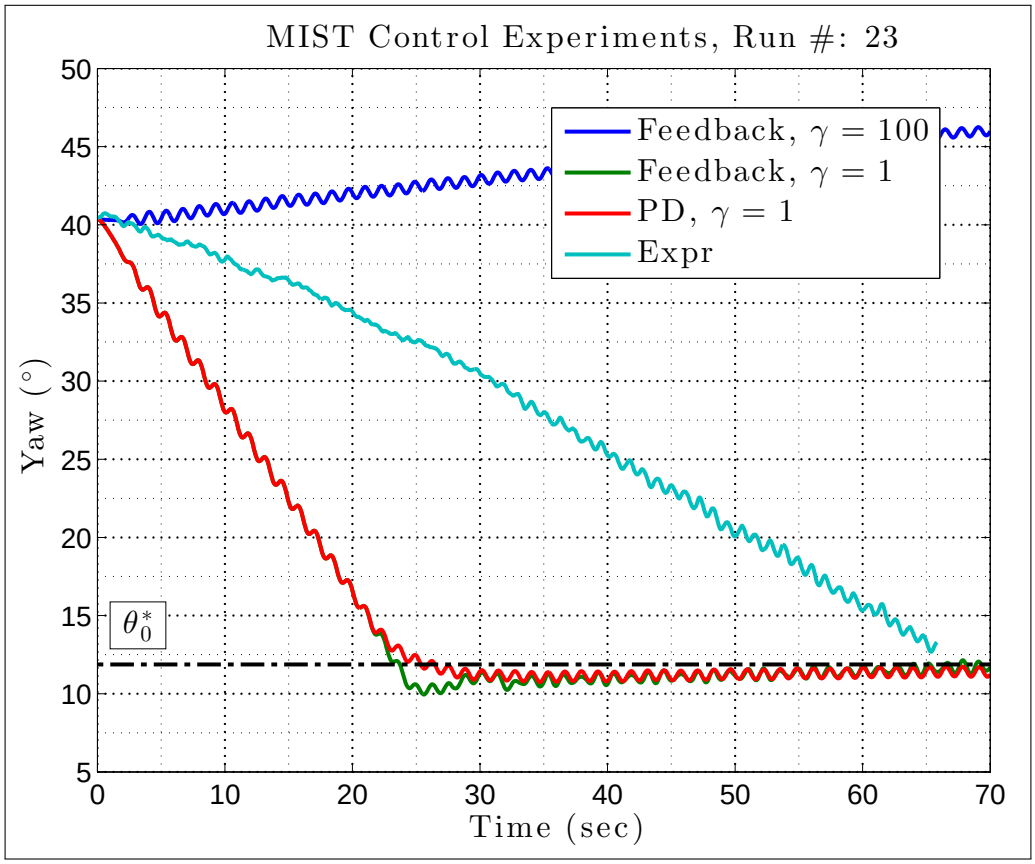

Figure 5.13: Time history of experimental platform motion (light blue curve) compared with time histories of numerical simulations, in the presence of waves. The gearbox ratio γ of the generators is varied.

and 5.13. A discussion on the relative importance of the gearbox ratio on controlling the platform yaw orientation is given in Sec. 5.8.

5.8 Effect of Gearbox on Platform Yaw Control

In this section, we estimate the possibility of controlling the yaw orientation of the platform simply using the aerodynamic torque from the counter-rotating turbines, as described in Chapter 4. In order to have any chance to control the platform we must have that,

$$\mathrm{O}\left(M_6^{aero}\right) \gtrsim \mathrm{O}\left(M_6^{hydro}\right), \tag{5.49}$$

where M_6^{aero}, M_6^{hydro} represent the yaw moment on the platform from the aerodynamics and hydrodynamics, respectively. First, we consider the order-of-magnitude of the steady moment on the platform from Fig. 2.18. From the potential flow calculations derived in

Chapter 2, we estimate that,

$$M_6^{hydro} = \mathrm{O}\left(\rho_o g N_{col} \pi a^2 A_o^2\right). \tag{5.50}$$

From Chapter 3 and the discussion on the drivetrain system in Sec 5.1, we estimate that the order of magnitude for the aerodynamic torque is,

$$M_6^{aero} = \mathrm{O}\left(\frac{\rho_a U_\infty^2 c N_b R H}{\gamma}\right). \tag{5.51}$$

To obtain this order of magnitude for the aerodynamic torque on the platform, we set $\ddot{\theta}_1 = \dot{\omega}_1 = 0$ and $B_1 = B_{max}$, $B_2 = 0$ in Eq. (5.8) to represent the case of a constant rotor speed and maximum applied differential torque to the platform. Then, the equation of motion for the platform becomes independent of the rotational speeds of the platform and rotor and the above expression comes from the fact that $\mathrm{O}\left(RF_{T1}^* - RF_{T2}^*\right) = \mathrm{O}\left(R \cdot \rho_a U_\infty^2 c N_b H\right)$. The gearbox ratio is in the denominator (with $\gamma > 1$) since the gearbox increases the rotational speed (so that the generator can operate at optimal efficiency) but reduces the torque applied on the platform.

To examine the relative size of these hydrodynamic, aerodynamic and geometric quantities, we make a few order-of-magnitude assumptions about the environmental conditions. In many locations,

$$\mathrm{O}\left(\frac{U_\infty^2}{g A_o}\right) = \mathrm{O}\left(10^1\right). \tag{5.52}$$

Comparing the remaining quantities, the controllability condition becomes

$$\mathrm{O}\left(\frac{N_b c R H}{\gamma}\right) > 10^2\, \mathrm{O}\left(N_{col} \pi a^2 A_o\right), \tag{5.53}$$

where we have inserted the orders of magnitude of the ratio of densities of air and water. Let us compare the order of magnitude of the surface areas of the of the turbine's blades and the platform, as

$$\frac{N_b c H}{N_{col} \pi a^2} \approx 5 \text{ for the MIST platform.} \tag{5.54}$$

Thus, one of the necessary conditions for control of the MIST platform is that

$$\boxed{R \gtrsim 20 A_o \gamma} \tag{5.55}$$

Since the MIST platform has $\gamma = 100$, this condition is generally not achievable. However, for a direct-drive system where $\gamma = 1$, it is generally possible, depending on the exact geometric dimensions of the turbines. As Figs. 5.12 and 5.13 show, the choice of gearbox ratio can determine whether the platform can achieve its desired orientation or not.

Chapter 6

Conclusions

This work has examined the concept of installing two, counter-rotating vertical-axis wind turbines on a single, floating platform. Current state-of-the-art floating offshore wind platforms use commercially-available, horizontal-axis wind turbines. However, these turbines inherently present challenges to ocean engineers who must design the platform to withstand large storms, such as those with 500-year return periods. Generally, these platforms are large and expensive per MW of installed capacity. Other researchers have begun to reconsider vertical-axis wind turbines to reduce the capital costs associated with these technologies. It has become evident, however, that in order for these turbines to gain traction in the offshore wind industry, a large gain in efficiency and reliability must be observed. Thus, building off of current onshore research, using closely-spaced, counter-rotating turbines may achieve a much greater power density per planform area of platform than would be possible using horizontal-axis turbines. The main determinants in the efficiency of the counter-rotating turbines are their rotational speeds (relative to the incident wind speed) and their orientation (relative to the incident wind direction). A strategy to control the platform's orientation and the turbine's rotational speed in the presence of regular waves is created for model tests.

In order to simulate the hydrodynamics of the floating platform, potential theory was utilized, taking into account the slow-drift yaw motion of the platform. The velocity potential takes the form of a double perturbation series– one with increasing orders related to the wave amplitude, the other related to the slow-drift velocities of the platform. Although this analysis had already been performed in many instances in the literature, no researcher had ever tried to compare the simulation of a body undergoing slow-drift yaw rotation to model tests in the time domain. Particular attention was paid to steady, second-order terms that are spatially dependent. For instance, the steady, second-order potential does not contribute to the total yaw moment on the platform because the platform is rotating about its geometric center. However, other terms arise due to the Taylor expansion of the pressure about the mean position of the platform. These terms depend on the orientation of the platform and the relative wave heading. Standard techniques, such as the decomposition of the convolution integral into a state-space representation, allowed the hydrodynamics problem, formulated in the frequency domain, to be simulated in the time-domain.

The accurate simulation of the aerodynamics of vertical-axis wind turbines is difficult to perform due to the varying conditions the airfoil faces as it circumnavigates the central rotor. This field is ripe with techniques to estimate the forces on the airfoil using analytical methodologies such as blade element momentum theory and vortex methods, as well as computational fluid dynamics techniques such as unsteady Reynolds-averaged numerical simulations and large-eddy simulations. An in-house software, 3DG, developed by researchers at the UC Berkeley Mathematics Department was employed for simulations with increasingly complex domains. At first, a single, static NACA0012 airfoil was simulated under a wide

variety of angles of attack in order to compare the results with published lift and drag data. Following validation of the code under a low-Reynolds regime, the method was extended to a constant spinning vertical-axis wind turbine. The results compared favorably to a model test performed by Sandia National Labs under similar circumstances. Finally, the method was used to simulate counter-rotating vertical-axis wind turbines using a novel element flipping technique, developed by a PhD student in the Mathematics Department. The magnitude of the results compare favorably to field tests performed by researchers at the California Institute of Technology, although the directional dependence is quite different.

A platform, called the Multiple, Integrated and Synchronized Turbines (MIST) platform was designed and built to prove the concept of controllability of a floating platform with counter-rotating turbines. The model was tested at the UC Berkeley Physical-Model Testing Facility, where it is difficult to provide laminar wind above the tow tank. Thus, a hybrid simulation technique was employed to emulate the effect of the vertical-axis wind turbines. The turbines were d with actuators called the Wind-Input Generators (WIGs). The actuators were controllable motor/propeller units that are used for remote controlled model airplanes. Using sensors and microcontrollers, the thrust force generated by these actuators could be controlled to mimic the tangential force developed by the airfoils on a vertical-axis wind turbine. The WIGs were attached to a transmission system that linked the counter-rotating turbines so that they had equal and opposite rotation speeds. The drivetrain system included gearboxes and generators that transformed the mechanical power to electrical power, much like in an actual wind turbine. The goal of the model tests was to control the orientation of the platform simply by modifying the electrical circuits of the generators. Thus, without using any additional power, the yaw orientation of the platform could be controlled to optimize the power produced by the counter-rotating turbines. Due to the hydrodynamic yaw moment, it was not possible to control the yaw orientation under all circumstances. However, there were a variety of tests in regular waves where the desired heading was achieved. In irregular waves with a directional spreading function the hydrodynamic yaw moment should be reduced and the control of the yaw orientation should be easier.

A numerical simulation tool was developed using hydrodynamic potential theory as well as a simplified aerodynamics module. A non-linear control strategy, called Feedback Linearization technique was implemented, along with a simpler proportional-derivative controller. These modules were coupled together in the time-domain using MATLAB's control software, Simulink. The simulations were compared to the experimental time series when the platform and turbine is subject to solely aerodynamics or hydrodynamics in order to find obtain the frictional and damping coefficients. When the system is subject to aerodynamics and hydrodynamics, the numerical model does not properly recreate the experimental time series. This discrepancy is most likely due to the non-linear nature of the universal joint and other simplifications made in the model, including ignoring the non-horizontal motion. However, the simulations prove that if the generator is direct-drive (no gearbox), then a controller can easily reorient the platform under normal circumstances. From the discussion in Sec. 5.2, it is clear that determining the stable equilibria positions of the platform in a variety of environmental conditions is critical to the successful power optimization of

the platform. Only a model test in a true wind-wave tank would prove it, but we expect that one or both of the 'doublet-like' and 'reverse-doublet-like' configurations to be stable equilibria positions for the platform. If this were true, the generator control could only be used sparingly, in order to reduce misalignment of the platform relative to the incident wind direction.

6.1 Synopsis of Key Findings

The main accomplishments of this work are categorized by chapter and are summarized in the following points:

- Hydrodynamics of Multi-Column Platform
  - Developed new expressions for the steady yaw moment on a multi-column platform using direct pressure integration technique
- Aerodynamics of Vertical-Axis Wind Turbines
  - Validated Implicit Large-Eddy Simulation model for static airfoils and single turbines with existing data at low Re
  - Utilized novel element flipping technique to extend numerical method to counter-rotating turbines
  - Confirmed existence of synergistic effect between counter-rotating turbines
- Time-Domain Simulations
  - Implemented non-linear control model to achieve position and velocity tracking of platform and rotors
  - Showed how direct-drive system can increase platform re-orientation capabilities

6.2 Parallels in Modern Industry

It was only after the design of the MIST platform that E. Koukina suggested a parallel in the model helicopter industry: the development of the tandem rotor helicopter. Figure 6.1 shows a picture of a standard single-rotor helicopter as well as a Boeing-Vertol CH-46 Chinook tandem rotor helicopter. In order to control the yaw orientation of the helicopter the tail rotor provides a thrust force. Otherwise, the reaction torque from the main rotor would cause the helicopter to spin out of control (this occurs when the tail rotor is damaged). In order to increase the payload of helicopters, aerospace engineers designed helicopters with dual rotors to increase the maximum lift. Rather than increasing the size of the tail rotor, engineers realized they could make it unnecessary by making the rotors counter-rotate. By

using swashplates on both of the rotors, the pilot is able to tilt the rotors in opposite directions. In this way, the net roll moment cancels out between the rotors, but a yaw moment is produced [119]. Clearly, the rotors must be synchronized through a single drive

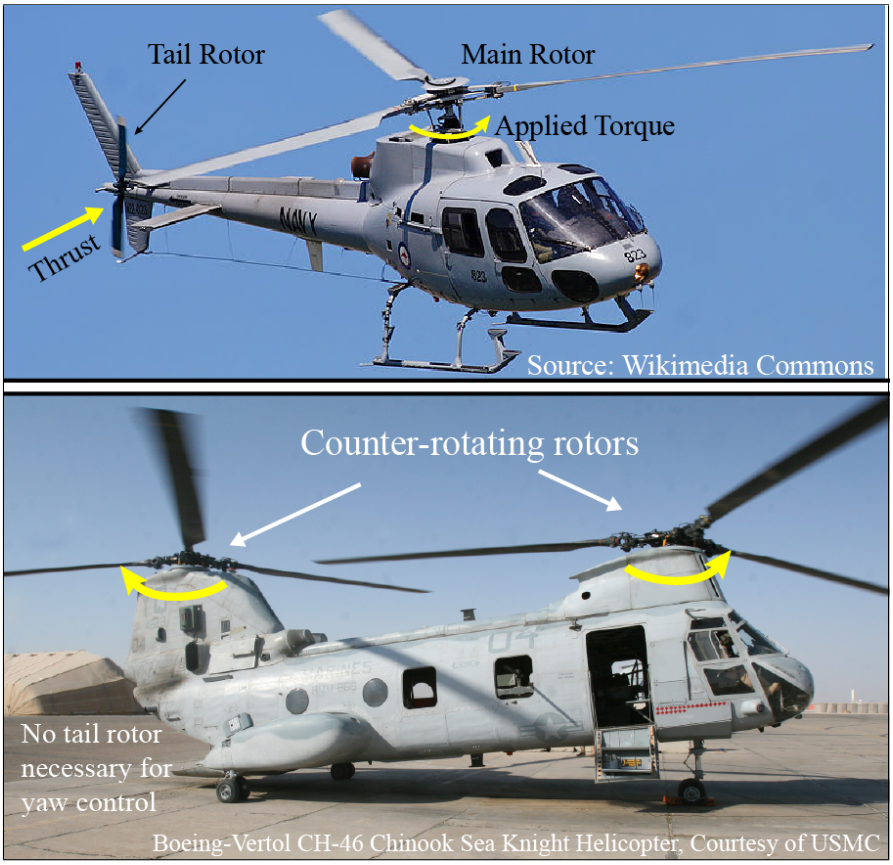

Figure 6.1: Single rotor with tail rotor and tandem rotor helicopters with counter-rotating rotors.

system or else the spinning helicopter blades would collide. Newer helicopter designs (not pictured) have counter-rotating rotors on a single rotor. A future design of the MIST platform would include many of the lessons learned from the development of this technology, if such information is publicly available.

6.3 Future Work

We discuss the many extensions of this work chapter by chapter, since the topics are quite widely varying.

- Chapter 2

    1. Include effect of interacting cylinders in slow-drift analysis

2. Extend method to bichromatic and fully irregular seas
3. Explicitly calculate wave-drift damping terms using direct pressure integration

- Chapter 3

1. Use URANS (or other middle fidelity method) to simulate VAWTs at a range of Re
2. Implement Detached-Eddy Simulation to increase Re range of implicit LES
3. Develop a coupled fluid-structure interaction algorithm to more accurately model the spinning turbine
4. Expand element flipping technique to 3D to model counter-rotating turbines with spanwise effects
5. Explore synergistic mechanism of counter-rotating turbines using spinning (or stationary) cylinders, instead of turbines

- Chapter 4

1. Change power take-off to a direct-drive system
2. Create new control strategy without use of timing belt
3. Explore other methods of wireless data transfer to increase latency
4. Install voltage regulator on motor controllers to ensure uniformity across models
5. Install load cells on every actuator
6. Implement a motion tracking system above tank to accurately capture slow-drift surge, sway and yaw motions
7. Change actuator to reduce inertia, such as a ducted fan

- Chapter 5

1. Estimate moment on platform from aerodynamic forces during misaligned wind conditions
2. Implement more robust control strategy, such as Sliding Mode Control
3. Incorporate one-way or two-way coupling between aerodynamics and hydrodynamics
4. Add irregular seas and directional spreading functions capabilities to the hydrodynamics module

We look forward to future researchers adding to the techniques and body of research regarding floating wind turbines.

6.4 Path to Commercialization

At the time of publication, a French company, Nenuphar, is attempting to commercialize this technology, which they call the *Twinfloat*[1]. Although the author was in communication with Nenuphar employees regarding a joint patent, the talks fell through and Nenuphar has continued independently. Their platform appears to be a multi-column semi-submersible with counter-rotating turbines, perhaps with a turret system to allow yaw rotation, as shown in Fig. 6.2. However, their freedom to operate is already limited due to a patent issued to

Figure 6.2: Rendering of Nenuphar Wind's *La Twinfloat*.

Technip in 2014 [120]. In this patent, the authors write that,

'*(The platform is) characterized by a first wind turbine of the pair having a clockwise rotation and a second wind turbine of the pair having a counter clockwise rotation..., wherein the first wind turbine is capable of operating at a different speed than the second wind turbine to create a gyroscopic torque differential in the system around a centroid of the system, wherein said gyroscopic torque differential is allowed to twist the floating module to a new orientation.*'

The optimization of energy from this platform is very much still an open topic and more research and development is needed in order to prove various control strategies. We are excited and humbled that the ideas contained in this thesis have spread around the world and may contribute to a cleaner energy future.

[1] www.nenuphar-wind.com

References

[1] E. Koukina, "Simulation of Wind-Loading Torque on Turbines at Model Scale," M.S. Thesis, University of California Berkeley, Berkeley, CA, Dec. 2014.

[2] M. F. Barone and J. Murray, "The development of CACTUS: a wind and marine turbine performance simulation code." Sandia National Laboratories, Tech. Rep., 2010. [Online]. Available: http://www.osti.gov/scitech/biblio/1038169

[3] I. Paraschivoiu, *Wind turbine design: with emphasis on Darrieus concept*. Presses inter Polytechnique, 2002.

[4] J. O. Dabiri, "Potential order-of-magnitude enhancement of wind farm power density via counter-rotating vertical-axis wind turbine arrays," *Journal of Renewable and Sustainable Energy*, vol. 3, no. 043104, p. 1:14, 2011.

[5] M. El-Ashry, "Renewables 2012 Global Status Report," Renewable Energy Policy Network for the 21st Century, Tech. Rep. REN21, 2012. [Online]. Available: http://www.ren21.net/Portals/0/documents/Resources/GSR2012_low%20res_FINAL.pdf

[6] T. D. Ashwill, "Measured Data for the Sandia 34-Meter Vertical-Axis Wind Turbine," Sandia National Labs., Albuquerque, NM (United States), Tech. Rep. SAND91-2228, 1992. [Online]. Available: http://www.osti.gov/energycitations/product.biblio.jsp?osti_id=10170111

[7] H. J. Sutherland, D. E. Berg, and T. D. Ashwill, "A retrospective of VAWT technology," Sandia National Laboratories, Tech. Rep. SAND2012-0304, Jan. 2012. [Online]. Available: http://energy.sandia.gov/wp/wp-content/gallery/uploads/SAND2012-0304.pdf

[8] B. C. Owens, J. E. Hurtado, J. A. Paquette, D. T. Griffith, and M. Barone, "Aeroelastic Modeling of Large Offshore Vertical-axis Wind Turbines: Development of the Offshore Wind Energy Simulation Toolkit," in *Proceedings of 54th AIAA/ASME/ASCE/AHS/ASC Structures, Structural Dynamics, and Materials Conference*, Boston, MA, Apr. 2013.

[9] M. Borg and M. Collu, "Offshore floating vertical axis wind turbines, dynamics modelling state of the art. Part III: Hydrodynamics and coupled modelling approaches," *Renewable and Sustainable Energy Reviews*, vol. 46, pp. 296–310, Jun. 2015.

[10] J. M. Jonkman and M. L. Buhl Jr, "FAST user's guide," Tech. Rep., 2005. [Online]. Available: https://wind.nrel.gov/designcodes/simulators/fast/FAST.pdf

[11] M. J. Dvorak, C. L. Archer, and M. Z. Jacobson, "California offshore wind energy potential," *Renewable Energy*, vol. 35, no. 6, pp. 1244–1254, 2010.

[12] A. Goupee, B. Koo, K. Lambrakos, and R. Kimball, "Model Tests for Three Floating Wind Turbine Concepts," Apr. 2012.

[13] J. Azcona, F. Bouchotrouch, M. González, J. Garciandía, X. Munduate, F. Kelberlau, and T. A. Nygaard, "Aerodynamic Thrust Modelling in Wave Tank Tests of Offshore Floating Wind Turbines Using a Ducted Fan," *Journal of Physics: Conference Series*, vol. 524, no. 1, Jun. 2014.

[14] M. J. Fowler, R. W. Kimball, D. A. Thomas, and A. J. Goupee, "Design and testing of scale model wind turbines for use in wind/wave basin model tests of floating offshore wind turbines," in *Proc. of 32nd International Conference on Ocean, Offshore and Arctic Engineering (OMAE-13)*, Nantes, France, 2013, OMAE2013-10122.

[15] I. Bayati, M. Belloli, A. Facchinetti, and S. Giappino, "Wind Tunnel Tests on Floating Offshore Wind Turbines: A Proposal for Hardware-in-the-Loop Approach to Validate Numerical Codes," *Wind Engineering*, vol. 37, no. 6, pp. 557–568, Dec. 2013.

[16] M. Hall, J. Moreno, and K. Thiagarajan, "Performance Specifications for Real-Time Hybrid Testing of 1:50-Scale Floating Wind Turbine Models," in *Proc. of 33rd ASME International Conference on Offshore Mechanics and Arctic Engineering (OMAE-14)*, San Francisco, CA, Jun. 2014, OMAE2014-24497.

[17] H. R. Martin, "Development of a scale model wind turbine for testing of offshore floating wind turbine systems," Ph.D. dissertation, Maine Maritime Academy, 2011.

[18] R. W. Yeung, "Added mass and damping of a vertical cylinder in finite-depth waters," *Applied Ocean Research*, vol. 3, no. 3, pp. 119–133, 1981.

[19] J. E. W. Wichers and V. Sluijs, "The Influence of Waves on the Low-Frequency Hydrodynamic Coefficients of Moored Vessels," in *Proc. of 11th Annual OTC*, Houston, TX, 1979, pp. 2313–2324.

[20] O. J. Emmerhoff, "The slow drift motions of offshore structures," PhD Thesis, Massachusetts Institute of Technology, Sep. 1994.

[21] P. D. Sclavounos and O. J. Emmerhoff, "The Slow-Drift Response of Multi-Leg Structures in Regular and Random Waves," Massachusetts Institute of Technology, Cambridge, MA, MIT Sea Grant Technical Report MITSG 93-10J, 1992.

[22] O. J. Emmerhoff and P. D. Sclavounos, "The Simulation of Slow-Drift Motions of Offshore Structures," *Applied Ocean Research*, vol. 18, no. 2–3, pp. 55–64, Apr. 1996.

[23] O. J. Emmerhoff and P. D. Sclavounos, "The slow-drift motion of arrays of vertical cylinders," *Journal of Fluid Mechanics*, vol. 242, pp. 31–50, Sep. 1992.

[24] J. N. Newman, "Wave-drift damping of floating bodies," *Journal of Fluid Mechanics*, vol. 249, pp. 241–259, Apr. 1993.

[25] S. Finne and J. Grue, "On the complete radiation-diffraction problem and wave-drift damping of marine bodies in the yaw mode of motion," *Journal of Fluid Mechanics*, vol. 357, pp. 289–320, Feb. 1998.

[26] J. Grue and E. Palm, "Wave drift damping of floating bodies in slow yaw motion," *Journal of Fluid Mechanics*, vol. 319, pp. 323–352, Jul. 1996.

[27] J. Grue, "Interaction Between Waves and Slowly Rotating Floating Bodies," in *Waves and Nonlinear Processes in Hydrodynamics*, ser. Fluid Mechanics and Its Applications, J. Grue, B. Gjevik, and J. E. Weber, Eds. Springer Netherlands, 1996, no. 34, pp. 71–82.

[28] W. Bao, T. Kinoshita, S. Sunahara, M. Li, and M. Tsukui, "Wave-drift damping in slow surge–sway–yaw coupling motions of a cylinder array," *Journal of Marine Science and Technology*, vol. 5, no. 4, pp. 189–203, Dec. 2000.

[29] T. Kinoshita and W. Bao, "Hydrodynamic forces acting on a circular cylinder oscillating in waves and a small current," *Journal of Marine Science and Technology*, vol. 1, no. 3, pp. 155–173, Jun. 1996.

[30] T. Kinoshita, W. Bao, and S. Sunahara, "The hydrodynamic forces acting on a cylinder array oscillating in waves and current," *Journal of Marine Science and Technology*, vol. 2, no. 3, pp. 135–147, Sep. 1997.

[31] Y. Liu and D. K. P. Yue, "On generalized Bragg scattering of surface waves by bottom ripples," *Journal of Fluid Mechanics*, vol. 356, pp. 297–326, Feb. 1998.

[32] J. Grue and E. Palm, "The mean drift force and yaw moment on marine structures in waves and current," *Journal of Fluid Mechanics*, vol. 250, pp. 121–142, May 1993.

[33] T. F. Ogilvie and E. O. Tuck, "A Rational Strip Theory of Ship Motions: Part I," University of Michigan, Technical Report, Mar. 1969. [Online]. Available: http://deepblue.lib.umich.edu/handle/2027.42/91655

[34] J. V. Wehausen, "Lecture Notes on Ship Hydrodynamics, Course NA241, Chapter IX," in *Hydrodynamics of Ships and Ocean Systems (for Course ME241), Chapter 7.* University of California at Berkeley, 1978.

[35] P. D. Sclavounos, "Slow-drift oscillations of compliant floating platforms." in *Proceedings of 7th BOSS Conference*, vol. 2. Boston, MA: Pergamon Press, 1994, pp. 525–568.

[36] C. J. R. Garrett, "Wave forces on a circular dock," *Journal of Fluid Mechanics*, vol. 46, no. 01, pp. 129–139, 1971.

[37] A. N. Williams and Z. Demirbilek, "Hydrodynamic interactions in floating cylinder arrays—I. Wave scattering," *Ocean Engineering*, vol. 15, no. 6, pp. 549–583, 1988.

[38] A. N. Williams and T. Rangappa, "Approximate hydrodynamic analysis of multi-column ocean structures," *Ocean Engineering*, vol. 21, no. 6, pp. 519–573, Aug. 1994.

[39] M. Okushu, "The Analysis of Wave Forces Acting Upon Multi-Float Platforms," in *Hydrodynamics in Ship and Ocean Engineering*, ser. Transactions of the West-Japan Society of Naval Architects (reprinted), 1976, M. Kashiwagi, Ed., Kyusu University, Apr. 2001, no. 51, pp. 211–232.

[40] T. Matsui and T. Tamaki, "Hydrodynamic interaction between groups of vertical axisymmetric bodies floating in waves," in *Proc. Int. Symposium on Hydrodynamics in Ocean Engineering*, vol. 2, Trondheim, Norway, 1981, pp. 817–836.

[41] O. Yilmaz, "Hydrodynamic Interactions of Waves with Group of Truncated Vertical Cylinders," *Journal of Waterway, Port, Coastal, and Ocean Engineering*, vol. 124, no. 5, pp. 272–279, 1998.

[42] Q. Zhong, "Fast Computational Method for Wave-Interference Effects of Multiple Truncated Vertical Cylinders," M.S. Thesis, University of California Berkeley, Berkeley, CA, Jun. 2015.

[43] A. N. Williams and A. G. Abul-Azm, "Hydrodynamic interactions in floating cylinder arrays—II. Wave radiation," *Ocean Engineering*, vol. 16, no. 3, pp. 217–263, 1989.

[44] K. R. Drake, R. Eatock Taylor, and S. M. Hung, "Comments on 'Wave diffraction by large offshore structures: an exact second-order theory by M. Rahman'," *Applied Ocean Research*, vol. 7, no. 1, pp. 61–62, Jan. 1985.

[45] M.-H. Kim and D. K. P. Yue, "The complete second-order diffraction solution for an axisymmetric body Part 1. Monochromatic incident waves," *Journal of Fluid Mechanics*, vol. 200, pp. 235–264, Mar. 1989.

[46] R. Eatock Taylor and S. M. Hung, "Second order diffraction forces on a vertical cylinder in regular waves," *Applied Ocean Research*, vol. 9, no. 1, pp. 19–30, Jan. 1987.

[47] R. Zhao and O. M. Faltinsen, "Interaction between waves and current on a two-dimensional body in the free surface," *Applied Ocean Research*, vol. 10, no. 2, pp. 87–99, Apr. 1988.

[48] A. J. Hermans, "Low-Frequency Second-Order Wave-Drift Forces and Damping," *Journal of Engineering Mathematics*, vol. 35, no. 1-2, pp. 181–198, Feb. 1999.

[49] M.-H. Kim, "A Simple Method to Compute Wave Loads on a TLP." ASCE, 1992, pp. 158–172.

[50] R. W. Yeung and S. H. Sphaier, "Wave-interference effects on a truncated cylinder in a channel," *Journal of Engineering Mathematics*, vol. 23, no. 2, pp. 95–117, Jun. 1989.

[51] P. W. Bearman, M. J. Downie, J. M. R. Graham, and E. D. Obasaju, "Forces on cylinders in viscous oscillatory flow at low Keulegan-Carpenter numbers," *Journal of Fluid Mechanics*, vol. 154, pp. 337–356, May 1985.

[52] A. W. Troesch and S. K. Kim, "Hydrodynamic forces acting on cylinders oscillating at small amplitudes," *Journal of Fluids and Structures*, vol. 5, no. 1, pp. 113–126, Jan. 1991.

[53] J. Morison, J. Johnson, and S. Schaaf, "The Force Exerted by Surface Waves on Piles," *Journal of Petroleum Technology*, vol. 2, no. 05, pp. 149–154, May 1950.

[54] L. E. Borgman, "Random Hydrodynamic Forces on Objects," *The Annals of Mathematical Statistics*, vol. 38, no. 1, pp. 37–51, Feb. 1967.

[55] W. Y. (Fred) Toh, "Shape and Viscosity Effects on Heaving and Rolling Floating Cylinders," Master of Science Project Report, University of California Berkeley, Berkeley, CA, Dec. 2009.

[56] N. Tom and R. W. Yeung, "Non-Linear Model Predictive Control Applied to a Generic Ocean-Wave Energy Extractor," in *Proc. of 32nd ASME International Conference on Offshore Mechanics and Arctic Engineering (OMAE-13)*, Nantes, France, Jun. 2013, OMAE2013-11247.

[57] E. Kristiansen, A. Hjulstad, and O. Egeland, "State-space representation of radiation forces in time-domain vessel models," *Ocean Engineering*, vol. 32, no. 17, pp. 2195–2216, 2005.

[58] N. Tom, "Design and Control of a Floating Wave-Energy Converter Utilizing a Permanent Magnet Linear Generator," PhD Dissertation, University of California Berkeley, Berkeley, CA, Dec. 2013.

[59] W. E. Cummins, "The impulse response function and ship motions." *Schiffstechnik*, vol. 9, pp. 101–109, 1962.

[60] A. A. Huskey and T. L. Forsyth, "NREL Small Wind Turbine Test Project: Mariah Power's Windspire Wind Turbine Test Chronology," National Renewable Energy Laboratory, Golden, CO, Technical Report NREL/TP-500-45552, Jun. 2009. [Online]. Available: http://www.nrel.gov/wind/smallwind/pdfs/mariah_report.pdf

[61] B. Froehle, Michael, "High-Order Discontinuous Galerkin Fluid-Structure Interaction Methods," PhD Dissertation, University of California Berkeley, Berkeley, CA, 2013.

[62] R. E. Sheldahl, P. C. Klimas, and L. V. Feltz, "Aerodynamic performance of a 5-metre-diameter Darrieus turbine with extruded aluminum NACA-0015 blades," National Technical Information Service, Albuquerque, NM, Technical Report SAND80-0179, 1980. [Online]. Available: http://prod.sandia.gov/techlib/access-control.cgi/1980/800179.pdf

[63] T. J. Mueller and J. D. DeLaurier, "Aerodynamics of Small Vehicles," *Annual Review of Fluid Mechanics*, vol. 35, no. 1, pp. 89–111, 2003.

[64] P. B. S. Lissaman, "Low-Reynolds-Number Airfoils," *Annual Review of Fluid Mechanics*, vol. 15, no. 1, pp. 223–239, 1983.

[65] B. H. Carmichael, *Low Reynolds number airfoil survey.* National Aeronautics and Space Administration, Langley Research Center, 1981.

[66] W. Shyy, Y. Lian, J. Tang, D. Viieru, and H. Liu, *Aerodynamics of Low Reynolds Number Flyers.* Cambridge: Cambridge University Press, 2007.

[67] W. J. McCroskey, "A Critical Assessment of Wind Tunnel Results for the NACA 0012 Airfoil," Tech. Rep., Oct. 1987.

[68] R. F. Huang, J. Y. Wu, J. H. Jeng, and R. C. Chen, "Surface flow and vortex shedding of an impulsively started wing," *Journal of Fluid Mechanics*, vol. 441, pp. 265–292, 2001.

[69] R. Huang and C. Lin, "Vortex Shedding and Shear-Layer Instability of Wing at Low-Reynolds Numbers," *AIAA Journal*, vol. 33, no. 8, pp. 1398–1403, Aug. 1995.

[70] M. M. Alam, Y. Zhou, H. X. Yang, H. Guo, and J. Mi, "The ultra-low Reynolds number airfoil wake," *Experiments in Fluids*, vol. 48, no. 1, pp. 81–103, Jan. 2010.

[71] S. Yarusevych, P. E. Sullivan, and J. G. Kawall, "Coherent structures in an airfoil boundary layer and wake at low Reynolds numbers," *Physics of Fluids*, vol. 18, no. 4, Apr. 2006.

[72] T. Ohtake, Y. Nakae, and T. Motohashi, "Nonlinearity of the aerodynamic characteristics of NACA0012 aerofoil at low Reynolds numbers," *Japan Society of Aeronautical Space Sciences*, vol. 55, pp. 439–445, 2007.

[73] J. Smagorinsky, "General circulation experiments with the primitive equations: I. the basic experiment," *Monthly weather review*, vol. 91, no. 3, pp. 99–164, 1963.

[74] H. Gao, H. Hu, and Z. J. Wang, "Computational study of unsteady flows around dragonfly and smooth airfoils at low Reynolds numbers," in *46th AIAA Aerospace Sciences Meeting and Exhibit*, 2008, pp. 7–10.

[75] A. Uranga, P.-O. Persson, M. Drela, and J. Peraire, "Implicit Large Eddy Simulation of transition to turbulence at low Reynolds numbers using a Discontinuous Galerkin method," *International Journal for Numerical Methods in Engineering*, vol. 87, no. 1-5, pp. 232–261, Jul. 2011.

[76] O. Lehmkuhl, I. Rodríguez, A. Baez, A. Oliva, and C. D. Pérez-Segarra, "On the large-eddy simulations for the flow around aerodynamic profiles using unstructured grids," *Computers & Fluids*, vol. 84, pp. 176–189, Sep. 2013.

[77] M. R. Visbal, R. E. Gordnier, and M. C. Galbraith, "High-fidelity simulations of moving and flexible airfoils at low Reynolds numbers," *Experiments in Fluids*, vol. 46, no. 5, pp. 903–922, May 2009.

[78] M. R. Visbal, "High-fidelity simulation of transitional flows past a plunging airfoil," *AIAA Journal*, vol. 47, no. 11, pp. 2685–2697, 2009.

[79] R. Kojima, T. Nonomura, A. Oyama, and K. Fujii, "Large-Eddy Simulation of Low-Reynolds-Number Flow Over Thick and Thin NACA Airfoils," *Journal of Aircraft*, vol. 50, no. 1, pp. 187–196, 2013.

[80] H. Shan, L. Jiang, and C. Liu, "Direct numerical simulation of flow separation around a NACA 0012 airfoil," *Computers & Fluids*, vol. 34, no. 9, pp. 1096–1114, Nov. 2005.

[81] M. Breuer and N. Jovičić, "An LES investigation of the separated flow past an airfoil at high angle of attack," in *Direct and Large-Eddy Simulation IV*. Springer, 2001, pp. 165–172.

[82] I. Rodríguez, O. Lehmkuhl, R. Borrell, and A. Oliva, "Direct numerical simulation of a NACA0012 in full stall," *International Journal of Heat and Fluid Flow*, vol. 43, pp. 194–203, Oct. 2013.

[83] S. Kanner and P.-O. Persson, "Validation of a High-Order Large-Eddy Simulation Solver Using a Vertical-Axis Wind Turbine," *AIAA Journal*, 2015.

[84] J. Peraire and P.-O. Persson, "The compact discontinuous Galerkin (CDG) method for elliptic problems," *SIAM Journal on Scientific Computing*, vol. 30, no. 4, pp. 1806–1824, 2008.

[85] P.-O. Persson and G. Strang, "A simple mesh generator in MATLAB," *SIAM review*, vol. 46, no. 2, pp. 329–345, 2004.

[86] P.-O. Persson and J. Peraire, "Curved mesh generation and mesh refinement using Lagrangian solid mechanics," in *Proceedings of the 47th AIAA Aerospace Sciences Meeting and Exhibit*, Orland, Florida, Jan. 2009.

[87] E. V. Laitone, "Aerodynamic lift at Reynolds numbers below 7 x 10e4," *AIAA journal*, vol. 34, no. 9, pp. 1941–1942, 1996.

[88] M. Drela, "XFOIL: An analysis and design system for low Reynolds number airfoils," in *Low Reynolds number aerodynamics*. Springer, 1989, pp. 1–12.

[89] R. F. Huang and H. W. Lee, "Effects of freestream turbulence on wing-surface flow and aerodynamic performance," *Journal of aircraft*, vol. 36, no. 6, pp. 965–972, 1999.

[90] R. E. Sheldahl and P. C. Klimas, "Aerodynamic characteristics of seven symmetrical airfoil sections through 180-degree angle of attack for use in aerodynamic analysis of vertical axis wind turbines," Sandia National Labs., Albuquerque, NM (USA), Tech. Rep. SAND80-2114, 1981. [Online]. Available: http://www.osti.gov/energycitations/product.biblio.jsp?osti_id=6548367

[91] D. Pagnutti and C. Ollivier-Gooch, "Two-dimensional Delaunay-based anisotropic mesh adaptation," *Engineering with Computers*, vol. 26, no. 4, pp. 407–418, Aug. 2010.

[92] A. Henderson, J. Ahrens, C. Law, and others, *The ParaView Guide*. Kitware Clifton Park, NY, 2004.

[93] J. H. Strickland, B. T. Webster, and T. Nguyen, "Vortex Model of the Darrieus Turbine: An Analytical and Experimental Study," Sandia National Labs., Albuquerque, NM (USA); Oregon State Univ., Corvallis (USA). Dept. of Mechanical Engineering, Tech. Rep. SAND-79-7058, Jun. 1979.

[94] J. H. Strickland, T. Smith, and K. Sun, "Vortex Model of the Darrieus Turbine: An Analytical and Experimental Study. Final Report," Sandia National Labs., Albuquerque, NM (USA); Oregon State Univ., Corvallis (USA). Dept. of Mechanical Engineering, Tech. Rep. SAND-81-7017, Jun. 1981. [Online]. Available: http://www.osti.gov/scitech/biblio/6215602

[95] P. O. Persson, J. Bonet, and J. Peraire, "Discontinuous Galerkin solution of the Navier–Stokes equations on deformable domains," *Computer Methods in Applied Mechanics and Engineering*, vol. 198, no. 17–20, pp. 1585–1595, Apr. 2009.

[96] P. Klimas and M. H. Worstell, "Effects of blade preset pitch/offset on curved-blade darreius vertical-axis wind turbine performance." Sandia National Labs., Albuquerque, NM ,USA, Tech. Rep. SAND-81-1762, 1981.

[97] M. Y. Okiishi, B. Munson, and D. Young, "Fundamentals of Fluid Mechanics," *John Wiley & Sons, Inc*, 2006.

[98] D. E. Berg, "Improved double-multiple streamtube model for the Darrieus-type vertical axis wind turbine," in *Presented at the Am. Solar Energy Soc. Meeting, Minneapolis, 1 Jun. 1983*, vol. 1, 1983.

[99] J. G. Leishman and T. S. Beddoes, "A generalised model for airfoil unsteady aerodynamic behaviour and dynamic stall using the indicial method," in *Proceedings of the 42nd Annual Forum of the American Helicopter Society, Washington DC*, 1986.

[100] L. Wang, "Discontinuous Galerkin Methods on Moving Domains with Large Deformations," PhD Dissertation, University of California Berkeley, Berkeley, CA, May 2015.

[101] M. Kinzel, Q. Mulligan, and J. O. Dabiri, "Energy exchange in an array of vertical-axis wind turbines," *Journal of Turbulence*, vol. 13, no. 1, 2012.

[102] T. Leclercq, "Numerical Simulation of the Flow About Vertical-Axis Turbines by a Vortex Method," M.S. Thesis, University of California Berkeley, Berkeley, CA, Dec. 2014.

[103] A. S. Chan, P. A. Dewey, A. Jameson, C. Liang, and A. J. Smits, "Vortex suppression and drag reduction in the wake of counter-rotating cylinders," *Journal of Fluid Mechanics*, vol. 679, pp. 343–382, Jul. 2011.

[104] E. Hau and H. Platz, *Wind Turbines-Fundamentals, Technologies, Application, Economics.* Heidelberg: Springer-Verlag Berlin Heidelberg, 2000.

[105] D. Roddier, C. Cermelli, A. Aubault, and A. Weinstein, "WindFloat: A floating foundation for offshore wind turbines," *Journal of Renewable and Sustainable Energy*, vol. 2, no. 3, Jun. 2010.

[106] J. M. Jonkman, S. Butterfield, W. Musial, and G. Scott, *Definition of a 5-MW reference wind turbine for offshore system development.* National Renewable Energy Laboratory Colorado, 2009.

[107] P. A. Berthelsen, I. Fylling, L. Vita, and U. Schmidt Paulsen, "Conceptual Design of a Floating Support Structure and Mooring System for a Vertical Axis Wind Turbine," in *Proc. of 31st ASME International Conference on Ocean, Offshore and Arctic Engineering.* Rio de Janeiro, Brazil, 2012, OMAE2012-83335.

[108] J. Wichers, *Guide to Single Point Moorings.* WMooring, 2013.

[109] F. Ottermo, S. Eriksson, and H. Bernhoff, "Parking Strategies for Vertical Axis Wind Turbines," *International Scholarly Research Notices*, vol. 2012, Nov. 2012.

[110] V. Saouma and M. Sivaselvan, *Hybrid Simulation: Theory, Implementation and Applications.* CRC Press, Jul. 2008.

[111] W. Premerlani and P. Bizard, "Direction cosine matrix imu: Theory," *DIY DRONE: USA*, pp. 13–15, 2009.

[112] M. Euston, P. Coote, R. Mahony, J. Kim, and T. Hamel, "A complementary filter for attitude estimation of a fixed-wing UAV," in *IEEE/RSJ International Conference on Intelligent Robots and Systems, 2008. IROS 2008*, Sep. 2008, pp. 340–345.

[113] E. Koukina, R. W. Yeung, and S. Kanner, "Actuation of Wind-Loading Torque on Vertical Axis Turbines at Model Scale," in *Proceedings of Marine Technology Society and Institute of Electrical and Electronics Engineers Conference*, Genova, Italy, May 2015.

[114] A. J. Coulling, A. J. Goupee, A. N. Robertson, J. M. Jonkman, and H. J. Dagher, "Validation of a FAST semi-submersible floating wind turbine numerical model with DeepCwind test data," *Journal of Renewable and Sustainable Energy*, vol. 5, no. 2, Mar. 2013.

[115] P. Tracy, A. Anderson, J.-M. Irazabal, and S. Blozis, "I2c / SMBus Repeaters, Hubs and Expanders," Philips Semiconductors, Application Note AN255-02, Dec. 2002.

[116] R. Faludi, *Building Wireless Sensor Networks*. O'Reilly Media, Inc., Dec. 2010.

[117] J. J. Slotine and W. Li, *Applied Nonlinear Control*. Prentice Hall, 1991.

[118] J. K. Hedrick and A. Girard, "Control of Nonlinear Dynamic Systems: Theory and Applications," " 2010.

[119] J. Watkinson, *Art of the Helicopter*. Butterworth-Heinemann, Dec. 2003.

[120] P. G. Harris and J. O'sullivan, "Floating vertical axis wind turbine module system and method," European Union Patent EP2 504 571 B1, Jun., 2014, nternational Classification F03D11/04, Cooperative Classification Y02E10/74, Y10T29/49718.

[121] J. V. Wehausen, W. C. Webster, and R. W. Yeung, "Hydrodynamics of Ships and Ocean Systems (for Course ME241), Chapter 7." University of California at Berkeley, 2005.

[122] J. V. Wehausen and E. V. Laitone, "Surface Waves," in *Fluid Dynamics / Strömungsmechanik*, ser. Encyclopedia of Physics / Handbuch der Physik, C. Truesdell, Ed. Springer Berlin Heidelberg., 1960, no. 3 / 9, pp. 446–778.

[123] J. V. Wehausen and E. V. Laitone, "Surface Waves -Online Edition, with Errata," 2002. [Online]. Available: http://www.surfacewaves.berkeley.edu

[124] R. W. Yeung, "Numerical Methods in Free-Surface Flows," *Annual Review of Fluid Mechanics*, vol. 14, no. 1, pp. 395–442, 1982.

[125] F. John, "On the motion of floating bodies II. Simple harmonic motions," *Communications on Pure and Applied Mathematics*, vol. 3, no. 1, pp. 45–101, Mar. 1950.

[126] P. M. Morse and H. Feshbach, *Methods of theoretical physics*, ser. International series in pure and applied physics. New York: McGraw-Hill, 1953.

[127] J. L. Black, "Wave forces on vertical axisymmetric bodies," *Journal of Fluid Mechanics*, vol. 67, no. 02, pp. 369–376, Jan. 1975.

[128] J. D. Fenton, "Wave forces on vertical bodies of revolution," *Journal of Fluid Mechanics*, vol. 85, no. 02, pp. 241–255, Mar. 1978.

[129] J. B. Huang and R. E. Taylor, "Semi-analytical solution for second-order wave diffraction by a truncated circular cylinder in monochromatic waves," *Journal of Fluid Mechanics*, vol. 319, pp. 171–196, Jul. 1996.

[130] Š. Malenica, P. J. Clark, and B. Molin, "Wave and current forces on a vertical cylinder free to surge and sway," *Applied Ocean Research*, vol. 17, no. 2, pp. 79–90, 1995.

[131] S. K. Lucas and H. A. Stone, "Evaluating infinite integrals involving Bessel functions of arbitrary order," *Journal of Computational and Applied Mathematics*, vol. 64, no. 3, pp. 217–231, Dec. 1995.

[132] J. T. Ratnanather, J. H. Kim, S. Zhang, A. M. J. Davis, and S. K. Lucas, "Algorithm 935: IIPBF, a MATLAB Toolbox for Infinite Integral of Products of Two Bessel Functions," *ACM Trans. Math. Softw.*, vol. 40, no. 2, pp. 14:1–14:12, Mar. 2014.

Appendices

Appendix A

Definition of Non-Linear, Free-Surface Boundary Conditions in Eq. (2.49c)

The non-linear, free-surface boundary conditions of $O(\epsilon\tau)$, represented by Eq. (2.49c) with m'_j terms, were first found by Ogilvie in [33] when developing the high-order strip theory for a ship advancing in waves. Also, Wehausen develops these boundary conditions when developing the problem of a ship with a forward speed in [34] (updated in [121]). We reproduce the results here, since we were not able to find the explicit definition of these terms in the literature for a truncated cylinder. Let the exterior potential of ϕ_{01}, which is shown in Eq. (2.91) be given by a separable function as $\bar{\psi}_j^{(e)} = \mathcal{R}_j(r)\mathcal{Z}_j(z)\Theta_j(\theta)$, where $\mathcal{R}(r)\mathcal{Z}(z) = \bar{\Psi}^{(e)}$. We utilize the vector identities shown in Appendix B of [20], so that the m_j terms are,

$$m'_1 = \frac{\partial^2\phi_{01}}{\partial r\partial x} = U_j\frac{\partial^2[\mathcal{R}_j(r)\mathcal{Z}_j(z)\Theta_j(\theta)]}{\partial r\partial x} \tag{A.1a}$$

$$m'_2 = \frac{\partial^2\phi_{01}}{\partial r\partial y} = U_j\frac{\partial^2[\mathcal{R}_j(r)\mathcal{Z}_j(z)\Theta_j(\theta)]}{\partial r\partial y} \tag{A.1b}$$

$$m'_6 = x_0 m'_2 - y_0 m'_1 \tag{A.1c}$$

where summation over the j modes of motion is assumed. Trigonometric identities allow us to rewrite the $x-$ and $y-$ derivatives as,

$$\frac{\partial}{\partial x}[\mathcal{R}_j(r)\mathcal{Z}_j(z)\cos(\theta)] = \frac{\mathcal{Z}(z)}{2}\left[\left(\mathcal{R}'_j(r) + \frac{\mathcal{R}_j(r)}{r}\right) + \left(\mathcal{R}'_j(r) - \frac{\mathcal{R}_j(r)}{r}\right)\cos 2\theta\right] \tag{A.2a}$$

$$\frac{\partial}{\partial y}[\mathcal{R}_j(r)\mathcal{Z}_j(z)\cos(\theta)] = \frac{\mathcal{Z}(z)}{2}\left[\left(\mathcal{R}'_j(r) - \frac{\mathcal{R}_j(r)}{r}\right)\sin 2\theta\right] \tag{A.2b}$$

$$\frac{\partial}{\partial x}[\mathcal{R}_j(r)\mathcal{Z}_j(z)\sin(\theta)] = \frac{\mathcal{Z}(z)}{2}\left[\left(\mathcal{R}'_j(r) - \frac{\mathcal{R}_j(r)}{r}\right)\sin 2\theta\right] \tag{A.2c}$$

$$\frac{\partial}{\partial y}[\mathcal{R}_j(r)\mathcal{Z}_j(z)\sin(\theta)] = \frac{\mathcal{Z}(z)}{2}\left[\left(\mathcal{R}'_j(r) + \frac{\mathcal{R}_j(r)}{r}\right) + \left(-\mathcal{R}'_j(r) + \frac{\mathcal{R}_j(r)}{r}\right)\cos 2\theta\right] \tag{A.2d}$$

We take the $r-$ derivatives of these functions, which yields,

$$\frac{\partial^2}{\partial r \partial x}[\cdot \cos(\theta)] = \frac{Z(z)}{2}\left[\left(\mathcal{R}_j''(r) + \frac{\mathcal{R}_j'(r)}{r} - \frac{\mathcal{R}_j(r)}{r^2}\right) + \left(\mathcal{R}_j''(r) - \frac{\mathcal{R}_j'(r)}{r} + \frac{\mathcal{R}_j(r)}{r^2}\right)\cos 2\theta\right] \tag{A.3a}$$

$$\frac{\partial^2}{\partial r \partial y}[\cdot \cos(\theta)] = \frac{Z(z)}{2}\left[\left(\mathcal{R}_j''(r) - \frac{\mathcal{R}_j'(r)}{r} + \frac{\mathcal{R}_j(r)}{r^2}\right)\sin 2\theta\right] \tag{A.3b}$$

$$\frac{\partial^2}{\partial r \partial x}[\cdot \sin(\theta)] = \frac{Z(z)}{2}\left[\left(\mathcal{R}_j''(r) - \frac{\mathcal{R}_j'(r)}{r} + \frac{\mathcal{R}_j(r)}{r^2}\right)\sin 2\theta\right] \tag{A.3c}$$

$$\frac{\partial^2}{\partial r \partial y}[\cdot \sin(\theta)] = \frac{Z(z)}{2}\left[\left(\mathcal{R}_j''(r) + \frac{\mathcal{R}_j'(r)}{r} - \frac{\mathcal{R}_j(r)}{r^2}\right) + \left(-\mathcal{R}_j''(r) + \frac{\mathcal{R}_j'(r)}{r} - \frac{\mathcal{R}_j(r)}{r^2}\right)\cos 2\theta\right] \tag{A.3d}$$

that collapse to the m' terms given in [20] for a bottom-fixed cylinder.

Appendix B

Fourier Coefficients in Linear Scattering Potential ψ_7

In this appendix, we solve for the coefficients, $B_q^{(m)}, C_q^{(m)}$ for $m, q = 0, 1, ...\infty$ introduced when the scattering potential ψ_7 of the zero-speed, first-order potential φ_{10} on the interior and exterior regions was defined in Eqs. (2.70) and (2.72) when providing the definitions of ${}_7\Psi_m^{(i),(e)}(r, z)$ in. This solution was first obtained by Garrett [36], but more closely follows the formulation of [37]. On the body sides, $r = a$, the interior dimensionless spatial solution ${}_7\Psi_m^{(i)}$ becomes a Fourier cosine series with coefficients $B_q^{(m)}$ given by,

$$B_q^{(m)} = \frac{2}{d}\int_0^d {}_7\Psi_m^{(i)}(a, z)\cos(\beta_q z)dz \quad m, q = 0, 1, 2... \tag{B.1}$$

Application of the matching condition, found in Eq. (2.68b), allows us to represent the $B_p^{(m)}$ as a linear combination of $C_p^{(m)}$, as

$$B_p^{(m)} + \sum_{q=0}^{\infty} G_{pq}^{(m)} C_q(m) = S_p^{(m)} \quad m, p = 0, 1, 2... \tag{B.2}$$

Likewise, the Fourier coefficients in the exterior solution ($C_p^{(m)}$) can be solved by differentiating Eq. (2.72) with respect to r, setting $r = a$, multiplying by $Z_p(z)$ and integrating over [0,h]. These computations yield,

$$C_p^{(m)} = \frac{1}{k_p h}\int_0^h \frac{\partial_7 \Psi_m^{(e)}(a, z)}{\partial r} Z_p(z)dz \quad m, p = 0, 1, 2... \tag{B.3}$$

We utilize the matching condition, shown in Eq. (2.67) and the structural boundary condition, given in Eq. (2.68b), to rewrite the series shown above as a linear combination of the $B_p^{(m)}$, as

$$C_p^{(m)} = \sum_{q=0}^{\infty} H_{pq}^{(m)} B_q(m) \quad m, p = 0, 1, 2... \tag{B.4}$$

For completeness, the coefficients are given as,

$$S_p^{(m)} = 2\frac{\epsilon_m i^{m+1}}{\cosh k_0 h}\left(J_m(k_0 a) - \frac{J'_m(k_0 a)}{H'_m(k_0 a)} H_m(k_0 a)\right)\frac{k_0 d(-1)^p \sinh(k_0 d)}{(k_0 d)^2 + (p\pi)^2} \tag{B.5}$$

with

$$G_{pq}^{(m)} = \begin{cases} -2\dfrac{H_m(k_0 a)}{H'_m(k_0 a)} Q_0^{-1/2} \dfrac{k_0 d(-1)^p \sinh(k_0 d)}{(k_0 d)^2 + (p\pi)^2}, & \text{for } q = 0, p \geq 0 \\ -2\dfrac{K_m(k_q a)}{K'_m(k_q a)} Q_q^{-1/2} \dfrac{k_q d(-1)^p \sin(k_q d)}{(k_q d)^2 - (p\pi)^2}, & \text{for } q > 0, p \geq 0 \end{cases} \tag{B.6}$$

The terms $H_{pq}^{(m)}$ are

$$H_{pq}^{(m)} = \begin{cases} \dfrac{m}{2}\dfrac{Q_0^{-1/2}}{k_0 h}\dfrac{\sinh k_0 d}{k_0 a}, & \text{for } q=0, p=0 \\ \dfrac{m}{2}\dfrac{Q_p^{-1/2}}{k_p h}\dfrac{\sin k_p d}{k_p a}, & \text{for } q=0, p>0 \\ \dfrac{q\pi d}{h}\dfrac{I_m'(\beta_q a)}{I_m(\beta_q a)}\dfrac{Q_0^{-1/2}(-1)^q \sinh(k_0 d)}{(k_0 d)^2+(\pi q)^2}, & \text{for } q>0, p=0 \\ \dfrac{q\pi d}{h}\dfrac{I_m'(\beta_q a)}{I_m(\beta_q a)}\dfrac{Q_p^{-1/2}(-1)^q \sin(k_p d)}{(k_p d)^2+(\pi q)^2}, & \text{for } q>0, p>0 \end{cases} \tag{B.7}$$

Thus, we can truncate the infinite series at $q = p = N_t$ for each m we have to solve a $(N_t+1 \times N_t+1)$ set of equations for $C_p^{(m)}$ or $B_p^{(m)}$ using standard matrix inversion techniques. To compare with results from [18] for an isolated cylinder, N_t was set to 40 and the results for the heave wave-exciting force (not explicitly derived here) are shown in Fig. 2.6.

Appendix C

Fourier Coefficients in Linear Radiation Potentials $\psi_1,\ \psi_2$

In this appendix, we explicitly solve for the radiation potential coefficients B_q^j, C_q^j for $q = 0, 1, ..., \infty$, $j = 1, 2$ corresponding to the surge and sway modes, respectively. These coefficients were introduced when defining the zero-speed, first-order radiation potential $\psi_j^{(i),(e)}$ in Eqs. (2.83a) and (2.83b). The solution to the radiation potential of a truncated cylinder in finite-depth waters was first obtained by [18], but the formulation repeated here more closely follows that of Williams and Abul-Azm, in [43]. When $r = a$, the Fourier coefficients B_p^j are

$$B_p^j = \frac{2}{d}\int_0^d \Psi_j^{(i)}(a, z)\cos(\beta_p z)dz. \tag{C.1}$$

Applying the matching condition, given in Eq. (2.67), we find that

$$B_p^j + \sum_{q=0}^{\infty} G_{pq}^j C_q^j = S_p^j, \quad p = 0, 1, 2, ..., \tag{C.2}$$

where $G_{pq}^j = G_{pq}^{(m=1)}$ as defined previously for $j = 1, 2$. However S_p^j for $j = 1, 2$ is null, since the surge and sway modes do not affect the wave field in the interior portion of the domain. We can differentiate Eq. (2.83b) with respect to r, set $r = a$ and then integrate over $[0, h]$, which yields,

$$C_p^j = \frac{1}{k_p h}\int_0^h \frac{\partial \Psi_j^{(e)}}{\partial r}(a, z)Z_p(z)dz, \quad p = 0, 1, 2... \tag{C.3}$$

Again, using the matching conditions, Eq. (2.67) and the structural boundary conditions, Eq. (2.49b), we find one expression for the Fourier coefficients as

$$C_p^j = \sum_{q=0}^{\infty} H_{pq}^j B_q^j + E_p, \tag{C.4}$$

where $H_{pq}^j = H_{pq}^{(m=1)}$ as defined previously and the last term is defined as,

$$E_p = \frac{Y_p}{m_p} \text{ for } p \geq 0. \tag{C.5}$$

Again, we can truncate the infinite series at $q = p = N_t$, and since surge motion is identical to sway motion the radiation potential will be identical for $j = 1, 2$. Thus, we have to solve a $(N_t + 1 \times N_t + 1)$ set of equations for C_p^j or B_p^j using standard matrix inversion techniques.

Appendix D

Solution of Slow-Drift Potential φ_{01}

In this section, we explicitly define the interior and exterior slow-drift Fourier coefficients $\bar{A}_q$ and $\bar{B}_q$. These coefficients were introduced to define the interior and exterior slow-drift potentials, $\bar{\psi}_j^{(i)}$ for $j = 1, 2, 6$ in Eqs. (2.94). The slow-drift potential of a truncated cylinder in finite-depth waters can be found in [29]. We rewrite the interior and exterior potentials so that we can easily see the dependence of the spatial variables r, θ, z as

$$\bar{\psi}_j^{(i)}(r,\theta,z) = \sum_{q=0}^{\infty} \bar{R}_q(r)\bar{A}_q^j \cos(\beta_q z)\cos(\theta - \chi_j) \tag{D.1a}$$

$$\bar{\psi}_j^{(e)}(r,\theta,z) = \sum_{p=0}^{\infty} \bar{S}_q(r)\bar{B}_p^j \cos(\beta_p \bar{d} z)\cos(\theta - \chi_j) \tag{D.1b}$$

where $\bar{S}_q(r)$ and $\bar{R}_q(r)$ can be inferred from Eqs. (2.94). From these equations, we find that

$$\frac{\partial}{\partial r}\bar{\psi}_j^{(i)}(r=a,\theta,z) = \sum_{q=0}^{\infty} \bar{a}_q\bar{A}_q^j \cos(\beta_q z)\cos(\theta - \chi_j) \tag{D.2a}$$

$$\frac{\partial}{\partial r}\bar{\psi}_j^{(e)}(r=a,\theta,z) = \sum_{p=0}^{\infty} \bar{b}_p\bar{B}_p^j \cos(\beta_p \bar{d} z)\cos(\theta - \chi_j) \tag{D.2b}$$

where

$$\bar{a}_0 = \frac{1}{2}, \tag{D.3a}$$

$$\bar{a}_q = a\beta_q \frac{I_1'(\beta_q a)}{I_1(\beta_q a)} \text{ for } q > 0, \tag{D.3b}$$

$$\bar{b}_0 = -\frac{1}{2}, \tag{D.3c}$$

$$\bar{b}_p = a\beta_p \bar{d}\frac{K_1'(\beta_p \bar{d} a)}{K_1(\beta_p \bar{d} a)} \text{ for } p > 0. \tag{D.3d}$$

Let the operator $\mathcal{L}_q^j[\phi]_0^h$ be defined as

$$\mathcal{L}_q^j[\phi]_0^h = \frac{1}{\pi h}\int_0^h\int_0^{2\pi} \phi(\theta, z)\cos(\beta_q z)\cos(\theta - \chi_j)d\theta dz. \tag{D.4}$$

Using this operator on the function matching condition in Eq. (2.67), over the valid range $z \in [0, d]$, we obtain

$$\frac{1}{2d}\int_0^d \sum_{m=0}^{\infty} \epsilon_m \bar{A}_m^j \cos(\beta_m z)\cos(\beta_q z)dz = \frac{1}{2d}\int_0^d \sum_{p=0}^{\infty} \epsilon_p \bar{B}_p^j \cos(\beta_p \bar{d} z)\cos(\beta_q z)dz \tag{D.5}$$

On account of the orthogonality of periodic functions, Eq. (D.5) simplifies to,

$$\frac{1}{4}\sum_{m=0}\epsilon_m \bar{A}^j_m \delta_{mq} = \frac{1}{2}\sum_{p=0}^{\infty}\epsilon_p \bar{g}_{pq}\bar{B}^j_p, \text{ for } q = 0, 1, 2, ... \tag{D.6}$$

with

$$\bar{g}_{pq} = \frac{1}{d}\int_0^d \cos(\beta_p \bar{d}z)\cos(\beta_q z)dz. \tag{D.7}$$

Thus, we can rewrite the equation to solve for the unknown coefficients $\bar{A}^j$ as,

$$\bar{A}^j_q = \sum_{p=0}^{\infty}\bar{G}_{pq}\bar{B}^j_p. \tag{D.8}$$

Equation (D.8) can be represented as a vector-matrix equation as,

$$\bar{\boldsymbol{A}} = [\bar{G}]\bar{\boldsymbol{B}}, \tag{D.9}$$

with the entries in the matrix $[\bar{G}]$ given by,

$$\bar{G}_{pq} = 2\frac{\epsilon_q \bar{g}_{pq}}{\epsilon_p}. \tag{D.10}$$

Utilizing the body boundary in Eq. (2.95), we have that

$$\sum_{q=0}^{\infty}\bar{b}_q\bar{B}^j_q\cos(\beta_q\bar{d}z) = n'_j \text{ for } d < z \leq h, \tag{D.11}$$

where $\boldsymbol{n}' = -[\cos\theta, \sin\theta]^T$ for $j = 1, 2$. We simplify the flux condition in Eq. (2.67) with our current definitions, which yields,

$$\sum_{m=0}\bar{a}_m\bar{A}^j_m\cos\beta_m z\cos(\theta-\chi_j) = \sum_{n=0}\bar{b}_n\bar{B}^j_n\cos\beta_n\bar{d}z\cos(\theta-\chi_j), \text{ for } 0 \leq z \leq d. \tag{D.12}$$

When Eqs. (D.12) and (D.11) are added together they represent a function defined from $0 \leq z \leq h$. Using the operator $\mathcal{L}^j_q[\phi]^h_0$ on Eqs. (D.12) and (D.11) we find that (for given q),

$$\frac{\bar{d}}{2}\sum_{p=0}\bar{a}_p\bar{A}_p\delta_{pq} - \bar{s}_q = \frac{1}{2}\sum_{p=0}^{\infty}\bar{b}_p\bar{B}_p\bar{h}_{pq}, \tag{D.13}$$

where δ_{ij} is the Kronecker delta, $\bar{h}_{pq}$ is

$$\bar{h}_{pq} = \frac{2}{h}\int_0^h \cos(\beta_p\bar{d}z)\cos(\beta_q z)dz, \tag{D.14}$$

and $\bar{s}_q$ is

$$\bar{s}_q = \frac{2}{h}\int_d^h \cos(\beta_q z)dz. \tag{D.15}$$

We can represent Eq. (D.13) as a matrix equation as,

$$[\bar{F}]\bar{\boldsymbol{A}} - \bar{\boldsymbol{S}} = [H]\bar{\boldsymbol{B}}, \tag{D.16}$$

where

$$\bar{F}_{pp} = \bar{d}\bar{a}_p \tag{D.17a}$$
$$\bar{F}_{pq} = 0 \text{ for } p \neq q \tag{D.17b}$$
$$\bar{H}_{pq} = \bar{b}_p\bar{h}_{pq} \tag{D.17c}$$

Thus, utilizing standard matrix solvers the unknown Fourier coefficients can be solved for by using Eqs. (D.9) and (D.16) where only a $(Q+1\times Q+1)$ matrix must be inverted. However, for certain d/h values, namely $h/d \in \mathbb{Z}$, this matrix becomes singular and care must be taken to correctly solve for the unknown coefficients.

Appendix E

Analysis of Interaction Potential φ_{11}

In the following section, we seek a solution to the potential of $\mathrm{O}(\epsilon\tau)$ that includes effects of the slow-drift motion as well as the incident wave. The k sub- and super-scripts denoting the k^{th} cylinder in a multi-cylinder array have been dropped for clarity. The solution to the potential φ_{11} closely follows that from [29] as well as in [20]. The decomposition of the potential φ_{11} is given in Eq. (2.98), but is repeated here for reference as,

$$\varphi_{11} \underset{\mathsf{Re}}{=} A_o\check{\psi}_D - i\sigma_o \sum_{j=1,2,6} \check{\psi}_j\mathcal{A}_j^{(0)} + \check{\psi}_j^{(\beta)}\mathcal{A}_{j,\beta}^{(0)} + \psi_j\mathcal{A}_j^{(1)}. \tag{E.1}$$

The last potential in Eq. (E.1) represents the linear radiation potential and was given in Appendix C. Thus, in the following sections we seek to setup the boundary value problem for the potentials $\check{\psi}_j$, $(j = 1, 2, 6, D)$ and $\check{\psi}_\ell^{(\beta)}$ $(\ell = 1, 2, 6)$ and then outline a solution for these potentials. We remind the reader that the superscript $(\check{})$ is simply used to differentiate these potentials from their lower-order counterparts.

E.1 Boundary Conditions in Local Coordinates

The free-surface and body boundary conditions for the potentials introduced in Eq. (E.1) can be rewritten from Eqs. (2.39), (2.49c), (2.53), for the diffraction potential as,

$$-\nu_o\check{\psi}_D + \frac{\partial\check{\psi}_D}{\partial z} = \mathcal{L}_D^{(1)}[\psi_D] + \mathcal{L}_D^{(2)}[\psi_D], \qquad \text{on } z = h, \tag{E.2a}$$

$$\frac{\partial\check{\psi}_D}{\partial n} = 0 \qquad \text{on } \mathcal{S}_o, \tag{E.2b}$$

and the radiation potentials as (for $j = 1, 2, 6$ only)

$$-\nu_o\check{\psi}_j + \frac{\partial\check{\psi}_j}{\partial z} = \mathcal{L}_j^{(1)}[\psi_j] + \mathcal{L}_j^{(2)}[\psi_j] \qquad \text{on } z = h, \tag{E.3a}$$

$$\frac{\partial\check{\psi}_j}{\partial n} = -\frac{m_j'}{i\sigma_o}, \qquad \text{on } \mathcal{S}_o \tag{E.3b}$$

$$-\nu_o\check{\psi}_j^{(\beta)} + \frac{\partial\check{\psi}_j^{(\beta)}}{\partial z} = \mathcal{L}_j^{(\beta)}[\psi_j], \qquad \text{on } z = h, \tag{E.4a}$$

$$\frac{\partial\check{\psi}_j^{(\beta)}}{\partial n} = 0, \qquad \text{on } \mathcal{S}_o. \tag{E.4b}$$

Like previous authors (for instance, [20], [29]), we have found it convenient to split the inhomogeneous (free-surface) forcing terms in Eq. (2.39) by those that involve only φ_{10}, ($\mathcal{L}_j^{(1)}[\psi_j]$) and those that also involve φ_{01}, ($\mathcal{L}_j^{(2)}[\psi_j]$) , as

$$\mathcal{L}_j^{(1)}[\psi_j] = \check{f}_j[\psi_j] + \check{g}_j[\psi_j], \qquad \text{for } j = 1, 2, 6, D, \tag{E.5a}$$

$$\mathcal{L}_j^{(2)}[\psi_j] = \left[\frac{i\sigma_o}{g}\left(2\nabla\varphi_{01}\cdot\nabla - \frac{\partial^2\varphi_{01}}{\partial z^2}\right)\right]\psi_j, \qquad \text{for } j = 1, 2, 6, D, \tag{E.5b}$$

$$\mathcal{L}_j^{(\beta)}[\psi_j] = \left[-2i\frac{\sigma_0}{g}U_6\right]\psi_j, \qquad \text{for } j = 1, 2, 6. \tag{E.5c}$$

where, (for $j = 1, 2, 6, D$),

$$\check{f}_j = \left[-\frac{2i\sigma_o}{g}\left((U_1 - y_0U_6)\frac{\partial}{\partial x} + (U_2 + x_0U_6)\frac{\partial}{\partial y} + U_6\frac{\partial}{\partial\theta} + ik_o\left(U_1\cos\beta + U_2\sin\beta\right)\right)\right] \tag{E.6}$$

and

$$\check{g}_j \begin{cases} 0, \text{ for } j = 1, 2, 6, \\ \left[-\frac{2i\sigma_o}{g}U_6\frac{\partial}{\partial\beta}\right], \text{ for } j = D. \end{cases} \tag{E.7}$$

E.2 General Solution

We follow the derivations for the potentials by using a combination of techniques found in [21], [20] and [25] and in [29]. We seek particular solutions to the problems posed in Eqs. (E.2)-(E.4) and then a general solution.

Let the velocity potentials $\check{\psi}_j, \check{\psi}_\ell^{(\beta)}$, for $j = 1, 2, 6, D$, and $\ell = 1, 2, 6$, be represented by a representative function $\check{\Psi}_j$, such that,

$$-\nu_o\check{\Psi}_j + \frac{\partial\check{\Psi}_j}{\partial z} = \mathcal{F}[\psi_j] \qquad \text{on } z = h,$$

$$\frac{\partial\check{\Psi}_j}{\partial n} = \check{h}_j(z) \qquad \text{on } \mathcal{S}_o, \tag{E.8a}$$

where the functions $\mathcal{F}$ and $\check{h}_j(z)$ could be represented by the functions in Eq. (E.2)-(E.4). As in [20] and [29], we can write the representative potential as a sum of three different potentials, such that

$$\check{\Psi}_j = \sum_{\ell=1}^{3}\check{\Psi}_j^{(\ell)}. \tag{E.9}$$

where the first two potentials solve for the inhomogeneous problem as

$$-\nu_o\check{\Psi}_j^{(1)} + \frac{\partial\check{\Psi}_j^{(1)}}{\partial z} = \mathcal{L}_j^{(1)}[\psi_j], \qquad \text{on } z = h, \tag{E.10a}$$

$$\frac{\partial\check{\Psi}_j^{(1)}}{\partial r} = h_j^{(1)}(z), \qquad \text{on } \mathcal{S}_o, \tag{E.10b}$$

and

$$-\nu_o \check{\Psi}_j^{(2)} + \frac{\partial \check{\Psi}_j^{(2)}}{\partial z} = \mathcal{L}_j^{(2)}[\psi_j], \qquad \text{on } z = h, \tag{E.11a}$$

$$\frac{\partial \check{\Psi}_j^{(2)}}{\partial r} = h_j^{(2)}(z), \qquad \text{on } \mathcal{S}_o, \tag{E.11b}$$

while the homogeneous solution is given by

$$-\nu_o \check{\Psi}_j^{(3)} + \frac{\partial \check{\Psi}_j^{(3)}}{\partial z} = 0, \qquad \text{on } z = h, \tag{E.12a}$$

$$\frac{\partial \check{\Psi}_j^{(3)}}{\partial r} = \check{h}_j(z) - h_j^{(1)}(z) - h_j^{(2)}(z), \qquad \text{on } \mathcal{S}_o, \tag{E.12b}$$

where $h_j^{(\ell)}$ are the normal velocities induced by $\check{\Psi}_j^{(\ell)}$, for $\ell = 1, 2$, $j = 1, 2, 6, D$.

E.3 Solution to $\check{\Psi}^{(1)}$

By comparing Eq. (E.10) with the free-surface boundary condition of φ_{10} in Eq. (2.37b), we realize that if we take the derivative of Eq. (E.10) with respect to ν_o and then apply the linear operator $\mathcal{L}_j^{(1)}[\ ]$, we arrive at the free-surface boundary condition in Eq. (E.10), such that

$$-\nu_o \mathcal{L}_j^{(1)}\left[\frac{\partial \psi_j}{\partial \nu_o}\right] + \mathcal{L}_j^{(1)}\left[\frac{\partial^2 \psi_j}{\partial \nu_o \partial z}\right] = \mathcal{L}_j^{(1)}[\psi_j]. \tag{E.13}$$

Thus, it follows that,

$$\check{\Psi}^{(1)} = \mathcal{L}_j^{(1)}\left[\frac{\partial \psi_j}{\partial \nu_o}\right]. \tag{E.14}$$

The normal velocity induced on the body by this potential is

$$h_j^{(1)} = \frac{\partial}{\partial r}\left(\mathcal{L}_j^{(1)}\left[\frac{\partial \psi_j}{\partial \nu_o}\right]\right) \text{ on } \mathcal{S}_o. \tag{E.15}$$

E.4 Analysis of $\check{\Psi}^{(2)}$

The solution to $\check{\Psi}_2$ follows the work of [29] and [30]. Kinoshita and Bao suggest representing the inhomogeneous term $\mathcal{L}_j^{(2)}$ as a moving pressure distribution on the free-surface and then solving for the potential by using Green's Theorem following the work of [122], which is currently available from [123] (see also [124]). Thus, we seek a Green function G, that is defined in a volume of fluid $\mathcal{V}$ bounded by $\partial\mathcal{V}$, which represents a cylinder with large radius R. That is, the volume of fluid is a cylinder that surrounds that physical cylinder with

$R >> a$. In the limit we take $R \to \infty$. For simplicity let us represent the potential we seek in this section by φ. A form of the divergence theorem states,

$$\iiint_{\mathcal{V}} G\nabla^2\varphi - \varphi\nabla^2 G d\mathcal{V} = \iint_{\partial\mathcal{V}} G\frac{\partial\varphi}{\partial n} - \varphi\frac{\partial G}{\partial n}dS \tag{E.16}$$

Let $P(r,\theta,z)$ be a field point and $Q(r',\theta',z')$ be a source point. Thus the Green function can be written as $G(r,\theta,z;,r',\theta',z')$. The boundary of $\mathcal{V}$ can be defined by the surfaces on the seabed, free surface, body and outer control surface, such that $\partial\mathcal{V} = \mathcal{S}_b \cup \mathcal{S}_f \cup \mathcal{S}_o \cup \mathcal{S}_r$. The left-hand side of Eq. (E.16) can readily be integrated leaving,

$$\varphi(P)\cdot\begin{cases}4\pi\\0\\2\pi\end{cases} = \iint_{\partial\mathcal{V}} G(P,Q)\frac{\partial\varphi(Q)}{\partial n} - \varphi(Q)\frac{\partial G(P,Q)}{\partial n}dS, \text{ for } P\begin{cases}\in\mathcal{V}\\\notin\mathcal{V}\\\in\mathcal{S}_o\end{cases} \tag{E.17}$$

The governing equations and boundary conditions for G are,

$$\nabla^2 G(P,Q) = 4\pi\delta(P-Q) \qquad \text{for } Q\in\mathcal{V} \tag{E.18a}$$

$$\frac{\partial G}{\partial z'} - \nu_o G = 0 \qquad \text{for } Q\in\mathcal{S}_f \tag{E.18b}$$

$$\frac{\partial G}{\partial z'} = 0 \qquad \text{for } Q\in\mathcal{S}_b \tag{E.18c}$$

$$\lim_{k_o r'\to\infty}\sqrt{k_o r'}\left(\frac{\partial G}{\partial r'} - ik_o G\right) = 0 \qquad \text{for } Q\in\mathcal{S}_r \tag{E.18d}$$

In 1950, John [125] obtained a Green function for a fluid layer, satisfying Laplace's equation, bounded below by a horizontal seabed and above by a free surface, on which waves were propagating. The equations are first written in an Appendix, in Eqs. [A10] and [A12] as well as surrounding equations. For a truncated body with a vertical-axis of symmetry in finite-depth waters, a method of obtaining a Green function was first outlined in Chapter 7 of [126] , more succinctly in [122] (who also cites John's work), updated (with errors) by [127] and then given in Eq. (2.3) of [128]. Most previous authors simply cite the work of [122], however, it is clear from the literature that other authors had a significant contribution to the work. The function is,

$$G(r,\theta,z;r',\theta',z') = \sum_{n=0}^{\infty} g_n(r,z;r',z')\cos n(\theta-\theta') \tag{E.19}$$

with

$$g_n(r,z;r',z') = \epsilon_n\sum_{m=0}^{\infty}\check{C}_m\check{Z}_m(z)\check{Z}_m(z')\begin{cases}R_n(k_m r)\check{R}_n(k_m r')\\\check{R}_n(k_m r')R_n(k_m r)\end{cases}\quad\text{for}\quad\begin{cases}r\geq r'\\r<r'\end{cases} \tag{E.20}$$

where

$$\check{R}_n(z) = \begin{cases} J_n(z) \text{ for } m = 0 \\ I_n(z) \text{ for } m > 0 \end{cases} \tag{E.21a}$$

$$R_n(z) = \begin{cases} H_n(z) \text{ for } m = 0 \\ K_n(z) \text{ for } m > 0 \end{cases} \tag{E.21b}$$

$$\check{C}_m = \begin{cases} \frac{2i\pi k_o^2}{(k_o^2-\nu_o^2)h+\nu_o} \text{ for } m = 0 \\ \frac{4k_m^2}{(k_o^2+\nu_o^2)h-\nu_o} \text{ for } m > 0 \end{cases} \tag{E.22}$$

and

$$\check{Z}_m(z) = \begin{cases} \frac{\cosh k_o z}{\cosh k_o h} \text{ for } m = 0 \\ \frac{\cos k_m z}{\cos k_m h} \text{ for } m > 0 \end{cases} \tag{E.23}$$

We refer the reader to [25] for the complete radiation and diffraction solution for this problem.

E.5 Solution to $\check{\Psi}^{(3)}$

The solution to $\check{\Psi}^{(3)}$ is very similar to the solution of the linear radiation problem ψ_j, developed in Sec. 2.4.1. Here, however, the body boundary condition is complicated by terms involving the lower-order potentials, φ_{01} and φ_{10}. If these potentials are known, then the potential $\check{\Psi}_3^k$ can be found in a similar manner to the radiation potential ψ_j ($j = 1, 2, 6$), developed in Sec. 2.4.1.

Appendix F

Explicit Expressions for Hydrodynamic Forces

In this appendix, we seek to find exact solutions of the hydrodynamic forces on a truncated cylinder in finite-depth waters using the technique of direct pressure integration over the mean wetted surface area of the body. This technique has been studied extensively for the linear problem. That is, the first-order wave exciting forces, added-mass and damping for an isolated truncated cylinder can be found in references such as [36] and [18]. The linear forces on a multi-column platform were given in [38]. The second-order steady drift forces (not taking into account slow-drift motion) for an axisymmetric body were given in [45]. We show (rather trivially) that for a multi-column platform rotating about the centroid of its waterplane area, there is no contribution from these terms for the steady yaw moment. To our knowledge, we believe we are the first to consider the other terms in the steady yaw moment, arising from the slow-drift motion of the platform using a direct pressure integration technique. Finally, we consider the direct pressure integration technique to solve for the wave-drift damping, although do not give the final results explicitly.

F.1 Linear Wave-Exciting Forces, Hydrodynamic Added-Mass and Damping

In this section we explicitly solve for the hydrodynamic coefficients, including the wave-exciting force as well as the added-mass and damping coefficients. Substituting the zero-speed, first-order potential φ_{10} into the pressure term of the same order and integrating over the wetted surface area of the body, we find the wave-exciting forces and the radiation forces in the frequency domain, as

$$\mathcal{X}_j^{(0)} = i\rho_o\sigma_o A_o \iint\limits_{\mathcal{S}_o} \psi_D n_j' dS \tag{F.1a}$$

$$\mu_{jk}^{(0)} + i\frac{\lambda_{jk}^{(0)}}{\sigma_o} = \rho_o \iint\limits_{\mathcal{S}_o} \psi_k n_j' dS. \tag{F.1b}$$

By examination, only the exterior solution will contribute to the surge and sway forces on the body. Thus,

$$\mathcal{X}_p^{k(0)} = i\rho_o\sigma_0 a \int_d^h \int_0^{2\pi} \psi_D^{k(e)} \Big|_{r=a} n_p' d\theta dz, \text{ for } p = 1, 2, \tag{F.2}$$

with $\boldsymbol{n'} = [-\cos\theta, -\sin\theta, 0]^T$ on the cylinder side walls. By inserting Eqs. (2.62) and 2.76

into Eq. (2.107), we obtain the surge and sway wave-exciting forces on the k^{th} cylinder is,

$$\frac{\mathcal{X}_p^{k(0)}}{\rho_o g\pi a^2} = iP_k \left\{ -2\frac{Y_0}{\cosh k_0 h}\left[J_1(k_0a) - \frac{H_1(k_0a)}{H_1'(k_0a)}\left(J_1'(k_0a) + C_0^{(1)}\frac{\cosh k_0 h}{2Q_0^{1/2}} \right) \right] + \sum_{q=1}^{\infty} C_q^{(1)} \frac{K_1(k_qa)}{K_1'(k_qa)} Q_q^{-1/2} Y_q \right\} \cos(\beta - \chi_p) \text{ for } p = 1, 2 \tag{F.3}$$

where the coefficients $C_q^{(m)}$ are given in Appendix B. Taking into account the interaction effects, we have

$$\begin{aligned} \frac{\mathcal{X}_{p,int}^{j(0)}}{\rho_o g\pi a_j^2} = \frac{\mathcal{X}_p^{j(0)}}{\rho_o g\pi a^2} - iY_0^j \Bigg\{ \sum_{\substack{k=1 \\ k\neq j}}^{N_{col}} \Bigg[\frac{c_{jk}}{\pi} \int_0^{2\pi} e^{-ik_0 a_j \cos(\alpha_{jk}-\theta_j)} \cos(\theta_k - \chi_p) \\ + \frac{P_k}{k_0 R_{kj}} \left(S_{jk}(\beta)\cos(\alpha_{jk} - \chi_p) - T_{jk}(\beta)\sin(\alpha_{jk} - \chi_p) \right) \\ + \sum_{\substack{\ell=1 \\ \ell\neq k}}^{N_{col}} \frac{c_{\ell k}}{k_0 R_{jk}} \left(S_{jk}(\alpha_{\ell k})\cos(\alpha_{jk} - \chi_p) - T_{jk}(\alpha_{\ell k})\sin(\alpha_{jk} - \chi_p) \right) \Bigg] \Bigg\}. \end{aligned} \tag{F.4}$$

For completeness, the heave force is

$$\frac{\mathcal{X}_3^{k(0)}}{\rho_o g\pi a^2} = -iP_k \left[\frac{B^{(0)}}{2} + \frac{2d}{a} \sum_{q=1}^{\infty} \frac{B_q^{(0)} \cos(\beta_q d)}{I_0(\beta_q a)} \frac{I_1(\beta_q a)}{\pi q} \right] \tag{F.5}$$

By inserting Eq. (2.80) into Eq. (2.107), we obtain the well-known result for the zero-speed, first-order radiation and damping, which is

$$\frac{\mu_{jk}^{(0)} + i\lambda_{jk}^{(0)}/\sigma_0}{\rho_o \pi a^3} = -\delta_{jk} \left\{ C_0^j \frac{H_1(k_0a)}{H_1'(k_0a)} Y_0 + \sum_{q=1}^{\infty} C_q^j \frac{K_1(k_qa)}{K_1'(k_qa)} Y_q \right\}, j, k = 1, 2 \tag{F.6}$$

where the coefficients C_q^j given in Appendix C.

F.2 Interaction Wave-Exciting Forces, Added-Mass and Damping

The solutions for the forward-speed, first-order wave-exciting, damping and added-mass will not be solved for explicitly, since they appear neither in the equations of motion for slow-drift motions nor the zero-speed, first-order motion. However, they can easily be found by

using the solution given in Appendix E. These hydrodynamic quantities as a function of the potentials $\check{\psi}$ and other lower-order potentials are,

$$\begin{aligned}\mathcal{X}_j^{(1)} &= i\rho_o\sigma_o A_o \iint\limits_{\mathcal{S}_o} \left[\check{\psi}_D - \frac{i}{\sigma_o}\left(\boldsymbol{s}\cdot\nabla\psi_D - \nabla\varphi_{01}\cdot\nabla\psi_D\right)\right] n_j' dS \\ &\quad + \frac{k_o}{\sigma_o}(U_1\cos\beta + U_2\sin\beta)\mathcal{X}_j^{(0)} + \frac{iU_6}{\sigma_o}\frac{\partial\mathcal{X}_j^{(0)}}{\partial\beta} \qquad \text{(F.7a)}\\ \mu_{ij}^{(1)} + i\frac{\lambda_{ij}^{(1)}}{\sigma_o} &= \rho_o \iint\limits_{\mathcal{S}_o} \left[\check{\psi}_i - \frac{i}{\sigma_o}\left(\boldsymbol{s}\cdot\nabla\psi_j - \nabla\varphi_{01}\cdot\nabla\psi_j\right)\right] n_j' dS \\ &\quad + \frac{k_o}{\sigma_o}(U_1\cos\beta + U_2\sin\beta)\left(\mu_{ij}^{(0)} + i\frac{\lambda_{ij}^{(0)}}{\sigma_o}\right) \qquad \text{(F.7b)}\end{aligned}$$

$$\mu_{ij}^{(\beta)} + i\frac{\lambda_{ij}^{(\beta)}}{\sigma_o} = \rho_o \iint\limits_{\mathcal{S}_o} \check{\psi}_i^{(\beta)} n_j' dS + i\frac{\rho_o}{\sigma_o}U_6\left(\mu_{ij}^{(0)} + i\frac{\lambda_{ij}^{(0)}}{\sigma_o}\right) \qquad \text{(F.8)}$$

F.3 Slow-Drift Forces

To our knowledge, this is the first attempt at describing the second-order, slow-drift forces using the direct pressure integration technique. We begin with considering a representation of the slow-drift forces, as solved by [20] and shown in Eq. (2.111) as,

$$\begin{aligned}F_j^{(20)} \underset{\text{Re}}{=} &-\frac{\rho_o}{4}\int\limits_{\mathcal{S}_o} \underbrace{\nabla\varphi_{10}\cdot\nabla\varphi_{10}^* n_j' dS}_{(a)} \\ &-\frac{i\rho_o\sigma_o}{2}\int\limits_{\mathcal{S}_o} \underbrace{\left[\boldsymbol{\xi}^{(0)} + \boldsymbol{\alpha}^{(0)}\times\boldsymbol{x}'\right]\cdot\nabla\varphi_{10}^*}_{(b)} n_j' dS \\ &-\frac{i\rho_o\sigma_o}{2}\int\limits_{\mathcal{S}_o} \underbrace{\varphi_{10}^*\left[\boldsymbol{\xi}_b^{(0)}\times(n_1', n_2', 0)\right]}_{(c)}\cdot\hat{e}_j dS \\ &+\frac{\rho_o\nu_o^2}{4}\int\limits_{\mathcal{C}_o} \underbrace{(\varphi_{10}\cdot\varphi_{10}^*)}_{(d)} n_j' d\ell.\end{aligned} \qquad \text{(F.9)}$$

We will proceed by considering each of these terms, (labeled (a), (b), (c), (d), in Eq. (F.9), as $F_j^{(20.a)}$, $F_j^{(20.b)}$, $F_j^{(20.c)}$, $F_j^{(20.d)}$, respectively) in order of their occurrence.

F.3.1 Term $F_j^{(20.a)}$

We consider the entire first-order potential (diffraction and radiation potentials), as given in Eq. (2.57). If we insert this potential into the (a) term from Eq. (F.9), we find that

$$\begin{aligned} F_j^{(20.a)} \underset{\text{Re}}{=} -\frac{1}{4}\rho_o \Bigg\{ & A_o^2 \iint_{S_0} \underbrace{|\nabla\psi_D^{(e)}|^2}_{(i)} n_j dS \\ & + i\sigma_o A_o \sum_{i=1,2,6} \iint_{S_0} \underbrace{\left(\mathcal{A}_i^{(0)*}\nabla\psi_i^{(e)*}\cdot\nabla\psi_D^{(e)} - \mathcal{A}_i^{(0)}\nabla\psi_i^{(e)}\cdot\nabla\psi_D^{(e)*}\right)}_{(ii)} n_j dS \\ & + \sigma_o^2 \sum_{i=1,2,6}\sum_{k=1,2,6} \mathcal{A}_i^{(0)}\mathcal{A}_k^{(0)*} \iint_{S_0} \underbrace{\nabla\psi_i^{(e)}\nabla\psi_k^{(e)*}}_{(iii)} n_j dS \Bigg\}, \end{aligned} \tag{F.10}$$

where the three terms, which are later referred to as 'Diffraction-Diffraction', 'Diffraction-Radiation' and 'Radiation-Radiation' terms, or (i), (ii), (iii), respectively.

In a similar let us define $\bar{\kappa}_{ij}$ as terms that are proportional to the product of the wave amplitude and linear body motion ('Diffraction-Radiation') as,

$$\bar{\kappa}_{ij} = \bar{\kappa}_{ij}^{(a)} + \bar{\kappa}_{ij}^{(b)} + \bar{\kappa}_{ij}^{(c)} + \bar{\kappa}_{ij}^{(d)}. \tag{F.11}$$

Likewise, for the 'Radiation-Radiation' terms,

$$\bar{\mu}_{jik}^{(2)} = \bar{\mu}_{jik}^{(2)b} + \bar{\mu}_{jik}^{(2)c}, \tag{F.12a}$$

$$\bar{\lambda}_{jik}^{(2)} = \bar{\lambda}_{jik}^{(2)b} + \bar{\lambda}_{jik}^{(2)c}, \tag{F.12b}$$

since we will show that the (a) and (d) related to this tensor are null.

Term $F_j^{(20.a.i)}$: Diffraction-Diffraction

Our analysis of these expressions begins with term (i) shown in Eq. (F.10), where we are considering the components proportional to the diffraction potential. We find that the second-order, steady slow drift forces in surge and sway due to term (a) on cylinder k are,

$$\bar{\mathcal{X}}_j^{k(a)} = -\frac{1}{4}\rho_o \iint_{S_0} |\nabla\psi_D^{k(e)}|^2 n_j dS, \text{ for } j = 1, 2. \tag{F.13}$$

The expansion of the gradient operator leads to the second-order drift forces, which are,

$$\bar{\mathcal{X}}_j^{k(a)} = \frac{1}{4}\rho_o a \int_0^{2\pi}\int_d^h \left(\left|\frac{\partial\psi_D^{k(e)}}{\partial z}\right|^2_{r_k=a} + \frac{1}{a^2}\left|\frac{\partial\psi_D^{k(e)}}{\partial\theta_k}\right|^2_{r_k=a} \right) \cos(\theta_k - \chi_j) dz d\theta_k \text{ for } j = 1, 2. \tag{F.14}$$

The solution for the incident and first-order diffraction potentials can be found in Eqs. (2.64), (2.69) and (2.72), where we do not consider the interaction effects on the cylinders in calculation of the drift force. We shall write the full expression in Sec. F.4.

Term $F_j^{(20.a.ii)}$: Diffraction-Radiation

We rewrite the relevant term from Eq. (F.10), under consideration in this section as,

$$F_j^{(20.a.ii)} \underset{\text{Re}}{=} -\frac{i\sigma_o\rho_o A_o}{4}\sum_{i=1,2,6}\iint_{S_0}\left(\mathcal{A}_i^{(0)*}\nabla\psi_i^{(e)*}\cdot\nabla\psi_D^{(e)} - \mathcal{A}_i^{(0)}\nabla\psi_i^{(e)}\cdot\nabla\psi_D^{(e)*}\right)\Big|_{r=a} n_j dS. \quad \text{(F.15)}$$

It is clear that the real part of the integrand is null, so we can rewrite the above expression as,

$$F_j^{(20.a.ii)} = \frac{\sigma_o\rho_o A_o}{2}\sum_{i=1,2,6}\iint_{S_0}\text{Im}\left[\mathcal{A}_i^{(0)}\nabla\psi_i^{(e)}\cdot\nabla\psi_D^{(e)*}\right]\Big|_{r=a} n_j dS. \quad \text{(F.16)}$$

Simply by using properties of complex numbers we find that,

$$F_j^{(20.a.ii)} \underset{\text{Re}}{=} -\frac{i\sigma_o\rho_o A_o}{2}\sum_{i=1,2,6}\mathcal{A}_i^{(0)}\iint_{S_0}\left(\nabla\psi_i^{(e)}\cdot\nabla\psi_D^{(e)*}\right)\Big|_{r=a} n_j dS. \quad \text{(F.17)}$$

We note here that in order to get a representation of the force in terms of the expression provided in Eq. (2.114c), we can define,

$$F_j^{(20.a.ii)} \underset{\text{Re}}{=} A_o\sum_{i=1,2,6}\frac{\bar{\kappa}_{ji}^{(a)}}{\rho_o g\pi a}\mathcal{A}_i^{(0)}, \quad \text{(F.18)}$$

where $\bar{\kappa}_{ji}^{(a)}$ is defined as,

$$\frac{\bar{\kappa}_{ji}^{(a)}}{\rho_o g\pi a} = -\frac{i\sigma_o}{2\pi g a}\iint_{S_0}\left(\nabla\psi_i^{(e)}\cdot\nabla\psi_D^{(e)*}\right)\Big|_{r=a} n_j dS. \quad \text{(F.19)}$$

Again, we expand the gradient operator and note that due to the no penetration condition, the gradient of the diffraction potential in the radial direction on the cylinder, evaluated on the surface of the cylinder is null. Thus,

$$\frac{\bar{\kappa}_{j\ell}^{k(a)}}{\rho_o g a_k\pi} = \frac{i\sigma_o}{2\pi g}\int_d^h\int_0^{2\pi}\left(\frac{\partial\psi_i^{(e)}}{\partial z}\frac{\partial\psi_D^{(e)*}}{\partial z} + \frac{1}{r^2}\frac{\partial\psi_i^{(e)}}{\partial\theta}\frac{\partial\psi_D^{(e)*}}{\partial\theta}\right)\Big|_{r=a}\cos(\theta-\chi_j)d\theta dz \quad \text{(F.20)}$$

On the k^{th} cylinder, the substitution of the gradients of the first-order potentials yields the following equation for $\bar{\kappa}_{ji}^{(a)}$,

$$\begin{aligned}\frac{\bar{\kappa}_{j\ell}^{k(a)}}{\rho_o g a_k\pi} &= -i\frac{P_k^*}{2}\sum_{p=0}^{\infty}\sum_{q=0}^{\infty}\bar{F}_{pq}^D H_p^\ell(a_k)(k_q a_k)(k_p a_k)G_q^{(0)*}(a_k)\cos[\chi_j-\chi_\ell] \\ &+\left(\bar{E}_{pq}^D + \frac{\bar{F}_{pq}^D}{2}(k_q a_k)(k_p a_k)\right)H_p^\ell(a_k)G_q^{(2)*}(a)\cos[2\beta-(\chi_j+\chi_\ell)],\ \text{for } j,\ell=1,2,\end{aligned} \quad \text{(F.21)}$$

The coefficients $\bar{E}^D_{pq}$ are

$$\bar{E}^D_{pq} = \frac{1}{a}\begin{cases} \int_d^h \cosh^2 k_o z dz, & \text{for } p=0, q=0, \\ \int_d^h \cosh k_o z \cos k_q z dz, & \text{for } p=0, q>0, \\ \int_d^h \cosh k_o z \cos k_p z dz, & \text{for } q=0, p>0, \\ \int_d^h \cos k_p z \cos k_q z dz, & \text{for } q=0, p>0, \end{cases} \tag{F.22}$$

and $\bar{F}^D_{pq}$ are

$$\bar{F}^D_{pq} = \frac{1}{a}\begin{cases} \int_d^h \sinh^2 k_o z dz, & \text{for } p=0, q=0, \\ -\int_d^h \sinh k_o z \sin k_q z dz, & \text{for } p=0, q>0, \\ -\int_d^h \sinh k_o z \sin k_p z dz, & \text{for } q=0, p>0, \\ \int_d^h \sin k_p z \sin k_q z dz, & \text{for } q=0, p>0, \end{cases} \tag{F.23}$$

For the rotational modes,

$$\bar{\kappa}^{k(a)}_{j\ell} = \begin{cases} y_0^k \bar{\kappa}^{k(a)}_{11} - x_0^k \bar{\kappa}^{k(a)}_{12} \text{ for } j=1, \ell=6 \\ -x_0^k \bar{\kappa}^{k(a)}_{22} + y_0^k \bar{\kappa}^{k(a)}_{21} \text{ for } j=2, \ell=6 \\ -y_0^k \bar{\kappa}^{k(a)}_{11} + x_0^k \bar{\kappa}^{k(a)}_{21} \text{ for } j=6, \ell=1 \\ x_0^k \bar{\kappa}^{k(a)}_{22} - y_0^k \bar{\kappa}^{k(a)}_{12} \text{ for } j=6, \ell=2 \\ x_0^k \bar{\kappa}^{k(a)}_{26} - y_0^k \bar{\kappa}^{k(a)}_{16} \text{ for } j=6, \ell=6. \end{cases} \tag{F.24}$$

Term $F_j^{(20.a.iii)}$

We claim that we can disregard term $F_j^{(20.a.iii)}$ since we can argue it is null using simple trigonometric arguments. Upon the examination of $F_j^{(20.a.iii)}$, we realize that the integration over the azimuthal direction occurs over an odd number (3) of sine or cosine terms, since $\psi_k^{(e)*}$, $\psi_i^{(e)}$ and n_j terms all contain a single sine or cosine. Due to the orthogonality of these functions, $F_j^{(20.a.iii)} = 0$.

F.3.2 Term $F_j^{(20.b)}$

We shift our analysis to the next term in Eq. (F.9), which is labeled (b). This term only is broken down into two parts, for the diffraction and radiation potentials ($F_j^{(20.b.ii)}$ and $F_j^{(20.b.iii)}$, respectively)

$$\begin{aligned} F_j^{(20.b)} \underset{\text{Re}}{=} -\frac{i\rho_o\sigma_o}{2}\Bigg\{ & A_o \iint_{S_0} \Bigg[\underbrace{\frac{\partial \psi_D^{(e)*}}{\partial r}\left(\mathcal{A}_1^{(0)}\cos\theta + \mathcal{A}_2^{(0)}\sin\theta\right)}_{(ii)} \\ & + \underbrace{\frac{1}{r}\frac{\partial \psi_D^{(e)*}}{\partial \theta}\left(-\mathcal{A}_1^{(0)}\sin\theta + \mathcal{A}_2^{(0)}\cos\theta + \mathcal{A}_6^{(0)} r\right)}_{(ii)} \Bigg]_{r=a} n_j dS \\ & + i\sigma_o \sum_{k=1,2,6} \iint_{S_0} \Bigg[\underbrace{\frac{\partial \psi_k^{(e)*}}{\partial r}\left(\mathcal{A}_1^{(0)}\cos\theta + \mathcal{A}_2^{(0)}\sin\theta\right)}_{(iii)} \\ & + \underbrace{\frac{1}{r}\frac{\partial \psi_k^{(e)*}}{\partial \theta}\left(-\mathcal{A}_1^{(0)}\sin\theta + \mathcal{A}_2^{(0)}\cos\theta + \mathcal{A}_6^{(0)} r\right)}_{(iii)} \Bigg]_{r=a} n_j dS \Bigg\}. \end{aligned} \tag{F.25}$$

We can use the no penetration condition on the cylinder wall to simplify the analysis, by applying the complex conjugate on both sides of Eq. (2.59), such that

$$\begin{aligned} F_j^{(20.b)} \underset{\text{Re}}{=} -\frac{i\rho_o\sigma_o}{2}\Bigg\{ & A_o \iint_{S_0} \underbrace{\frac{1}{r}\frac{\partial \psi_D^{(e)*}}{\partial \theta}\left(-\mathcal{A}_1^{(0)}\sin\theta + \mathcal{A}_2^{(0)}\cos\theta + \mathcal{A}_6^{(0)} r\right)}_{(ii)} \Bigg|_{r=a} n_j dS \\ & + i\sigma_o \sum_{k=1,2,6} \iint_{S_0} \underbrace{\frac{1}{r}\frac{\partial \psi_k^{(e)*}}{\partial \theta}\left(-\mathcal{A}_1^{(0)}\sin\theta + \mathcal{A}_2^{(0)}\cos\theta + \mathcal{A}_6^{(0)} r\right)}_{(iii)} \Bigg|_{r=a} n_j dS. \Bigg\} \end{aligned} \tag{F.26}$$

Term $F_j^{(20.b.i)}$

As previously noted, there is no term proportional to the square of the wave amplitude for $F_j^{(20.b)}$.

Term $F_j^{(20.b.ii)}$: Diffraction-Radiation

By inserting the pressure term p_{10} from Eq. (2.104b) into the (b) term in Eq. (2.111), and only condsidering the components proportional to the diffraction potential, we obtain,

$$F_j^{(20.b)} \underset{\text{Re}}{=} -\frac{i\rho_o\sigma_o a A_o}{2}\int_d^h\int_0^{2\pi}\left[-\frac{1}{r}\frac{\partial\psi_D^*}{\partial\theta}\sin\theta\left(\mathcal{A}_1^{(0)}-\mathcal{A}_6^{(0)}r\sin\theta\right)\right.$$
$$\left.+\frac{1}{r}\frac{\partial\psi_D^*}{\partial\theta}\cos\theta\left(\mathcal{A}_2^{(0)}+\mathcal{A}_6^{(0)}r\cos\theta\right)\right]\Bigg|_{r=a} n_j d\theta dz. \tag{F.27}$$

Considering the k^{th} cylinder, we substitute the zero-speed diffraction potential, given in Eqs. (2.64), (2.69) and (2.72) and find that,

$$F_j^{k(20.b)} \underset{\text{Re}}{=} \frac{i\rho_o g a A_o P_k^*}{2}\sum_{m=0}^{\infty}\sum_{p=0}^{\infty}\int_d^h\int_0^{2\pi}\check{Z}_q(z)G_q^{(m)*}(a)m\sin m(\theta-\beta)$$
$$\left(-\mathcal{A}_1^{(0)}\sin\theta+\mathcal{A}_2^{(0)}\cos\theta+a\mathcal{A}_6^{(0)}\right)\cos\left(\theta-\chi_j\right)d\theta dz. \tag{F.28}$$

Using the definition of $\bar{\kappa}_{ij}^{k(b)}$ in Eq. (2.114c) and canceling terms due to the orthogonality of the $\check{Z}_q(z)$ functions, we obtain for the translational modes,

$$\frac{\bar{\kappa}_{j\ell}^{k(b)}}{\rho_o g a\pi} = -i\frac{P_k^*}{2}\sum_{q=0}^{\infty}\check{D}_q G_q^{(2)*}(a)\cos[2\beta-(\chi_j+\chi_\ell)],\ \text{for } j,\ell=1,2, \tag{F.29}$$

where

$$\check{D}_q = \frac{1}{a}\int_d^h \check{Z}_q(z)dz. \tag{F.30}$$

For the rotational modes,

$$\bar{\kappa}_{j\ell}^{k(b)} = \begin{cases} \frac{1}{2}\mathcal{X}_2^{*k(0)} \text{ for } j=1,\ell=6 \\ -\frac{1}{2}\mathcal{X}_1^{*k(0)} \text{ for } j=2,\ell=6 \\ -y_0^k\bar{\kappa}_{11}^{k(b)}+x_0^k\bar{\kappa}_{21}^{k(b)} \text{ for } j=6,\ell=1 \\ -y_0^k\bar{\kappa}_{12}^{k(b)}+x_0^k\bar{\kappa}_{22}^{k(b)} \text{ for } j=6,\ell=2 \\ x_0^k\bar{\kappa}_{26}^{k(b)}-y_0^k\bar{\kappa}_{16}^{k(b)} \text{ for } j=6,\ell=6 \end{cases} \tag{F.31}$$

Term $F_j^{(20.b.iii)}$: Radiation-Radiation

The terms proportional to the square of the complex motion amplitudes are found by inserting the radiation potentials into Eq. (F.9). Due to the orthogonality of the sine functions, the first term of the integrand in Eq. (F.27) is null. The only surviving term from (b) for the force in the j^{th} direction to the k^{th} mode of motion is,

$$F_{jk}^{(20.b)} = -\frac{i\rho_o\sigma_o a^2}{2}(i\sigma_o\mathcal{A}_k^{(0)*})\mathcal{A}_6^{(0)}\int_d^h\int_0^{2\pi}\frac{\partial\psi_k^*}{\partial\theta}\cos(\theta-\chi_j)d\theta dz,\ \text{for } j,k=1,2. \tag{F.32}$$

The substitution of the radiation potential into the above equation yields,

$$F_{jk}^{(20.b)} = \frac{\rho_o \sigma_o^2 a^2 \mathcal{A}_k^{*(0)} \mathcal{A}_6^{(0)}}{2} \sum_{q=0}^{\infty} \int_d^h \int_0^{2\pi} \check{Z}_q(z) H_q^{*k}(a) \sin(\theta - \chi_k) \cos(\theta - \chi_j) d\theta dz, \tag{F.33}$$

which simplifies to

$$F_{jk}^{(20.b)} = -\frac{\rho_o \sigma_o^2 a^3 \pi \mathcal{A}_k^{*(0)} \mathcal{A}_6^{(0)}}{2} \sum_{q=0}^{\infty} \check{D}_q H_q^{*k}(a)(1 - \delta_{jk})(-1)^k \tag{F.34}$$

We recognize that this terms holds the complex conjugate of the radiation added-mass and damping, which is

$$\begin{aligned} \rho_o \sigma_o^2 \iint_{\mathcal{S}_o} \psi_k^* n_j' dS &= -\rho_o \pi a^3 \sigma_o^2 \sum_{q=0}^{\infty} \check{D}_q H_q^{*k}(a) \\ &= \left(\sigma_o^2 \mu_{jk}^{(0)} - i\sigma \lambda_{jk}^{(0)} \right), \end{aligned} \tag{F.35}$$

where the last equality comes from the facts that,

$$\mu_{jk}^{(0)} = \rho_o \operatorname{Re} \left[\iint_{\mathcal{S}_o} \psi_k^* n_j' dS \right] \tag{F.36a}$$

$$\lambda_{jk}^{(0)} = -\frac{\rho_o}{\sigma_o} \operatorname{Im} \left[\iint_{\mathcal{S}_o} \psi_k^* n_j' dS \right] \tag{F.36b}$$

Since $\mu_{11}^{(0)}$=$\mu_{22}^{(0)}$, due to circumferential symmetry (and since the same holds for $\lambda_{jj}^{(0)}$, for $j = 1, 2$), we can write,

$$F_{jk}^{(20.b)} = \frac{1}{2} \mathcal{A}_k^{*(0)} \mathcal{A}_6^{(0)} \left(\sigma_o^2 \mu_{11}^{(0)} - i\sigma_o \lambda_{11}^{(0)} \right) (1 - \delta_{jk})(-1)^k \text{ for } j, k = 1, 2. \tag{F.37}$$

In terms of the $\bar{\mu}_{j6k}^{(2)b}$, defined in Eq. (2.114c), we obtain for the translational cases

$$\sigma_o^2 \bar{\mu}_{j6k}^{(2)b} + i\sigma_o \bar{\lambda}_{j6k}^{(2)b} = \frac{1}{2} \left(\sigma_o^2 \mu_{11}^{(0)} - i\sigma_o \lambda_{11}^{(0)} \right) \begin{cases} 1 \text{ for } j = 1, k = 2 \\ -1 \text{ for } j = 2, k = 1 \end{cases} \tag{F.38}$$

and for the rotational cases

$$\sigma_o^2 \bar{\mu}_{j6k}^{(2)b} + i\sigma_o \bar{\lambda}_{j6k}^{(2)b} = -\frac{1}{2} \left(\sigma_o^2 \mu_{11}^{(0)} - i\sigma_o \lambda_{11}^{(0)} \right) \begin{cases} x_0 \text{ for } j = 1, k = 6 \\ y_0 \text{ for } j = 2, k = 6, \\ x_0 \text{ for } j = 6, k = 1 \\ y_0 \text{ for } j = 6, k = 2, \\ 0 \text{ otherwise.} \end{cases} \tag{F.39}$$

F.3.3 Term $F_j^{(20.c)}$

The analysis of the (c) term proceeds much in a similar manner as that found in Sec. F.3.2. A major simplification can be made by noting that the first-order hydrodynamic forces can be recovered from this term.

$$F_j^{(20.c)} = -\frac{i\sigma_o\rho_o}{2}\iint\limits_{\mathcal{S}_o}\Bigg\{\underbrace{\psi_D^*\left(\boldsymbol{\xi_b}\times[n_1',n_2',0]^T\right)\cdot\hat{e}_j}_{(ii)}\,dS + i\sigma_o\sum_{k=1,2,6}\iint\limits_{\mathcal{S}_o}\underbrace{\psi_k^*\left(\boldsymbol{\xi_b}\times[n_1',n_2',0]^T\right)\cdot\hat{e}_j}_{(iii)}\,dS\Bigg\}\quad\text{for } j=1,2,6. \tag{F.40}$$

Term $F_j^{(20.c.i)}$

Again, there is no term related to the square of the wave amplitude for term (c).

Term $F_j^{(20.c.ii)}$: Diffraction-Radiation

The force in the j^{th} direction due to the diffraction of the incident wave involves inserting ψ_D into term (c) of Eq. (F.9), which is

$$F_j^{(20.c.ii)} = -\frac{i\sigma_o\rho_o A_o}{2}\iint\limits_{\mathcal{S}_o}\psi_D^*\left(\boldsymbol{\xi_b}\times[n_1',n_2',0]^T\right)\cdot\hat{e}_j dS \tag{F.41}$$

We notice that this is simply one-half of the complex conjugates of the first-order wave-exciting forces. If we neglect the roll and pitch moment, we have,

$$\bar{\kappa}_{ij}^{k(c)} = \frac{1}{2}\begin{cases}-\mathcal{X}_2^{(0)*}\text{ for } i=1, j=6,\\ \mathcal{X}_1^{(0)*}\text{ for } i=2, j=6,\\ \mathcal{X}_2^{(0)*}\text{ for } i=6, j=1,\\ -\mathcal{X}_1^{(0)*}\text{ for } i=6, j=2,\\ 0\text{ otherwise .}\end{cases} \tag{F.42}$$

Term $F_j^{(20.c.iii)}$: Radiation-Radiation

The force proportional to the added-mass and damping terms can be found by inserting the radiation potential into term (c) of Eq. (F.9). By inspection,

$$\sigma_o^2\bar{\mu}_{jik}^{(2)c}+i\sigma_o\bar{\lambda}_{jik}^{(2)c}=\frac{1}{2}\left(\sigma_o^2\mu_{11}^{(0)}-i\sigma_o\lambda_{11}^{(0)}\right)\begin{cases}-1 \text{ for } j=1,i=6,k=2\\ -x_0 \text{ for } j=1,i=6,k=6\\ 1 \text{ for } j=2,i=6,k=1\\ -y_0 \text{ for } j=2,i=6,k=6\\ 1 \text{ for } j=6,i=1,k=2\\ -1 \text{ for } j=6,i=2,k=1\\ x_0 \text{ for } j=6,i=1,k=6\\ y_0 \text{ for } j=6,i=2,k=6\\ 0 \text{ otherwise.}\end{cases} \tag{F.43}$$

F.3.4 Term $F_j^{(20.d)}$

The analysis for this term proceeds much like that found in Sec. F.3.1. The term $F_j^{(20.d)}$ can be rewritten as,

$$\begin{aligned}F_j^{(20.d)} &\underset{\text{Re}}{=}\frac{\rho_o\sigma_o^2}{4g}\Bigg\{A_o^2\int_{\mathcal{C}_0}\underbrace{|\psi_D^{(e)}|^2}_{(i)}n_j d\ell\\ &+i\sigma_o A_o\sum_{i=1,2,6}\int_{\mathcal{C}_0}\underbrace{\left(\mathcal{A}_i^{(0)*}\psi_i^{(e)*}\psi_D^{(e)}-\mathcal{A}_i^{(0)}\psi_i^{(e)}\psi_D^{(e)*}\right)}_{(ii)}n_j d\ell\\ &+\sigma_o^2\sum_{i=1,2,6}\sum_{k=1,2,6}\mathcal{A}_i^{(0)}\mathcal{A}_k^{(0)*}\int_{\mathcal{C}_0}\underbrace{\psi_i^{(e)}\psi_k^{(e)*}}_{(iii)}n_j d\ell\Bigg\}.\end{aligned} \tag{F.44}$$

Term $F_j^{(20.d.i)}$: Diffraction-Diffraction

We shall expand on the expression of the steady, wave-exciting moment in Sec. F.4. For now, we simply write the expression for the steady moment from Eq. (F.44) as,

$$\bar{\mathcal{X}}_j^{k(d)}=\frac{\rho_o\sigma_o^2}{4g}\int_{\mathcal{C}_0}|\psi_D^{k(e)}|^2 n_j d\ell, \text{ for } j=1,2. \tag{F.45}$$

Term $F_j^{(20.d.ii)}$: Diffraction-Radiation

In a similar manner as done in Sec. F.3.1, we can rewrite the term $F_j^{(20.d.ii)}$, as,

$$F_j^{(20.d.ii)} \underset{\text{Re}}{=} -\frac{i\sigma_o\rho_o A_o}{4}\sum_{i=1,2,6}\int_{\mathcal{C}_0}\left(\mathcal{A}_i^{(0)*}\psi_i^{(e)*}\psi_D^{(e)} - \mathcal{A}_i^{(0)}\psi_i^{(e)}\psi_D^{(e)*}\right)\Big|_{r=a} n_j d\ell. \tag{F.46}$$

Using the same argument to obtain Eq. (F.17)), we find,

$$F_j^{(20.d.ii)} \underset{\text{Re}}{=} -\frac{i\sigma_o\rho_o A_o}{2}\sum_{i=1,2,6}\mathcal{A}_i^{(0)}\int_{\mathcal{C}_0}\left(\ \psi_i^{(e)}\psi_D^{(e)*}\right)\Big|_{r=a} n_j d\ell. \tag{F.47}$$

Using as similar (albeit, simpler) procedure as described in the section concerning the (a) terms, we arrive at the follow expression for $\bar{\kappa}_{j\ell}^{k(d)}$:

$$\begin{aligned}\frac{\bar{\kappa}_{j\ell}^{k(d)}}{\rho_o g a\pi} = -\frac{i\nu_o a_k P_k^*}{2}\sum_{p=0}^{\infty}\sum_{q=0}^{\infty}\check{Z}_p(h)\check{Z}_q(h)H_p^{\ell}(a)\\ \left[G_q^{(0)*}(a)\cos[\chi_j-\chi_\ell] + \frac{G_q^{(2)*}(a)}{2}\cos[2\beta-(\chi_j+\chi_\ell)]\right],\ \text{for } j,\ell=1,2.\end{aligned} \tag{F.48}$$

The rotational modes can be written in a similar manner as in Eq. (F.24).

Term $F_j^{(20.d.iii)}$

Using a similar argument found in the section concerning the (a) terms, we find the radiation tensor to be null for all modes of motion. In the following section, we combine the analysis of the previous sections to represent three hydrodynamic forces: the steady, slow-drift moment, a moment proportional to the wave amplitude and the body motion and a moment proportional to the products of body motions.

F.4 Slow-Drift Moment Proportional to Square of Wave Amplitude

The combination of Eqs. (F.14) and (F.14), yield the following second-order drift forces for a vertical, truncated cylinder:

$$\begin{aligned}\bar{\mathcal{X}}_j^{k(2)} = \frac{1}{4}\rho_o a\left\{\int_0^{2\pi}\int_d^h\left(\left|\frac{\partial\psi_D^{k(e)}}{\partial z}\right|_{r_k=a}^2 + \frac{1}{2a}\left|\frac{\partial\psi_D^{k(e)}}{\partial\theta_k}\right|_{r_k=a}^2\right)\cos(\theta_k-\chi_j)dzd\theta_k\right.\\ \left.-\frac{\sigma_0^2}{g}\int_0^{2\pi}\left|\psi_D^{k(e)}\right|_{r_k=a}^2\cos(\theta_k-\chi_j)d\theta_k\right\}\ \text{for } j=1,2.\end{aligned} \tag{F.49}$$

Integrating the expression in Eq. (F.49), we find the drift-force to be,

$$\begin{aligned}\frac{\bar{\mathcal{X}}_j^{(2)}}{\rho_o g\pi a^2} = \frac{k_o A_o \cos(\beta-\chi_j)}{8\tanh m_0}\sum_{n=0}^{\infty}\left(G_0^{(n+1)n*}(a)+G_0^{n(n+1)*}\right)\bar{C}_0^{n+1,n} \\ +\sum_{q=1}^{\infty}\left(G_q^{(n+1)}G_0^{n*}+G_0^{(n+1)}G_q^{n*}+G_q^{n}G_0^{(n+1)*}+G_0^{n}G_{jq}^{(n+1)*}\right)\bar{C}_q^{n+1,n} \\ +\sum_{p=1}^{\infty}\left(G_q^{(n+1)}G_{pj}^{n*}+G_q^{n}G_{pj}^{(n+1)*}\right)\bar{C}_{pq}^{n+1,n}\end{aligned} \tag{F.50}$$

where we have only indicated the fact that the $G_p^{(n)}(r)$ functions are evaluated at $r=a$ once for clarity. The other coefficients $\bar{C}_q^{(m,n)}$ are

$$\bar{C}_q^{(m,n)} = \begin{cases} \bar{\epsilon}_n F_{00}^D + \dfrac{mn}{(k_0a)^2}E_{00}^D - \dfrac{\bar{\epsilon}_n\tanh m_0}{k_0 a}\cosh^2 m_0, & \text{for } q=0, \\ +\dfrac{\bar{\epsilon}_n k_q}{k_0}F_{0q}^D + \dfrac{mn}{(k_0a)^2}E_{0q}^D - \dfrac{\bar{\epsilon}_n\tanh m_0}{k_0 a}\cosh m_0\cos m_q, & \text{for } q>0, \end{cases} \tag{F.51}$$

with

$$\bar{C}_{pq}^{(m,n)} = \frac{\bar{\epsilon}_n k_q k_q}{k_0^2}F_{pq}^D + \frac{mn}{(k_0a)^2}\bar{E}_{pq}^D - \frac{\bar{\epsilon}_n\tanh m_0}{k_0 a}\cos m_p\cos m_q, \tag{F.52}$$

where $\bar{\epsilon}_n = 2/\epsilon_n$ with ϵ_n as defined in Sec. 2.4.1. The most important property to note about these forces is that they are temporally (by definition) and *spatially* independent, due to the phase-factors canceling out, that is, $P_k P_k^* = 1$. Thus, for a multi-column platform, whose center of rotation coincides with its geometric center, these drift forces will never produce a moment. The summation of the moments on the cylinders allows us to obtain the moment on the platform, which is,

$$\bar{\mathcal{X}}_6^{(2)} = \sum_{k=1}^{N_{col}} x_0^k\bar{\mathcal{X}}_2^{k(2)} - y_0^k\bar{\mathcal{X}}_1^{k(2)} = \bar{\mathcal{X}}_2^{(2)}\sum_{k=1}^{N_{col}}x_0^k - \bar{\mathcal{X}}_1^{(2)}\sum_{k=1}^{N_{col}}y_0^k = 0 \tag{F.53}$$

where the last equality is due to the fact the platform's geometric center is the origin of the inertial system (about which the platform is rotating) and we assume that $U_1 = U_2 = 0$.

F.5 Slow-Drift Moment Proportional to Wave and Body Oscillation Amplitude

We solve for the slow-drift force proportional to the body oscillation amplitude $\mathcal{A}_j^{(0)}$ by recognizing that all terms in Eq. (2.111) have components that are proportional to both

A_o and $\mathcal{A}_j^{(0)}$. We bring together the results from the previous sections and find that for $j, \ell = 1, 2$,

$$\begin{aligned}\frac{\bar{\kappa}_{j\ell}^k}{\rho_o g a_k \pi} = -i\frac{P_k^*}{2}\Bigg\{&\sum_{q=0}^{\infty} G_q^{(2)*}\cos[2\beta-(\chi_j+\chi_\ell)]\\ &\left[\underbrace{\check{D}_q}_{(b)} + \sum_{p=0}^{\infty} H_p^\ell(a_k)\left(\underbrace{\bar{E}_{pq}^D + \frac{\bar{F}_{pq}^D(k_q a_k)(k_p a_k)}{2}}_{(a)} + \underbrace{(\nu_o a_k)\check{Z}_p(h)\check{Z}_q(h)}_{(d)}\right)\right]\\ &+ G_q^{(0)*}\cos(\chi_j-\chi_\ell)\sum_{p=0}^{\infty} H_p^\ell(a_k)\left(\underbrace{\bar{F}_{pq}^D(k_q a_k)(k_p a_k)}_{(a)} + \underbrace{(\nu_o a_k)\check{Z}_p(h)\check{Z}_q(h)}_{(d)}\right)\Bigg\},\end{aligned} \tag{F.54}$$

where we have highlighted the contributions from each of the terms described in the previous sections. The term $\bar{\kappa}_{j\ell}^{k(t)}$ is identical to the expression in Eq. (F.54), with the $\check{D}_q$ term removed, as it is the sole contribution from the (b) term. In sum, we have for $\bar{\kappa}_6$,

$$\frac{\bar{\kappa}_6^k}{\rho_o g\pi a^2} = \begin{bmatrix} -\frac{y_0^k}{a}\bar{\kappa}_{11}^k + \frac{x_0^k}{a}\bar{\kappa}_{21}^k + \frac{\bar{\mathcal{X}}_2^{(0)*}}{2} \\ \frac{x_0^k}{a}\bar{\kappa}_{22}^k - \frac{y_0^k}{a}\bar{\kappa}_{12}^k - \frac{\bar{\mathcal{X}}_1^{(0)*}}{2} \\ 2\frac{x_0^k y_0^k}{a^2}\bar{\kappa}_{12}^{k(t)} - \left(\frac{y_0^k}{a}\right)^2\bar{\kappa}_{11}^{k(t)} - \left(\frac{x_0^k}{a}\right)^2\bar{\kappa}_{22}^{k(t)} - \frac{x_0^k}{a}\frac{\bar{\mathcal{X}}_1^{(0)*}}{2} - \frac{y_0^k}{a}\frac{\bar{\mathcal{X}}_2^{(0)*}}{2} \end{bmatrix} \tag{F.55}$$

where we have used the that $\bar{\kappa}_{12}^k = \bar{\kappa}_{21}^k$. The total moment on the k^{th} cylinder requires multiplying these terms by the respective RAOs, which is

$$\begin{aligned}\frac{F_{6,\kappa}^{k(20)}}{\rho_o g\pi a^2 A_o^2} \underset{\text{Re}}{=}& \frac{\mathcal{A}_1^{(0)}}{A_o}\left(-\frac{y_0^k}{a}\bar{\kappa}_{11}^k + \frac{x_0^k}{a}\bar{\kappa}_{21}^k + \frac{\bar{\mathcal{X}}_2^{k(0)*}}{2}\right)\\ &+ \frac{\mathcal{A}_2^{(0)}}{A_o}\left(\frac{x_0^k}{a}\bar{\kappa}_{22}^k - \frac{y_0^k}{a}\bar{\kappa}_{12}^k - \frac{\bar{\mathcal{X}}_1^{k(0)*}}{2}\right)\\ &+ \frac{\mathcal{A}_6^{(0)}}{k_o A_o}\left(2k_o x_0^k\frac{y_0^k}{a}\bar{\kappa}_{12}^{k(t)} - k_o y_0^k\frac{y_0^k}{a}\bar{\kappa}_{11}^{k(t)} - k_o x_0^k\frac{x_0^k}{a}\bar{\kappa}_{22}^{k(t)}\right)\\ &- \frac{k_o a}{2}\frac{\mathcal{A}_6^{(0)}}{k_o A_o}\left(\frac{x_0^k}{a}\bar{\mathcal{X}}_1^{k(0)*} + \frac{y_0^k}{a}\bar{\mathcal{X}}_2^{k(0)*}\right).\end{aligned} \tag{F.56}$$

The total moment on the platform then becomes,

$$\frac{F^{(20)}_{6,\kappa}}{\rho_o g\pi a^2 A_o^2} = \underset{\text{Re}}{=} \frac{\mathcal{A}^{(0)}_1}{A_o}\sum_k^{N_{col}}\left(-\frac{y_0^k}{a}\bar{\kappa}^k_{11}+\frac{x_0^k}{a}\bar{\kappa}^k_{21}+\frac{\bar{\mathcal{X}}_2^{k(0)*}}{2}\right) + \frac{\mathcal{A}^{(0)}_2}{A_o}\sum_k^{N_{col}}\left(\frac{x_0^k}{a}\bar{\kappa}^k_{22}-\frac{y_0^k}{a}\bar{\kappa}^k_{12}-\frac{\bar{\mathcal{X}}_1^{k(0)*}}{2}\right) + \frac{\mathcal{A}^{(0)}_6}{k_o A_o}\sum_k^{N_{col}}\left(2k_o x_0^k\frac{y_0^k}{a}\bar{\kappa}^{k(t)}_{12}-k_o y_0^k\frac{y_0^k}{a}\bar{\kappa}^{k(t)}_{11}-k_o x_0^k\frac{x_0^k}{a}\bar{\kappa}^{k(t)}_{22}-\frac{k_o a}{2}\left[\frac{x_0^k}{a}\bar{\mathcal{X}}_1^{k(0)*}+\frac{y_0^k}{a}\bar{\mathcal{X}}_2^{k(0)*}\right]\right). \tag{F.57}$$

F.6 Slow-Drift Moment Proportional to Products of Body Oscillation Amplitudes

For terms related to the steady yaw moment $\bar{\mu}^{(2)}_{6ik}$, $\bar{\lambda}^{(2)}_{6ik}$, which are coefficients of the products of body oscillation amplitudes, we have,

$$\sigma_o^2\bar{\mu}^{(2)}_{6ik}+i\sigma_o\bar{\lambda}^{(2)}_{6ik} = \frac{1}{2}\begin{bmatrix}0 & 1 & x_0\\ -1 & 0 & y_0\\ -x_0 & -y_0 & 0\end{bmatrix}\left(\sigma_o^2\mu^{(0)}_{11}-i\sigma_o\lambda^{(0)}_{11}\right) \tag{F.58}$$

As depicted in Eq. (2.114c), we sum over the i and k directions. The summation over all the directions allows us to write the nondimensional radiation slow-drift yaw moment as

$$\frac{F^{(20)}_{6,\mu}}{\rho_o g\pi a^2 A_o^2} = \underset{\text{Re}}{=} \frac{1}{2}\nu_o a(\mu^{(0)}_{11}-i\lambda^{(0)}_{11})\left\{\left[\frac{\mathcal{A}_1}{A_o}\frac{\mathcal{A}_2^*}{A_o}-\frac{\mathcal{A}_2}{A_o}\frac{\mathcal{A}_1^*}{A_o}\right]+ k_o a\left(\frac{x_o}{a}\left[\frac{\mathcal{A}_1}{A_o}\frac{\mathcal{A}_6^*}{k_oA_o}-\frac{\mathcal{A}_6}{k_oA_o}\frac{\mathcal{A}_1^*}{A_o}\right]+\frac{y_o}{a}\left[\frac{\mathcal{A}_2}{A_o}\frac{\mathcal{A}_6^*}{k_oA_o}-\frac{\mathcal{A}_6}{k_oA_o}\frac{\mathcal{A}_2^*}{A_o}\right]\right)\right\}=0, \tag{F.59}$$

where the last equality comes from the fact that the real parts of each of the square bracket terms cancel each other.

F.7 Wave-Drift Added-Mass and Damping

The wave-drift added-mass stems from the time-derivative of the double-body pressure term p_{01}, while the wave-drift damping comes from the terms proportional to the slow-drift velocity in $F_j^{(21)}$. We first describe the wave-drift added-mass briefly and then include a longer discussion on the wave-drift damping.

F.7.1 Wave-Drift Added-Mass

The wave-drift added-mass comes from the potential ϕ_{01} given in Sec. 2.4.2. The force from this potential is found in Eq. (2.114d), and is represented by,

$$F_j^{(02)} = \int_{\mathcal{S}_o} -\rho_o \left(\sum_k \dot{U}_k \bar{\psi}_k - \boldsymbol{s} \cdot \nabla \varphi_{01} + \frac{1}{2} \nabla \varphi_{01} \cdot \nabla \varphi_{01} \right) n_j' dS. \tag{F.60}$$

If we neglect $\mathrm{O}\left(U_j U_k\right)$, but keep $\mathrm{O}\left(\dot{U}_j\right)$ we are only left with the first term, which is related to the double-body added-mass. Thus,

$$\bar{\mu}_{jk} = \rho_o \int_{\mathcal{S}_o} \bar{\psi}_k n_j dS. \tag{F.61}$$

Since we only are interested in the horizontal motion, we use the exterior potential defined in Eqs. (2.93) and (2.94), to express the double-body added-mass as,

$$\bar{\mu}_{jk} = a\rho_o \int_0^{2\pi} \int_d^h \left(\frac{\bar{B}_0}{2} + \sum_{q=1}^{\infty} \bar{B}_q \cos(\beta_q z) \right) \cos(\theta - \chi_k) n_j a d\theta dz. \tag{F.62}$$

The integration of the above equation yields,

$$\frac{\bar{\mu}_{jk}}{\rho_o \pi a^3} = \frac{\delta_{jk}}{2} \sum_{q=0}^{\infty} \epsilon_q \bar{B}_q \bar{E}_q, \text{ for } j,k = 1,2 \tag{F.63}$$

where

$$\bar{E}_q = \frac{1}{a} \int_d^h \cos(\beta_q z) dz. \tag{F.64}$$

F.7.2 Wave-Drift Damping

The wave-drift damping stems from the forces described in Eq. (2.112). Thus we will go through them, labeled (a)-(f) in order of occurrence. Again, we note that only the diffraction potential of $\bar{\varphi}_{20}$ will lead to wave-drift damping terms, as noted in [26].

Term F_j^{21a}

From Eq. (2.112), we define the term F_j^{21a} as,

$$\begin{aligned} F_j^{21a} &= \mathrm{Re}\left[\int_{\mathcal{S}_o} p_{21} n_j' dS \right] \\ &= -\rho_o \int_{\mathcal{S}_o} \mathrm{Re}\left[\underbrace{-U_6 \frac{\partial \bar{\varphi}_{20}^D}{\partial \beta}}_{(i)} \underbrace{- \boldsymbol{s} \cdot \nabla \bar{\varphi}_{20}^D}_{(ii)} \underbrace{+ \nabla \bar{\varphi}_{20}^D \cdot \nabla \varphi_{01}}_{(iii)} \underbrace{+ \frac{1}{2} \nabla \varphi_{11}^* \cdot \nabla \varphi_{10}}_{(iv)} \right] n_j' dS. \end{aligned} \tag{F.65}$$

To our knowledge, the steady, second-order potential has not been found explicitly in the literature. Most authors, such as [45] and [129], only consider the unsteady potential because in the zero-speed problem the steady potential does not contribute to the first or second-order forces. Thus, we seek to transform the terms related to $\bar{\varphi}_{20}^D$ into forms related to lower order potentials. This procedure was performed in [32] for the $(a.iii)$ term using Stokes' Theorem and will be shown in greater detail in the forthcoming section. Similar analysis is used for the terms $(a.i)$, $(a.ii)$ and $(a.iv)$.

The strategy to convert these terms into lower order potentials is to use Green's Theorem on an imaginary boundary surrounding the body. This boundary takes the form of a cylinder with radius R, where $R >> a$. We apply Green's Theorem using two potentials: $\bar{\varphi}_{20}^D$ and $\bar{\varphi}_{01}$. We attempt to write the terms in the integrand of Green's Theorem as normal derivatives so that we can insert the boundary conditions for φ_{20}^D on the body surface and the surface $z = h$. We note that due to the Sommerfield radiation condition $|\nabla\bar{\varphi}_{20}| \to 0, r \to \infty$. We apply Green's Theorem to $\bar{\varphi}_{20}$ and $\bar{\varphi}_{01}$, which yields

$$\iint\limits_{\mathcal{S}_b \cup \mathcal{S}_f \cup \mathcal{S}_o \cup \mathcal{S}_r} \bar{\varphi}_{20}^D \frac{\partial \varphi_{01}}{\partial n} - \varphi_{01} \frac{\partial \bar{\varphi}_{20}^D}{\partial n} dS = 0, \tag{F.66}$$

where the boundary can be defined by the surfaces on the seabed, free surface, body and outer control surface, $\mathcal{S}_b \cup \mathcal{S}_f \cup \mathcal{S}_o \cup \mathcal{S}_r$. Due to the no penetration condition on the seabed, the terms integrated over $\mathcal{S}_b$ will be null. Using the boundary condition in 2.49a and Eq. (2.37b), we have,

$$\iint\limits_{\mathcal{S}_o} U_j \bar{\varphi}_{20}^D n_j' dS = \iint\limits_{\mathcal{S}_f \cup \mathcal{S}_o \cup \mathcal{S}_r} \varphi_{01} \frac{\partial \bar{\varphi}_{20}^D}{\partial n} dS - \iint\limits_{\mathcal{S}_r} \bar{\varphi}_{20}^D \frac{\partial \varphi_{01}}{\partial n} dS. \tag{F.67}$$

We note that the flux of the second-order diffraction potential as well as the first-order potential out of the far-field boundary must decay to 0 as $R \to \infty$. Thus,

$$U_j \iint\limits_{\mathcal{S}_o} \bar{\varphi}_{20}^D n_j' dS = \iint\limits_{\mathcal{S}_f} \varphi_{01} \frac{\partial \bar{\varphi}_{20}^D}{\partial n} dS \tag{F.68}$$

To transform $F_j^{21a.i}$, we note that φ_{01} is independent of β (since there is no incident wave taken into account for this potential). Clearly,

$$U_j \iint\limits_{\mathcal{S}_o} \frac{\partial \bar{\varphi}_{20}}{\partial \beta} n_j' dS = \iint\limits_{\mathcal{S}_f} \varphi_{01} \frac{\partial}{\partial \beta} \frac{\partial \bar{\varphi}_{20}}{\partial n} dS. \tag{F.69}$$

Thus, we can insert the boundary conditions in Eqs. (2.49d) and (2.42) and solve for $F_j^{21a.i}$. Let $f^{(20)}$ represent the linearized free surface such that,

$$f^{(20)} = -\frac{\sigma_o}{2g} \operatorname{Im}\left[\varphi_{10} \frac{\partial^2 \varphi_{10}^*}{\partial z^2}\right]. \tag{F.70}$$

Setting $j = 6$, we can rewrite the previous equation as,

$$\iint\limits_{\mathcal{S}_o} \frac{\partial \bar{\varphi}_{20}}{\partial \beta} n_6' dS = -\frac{\sigma_o A_o^2}{2g} \iint\limits_{\mathcal{S}_f} \bar{\psi}_6 \operatorname{Im}\left[\frac{\partial \psi_D}{\partial \beta}\frac{\partial^2 \psi_D^*}{\partial z^2}\right] + \bar{\psi}_6 \operatorname{Im}\left[\psi_D \frac{\partial^3 \psi_D^*}{\partial z^2 \partial \beta}\right] dS \tag{F.71}$$

We discuss how this integration can be performed over the entire free-surface in Appendix G.

To solve for $F_j^{21a.ii}$ we only consider the case for $U_1 = U_2 = 0$. Thus, $\boldsymbol{s} \cdot \nabla = U_6 \partial/\partial\theta$. We will follow the same logic as done for $F_j^{21a.i}$, with the addition of one more piece of information. We note that many authors who have solved the unsteady potential explicitly, as in [45] and [129], take advantage of the circumferential symmetry of the problem and decompose the incident and scattering potentials into the form,

$$\bar{\varphi}_{20}^D = \sum_{n=0}^{\infty} \bar{\varphi}_n^{D(20)}(r, z) \cos\left[n(\theta - \beta)\right] \tag{F.72}$$

Further,

$$\frac{\partial \bar{\varphi}_{20}^D}{\partial \theta} = -\sum_{n=0}^{\infty} \bar{\varphi}_n^{D(20)}(r, z) n \sin\left[n(\theta - \beta)\right] \tag{F.73}$$

Thus, we follow the Green function decomposition replacing $\bar{\varphi}_{20}^D$ with $\partial \bar{\varphi}_{20}^D/\partial\theta$ in Eq. (F.66), and reorder the derivatives, such that

$$U_6 \iint\limits_{\mathcal{S}_o} \frac{\partial \bar{\varphi}_{20}^D}{\partial \theta} n_6' dS = -U_6 \frac{\sigma_o A_o^2}{2g} \iint\limits_{\mathcal{S}_f} \bar{\psi}_6 \operatorname{Im}\left[\frac{\partial \psi_D}{\partial \theta}\frac{\partial^2 \psi_D^*}{\partial z^2}\right] + \bar{\psi}_6 \operatorname{Im}\left[\psi_D \frac{\partial^3 \psi_D^*}{\partial z^2 \partial \theta}\right] dS \tag{F.74}$$

These integrals are very similar to the ones in Appendix G, since θ and β appear similarly in the trigonometric functions.

The next term considered in this section is $(a.iii)$, which has appeared in other analyses involving a body subject to waves and a constant current. We follow the derivation of [32]. However, we re-derive the equations because although our analysis agrees with the final result, there are some differences in the intermediary steps, such as in their Eq. (53). The conclusion also agrees with Eq. (60) in [130].

We start with a vectorized form of Green's Theorem, using the potential $\bar{\varphi}_{(20)}^D$ and the gradient of the double-body potential φ_{01},

$$\iint\limits_{\mathcal{S}_b \cup \mathcal{S}_f \cup \mathcal{S}_o \cup \mathcal{S}_r} \bar{\varphi}_{20}^D \frac{\partial \nabla \varphi_{01}}{\partial n} - \nabla \varphi_{01} \frac{\partial \bar{\varphi}_{20}^D}{\partial n} dS = 0. \tag{F.75}$$

We utilize the no-penetration condition on the bottom boundary, the far-field conditions and the free-surface condition for $\bar{\varphi}_{01}$, and the body boundary condition for $\bar{\varphi}_{20}^D$, such that

$$\iint\limits_{\mathcal{S}_o} \bar{\varphi}_{20}^D (\boldsymbol{n} \cdot \nabla) \nabla \varphi_{01} dS = \iint\limits_{\mathcal{S}_f} \nabla \varphi_{01} \frac{\partial \bar{\varphi}_{20}^D}{\partial n} dS, \tag{F.76}$$

where we have used the definition $\boldsymbol{n}\cdot\nabla = \partial/\partial n$. We now take a digression into a discussion involving a variant of Stokes' Theorem so that we may transform the left-hand side of the equation.

A variant of Stokes' Theorem is,

$$\iint_{\mathcal{S}} \nabla(\boldsymbol{F}\cdot\boldsymbol{n}) - (\nabla\cdot\boldsymbol{F})\boldsymbol{n}dS = \int_{\mathcal{C}} \hat{\boldsymbol{r}}\times\boldsymbol{F}dl \tag{F.77}$$

where $\mathcal{C}$ is a boundary of the surface $\mathcal{S}$, and r is a unit vector along that boundary, following the right-hand rule. We substitute $\boldsymbol{F} = \bar{\varphi}_{20}^{D}\nabla\varphi_{01}$, such that

$$\iint_{\mathcal{S}} \nabla(\bar{\varphi}_{20}^{D}\nabla\varphi_{01}\cdot\boldsymbol{n}) - (\nabla\bar{\varphi}_{20}^{D}\cdot\nabla\varphi_{01})\boldsymbol{n}dS = \int_{\mathcal{C}} \bar{\varphi}_{20}^{D}(\hat{\boldsymbol{r}}\times\nabla\varphi_{01})dl \tag{F.78}$$

The first term can be rewritten using vector identities as,

$$\begin{aligned}\nabla(\bar{\varphi}_{20}^{D}\nabla\varphi_{01}\cdot\boldsymbol{n}) = {}& (\bar{\varphi}_{20}^{D}\nabla\varphi_{01}\cdot\nabla)\boldsymbol{n} + (\boldsymbol{n}\cdot\nabla\bar{\varphi}_{20}^{D})\nabla\varphi_{01} \\ & + \bar{\varphi}_{20}^{D}(\boldsymbol{n}\cdot\nabla)\nabla\varphi_{01} + \bar{\varphi}_{20}^{D}\nabla\varphi_{01}\times(\nabla\times\boldsymbol{n}) + \bar{\varphi}_{20}^{D}\boldsymbol{n}\times(\nabla\times\nabla\varphi_{01}).\end{aligned} \tag{F.79}$$

The last term is null due to vector identities. For a vertical cylinder, $\nabla\times\boldsymbol{n} = 0$ on the wall boundary, canceling the fourth term, which also renders the first term null. We use the body boundary condition for $\bar{\varphi}_{20}^{D}$ to render the second term null. Thus only the third term non-zero. Therefore, we have

$$\iint_{\mathcal{S}} \bar{\varphi}_{20}^{D}(\boldsymbol{n}\cdot\nabla)\nabla\varphi_{01}dS = \iint_{\mathcal{S}} (\nabla\bar{\varphi}_{20}^{D}\cdot\nabla\varphi_{01})\boldsymbol{n}dS, \tag{F.80}$$

where we have used the fact that for a cylinder moving in the horizontal plane $\hat{\boldsymbol{r}} = [0\hat{e}_\theta, 1\hat{e}_r, 0\hat{k}]^T$ in cylindrical coordinates. The insertion of this term into Eq. (F.76), yields,

$$\iint_{\mathcal{S}_o} (\nabla\bar{\varphi}_{20}^{D}\cdot\nabla\varphi_{01})\boldsymbol{n}dS = \iint_{\mathcal{S}_f} \nabla\varphi_{01}\frac{\partial\bar{\varphi}_{20}^{D}}{\partial n}dS, \tag{F.81}$$

which is Eq. (57) in [32] and Eq. (60) in [130]. Since $U_1 = U_2 = 0$ and $n_6 = -x_0 n_2 + y_0 n_1$

$$\iint_{\mathcal{S}_o} \nabla\bar{\varphi}_{20}^{D}\cdot\nabla\varphi_{01}n_6 dS = -x_0 U_6 \iint_{\mathcal{S}_f} f^{(20)}\frac{\partial\bar{\psi}_D}{\partial y'}dS + y_0 U_6 \iint_{\mathcal{S}_f} f^{(20)}\frac{\partial\bar{\psi}_D}{\partial x'}dS \tag{F.82}$$

This integration is very similar to the one done for the previous terms and the reader is referred to Appendix G for further discussion on the integration over the free-surface.

The term in $(a.iv)$ can be dealt with in exactly the same way, since we are disregarding terms $\mathrm{O}(\mathcal{A}_k U_j)$ and thus only considering $\check{\psi}_D$. The term $F^{(a.iv)}$ can be represented by,

$$\iint_{\mathcal{S}_o} (\nabla\varphi_{11}\cdot\nabla\varphi_{10})\boldsymbol{n}dS = \iint_{\mathcal{S}_f} \nabla\varphi_{10}\frac{\partial\check{\psi}_D}{\partial n}dS, + \mathrm{O}\left(\mathcal{A}_k^{(0)}U_j\right) + ... \tag{F.83}$$

where the inhomogeneous free-surface boundary condition for φ_{11} given in the right-hand side of Eq. (2.39) can be utilized. With $U_1 = U_2 = 0$, the inhomogeneous term is,

$$\begin{aligned}\mathcal{F}_D[\psi_D]\Big|_{U_1=U_2=0} = &-U_6\frac{2i\sigma_o A_o}{g}\left(-y_0\frac{\partial\psi_D}{\partial x}+x_0\frac{\partial\psi_D}{\partial y}+\frac{\partial\psi_D}{\partial\theta}-\nabla\bar{\psi}_6\cdot\nabla\psi_D\right)\\ &-U_6\frac{2i\sigma_o A_o}{g}\left(\frac{\partial\psi_D}{\partial\beta}+\frac{1}{2}\psi_D\frac{\partial^2\bar{\psi}_6}{\partial z^2}\right),\end{aligned} \tag{F.84}$$

Let,

$$f^{(11)} = \frac{1}{U_6}\mathcal{F}_D[\psi_D]\Big|_{U_1=U_2=0}. \tag{F.85}$$

Thus,

$$\iint_{\mathcal{S}_o}(\nabla\varphi_{11}\cdot\nabla\varphi_{01})n_6 dS = -x_0U_6A_o\iint_{\mathcal{S}_f}f^{(11)}\frac{\partial\psi_D}{\partial y'}dS + y_0U_6A_o\iint_{\mathcal{S}_f}f^{(11)}\frac{\partial\psi_D}{\partial x'}dS. \tag{F.86}$$

The integrand consists of terms that are either products of the diffraction potential, alone, or multiplied by the yaw slow-drift potential. The integration of the terms can be solved using the algorithm described in Appendix G, by setting the arbitrary function $f(r) = r$. For compactness, these terms will not be solved for explicitly.

Terms F_j^{21b-d}

All terms in F_j^{21b-d} are at least $\mathrm{O}\left(\mathcal{A}_j^{(0)}U_k\right)$ and will not be considered for the wave-drift damping.

Term F_j^{21e}

$$F_j^{21e} = \frac{1}{2}\,\mathrm{Re}\left[\boldsymbol{\alpha}^{(\mathbf{1})}\times\boldsymbol{F}^{(\mathbf{10})*}+\boldsymbol{\xi}^{(\mathbf{1})}\times\boldsymbol{M}^{(\mathbf{10})*}\right]. \tag{F.87}$$

Thus $F_j^{21e} = \mathrm{O}\left((A_o+\mathcal{A}_j^{(0)})\mathcal{A}_k^{(1)}\right)$ and is not relevant to this section.

Term F_j^{21f}

We substitute the linearized free-surface conditions found in Eqs. (2.23a) and (2.23b), into Eq. (2.112) and obtain

$$F_j^{21f} \underset{\mathsf{Re}}{=} \frac{\rho_o}{2g}\int_{\mathcal{C}_o}\Bigg(\underbrace{\sigma_o^2\varphi_{10}\varphi_{11}^*}_{(i)} + \underbrace{i\sigma_o\varphi_{10}\boldsymbol{s}\cdot\nabla\varphi_{10}^*}_{(ii)} - \underbrace{i\sigma_o\nabla\varphi_{01}\cdot\nabla\varphi_{10}^*}_{(iii)} \\ - \underbrace{\sigma_o k_o(U_1\cos\beta + U_2\sin\beta)(\varphi_{10}^*\cdot\varphi_{10})}_{(iv)} - \underbrace{i\sigma_o U_6\left(\frac{\partial\varphi_{10}^*}{\partial\beta}\cdot\varphi_{10}\right)}_{(v)}\Bigg) n_j' dl \tag{F.88}$$

Only terms $F_j^{21f.ii-v}$ will contribute to the slow-drift wave damping. Further if $U_1 = U_2 = 0$, then term $F_j^{21f.iv}$ is null and $\boldsymbol{s}\cdot\nabla = U_6\partial/\partial\theta$. Therefore,

$$F_j^{21f} \underset{\mathsf{Re}}{=} -\frac{i\sigma_o\rho_o a A_o^2}{2g}U_6\int_0^{2\pi}\left(\psi_D\frac{\partial\psi_D^*}{\partial\theta} - \nabla\bar{\psi}_6\cdot\nabla\psi_D^* - \frac{\partial\psi_D^*}{\partial\beta}\psi_D\right)(x_o\sin\theta - y_o\cos\theta)d\theta. \tag{F.89}$$

The integration here is only over the azimuthal angle and is similar to the integration performed for $\bar{\mathcal{X}}_j^{(2)}$, shown in Eq. (F.50).

Appendix G

Methods for Integration of Bessel Functions over Infinite, Free Surface

In this section, we consider the integration of the terms that arose in the calculation of the wave-drift damping in Appendix F.7.2, in such equations as Eq. (F.71). Using our definitions of the diffraction potentials in Eq. (2.76), we can write the first integral in Eq. (F.71) as,

$$
\begin{aligned}
-\frac{gA_o^2}{2a\sigma_o}\int_0^{2\pi}\int_a^{\infty}\bar{\psi}_6\,\mathrm{Im}\left[\frac{\partial\psi_D}{\partial\beta}\frac{\partial^2\psi_D^*}{\partial z^2}\right] = \\
\left(-y_0\sum_{\ell=0}^{\infty}\cos(\beta_\ell)L_\ell(r)\cos\theta + x_0\sum_{\ell=0}^{\infty}\cos(\beta_\ell)L_\ell(r)\sin\theta\right) \\
\mathrm{Im}\left[\sum_{m=0}^{\infty}\sum_{p=0}^{\infty}Z_p(h)G_p^{(m)}(r)m\sin(m(\theta-\beta))\sum_{n=0}^{\infty}\sum_{q=0}^{\infty}Z_q''(h)G_q^{(n)*}(r)\cos(n(\theta-\beta))rdrd\theta\right]
\end{aligned}
\tag{G.1}
$$

Much like when solving for the steady, second-order forces, F_j^{20} the summations can be simplified by noting that the integration over the azimuthal angle θ will only be non-zero when $m = n+1$, $n = m+1$ or $n+m = 1$. Since performing this integration is trivial, we restrict our attention to the integration in the radial direction. In order to explicitly see how the Bessel and Hankel functions come in, we write

$$G_0^{(n)}(r) = g_J^{(n)}J_n(k_or) + g_H^{(n)}H_n(k_or) \tag{G.2a}$$
$$G_q^{(n)}(r) = g_q^{(n)}K_n(k_qr) \tag{G.2b}$$
$$L_0(r) = \ell_0\frac{1}{r} \tag{G.2c}$$
$$L_\ell(r) = \ell_\ell K_1(k_or) \tag{G.2d}$$

where $g_J^{(n)}$, $g_H^{(n)}$, $g_q^{(n)}$, ℓ_ℓ can be inferred from Eq. (2.78). The Hankel function of the first kind $H_n(k_or)$ is simply a summation of Bessel functions of the first and second kind,

$$H_n(k_or) = J_n(k_or) + iY_n(k_or). \tag{G.3}$$

We note that $Y_n(k_or) \in \mathbb{R}$ for any $n \in \mathbb{Z}$ and $r > 0$. We first focus on the integrals that include terms where the integration is over an infinite domain and the integrand does not exponentially decay, that is when $\ell = p = q = 0$. The substitution of the G_q and L_ℓ terms found in Eq. (G.2) into Eq. (G.1) and ignoring constants, we find that there will be multiple

types of integrals that will naturally occur, such as

$$JJ_n = \int_a^\infty J_{n+1}(k_o r) J_n(k_o r) dr \tag{G.4a}$$

$$JY_n = \int_a^\infty J_{n+1}(k_o r) Y_n(k_o r) dr \tag{G.4b}$$

$$YJ_n = \int_a^\infty Y_{n+1}(k_o r) J_n(k_o r) dr \tag{G.4c}$$

$$YY_n = \int_a^\infty Y_{n+1}(k_o r) Y_n(k_o r) dr \tag{G.4d}$$

$$\tag{G.4e}$$

These integrals are well-studied since they occur in other scientific fields such as elasticity, electrodynamics, biophysics, and geophysics. The author of [131] developed an algorithm to use the Integration, Summation and Extrapolation (ISE) technique on products of Bessel functions of arbitrary order. The trick is to recast the product of the Bessel functions as the sum of two oscillating functions, one fast and one slow and then use the ISE technique twice. To get an actual error of less than 10^{-6} for an integral similar to JJ_0 only 200-250 function evaluations are necessary (see Fig. 4 in [131]). This type of algorithm was updated and implemented in MATLAB by the authors of [132] in the function *IIPBF.m* to compute the integrals of products of Bessel functions and an arbitrary well-behaved function on the interval $[0, \infty)$. With few small tweaks to their algorithm, the integrals can be computed on the interval $[a, \infty)$. In this way the integration over the entire free-surface can be computed in an efficient, complete and robust manner.

If we restrict our attention to the case when $l > 0$ or $p > 0$ or $q > 0$, then a modified Bessel function of the second kind appears in the integrand. Thus, we shall see terms such as

$$KZZ_n = \int_a^\infty K_1(k_o r) Z_{n+1}(k_o r) Z_n(k_o r) r dr \tag{G.5a}$$

$$KZ_n = \int_a^\infty K_{n+1}(k_o r) Z_n(k_o r) dr \tag{G.5b}$$

$$ZK_n = \int_a^\infty Z_{n+1}(k_o r) K_n(k_o r) dr. \tag{G.5c}$$

where Z_n represents a Bessel function such as J_n, Y_n or K_n. These integals can be solved using standard integration techniques (such as Gaussian quadrature) due to the convergence of the integrand. The exponential decay of the modified Bessel function of the second kind $K_n(k_o r)$, which represent the evanescent modes of the solution, drives the integrand to zero as $r \to \infty$. In fact, the standard MATLAB library includes the adaptive Gauss-Kronrod quadrature function *quadgk*, which can carry out integration over an infinite interval. For arbitrary n, the integral can be computed in approximately 0.5 sec on a standard workstation.